



HAL
open science

Study of a MagnetoElectric Transducer to Wireless Power Medical Implants

Giulia Rizzo

► **To cite this version:**

Giulia Rizzo. Study of a MagnetoElectric Transducer to Wireless Power Medical Implants. Electromagnetism. Université Paris-Saclay, 2020. English. NNT : 2020UPAST012 . tel-03182754

HAL Id: tel-03182754

<https://theses.hal.science/tel-03182754v1>

Submitted on 26 Mar 2021

HAL is a multi-disciplinary open access archive for the deposit and dissemination of scientific research documents, whether they are published or not. The documents may come from teaching and research institutions in France or abroad, or from public or private research centers.

L'archive ouverte pluridisciplinaire **HAL**, est destinée au dépôt et à la diffusion de documents scientifiques de niveau recherche, publiés ou non, émanant des établissements d'enseignement et de recherche français ou étrangers, des laboratoires publics ou privés.

Study of a MagnetoElectric Transducer to Wireless Power Medical Implants

Thèse de doctorat de l'université Paris-Saclay

École doctorale n°575 Electrical, optical, bio-physics, and engineering (EOBE)
Spécialité de doctorat : Electronique et Optoélectronique, Nano- et Microtechnologies
Unité de recherche : Université Paris-Saclay, CNRS, Centre de Nanosciences et
de Nanotechnologies, 91120, Palaiseau, France
Réfèrent : Faculté des sciences d'Orsay

Thèse présentée et soutenue à Paris-Saclay,
le 18/12/2020, par

Giulia RIZZO

Composition du Jury

Adrien BADEL

Professeur, Université Savoie Mont Blanc

Président

Mickaël LALLART

Professeur, INSA de Lyon

Rapporteur & Examineur

Hakeim TALLEB

Maître de Conférences, HDR, Sorbonne Université

Rapporteur & Examineur

Ilangko BALASINGHAM

Professeur, Norwegian University of Science, and Technology

Examineur

Vincent LOYAU

Maître de Conférences, ENS Paris-Saclay

Examineur

Elie LEFEUVRE

Professeur, Université Paris Saclay

Directeur de thèse

Jean Christophe LOURME

CEO ValoTec, and MELLISIM

Co-Encadrant de thèse

À ma mère

Acknowledgements

Je tiens à remercier tout particulièrement les membres de mon jury Mr. Badel, Mr. Lallart, Mr. Talleb, Mr. Balasingham et Mr. Loyau, pour avoir acceptés de lire ce manuscrit et d'évaluer mon travail de thèse.

Je souhaite dire vraiment merci à mon directeur de thèse, Mr. Elie Lefevre, et mon co-encadrant, Mr. Lourme, pour avoir acceptés de me suivre et m'encadrer tout au long de cette thèse. Merci pour m'avoir donné la possibilité de faire partie du projet européen WIBEC, pour tous les trainings suivis et aussi pour toutes les conférences auxquelles j'ai pu assister.

Thank you to all the WiBEC team for the incredible journey that was this ITN. I could not have imagined a better PhD program. I had the possibility to join the groups of Ovesco Endoscopy AG, MicroPort CRM and Oslo University Hospital during the secondments, and meet new colleagues. Thank you for these amazing experiences.

Merci aux collègues du C2N pour m'avoir accueillie dans leur équipe pendant les trois années de thèses. Merci pour toute la connaissance transmise, les aides, les pauses café ensemble, les moments partagés. Merci à tous les professeurs, les post-docs et les doctorants. Merci surtout à Alexiane pour la précieuse amitié née à un tournoi de baby-foot et qui restera pour l'avenir.

Également je remercie le groupe de ValoTec, avec une mention spéciale pour Thomas pour tous les moments partagés à VTC et dehors, avec et sans café, en face d'un oscilloscope ou derrière son écran pc.

Un grazie speciale a Maria Luisa, Maria José e Chloé che ci sono sempre. Grazie agli amici di Parigi, del 2Bis, gli amici di Torino, di Houston, del Vietnam, di Mirandola, di Grenoble. Un grazie enorme, perchè non sarebbe stato lo stesso senza di voi !

Infine, ultimo ma assolutamente non ultimo, vorrei ringraziare la mia famiglia che mi è sempre stata accanto e permesso di fare questo percorso. Grazie per i vostri insegnamenti, i vostri valori e la vostra fiducia. Grazie ai miei genitori, a mio fratello e a Piera.

Résumé en français

De nos jours, les dispositifs médicaux actifs implantables jouent un rôle important dans la surveillance, le diagnostic et le traitement des patients, grâce à des fonctionnalités de plus en plus étendues. Au cours des dernières décennies, l'accent a été mis sur le développement de dispositifs implantables plus durables et moins invasifs. Ces deux aspects sont directement liés aux sources d'énergie utilisées pour alimenter les implants. En fait, dans un dispositif implantable, la majeure partie du volume disponible n'est pas occupée par l'électronique qui gère ses fonctions, mais par la batterie qui l'alimente. Le volume occupé par la batterie est assez directement lié à la durée de vie de l'appareil, avec toutefois une limite liée au phénomène d'auto-décharge. Pour certains types d'implants à long terme tels que les stimulateurs cardiaques, il est nécessaire de remplacer l'implant déchargé au moyen de procédures chirurgicales coûteuses et invasives. Aujourd'hui, deux approches ont été développées, afin d'éviter les batteries à usage unique et les inconvénients associés. La première approche consiste à récupérer l'énergie présente à l'intérieur du corps, disponible au niveau de l'implant, et la deuxième consiste à transmettre l'énergie depuis l'extérieur du corps humain. Dans le premier cas, par exemple, il est possible d'alimenter un stimulateur cardiaque de nouvelle génération en convertissant l'énergie mécanique provenant des battements cardiaques, grâce à un MEMS piézoélectrique. Dans le second cas, la télé-alimentation utilisant le phénomène d'induction magnétique entre deux bobines (l'une implantée, l'autre à l'extérieur du corps) est une technologie de plus en plus répandue dans le domaine biomédical, comme pour la recharge d'un téléphone portable sans contact dans la vie de tous les jours. La principale différence entre ces deux approches est le niveau de puissance qui peut être obtenu : les MEMS de récupération d'énergie mécanique peuvent fournir des microwatts d'énergie électrique, tandis que la transmission d'énergie sans fil implique des puissances allant du milliwatt au watt.

Cette thèse porte sur l'étude d'un système de télé-alimentation. En général, cette technologie permet d'alimenter les dispositifs médicaux implantables grâce aux interactions magnétiques entre une bobine émettrice externe et une bobine réceptrice implantée dans le corps. L'originalité de l'approche développée dans cette thèse consiste à utiliser un transducteur magnétoélectrique (ME) à la place de la bobine réceptrice. Ce transducteur magnétoélectrique est un dispositif hybride, formé de deux matériaux liés mécaniquement, l'un magnétostrictif et l'autre piézoélectrique. Le matériau magnétostrictif présente un couplage entre les grandeurs magnétiques et mécaniques. Il est capable de se déformer élastiquement sous l'effet d'un champ magnétique. Cette propriété est réversible, et elle est liée à un changement de son aimantation interne. Le matériau piézoélectrique assure un couplage entre les grandeurs mécaniques et électriques. Soumis à une contrainte mécanique, sa déformation élastique opère une conversion d'énergie mécanique en énergie électrique (effet piézoélectrique direct). Cette propriété est également réversible (effet piézoélectrique inverse). Par conséquent, le dispositif ME considéré assure le couplage entre les grandeurs électriques et magnétiques par l'intermédiaire d'une déformation mécanique. Le transducteur magnétoélectrique assure ainsi la conversion d'énergie du domaine magnétique et au domaine électrique et vice versa. Dans l'application considérée, le champ magnétique est généré par la bobine émettrice externe. Il en résulte une déformation élastique du transducteur qui permet de générer de l'électricité. Cette énergie électrique peut ensuite être extraite et utilisée pour recharger ou alimenter le dispositif implanté. Comparativement à une bobine réceptrice classique, le

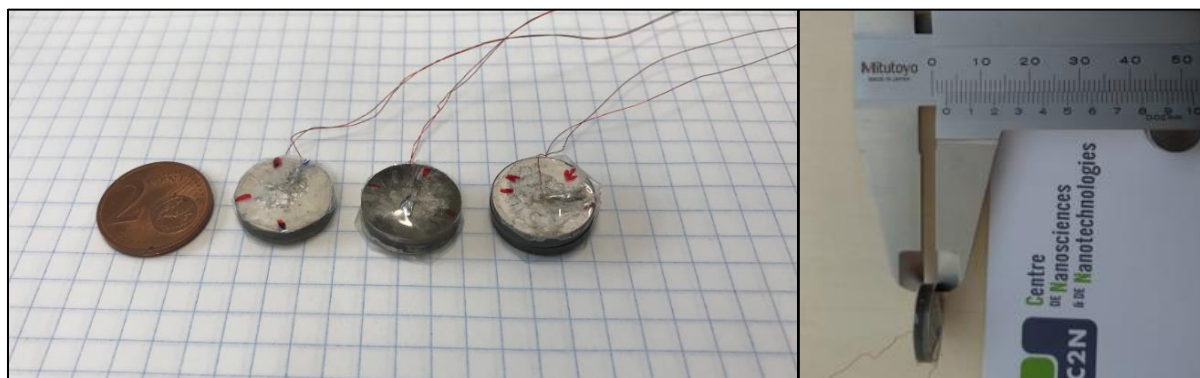


Figure 0.1 – Photo de composites magnétoélectriques de 16 mm de diamètre et d'épaisseurs différentes étudiés au cours de cette thèse.

transducteur ME pourrait permettre de réduire la dépendance de l'efficacité du système de transmission d'énergie à un bon alignement entre l'émetteur et le récepteur. Cet aspect est très important dans le domaine des implants médicaux actifs, dont la localisation et l'orientation sont parfois difficiles à connaître précisément et à suivre en temps réel, notamment pour les implants connectés à des organes ou des muscles. Dans ce but, un transducteur magnétoélectrique a été développé en se basant sur les propriétés magnétostrictives et piézoélectriques de matériaux disponibles commercialement. Plusieurs échantillons ont été fabriqués et caractérisés dans le but de quantifier expérimentalement la relation entre les dimensions, la composition et l'efficacité du composite en termes de transduction d'énergie. La littérature du domaine, peu abondante, présente quelques exemples de transducteur ME, notamment sous la forme d'empilements de plaques rectangulaires. Dans cette thèse, la forme de disque a été choisie pour favoriser la pénétration du champ magnétique dans le transducteur. Deux diamètres de 10 mm et 16 mm ont été retenus (Figure 0.1). Plusieurs configurations et compositions de matériaux ont été étudiées, avec une épaisseur totale comprise entre 2 mm et 5 mm.

Un dispositif de test, assez éloigné d'une configuration implantée, a été réalisé dans le but d'étudier l'influence respective des composantes continue et alternative du champ magnétique appliqué sur l'échantillon sur la tension et la puissance électrique générée. Dans ce dispositif, le champ magnétique continu est généré par une paire d'aimants permanents, tandis que le champ magnétique alternatif est généré à l'aide d'une bobine placée autour de l'échantillon (Figure 0.2).

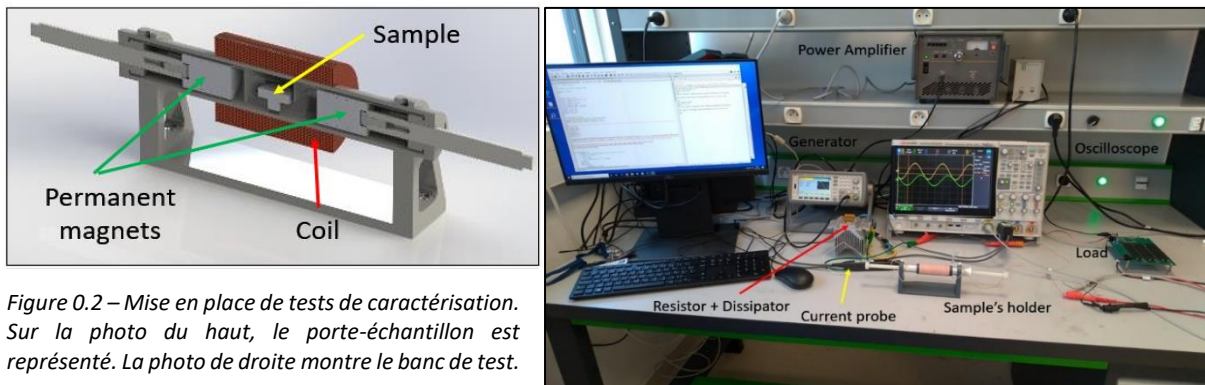


Figure 0.2 – Mise en place de tests de caractérisation. Sur la photo du haut, le porte-échantillon est représenté. La photo de droite montre le banc de test.

Ce travail de caractérisation a permis d'identifier la gamme de fréquences optimale, c'est-à-dire celle dans laquelle on bénéficie d'un mode de résonance favorable du transducteur. Les échantillons de grand diamètre (16 mm) permettent d'atteindre une puissance de sortie de 40 mW (Figure 0.3) dans les conditions optimales de champ continu et dans les conditions maximales de champ alternatif que le banc de test permet de générer. Les tendances observées tendent à montrer que les échantillons les plus épais, avec une fraction volumique de matériau magnétostrictif plus faible, délivrent une puissance électrique inférieure (de l'ordre de 30%) et ont une densité de puissance plus faible que celle des échantillons les plus mince, avec une fraction volumique de matériau magnétostrictif plus élevée. Ainsi, un échantillon de 16 mm de diamètre et de 5 mm d'épaisseur contenant 20% de matériau magnétostrictif délivre une puissance inférieure à celle d'un échantillon de 10 mm de diamètre et de 2 mm d'épaisseur contenant 50% de matériau magnétostrictif (respectivement PMP-20% et MP-50%, Figure 0.3). L'ensemble des résultats obtenus ouvre des perspectives intéressantes de miniaturisation du transducteur ME tout en conservant une bonne efficacité de transfert d'énergie sans fil.

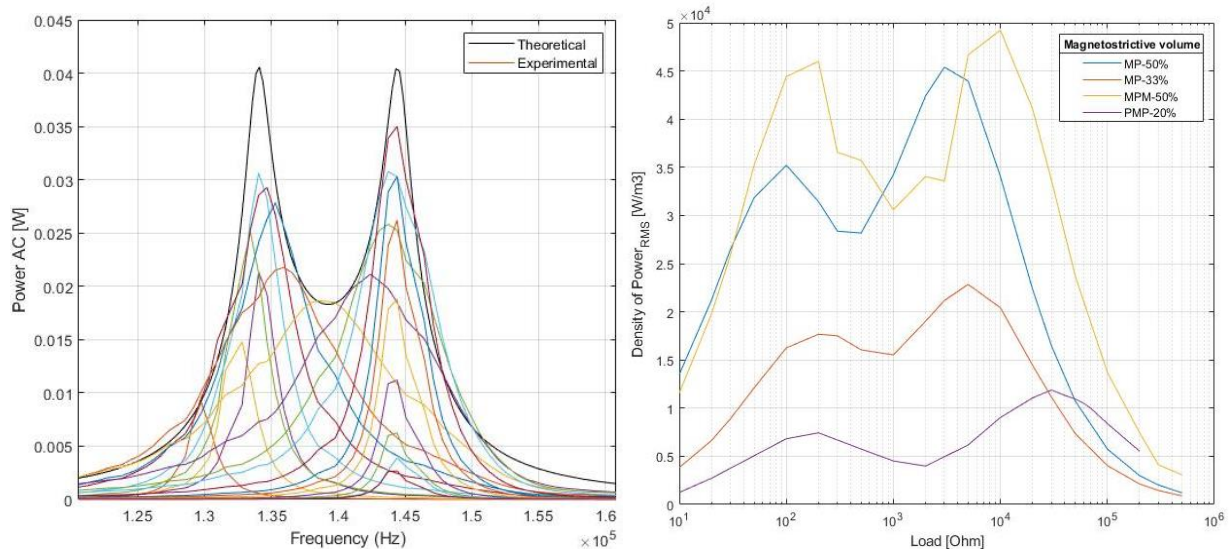


Figure 0.3 – Courbes de gauche : puissance en fonction de la fréquence pour différentes charges résistives connectées à l'échantillon. Les courbes colorées représentent les valeurs expérimentales, la courbe noire correspond à la puissance maximale donnée par modèle théorique linéaire. Le graphique de droite représente les valeurs maximales de densité de puissance de quatre échantillons différents.

Les résultats expérimentaux ont également été utilisés pour identifier les paramètres d'un modèle théorique linéaire permettant de reproduire le comportement du transducteur ME. Il s'agit d'un modèle assez classique, basé sur celui d'un résonateur piézoélectrique (modèle de Mason) auquel est ajouté un terme de couplage magnétostrictif. Les phénomènes couplés entre la partie magnétostrictive et la couche piézoélectrique du transducteur sont représentés par trois blocs principaux, reliés par deux coefficients de couplage. Le premier coefficient, φ_m , traduit le couplage magnéto-mécanique provenant du matériau magnétostrictif ; le deuxième, φ_p , représente l'effet élasto-électrique du matériau piézoélectrique (Figure 4.9).

Afin de déterminer les paramètres du modèle, une première mesure de tous les dispositifs a été réalisée en régime statique (champ magnétique continu uniquement). L'impédance du dispositif magnétoélectrique a été mesurée sous différents champs magnétiques DC. A partir de ce premier test, il a été possible de quantifier l'influence du champ DC sur la fréquence de résonance du système et sur les paramètres de rigidité mécanique et d'amortissement. Une deuxième série de mesures a été réalisée en régime dynamique, en appliquant un champ magnétique alternatif et un champ DC, et en mesurant la tension de sortie en condition de circuit ouvert. À partir de ces deux séries de mesures, il est théoriquement possible de prédire le comportement des dispositifs ME, comme par exemple déterminer la puissance de sortie sur une charge résistive.

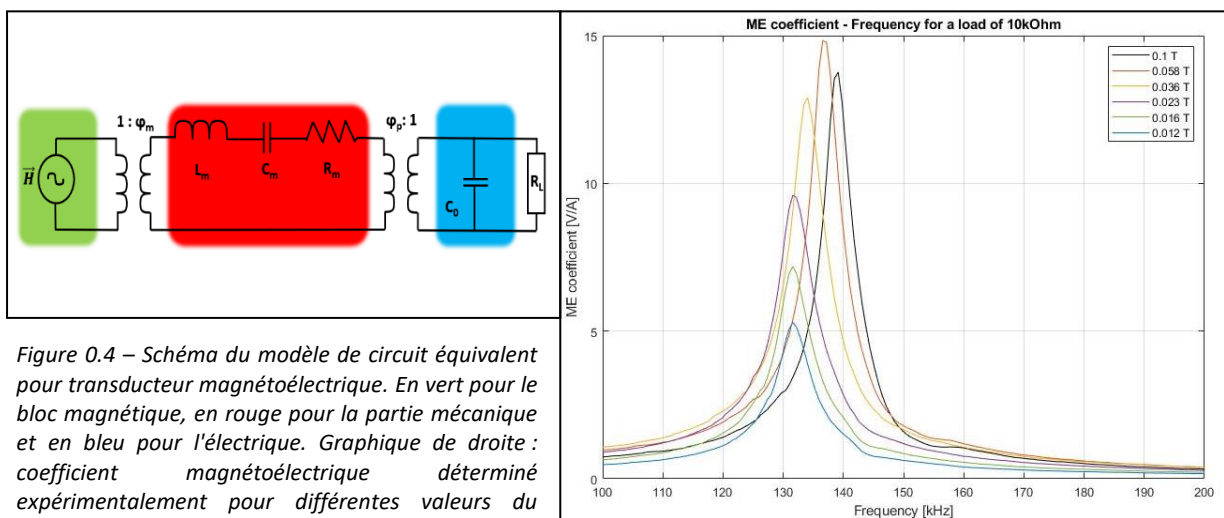


Figure 0.4 – Schéma du modèle de circuit équivalent pour transducteur magnétoélectrique. En vert pour le bloc magnétique, en rouge pour la partie mécanique et en bleu pour l'électrique. Graphique de droite : coefficient magnétoélectrique déterminé expérimentalement pour différentes valeurs du champ DC.

La méthode d'identification permet de déterminer l'ensemble des paramètres à partir d'une mesure expérimentale. Les puissances calculées à l'aide du modèle présentent un écart de l'ordre de 10% par rapport aux mesures expérimentales, ce qui est acceptable. Il pourrait être amélioré en tenant compte des non-linéarités, notamment celles qui proviennent du matériau magnétostrictif. La prise en compte de l'échauffement induit par les courants de Foucault et de l'effet de la température sur le comportement du système serait un prolongement intéressant.

De manière à s'approcher davantage de l'application visée, dans laquelle le transducteur magnétoélectrique étudié contribue à alimenter un dispositif médical implantable par la charge de sa batterie interne, un circuit redresseur a été ajouté dans le dispositif étudié. En effet, le transducteur magnétoélectrique génère une tension alternative qu'il convient de redresser pour recharger la batterie. Un circuit redresseur en pont complet et un circuit redresseur en demi-pont ont été successivement ajoutés au circuit. L'ensemble des caractérisations a été répété avec l'ensemble des échantillons et le modèle théorique a été modifié pour intégrer cette partie du circuit. Le transducteur ME associé à un redresseur conduit à une puissance de sortie plus faible que sans redresseur (34 mW au maximum, contre 40 mW), ce qui s'explique en partie par les pertes dues aux diodes. Les puissances obtenues avec les deux types de redresseur sont assez similaires, la tension de sortie du demi-pont étant pratiquement deux fois plus importante que celle du pont complet. Les pertes dues aux diodes sont plus faibles en raison de leur nombre déduit dans le circuit en demi-pont et de la tension plus élevée du transducteur. Du point de vue du modèle, l'écart se situe toujours aux alentours de 10% par rapport aux valeurs expérimentales.

Une partie du travail expérimental est axé sur la comparaison qualitative de l'efficacité du transfert de puissance d'un système de bobine-ME et d'un système de bobine-bobine, sous différentes orientations relatives de l'émetteur et du récepteur. L'objectif était de recréer les conditions pratiques d'incertitude de positionnement relatif du bloc émetteur hors corps et du bloc récepteur interne. Les échantillons ont été successivement fixés sur le bras d'un robot mécanique à 5 degrés de liberté, permettant de déplacer l'échantillon avec précision selon différentes orientations et distances de l'émetteur. Pour cette expérience, le dispositif émetteur de champ magnétique utilisé est composé d'une bobine sur ferrite et de deux aimants permanents. La configuration originale de cet émetteur de champs continu et alternatif présente l'intérêt d'être assez efficace et utilisable dans le cas d'un implant (Figure 2.11).

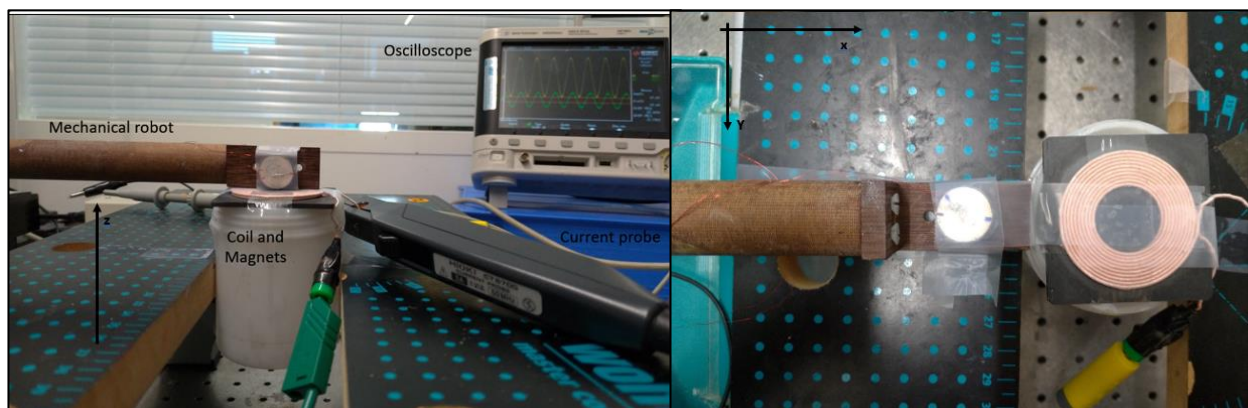


Figure 0.5 – Banc de test utilisé pour les tests *in vitro*.

Trois récepteurs différents ont été comparés : une bobine sans noyau, une bobine avec noyau de ferrite et un transducteur ME de mêmes dimensions. Le récepteur ME présente l'avantage de produire de l'énergie électrique dans toutes les orientations par rapport à l'émetteur. Le matériau magnétostrictif présente un axe préférentiel de magnétisation le long duquel le transducteur ME est le plus efficace. Cependant, l'expérience montre que l'on atteint un niveau de tension de sortie (et donc de puissance) exploitable même en dehors de l'alignement optimal. Par exemple, on mesure 1,5 V en sortie du récepteur à 30 mm de distance de l'émetteur dans la condition de pire alignement, alors que la tension des bobines réceptrices est nulle dans le cas du pire alignement. Le transducteur ME permet donc d'avoir une transmission de puissance non-nulle quelle que soient la position et l'orientation relative entre le bloc externe et l'implant. Rappelons qu'il s'agit d'un aspect important pour l'application visée, la position des implants étant très difficile à suivre en temps réel, en particulier pour les dispositifs connectés à des organes ou des muscles. L'intérêt de la configuration particulière de l'émetteur a été confirmée dans le cadre d'une expérience réalisée dans un milieu constitué de viande animale. Ces tests ont permis de vérifier la répétabilité des mesures précédemment réalisées avec le robot sous différentes orientations du récepteur. La viande de canard a été choisie pour la conformation des tissus adipeux à l'intérieur de la viande. Les résultats obtenus sont très encourageants, aussi bien au niveau de l'émetteur que du récepteur, et ouvrent d'intéressantes perspectives pour la télé-alimentation (ou télé-recharge) de dispositifs implantables.

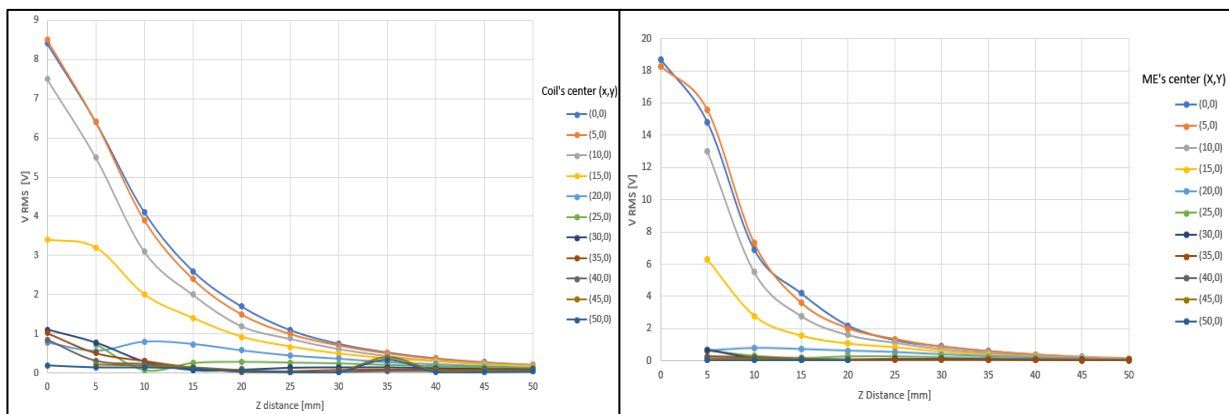


Figure 0.6 – Résultats de tests in-vitro. Le graphique à gauche représente le système bobine-bobine en position parallèle et le graphique de droite le système bobine-transducteur magnétoélectrique en position parallèle, pour différents hauteurs (z) et décalage horizontales (x).

En conclusion, cette thèse rapporte des résultats prometteurs concernant l'utilisation de transducteurs magnétoélectriques pour le transfert d'énergie sans fil pour la recharge et l'alimentation de dispositifs médicaux implantables. L'approche expérimentale développée permet de tirer des conclusions générales concernant l'effet de la composition du transducteur sur ses performances. Cependant, aller vers un transducteur ME optimisé nécessiterait de développer un modèle multiphysique à éléments finis en tenant compte des propriétés physiques réelles des matériaux, et en particulier des non-linéarités du matériau magnétostrictif. Un tel modèle permettrait également de rendre compte de l'échauffement induit par les courants de Foucault et d'éventuelles contraintes thermomécaniques influant sur les propriétés et performances du composite ME. Un tel modèle s'avère nécessaire pour déterminer la composition et les dimensions optimales du transducteur dans des conditions de fonctionnement données. Comme indiqué précédemment, les résultats expérimentaux obtenus ouvrent la perspective de miniaturiser le transducteur ME sans perdre en efficacité ni en densité de puissance. Dans cette perspective, il serait intéressant d'étudier le potentiel de nano-composites ME. De tels développements permettraient d'aller vers des transducteurs magnétoélectriques intégrés, compact et performants adaptés aux contraintes des dispositifs médicaux implantables. Des matériaux à magnétostriction géante autres que le Terfenol-D utilisé au cours de cette thèse, tels que le Galfenol et le MetGlas sont disponibles sur le marché. Il serait intéressant d'explorer les avantages et les limites de la transduction ME en utilisant et en associant ces matériaux par rapport aux résultats de cette thèse et de la littérature. Des ferrites à base de Ni-Zn-Co qui présentent des coefficients de magnétostriction géants pourraient également constituer une alternative intéressante. Enfin, la possibilité d'utiliser un matériau magnétostrictif auto-polarisé, qui ne nécessitant pas de champ magnétique continu, permettrait de simplifier la mise en œuvre de ce mode de transduction dans le contexte d'applications biomédicales.

Les perspectives de poursuite de ce travail sont donc multiples, du point de vue des matériaux, de la fabrication des composites, de la miniaturisation et des modèles multiphysiques. De tels approfondissements permettraient d'aboutir à des solutions performantes ultra compactes pour la transmission d'énergie et la télé-alimentation de dispositifs médicaux implantables.

Cette thèse a été financée par le programme de formation du réseau de formation innovant Marie Skłodowska-Curie Actions de l'Union européenne pour le projet 'Wireless In-Body Environment Communication – (WiBEC)' dans le cadre de la convention de subvention n. 675353

Contextual foreword

This Ph.D. was carried out from the 19th of June 2017 to the 18th of December 2020 (date of the defense) in the Île-de-France region of France.

The Ph.D. was performed between the enterprise ValoTec and the Center for Nanoscience and Nanotechnology (C2N) of the Université Paris-Saclay.

ValoTec stems from Ecole Normale Supérieure de Paris-Saclay (SATIE laboratory), as an enterprise, specialized in their R&D and production projects since 2005. The domain of expertise in technology development is related to active innovative devices (all industries), class IIa IIb and III medical devices (medical technologies), implantable devices, patient treatment devices, and diagnostic devices.

The Université Paris-Saclay is a research university conglomerate existing in various locations of the Île-de-France region including the Saclay plateau near Palaiseau, south-west of Paris. Initially, this Ph.D. was (jointly) performed at the C2N laboratory of the Université Paris-Sud, near Orsay. It was not until late 2018, however, that the laboratory was moved to the Saclay plateau once Université Paris-Sud was absorbed by Université Paris-Saclay.

The Ph.D. also formed part of the European Commission-funded Innovative Training Network 'WiBEC' (Wireless In-Body Environment Communication) consisting of several academic, clinical, and industrial members located throughout Europe. Various training courses (technical and non-technical/horizontal), presentations, and conferences were carried out at all of these member institutions throughout the Ph.D. Several brief secondments were also performed within this context, two-months secondment at Ovesco Endoscopy AG, in Tubingen, Germany, two-months secondment at MicroPort CRM in Clamart, France, and one-month secondment in the University Hospital of Oslo in Oslo, Norway.

Contents

Acknowledgements.....	4
Résumé en français.....	5
Contextual foreword.....	11
List of Abbreviation.....	16
Chapter 1 Active Implantable Medical Devices and their energy sources	17
1. Introduction	19
2. Implantable Medical Device	20
3. Active Implantable Medical Devices.....	21
3.1 Physiological Function.....	21
3.1.1 Cardiovascular devices.....	22
3.1.2 Gastroenterology devices	23
3.1.3 Neural devices.....	24
3.2 Packaging Materials	25
3.2.1 Metals	27
3.2.2 Ceramics, and Composites.....	27
3.2.3 Polymers.....	28
3.3 Power Consumption	28
3.4 Energy sources	29
3.4.1 Battery.....	29
3.4.2 Wireless Power Transmission	30
3.4.3 Energy Harvester.....	32
4. Medical Regulatory	35
5. Conclusion.....	38
6. Bibliography	40
7. List of figures.....	42
8. List of tables.....	43
Chapter 2 Model and Application of a MagnetoElectric transducer	45
1. Introduction	47
2. Magnetic Materials.....	48
2.1 Principles, and structures.....	49
2.2 Fundamental Equations	51
2.3 Magnetostriction	54
2.3.1 Piezomagnetism.....	55
2.3.2 Magnetostrictive materials.....	56

2.4	Applications.....	57
3.	Piezoelectric Materials.....	59
3.1	Principles, and Structures	60
3.2	Fundamental Equations	62
3.3	Oscillation modes/Dynamic Behavior	63
3.4	Type of piezoelectric materials	65
3.5	Applications.....	66
4.	MagnetoElectric Composites	68
4.1	Principles, and structures.....	69
4.2	Fundamental Equations	71
4.2.1	Magnetostrictive Constitutive Equations	72
4.2.2	Piezoelectric Constitutive Equations.....	72
4.2.3	MagnetoElectric Constitutive Equations.....	73
4.3	Equivalent circuit model	74
4.3.1	Static Regime.....	76
4.3.2	Dynamic Regime	78
4.3.3	Output Power, and Optimal Electrical Load.....	79
4.3.4	Model with Rectifier	80
4.4	Considered Materials	82
4.4.1	Magnetostrictive material	82
4.4.2	Piezoelectric material.....	84
4.4.3	Description of the MagnetoElectric Samples.....	85
4.4.4	FEM analysis of radial resonance modes	86
4.5	Application	88
5.	Conclusion.....	90
6.	Bibliography	91
7.	List of figures.....	94
8.	List of tables	95
	Chapter 3 Experimental measurements of a MagnetoElectric transducer	97
1.	Introduction	99
2.	Characterization test.....	100
2.1	Measurement Set up	100
2.2	Circuit Model.....	103
2.2.1	Static regime	103
2.2.2	Dynamic regime	108
2.2.3	Output power.....	111

2.3	MagnetoElectric Samples.....	115
2.4	Characterization Method.....	116
2.5	Results, and Discussion.....	119
3.	Medical Regulatory Compatibility.....	131
4.	In-vitro Test.....	132
4.1	Measurement Set up	133
4.2	Tested Samples	134
4.3	Method.....	136
4.4	Results, and Discussion	137
5.	Phantom Test.....	144
5.1	Measurement Set up	144
5.2	Tested Samples	145
5.3	Method.....	146
5.4	Results, and Discussion	147
6.	Conclusion.....	149
7.	Bibliography	151
8.	List of figures.....	152
9.	List of tables	155
	Chapter 4 Conclusion	157
1.	Conclusion.....	159
2.	Bibliography	161
	Appendix I	163
	Appendix II	165
	Appendix III	168
	Abstracts	205

List of Abbreviation

AIMD – Active Implantable Medical Device

BMI – Brain Machine Interface

CRT - Cardiac Resynchronization Therapy

D.U.T. – Device Under Test

EMF – Electro Magnetic Field

GI - Gastro-Intestinal

ICD - Implantable Cardioverter - Defibrillators

IMD – Implantable Medical Device

LCP – Leadless Cardiac Pacemaker

LED – Light Emitting Diode

LVAD – Left Ventricular Assist Device

ME – MagnetoElectric

MERAM - Magnetolectric random access memories

MS – Magnetostrictive material

NIR – Near-Infrared Region

OC – Open Circuit

PE – Piezoelectric material

PZT – Lead ZirconateTitanium

RF – Radio Frequency

SAR – Specific Absorption Rate

WCE – Wireless Capsule Endoscope

Chapter 1

Active Implantable Medical Devices and their energy sources

Table of Contents

Chapter 1 Active Implantable Medical Devices and their energy sources	17
1. Introduction	19
2. Implantable Medical Device	20
3. Active Implantable Medical Devices	21
3.1 Physiological Function.....	21
3.1.1 Cardiovascular devices.....	22
3.1.2 Gastroenterology devices	23
3.1.3 Neural devices.....	24
3.2 Packaging Materials	25
3.2.1 Metals	27
3.2.2 Ceramics, and Composites.....	27
3.2.3 Polymers.....	28
3.3 Power Consumption	28
3.4 Energy sources	29
3.4.1 Battery.....	29
3.4.2 Wireless Power Transmission	30
3.4.3 Energy Harvester.....	32
4. Medical Regulatory	35
5. Conclusion.....	38
6. Bibliography	40
7. List of figures.....	42
8. List of tables	43

1. Introduction

The first chapter of this thesis gives a general view of the context of implantable medical devices. Nowadays, the market of medical systems is very wide, heterogeneous, and in continuous evolution. Figure 1.1 shows the trend of the European medical devices market in the last, and next years. These systems are almost able to monitor the human physiological responses, diagnose pain, and issues, and treat medicine; all these functions to afford a better quality of life for the patient.

For the interest of this thesis, specific attention on the active implantable medical devices is reported. The focus of this analysis consisted of the study of medical implants from four points of view: physiological applications, packaging materials, power consumption, and energy sources. The physiological applications analyze the medical device’s functionalities inside the patient’s body, the part of packaging explores the main used materials to encapsulate the implants, the power consumption, and energy sources are linked to the working conditions of the system. Each aspect contributes to producing a complete, reliable, and safe medical device for the patient’s use.

A main investigation of the most employed energy sources is conducted, to understand the advantages and disadvantages of the actual technologies. From this basis, the study of a MagnetoElectric transducer from the perspective of developing compact, and efficient wireless power transmission systems will be introduced.

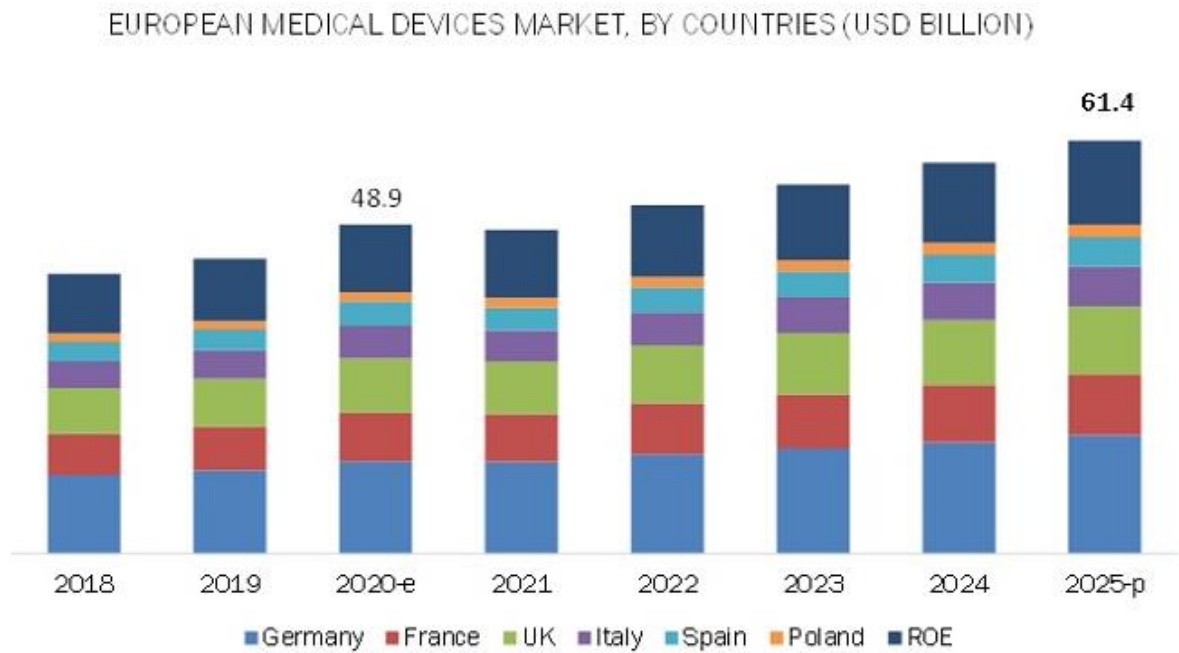


Figure 1.1 - Trend of European medical devices [1].

2. Implantable Medical Device

Every year, millions of patients improve their quality of life through surgical procedures that involve implanted medical devices. Jiang and Zhou [2] have described that at least 8% to 10% of the population of all Americas (20 million to 25 million people), and about 1 over 17 people in industrialized countries have experienced a medical implant for rebuilding body functions, achieving a better quality of life, or expanding longevity.

In general, the term implant is used for devices that replace a missing or support a damaged biological structure. In specific, a medical device is defined as implantable, if it is either partly or totally introduced, surgically or medically, into the human body or natural orifice, and it is intended to remain there after the procedure [3][4]. Nowadays, advances in microfabrication, and bio/chemical engineering technology are enabling a large variety of miniaturized implantable systems for diagnosing, healthy monitoring, treatment, and injury compensation. This trend of progress in medical implants will continue for the coming super-aged society, which will result in more consumers of these devices, especially for one or more diseases: estimates show that 90% of the population over the age of 40 suffers from some degree of degenerative joint disease [5].

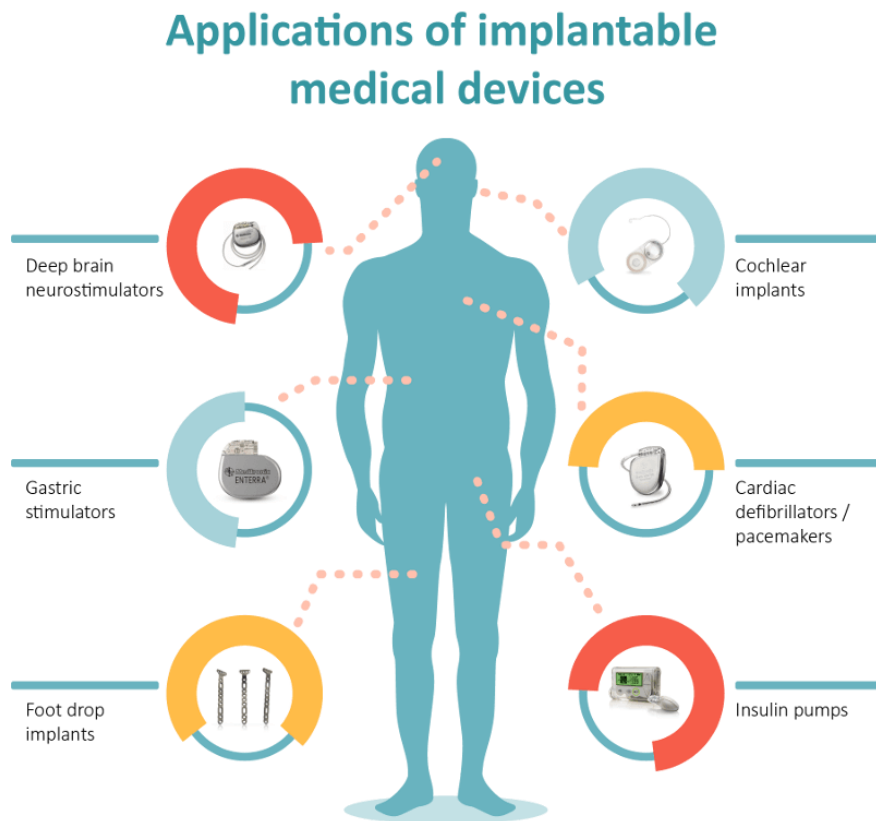


Figure 2.1 – Examples of IMDs [6].

The IMD technologies are continuously assisted, and supervised by the regulatory authorities, like the Food, and Drug Administration (FDA), and the European Commission (CE). They can control the device production, and to guarantee patient safety. In general, the medical regulatory recognizes different classes of medical devices, based on their design complexity, their usage, and their potential of risk, if misused.

Each country or region defines these categories in different ways. When some devices are provided with drugs, the combination of them will be controlled by the regulation. The FDA and CE classification of medical devices is based upon the level of control required to ensure the safety, and effectiveness of the device. The classification procedures are described in the Code of Federal Regulations, Title 21, part 860 (usually known as 21 CFR 860).

Class I devices are subject to the least regulatory control “general controls”. Class I devices are not intended for use in supporting or sustaining life or to be of substantial importance in preventing impairment to human health, and they may not present a potential unreasonable risk of illness or injury. Examples of Class I devices include elastic bandages, examination gloves, and hand-held surgical instruments.

Class II devices are those for which general controls alone are insufficient to ensure safety, and effectiveness for the patient and existing methods are available to provide such insurances. In addition to complying with general controls, Class II devices are also subjected to special controls. A few class II devices are exempt from the premarket notification. Special controls may include special labeling requirements, mandatory performance standards, and post-market surveillance. Examples of class II devices include powered wheelchairs, infusion pumps, and surgical drapes.

Class III device is one for which insufficient information exists to ensure safety and effectiveness. Such a device needs premarket approval, a scientific review to ensure the device’s safety, and effectiveness, in addition to the general controls of Class I, and II. Class III devices are usually those that support or sustain human life and are of substantial importance in preventing impairment of human health or those which present a potential, unreasonable risk of illness or injury. Examples of class III devices include implantable pacemaker, pulse generators, HIV diagnostic tests, automated external defibrillators, and osseous implants. The devices discussed in this chapter belong to class III. These implants mostly find their applications in the orthopedic, neural, gastroenterology, and cardiovascular fields as well as soft tissue implants such as implants used in plastic surgery.

Over this general review, the medical implantable systems can be further classified into two macro groups, active (mostly class II, and III), and passive (class I, and II). The IMDs that do not need power are termed as passive devices, e.g. artificial joints, vascular grafts, and dental implants. On the contrary, the active IMDs depend on a source of energy, which can be directly generated by the human body or by external phenomena/system, e.g. cardiac pacemaker, cochlear implants, and insulin pumps. This thesis will be focused on the Active Implantable Medical Devices.

3. Active Implantable Medical Devices

Over the last six decades, numerous engineering, and medical activities for Active Implantable Medical Device (AIMD) development have faced challenges in functionality, electrical consumption, packaging materials, wireless communications, and power supply. Since the first pacemaker implant in 1958, this progress is driving physicians, and patients to express an increasing desire for miniaturized implantable devices, as they are offering less invasive implantation procedures, greater comfort for the patient, improved performances, and often provide innovative measurements, and treatments [5].

Since the market of the Implantable Medical Devices is very wide, and heterogeneous, this chapter will analyze the AIMDs from the point of view of four main aspects: physiological function, power consumption, packaging materials, and energy sources.

3.1 Physiological Function

The design of an active implantable system typically comprises two blocks, an indwelling module which resides inside the patient, and an external device located outside the body with which the implant communicates, and/or is powered. Within the host body, the electrical system can reside intracavity, e.g. within intestinal systems, or be subcutaneously or deeply implanted [7]. In the following paragraphs three AIMDs, one for each type of implantation, will be described on the base of the most common patients’ disorders, and WIBEC’s project applications:

- Cardiac Pacemaker (long-term deep implant)
- Capsule Endoscope (temporary intracavity implant)
- Neural stimulator (long-term subcutaneous implant).

3.1.1 Cardiovascular devices

Cardiovascular diseases are the leading causes of mortality in the Western World, and responsible for 37.5% of all deaths in the EU [9]. Disturbance of cardiac rhythm and malfunction of the heart's conduction system is the result of disease processes such as hypertension or coronary artery-, and valvular- heart disease. Cardiac rhythm management devices are developed to maintain, improve, or restore heart rhythm [10]. They are mainly divided into three classes:

1. Anti-bradycardia (heart rate is abnormally slow, fewer than 60 beats per minute) or tachycardia- (heart rate is abnormally fast, more than 100 beats per minute) - pacemakers
2. Implantable cardioverter-defibrillators (ICD)
3. Cardiac resynchronization therapy devices (CRT).

In general, implanted cardiac rhythm management devices consist of a subcutaneous metallic can, containing the control unit, and the energy source. The can is connected to single, double, or multiple leads with electrodes at the tips, which detect cardiac activity, and stimulate the myocardium to contract when required [9]. The control unit communicates with the external programmer during follow-up visits, to obtain stored or real-time records of cardiac, and pacing activities. Modern implanted cardiac devices have at least three functions: sensing electric pulses of the heart through one or more electrical leads, processing the information by the control unit, and pacing or defibrillation action, through the leads [9]. An implanted cardiac pacemaker is represented in Figure 3.1A.

Since the development of the first implantable pacemaker in 1958, pacing technology has dramatically improved. Size has been reduced, the battery lasts longer (until 10 years), sensors and algorithms are smarter, and surgical methods are safer. However, the components of the leads remain the "weak point" of the system, with issues such as infection, venous occlusion, high risk-extraction [8]. One of the solutions is to merge the can, and the lead into one single device, the leadless cardiac pacemaker (LCP). Leadless cardiac pacemaker (Figure 3.1B) shall be the miniaturized all-in-one self-contained cardiac pacing device that must sense, process the signals, communicate with physicians, and pace.

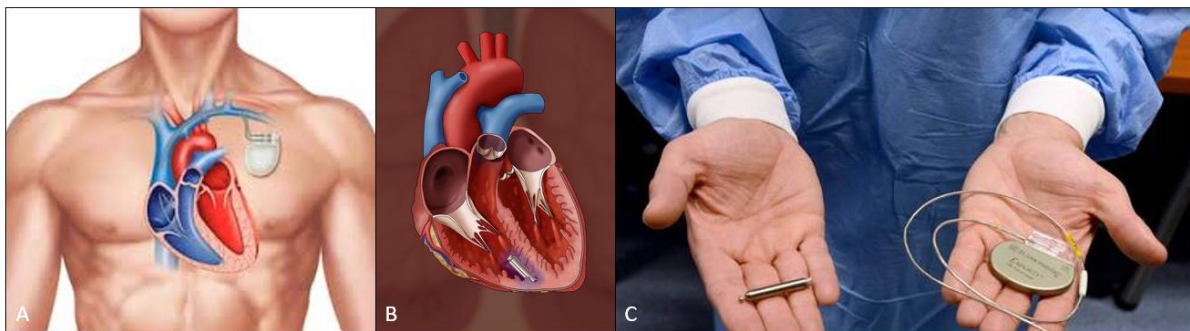


Figure 3.1 – Figure A) represents an implanted cardiac pacemaker. Figure B) represents a leadless cardiac pacemaker. Figure 2C shows the different sizes of leadless pacemaker (in the left hand), and an old-generation pacemaker (in the right hand) [39].

LCP is a long-term deep implant, which consists of a power generator, sensors, current injector, and an integrated battery unit. The concept was proposed 40 years ago, but only recently became a clinical reality [9]. Two commercial systems are already available on the market: Micra™ (Medtronic Inc., Minneapolis, USA), and Nanostim™ (St. Jude Medical Inc., Minneapolis, USA). Neither Micra™ and Nanostim™ have a permanent power solution, making battery replacement a technical challenge. This limitation may potentially be overcome by new sources of energy (paragraph 3.4).

Furthermore, the new challenge studied in the context of the WIBEC project and addressed to different cardiac diseases consists of using multiple LCPs; one LCP in each of the major myocardium chambers, to have control over the entire heart. The challenge consists of obtaining a complete synchronization between all the cardiac implants, and the external recorder, through different techniques such as Human Body Communications [11] or Radio Frequency Communications [12].

3.1.2 Gastroenterology devices

Among digestive diseases, colorectal cancer has the highest mortality rates worldwide [13]. At present, the primary tool for gastrointestinal screening is the flexible endoscope. Unfortunately, it is accompanied by a non-negligible risk of trauma, breach, and sometimes infections. To overpass these issues, a Wireless Capsule Endoscope (WCE) emerged in the 21st century as a painless, and non-invasive diagnostic IMD. Wireless Capsule Endoscope is a temporary intracavity AIMD, able to explore the Gastro-Intestinal (GI) tract by wirelessly transmitting images from a disposable capsule to a data recorder (Figure 3.2).

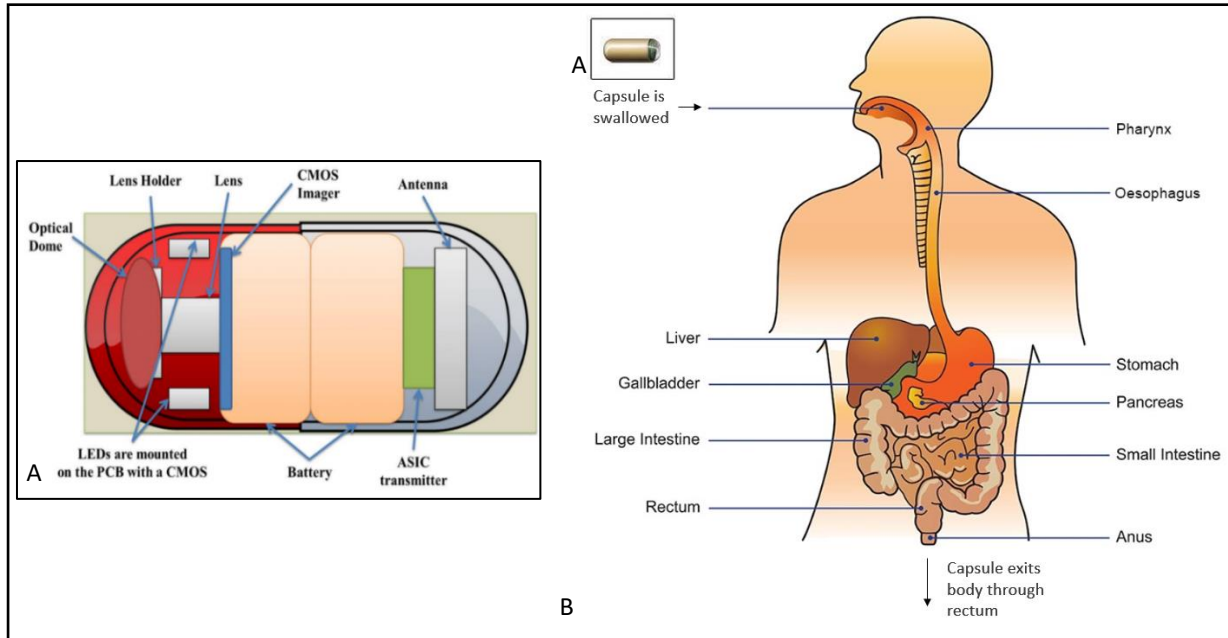


Figure 3.2 – Figure 3A represents the scheme of a Wireless Capsule Endoscope. Figure 3B represents the endoscopy process, with a pain-less Wireless Capsule Endoscope [14].

The WCE system consists of 3 blocks: a capsule endoscope, sensing, and data record system, and a computer for image review, and interpretation. All capsule endoscopes have similar components: a disposable plastic capsule, a CMOS or high-resolution image capture system, a compact lens, white-light-emitting diode illumination sources, and an internal battery source [15].

The first capsule model for the small bowel was approved by the FDA in 2001 [15]. Nowadays in the market, there are different products as PillCam (Medtronic Inc., Minneapolis, USA), EndoCapsule (Olympus America, Inc., Center Valley, USA), and MiroCam (IntroMedic Co Ltd, Seoul, Korea).

WCE Company	Size (mm)	Weight (g)	Image/s	Battery life	Resolution (pixels)
EndoCapsule, Olympus America	11 x 26	3.5	2	8 hours	512 x 512
PillCam, Medtronic	11 x 26	2.8	2	12 hours	256 x 256
MiroCam, IntroMedic Co Ltd	11 x 24	3.3	3	11 hours	320 x 320

Table 3.1 – Comparison between WCE systems.

The mode of transmission data can be either via ultra-high RF (PillCam, EndoCapsule) or human body communications (MiroCam). In Table 3.1 all three products are compared, based on the data of [15]. The new challenges addressed to this innovative device and explored in the context of the WIBEC project, aim to externally control the WCE and to automatically recognize the polyps during the image processing. The first challenge consists of magnetic control of the capsule stabilization, and locomotion, to address it to a specific area if needed [16]. The second one is based on automatic detection in frames of CE videos, through machine learning techniques, to detect risky regions in the small bowel, before proceeding with biopsy [17].

3.1.3 Neural devices

Neurological disorders such as epilepsy, multiple sclerosis, Parkinson’s disease affects the central, and peripheral nervous system, e.g. the brain, spinal cord, peripheral nerves. Recent neural interfaces have shown great potential in the diagnosis, and prediction of neurological events. In fact, Brain Machine Interface (BMI) can simultaneously record, and elaborate neurophysiological signals from large numbers of single neurons, across a wide range of spatial, and temporal scales. Most current recording systems require a wired percutaneous connection between the electrodes and external recording units.

In the market, there are already some examples of neurorecording, and stimulator implantable systems, e.g. RestoreSensor™ (Medtronic Inc., Minneapolis, USA). The 16-electrode medical system is a long-term implant, supplied by a rechargeable battery, which consists of three parts: neurostimulator, leads, and patient’s programmer. The implantable device delivers mild electrical signals to the epidural space near the spinal cord through leads.

Unfortunately, the wired percutaneous connections severely restrict the subject’s mobility, present possible brain infection, and cause potential contamination of the signals, due to the external noise/interference. The new challenge, proposed by the research community, and in particular by *Yin M. et al* [18], presents a wireless neural recording device system (Figure 3.3). The AIMD integrates 100 wideband neural recording channels and a GHz wireless telemetry module for data transfer.

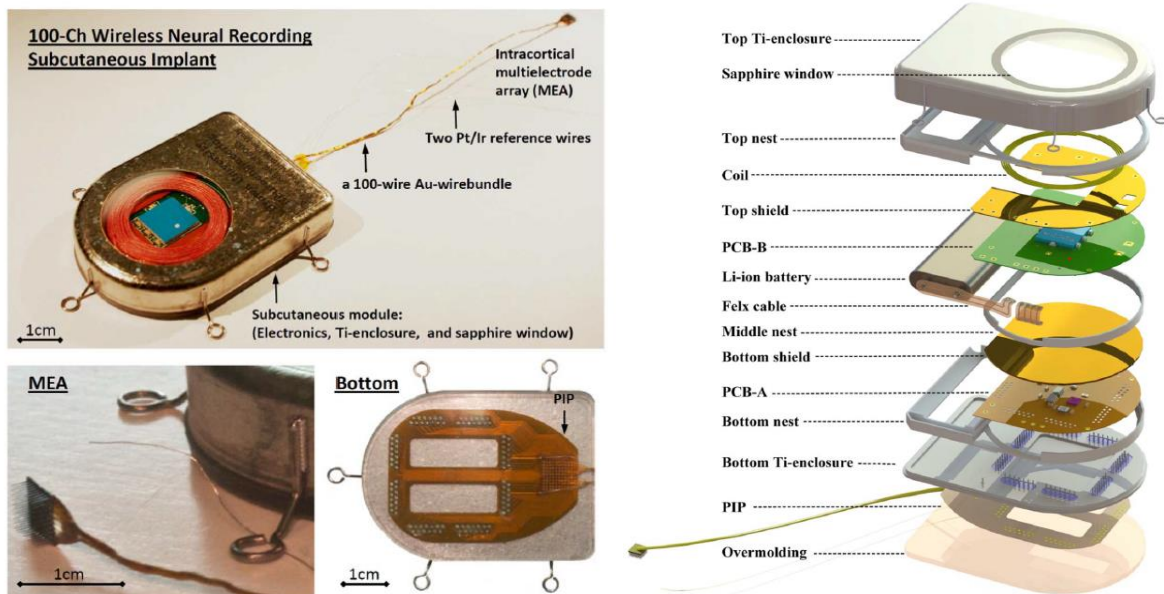


Figure 3.3 – Photographs (on the left), and scheme (on the right) of the 100-Ch fully implantable wireless neurosensing device [18].

The implant is a long-term device, hermetically sealed in a titanium enclosure, and subcutaneously located over the skull [18]. The neural sensing is performed by a 100-electrode intracortical array (Blackrock Microsystem MEA [19]). The system is powered by a medical grade 200 mAh rechargeable Li-ion battery, charged by inductive coupling. Wireless powering through induction is one of the possible solutions to the finite-lifetime of the common battery. This technology found a wide range of activities for AIMD, making them less invasive, and theoretically infinite lifetime (paragraph 33.4.1).

3.2 Packaging Materials

In general, the choice of packaging is mostly influenced by the expected lifetime of the device, to guarantee its hermeticity, and its biocompatibility with the interactive tissues, organs, and blood. The elasticity, yield strength, ductility, fatigue strength, and hardness are some of the important mechanical evaluated properties of materials. For example, the yield strength determines the load-bearing capability of the implant; the elastic modulus measures the resistance to the elastic deformation, when stress is applied, or the tensile strength measures the ability to withstand loads tending to elongate. All these aspects have been evaluated during the choice of the implants' encapsulation. Furthermore, an estimation of the device's hermeticity has been done. All materials leak, or more accurately, all materials are permeable to some gas to some degree. Welds and joints between materials may have pre-existing cracks or pores that provide a leakage path. The total "leak" is thus a combination of both the bulk permeation through the material and any open leak paths that lead directly from the internal to the external environment. Therefore, the process of ensuring hermeticity can be described as the selection of materials, and manufacturing techniques that yield an enclosure that has sufficient material thickness to impede the diffusion of gas into the internal package cavity, and that can be sealed without pinholes, cracks, or other discontinuities that provide a direct leak path. The following figure can give, an index of the permeability of different materials (Figure 3.4).

Therefore, the device failure can be induced either by the effect of the materials/device's package, but also by the host environment. In 1987, Williams defined biocompatibility as "the ability of a material to perform with an appropriate host response in a specific application" [21]. Biocompatibility is not a single event or a single phenomenon, but it involves different mechanisms of interaction between materials, and tissues. Furthermore, no material is unequivocally biocompatible; it may be biocompatible under one or more specific conditions but cannot be assumed to display biocompatibility under all conditions [22].

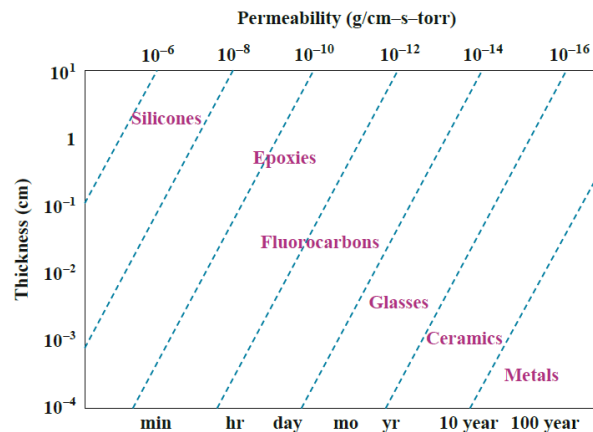


Figure 3.4 - Permeability chart for common classes of packaging materials [20].

The research community is investigating new biomaterials, to tailor, and control the biological reaction to an IMDs. With the development of new biomaterials, a new branch of science came out: *Biomaterials science*. This term refers to the physical, and biological study of materials, and their interactions with the biological environment. It includes the synthesis, optimization, characterization, and testing of host-material interactions.

In general, most of the materials used for AIMDs can be divided into three categories: metals, ceramics, and polymers. Metals are formed by metallic bonds, and include pure metals, and alloys; ceramics are principally based on ionic bonds and include glasses, glass-ceramics, and carbons. On the contrary, polymers are made by covalent bonds and include thermosets, thermoplastics, elastomers, and textiles. In the following (Figure 3.5), they are compared from a mechanical point of view. As biomaterial is very vast and complex, just some materials will be analyzed in the following paragraphs, on the base of the studied implants.

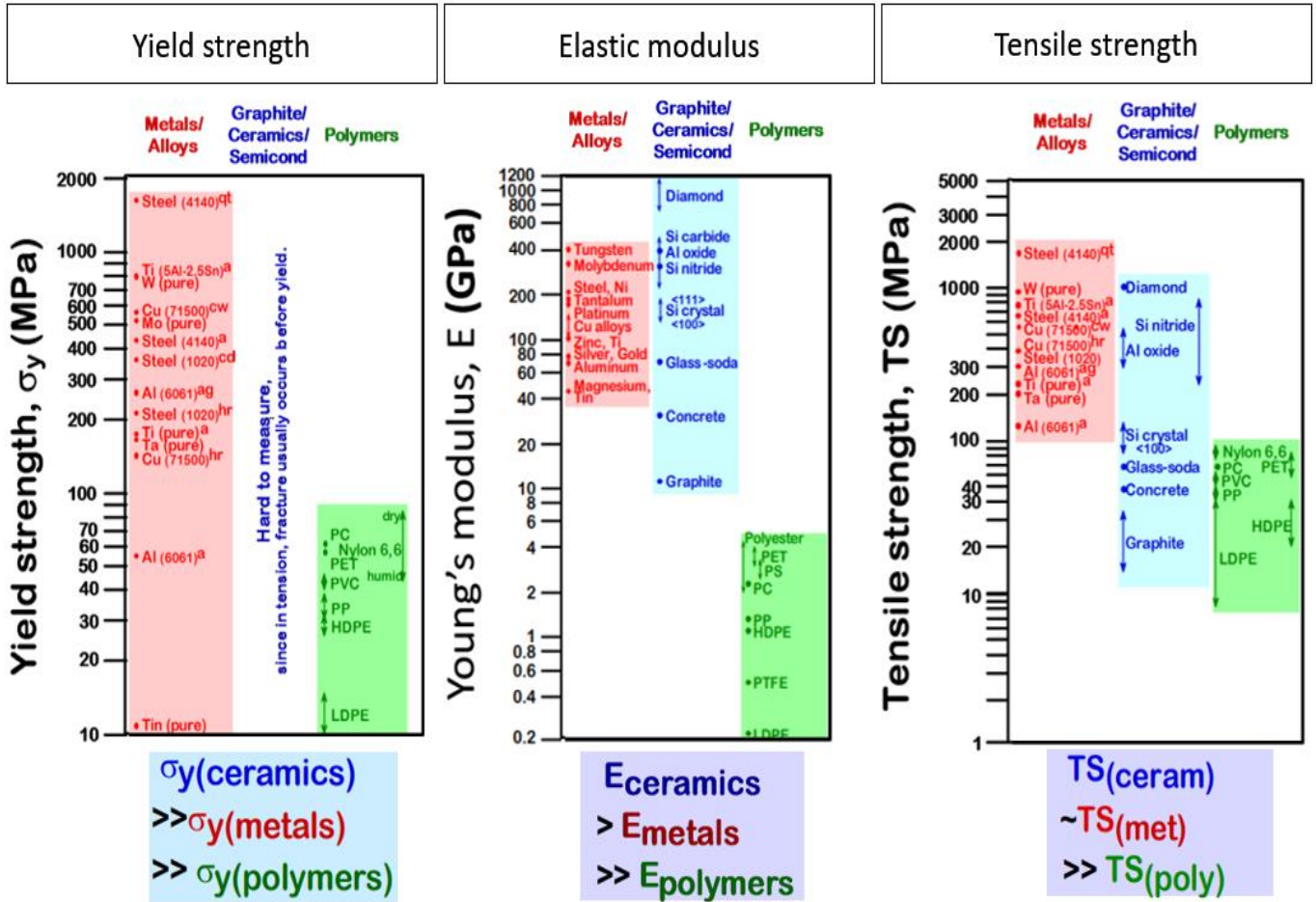


Figure 3.5 - Mechanical comparison of materials, based on [24].

3.2.1 Metals

As a class of materials, metals are the most widely used for load-bearing implants. In general, they are chosen for the high corrosion rates, and good biocompatibility, ideal to guarantee long-term devices' hermeticity. Metals are employed either in passive IMDs, for example for orthopaedic applications as artificial joints or fracture fixation plates, but also in active IMDs, for example for cardiovascular devices as pacemakers' case or ventricular assist devices. The mainly used metals are stainless steels, cobalt-base alloys, and pure titanium/titanium alloys.

Stainless steels are iron-base alloys, which achieve very high corrosion rates, and the ability of self-healing, once damaged, thanks to the formation of an invisible, and adherent chromium-rich oxide surface film [23]. Based on the characteristic crystallographic structure/microstructures of the alloys, stainless steels are classified into four classes: martensitic, ferritic, austenitic, and duplex. In the following chapter, the ferritic materials will be further explained and used for transducer fabrication (Chapter 2, Paragraph 2.4.4.3).

Cobalt-chromium alloys are highly corrosion resistant. Compared to stainless steel, they exhibit higher elastic modulus, strength, and hardness, but they have relatively low ductility and are difficult to machine. They possess adequate fatigue properties to serve as artificial joints or total joint prostheses and are used extensively for this purpose [23].

Commercially pure titanium is well known for its excellent corrosion resistance, and excellent grade of biocompatibility. Various percentages of unalloyed titanium are available with oxygen, and iron as primary variants. Biomedical applications for commercially pure titanium grades include pacemaker cases, enclosure for ventricular assist devices, and neuronal stimulators [23].

In the following (Table 3.2), the 3 classes of metals are compared on the base of their characteristics, and mechanical properties.

	Stainless steels	Cobalt-base alloys	Ti, and Ti-base alloys
Principal element	Fe	Co	Ti
Variants	Ni, Cr, Mo	Ni, Mo, Cr	Al, Nb, V
Young's modulus (GPa)	200	230	110
Tensile strength (MPa)	540 – 1000	900 – 1540	950
Advantages	Cost, availability, manufacture	Wear resistance, corrosion rate, fatigue strength	Biocompatibility, corrosion rate, minimum modulus, fatigue strength
Disadvantages	Long-term behavior, high modulus	High modulus, biocompatibility	Lower wear resistance, low shear strength
Applications	Temporary devices as fracture plates, screws, hip replacements.	Orthopaedic prostheses, total joint replacements, dentistry casting.	Long-term devices as modular femoral heads, cardiovascular devices.

Table 3.2 - Comparison of characteristics, and mechanical properties of metallic implants materials [21].

3.2.2 Ceramics, and Composites

Ceramics, glasses, and glass-ceramics have been essential for a long time in the medical industry for repair or replacement of musculoskeletal hard connective tissues, such as the bone, and dental implants. They are generally chosen for the high stability in the attachment, and good insulation to heating, and electricity. The bone itself is a composite, comprising an organic phase, and a ceramic phase, which is predominantly calcium hydroxyapatite with a Ca/P ratio of 1.67.

Thus, synthetic calcium hydroxyapatite is a good candidate for a successful biomaterial. Several dental and orthopaedic metal implants are coated with it to ensure long-term fixation in bones [23]. The poor fracture toughness and low plasticity of ceramics severely limit their employment for load-bearing applications. A specific ceramic that is used in load-bearing applications is high-density, and high-purity alumina (Al₂O₃). It is used in load-bearing hip prostheses, and dental implants, for its combination of excellent corrosion resistance, good biocompatibility, high wear resistance, and high strength [21].

On the contrary, certain compositions of glasses, and glass-ceramics are specialized in soft tissue bonding and defined as bioactive glasses. A common characteristic of bioactive ceramics is a time-dependent, kinetic modification of the surface that occurs on implantation. The surface forms a biologically active adherent layer, that provides the bonding interface with tissues, and resists substantial mechanical forces [21].

For this thesis, the ceramic materials will be further investigated in the paragraph (Chapter 2, Paragraph 2.4.4.2).

3.2.3 Polymers

Polymeric materials are rapidly replacing for biomedical uses other material classes, such as metals alloys, and ceramics, for their versatility, especially for temporary device. Their application is very wide, in the following (Table 3.3) there are some examples with the respective employments in implantable medical devices.

Polymers	Applications
Poly (ether urethane urea)	Artificial heart components, heart valve
Low, and high-density polyethylene	Tubing, knee, hip, shoulder joints
Polysulfones	Artificial heart components, heart valve
Polypropylene	Heart valve structures
Parylene	Endoscopic capsule
Polyesters	Drug delivery system
Polyamides (nylons)	Hemodialysis membrane

Table 3.3 – Examples of polymers, and their applications in IMDs [23].

Polymeric materials are generally classified into three different classes, depending on their origin: natural polymers, obtained from natural sources, including animals, and plants; synthetic polymers, and bio-inspired polymers, which comprise materials synthesized to mimic a naturally occurring polymer [23]. Natural polymers suffer from various disadvantages, such as the possibility of antigenicity, and microbial contamination. Hence, synthetic (and bio-inspired) polymers are preferred for implants application, for the easy production, availability, and versatility of manipulation [23].

3.3 Power Consumption

In the past few decades, tremendous developments in electronics, micro-, and nanofabrication, and wireless technology have greatly enhanced the quality, and efficacy of healthcare as well as life-science research. Nowadays, the AIMDs are used for diagnosis, monitoring, and treatment, but to ensure proper operations they need to rely on permanent, and sufficient power supply. Before analyzing the different powering technologies, it is necessary to understand the range of power consumption of the most common AIMDs. It is possible to classify them into three groups: *W*-consumption, as the Left Ventricular Assist Device (LVAD), *mW*-consumption, as the neural stimulator, and μW -consumption, as the cardiac pacemaker, (see Table 3.4).

Device	Device functionalities	Power consumption
LVAD	Mechanical pumping the heart blood	5 - 15 W
Leadless Pacemaker	Cardiac rhythm management	1 – 10 μW
ICD	Cardiac rhythm management	40 – 60 μW
Vagus nerve stimulation	Delivering electrical impulses to the vagus nerve	60 – 70 μW
Implantable drug pump	Delivering medication through the spinal cord/body	1 mW
Cochlear implant	Electrical stimulation of the cochlear nerve	10 mW
Neurostimulator	Electrical brain stimulation	100 mW
Wireless Capsule Endoscope	Wireless exploration of Gastro-Intestinal tract	500 mW

Table 3.4 - Typical implants power requirements [25].

From these power requirements, numerous energy sources for AIMDs have been widely investigated in the last decades, respecting the main constraints of size limitations, device's localization (deep/subcutaneous implant), source's continuity, and biocompatibility.

3.4 Energy sources

Since the late 1950s, most of the implantable medical electronic devices such as cardiac pacemakers, vagus nerve stimulators, and deep brain stimulators, have been powered by batteries [26]. However, the use of batteries imposes several limitations to the current AIMDs. Firstly, due to the finite lifetime of batteries, surgeries are often required to replace the discharged units. Secondly, while electronic circuits get smaller dimensions with the rapid development of semiconductor integrated circuit (IC) technologies, the batteries' volumetric capacity has improved rather slowly in the past few decades [27]. Thirdly, the battery has an impact also in the weight of the implantable system, which becomes a major hurdle in minimizing the overall device's size. In addition, even though AIMD are tightly sealed with biocompatible encapsulation materials, there is a risk for electrolytes leakage from the battery, which may cause toxic effects and inflammatory reaction in tissues [27]. For these reasons, researchers have been developing fully implantable microsystems without batteries as internal power sources and exploring various types of wireless powering methods.

In many cases, external power transmitters deliver energy in the form of radiofrequency (RF) waves, ultrasound, or light, and implantable microsystems receive the energy through specific energy harvesting components or antennas. Additionally, there are cases where implantable microsystems are directly equipped with energy harvesters to capture energy from the biological environment [27]. In general, when power is transferred to implanted microsystems through biological tissues, many factors must be considered such as transmission depth, amount of necessary energy, exposition to movements-mechanical stress. The tissues have multi-layer structures with relatively high scattering, and absorption characteristics, which can result in high energy losses, low transfer efficiency, and at the same time highly damage risk, due to heating, and energy absorption.

In the following paragraphs, three types of power supply systems will be described: battery, wireless power transmission, and energy harvesting.

3.4.1 Battery

The first battery was invented by Volta in 1796, and since then numerous types have been discovered and applied to different uses in human life. In general, batteries store energy in the form of chemical substances, which can produce electricity. Batteries contain anodes, cathodes, and electrolytes to allow ions to move thus forming currents. Power capabilities of batteries can have different performances (low rate, medium rate, and high rate) on the base of the AIMD functionalities [25]. Figure 3.6 shows some examples of implantable medical devices powered by batteries, and their lifetimes.

IMD	Power	Battery life time
Pacemaker	10 μ W–30W	5–7 years
Insulin pump	70 μ W	Up to 5 years
Neurological stimulator	0.03 mW–3 mW	Up to 3 years
Cochlear implant	0.02 W–1 W	–
Artificial Organs	30 W	Several hours

Figure 3.6 – Example of IMD powered by battery, and their lifetime [25].

The most employed battery is Li-based, where Li metal anodes are associated with ion-cathode systems, such as iodine (Li/I₂), manganese oxide (Li/MnO₂), or carbon monofluoride (Li/CF_x). As reliable sources for long-term applications such as cochlear implants, pacemakers, cardiac defibrillators, or drug delivery, these Li batteries have been widely employed to provide appropriate power levels ranging from μ A to A [25]. Among those, Li/I₂ batteries have been proved to be safer, and more reliable than others for implantable devices. Li/I₂ batteries

have a discharge voltage of up to 3.6 V, which is equal to three times the voltage generated by Ni-based cells. Their energy density can reach 210 Wh/kg, which can power a cardiac pacemaker for several years [5].

Another alternative, more durable, could be the nuclear battery, in which power is transformed into electricity through energy carried by particles emitted from radioisotopes. This process could be produced by the particles, emitted from the radioisotopes, or coming from the ionization of emitted particle bundles, or the photoelectrical conversion prompted by a fluorescent material [25]. The advantages of nuclear batteries lie in providing much longer service life (>15 years) than all other competitors, and their output energy is extremely stable, regardless of environmental factors (temperature, pressure, and electric field).

Furthermore, their safety has been proved for as long as they are kept hermetic, however, the potential radioactivity danger, as well as their expensive cost, make them still unacceptable [25].

3.4.2 Wireless Power Transmission

Wireless Power Transmission is a technology, which allows transferring a high amount of energy with the constant availability of the energy source. The three major wireless powering transfers are based on radio-frequency (RF) electromagnetic waves (working frequency $10^3 - 10^9$ Hz), ultrasound (1 – 10 MHz), and infrared light (100 THz) (see scheme on Figure 3.7).

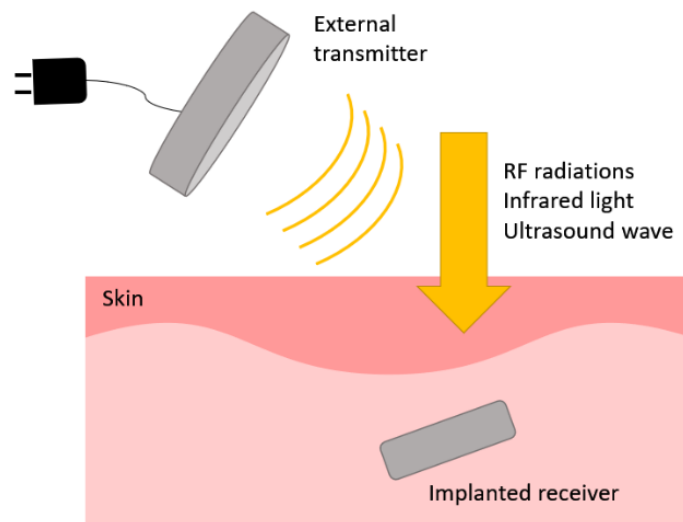


Figure 3.7 – Schematic transcutaneous wireless energy transfer concept: an external device transmits power to the implantable device through RF waves, infrared light, and ultrasounds [5].

RF Electromagnetic Wave Transmission

Delivery energy through RF electromagnetic waves has been widely used in many areas of electrical engineering, especially for powering biomedical implants. The electromagnetic energy can be transferred by inductive coupling through two coils or antennas, with a range of frequency comprised between kHz to GHz. The first case is typical of a near-field electromagnetic interaction, the second one is related to a far-field transfer.

For the near-field technique, the power transfer method consists of using a slowly changing magnetic field, created by the primary coil, to generate an electromotive force, and electric power at the secondary coil (see Figure 3.8). The requirements to have an efficient transmission are linked to the resonance frequency, distance, alignment, coupling, and size of coils. Therefore, implantable microsystems using inductive coupling are usually designed to deliver a large amount of energy to a receiver with a large coil, located within a short distance [27].

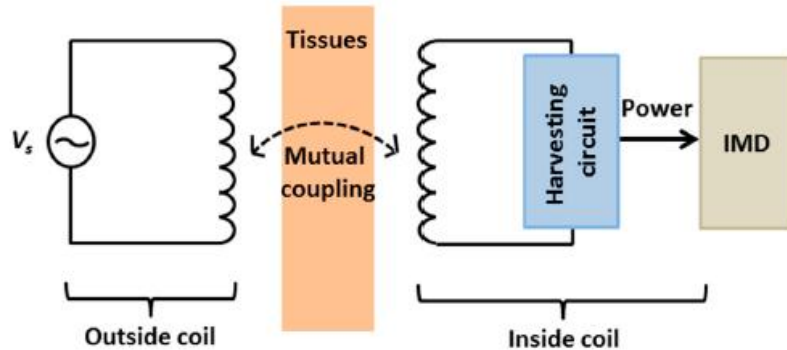


Figure 3.8 – Inductive coupling overview [5].

In the precedent paragraph 13.1.3, a neural stimulator, inductively powered, has been described. The inductive wireless power transmission was used, in that case, to recharge a 200 mAh Li-ion battery at 150 kHz.

On the contrary, the RF radiative energy transfer, also called a far-field transfer, uses antennas with resonance frequencies usually higher than those used in inductive coupling (high RF waves up to GHz).

Transmission, between antennas in the far-field area, may provide energy to multiple microsystems at different depths, and do not require accurate alignment. However, this technology shows relatively lower power transmission efficiency, because the radiative power density decreases rapidly at the far-field region; in general, RF attenuation in a human body is larger at higher frequencies [27]. Additionally, it exposes the tissues to a high risk of damage, and heating. An example of this energy transmission is explained by *Montgomery KL. et al* [28], who reports the development of an implantable wireless neural device, RF powered, which controls the behavior of mice throughout the nervous system (brain, spinal, and peripheral nerve endings).

Ultrasound Wave Transmission

The ultrasound wave is a mechanical wave with oscillating frequencies higher than the upper limit of the human hearing; typical frequencies in the range of [3 – 6] MHz, acoustic velocities in body tissues about 1500 – 2000 m/s, and wavelengths of 0.3 – 0.7 mm [29]. This phenomenon is already employed in the biomedical field for medical imaging, and therapy [30]. Regarding the energy transfer, it consists of an external mechanical source, as a piezoelectric material, which generates the ultrasound waves. The last ones propagate inside the body and arrive at a piezoelectric harvester, which converts it into electric power.

Since the acoustic wavelength results shorter than the RF one at the same frequency, the ultrasounds show a higher transfer efficiency, and penetration depth than the radiative transmission, especially for large separation between source, and receiver [29]. The conversion rate between the ultrasonic transmitter and received power is estimated at 80%, which brings the ultrasound waves more effective than the conventional RF energy transfer [31]. For example, *Tsai JY. et al* [32], presented a neural stimulator, which uses ultrasounds in the MHz-range for power, and data transmission. At an acoustic power of 112 mW from the transmit transducer, 4.15 mW can be received, and made available by the device, which only consumes a power of 1,8 mW for neural stimulation.

Unlikely, the disadvantage of this technology is mostly linked to the low ultrasound transmittance in the bones, especially for the skull, due to the impedance mismatch between the bone, and the other media, and the tissue heating, due to the mechanical vibration at high frequencies [29]. This problem is noticed also in the infrared light energy transmission.

Infrared Light Energy Transmission

The most efficient optical transmission through biological tissues is recorded for near-infrared (NIR) light, in the interval of 800 nm, and 1000 nm wavelengths. For this reason, wireless optical power transmission results more efficient in NIR for active biomedical implants [27].

In these devices, the external light source, such as lasers or light-emitting diodes (LEDs), is located above the skin and emits light through the tissues. The optical power is received, and converted to electric power by photovoltaic components, subcutaneously implanted. The transformation process consists of the photonic stimulation of two materials in close contact, and the production of electric voltage, through the excited carriers. Even though the penetration depth of near-infrared light is longer than that of other wavelength light, it is still scattered, and absorbed inside the tissue, due to its highly dispersive characteristics [27]. For this reason, the implantable devices using infrared light energy transfer are subcutaneous or connected to subcutaneous components. Furthermore, this technology presents a disadvantage linked to tissue heating.

Saha A. *et al* [33], presented the alternative method to power supply an artificial cardiac pacemaker with a 750 nm laser. The implantable system was tested to recharge a 150 mAh LiPO battery embedded under the skin (thickness 3.0 mm), for a low power medical implant (< 10 mW), (see Figure 3.9).

The light flux is collimated through converging lens, and skin tissue, to illuminate the embedded cell array, and a Schottky diode is used to ensure the unidirectional current flow from the receiver to the pacemaker. The system is still in development, for instance, no prototype is ready, but it could open a new perspective for the application of this technology in the biomedical field.

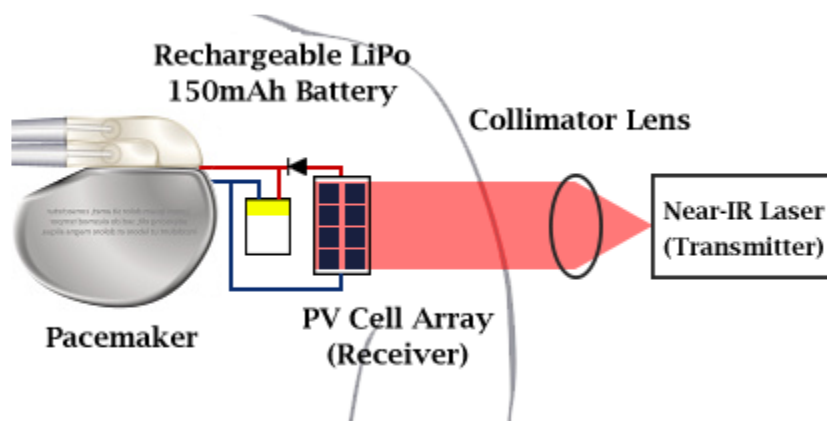


Figure 3.9 – Working principle of the optical WPT system as intended for a cardiac pacemaker, and other IMDs [33].

3.4.3 Energy Harvester

Energy harvesting is a technology by which energy is derived from external sources (e.g. solar power, kinetic energy, also known as ambient energy), captured, and stored to wireless power devices. Researchers tried to apply this concept to the AIMDs, harvesting the energy from inside, or from the surface, of a human body, with the final aim to make a fully autonomous biomedical implant. The human body contains or releases many forms of energy, including heat, the chemical energy of organic molecules such as glucose, and physical forms of energy such as breathing, and the motion of the limbs [37]. Figure 3.10 shows some examples of human energy.

In this case, thermal, mechanical, and chemical processes inside the body can be used as energy sources, avoiding external energy transmitters, and receiving devices. The main disadvantages of this technology are linked to the low amount of the harvested power, and the availability of the energy source. Although recent nanotechnology-driven energy-harvesting devices provide dramatically enhanced energy conversion [27]. In this optics, two types of energy harvesters will be described based on piezoelectric energy harvester, and biofuel cell technology.

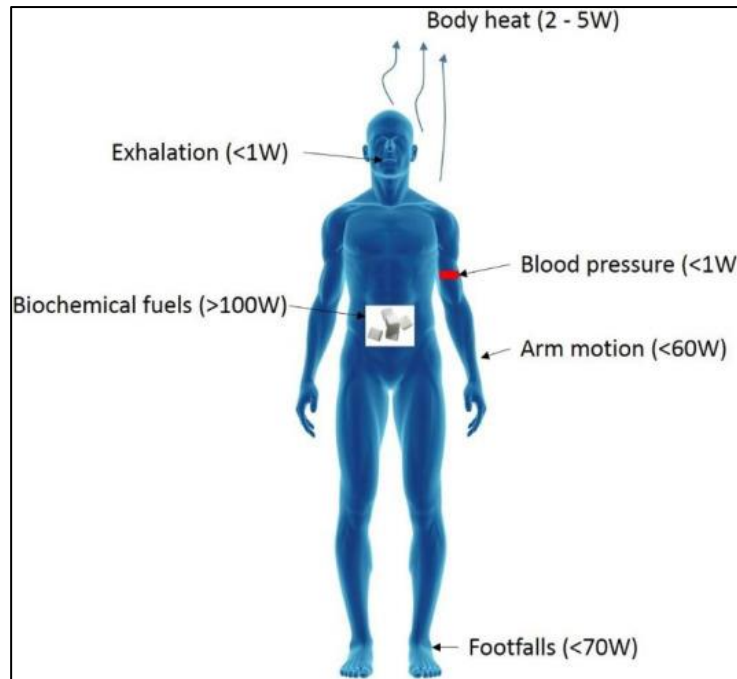


Figure 3.10 – Examples of energy in human body [37].

Piezoelectric energy harvester

Piezoelectricity defines the relationship between mechanical deformation and electricity; in specific, it qualifies the coupling behavior between mechanical strain, and electrical field in some specific polarized materials (e.g. crystals, and certain ceramics). The direct piezoelectric effect consists of the creation of an electric voltage due to the mechanical deformation of the material, and the indirect piezoelectric effect causes a mechanical deformation due to an applied electric field.

In the last decades, this technology has found its application in the biomedical field. A piezoelectric device, implanted in moving parts of the body, can convert vibration or mechanical energy to electrical energy, that activates electronic circuits in the AIMD [27]. However, it is difficult to have high-frequency biological vibrations or strong forces inside the human body. Therefore, energy-harvesting components with piezoelectric materials are rarely used to supply devices with high consumption of power, they are preferred for smaller devices as the leadless cardiac pacemaker.

Deterre M. [5] worked on the development, and design of an energy harvesting device to power supply a miniaturized leadless pacemaker without battery, directly placed in heart chambers. A power density of $3\text{mJ}/\text{cm}^3/\text{cycle}$ was experimentally achieved, providing enough energy to power autonomously, and virtually perpetually the next generation of pacemakers.

Biofuel cells

Another alternative to the common batteries could be biofuel cells. The fuel cell is an energy source for low power electronic devices, that converts chemical energy into useable electrical energy, without any requirements of moving parts or generation of mechanical energy. It can generate power through the electrochemical reaction of a fuel, in the presence of a catalyst.

The link between biology and electricity was first discovered by Galvani in his experiments with frogs' legs in 1791. He found the muscles of dead frogs' legs twitched when electrical sparks were applied. The concept of the *fuel cell* was lately demonstrated in 1839 when Grove fully reversed the electrolysis process of water. He was able to recombine oxygen, and hydrogen to produce water, and interestingly, an electrical current [25].

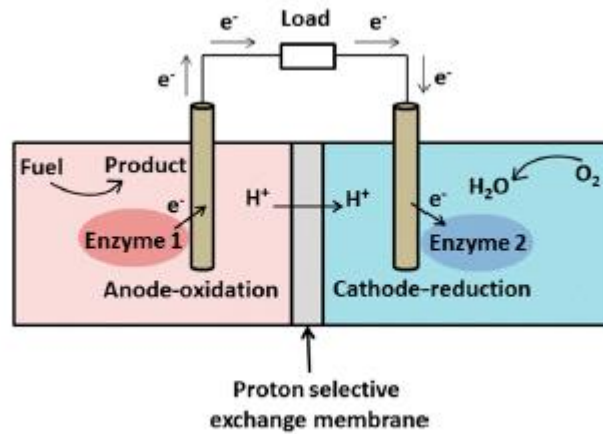


Figure 3.11 – Schematic of a bio-fuel cell [25].

The biofuel cell takes, from the body, their reactants, and catalysts for the oxidation-reduction processes, such as glucose, oxygen, and adenosine triphosphate (ATP).

First works on implantable biofuel cells have been reported in the seventies [34]. Since then, significant progress has been made, especially in the system stabilization for energy harvesting. Glucose fuel cells could use inorganic, organic, or micro-organisms catalysts. In the case of fuel cells with inorganic catalysts, electrodes can be relatively easily fabricated using semiconductor processing techniques, since there is no enzyme fixation process, but they could only generate $3.4 \mu\text{W}/\text{cm}^2$ [35]. On the other hand, fuel cells using organic catalysts show higher energy density in a favorable environment, but the isolation, and fixation of enzymes results in challenges, and degradation of enzymes limit the lifetime of the device [36].

To briefly resume the cited, and analyzed technologies to power supply AIMDs, a schematic comparison is reported in Table 3.5:

Energy Source	Longevity	Energy density	Advantages	Disadvantages
Batteries	Finite	High	Cost, compatibility	Finite lifetime, size, toxicity
Inductive coupling	Regular charge	Medium	High power transfer	Heating, alignment, coupling, side effects
Ultrasound wave	Regular charge	Medium	Source availability, depth of penetration	Low transfer, side effects
Infrared light	Regular charge	Low	High output power	Heating, dimensions
Piezoelectric harvester	Infinite	Low	Cost, longevity, no external sources	Specific location, biocompatibility
Biofuel cell	Estimated infinite	Low	Recycle materials, biocompatibility	Availability of the source, lifetime, low output power

Table 3.5 – Scheme of the different technologies, used to charge an AIMD.

4. Medical Regulatory

Since the domain of application of this thesis concerns the WPT for the biomedical field, an overview of the applicable medical regulatory is given. The considered regulatory must be respected for practical applications of WPT in the human body, because they may limit the system performances.

Radiofrequency electromagnetic fields (EMFs) are used to enable several modern devices, including mobile telecommunications, infrastructure, phones, Wi-Fi, and Bluetooth. As radiofrequency EMFs at sufficiently high-power levels can adversely affect health, International Commission on Non-Ionizing Radiation Protection (ICNIRP) published guidelines for human exposure to time-varying EMFs. The regulatory, reported in this paragraph, concerns the protection of humans exposed to both, short, and long-term, continuous, and discontinuous EMFs in the range of 100 kHz to 300 GHz, and refers to Health Phys. 118(5):483–524; 2020 [40].

To be more accurate possible, the guidelines consider the difference between occupationally exposed individuals and members of the general public. Occupationally exposed individuals are defined as adults, who are exposed under controlled conditions associated with their occupational duties, trained to be aware of potential radiofrequency EMF risks and to employ appropriate harm-mitigation measures. The general public is defined as individuals of all ages, and of different health statuses, which includes more vulnerable groups or individuals, and who may have no knowledge of or control over their exposure to EMFs.

Radiofrequency EMF consists of oscillating electric and magnetic fields. As the field propagates in media, it transfers power from its source to the materials with which it interacts. When a biological body is exposed to radiofrequency EMFs, some of the electromagnetic power is absorbed, and some are reflected away. The absorbed part can interact with superficial tissues, and/or deeply penetrate, interacting with internal organs. This results in complex patterns of electromagnetic fields inside the body that is heavily dependent on the initial EMF characteristics as well as the physical properties, and dimensions of the body.

Firstly, the induced electric field in the body exerts a force on both polar molecules (mainly water molecules), and free moving charged particles, such as electrons, and ions. In both cases, a portion of the EMF energy is converted to kinetic energy, forcing the polar molecules to rotate, and charged particles to move as a current. Rotating, and moving, they typically interact with other polar molecules, and charged particles, causing the kinetic energy to be converted to heat. This heat can adversely affect health in a range of ways.

Secondly, if the induced electric field is below about 10 MHz, and sufficiently strong, it can exert electrical forces that are enough to stimulate nerves. If the pulse is sufficiently intense, and brief, exposure to the resultant EMFs may cause dielectric breakdown of biological membranes, as the permeabilization of the cell membrane, which can lead to other cellular changes [40]. In Figure 4.1, there is reported the electromagnetic spectrum, with common medical applications.

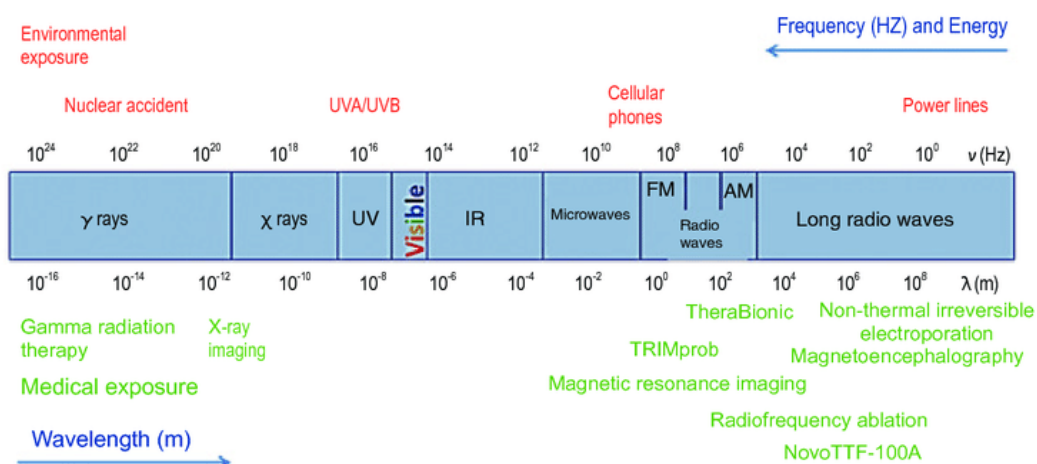


Figure 4.1 – Electromagnetic spectrum [40].

From a health risk perspective, the guidelines are generally interested in how much EMF is absorbed by the human body and its penetration depths through the tissues. The physical quantities used to specify the restrictions, mostly concern specific absorption rate (SAR), incident magnetic field (H), an electric field (E), current density (J), and power density (U).

The *Specific Absorption Rate* (SAR) is defined as the time derivative of the incremental energy consumption by heat, δW , absorbed or dissipated in an incremental mass, δm , contained in a volume element, δV , of a given mass density of the tissue, ρ , and is expressed in (W/kg):

$$SAR = \frac{\delta}{\delta t} \left(\frac{\delta W}{\delta m} \right) = \frac{\delta}{\delta t} \left(\frac{\delta W}{\rho \delta V} \right) \quad (4.I)$$

Dielectric properties of biological tissues or organs are generally considered as dielectric lossy material, and magnetically transparent because the relative magnetic permeability, μ_R , is 1. Therefore, the SAR is usually derived through tissue conductivity, σ , and the internal electric field (RMS-value):

$$SAR = \frac{\sigma |E|^2}{\rho} \quad (4.II)$$

Furthermore, it is strictly correlated to temperature rise, and specific heat capacity of tissues, C:

$$SAR = C \frac{dT}{dt} \quad (4.III)$$

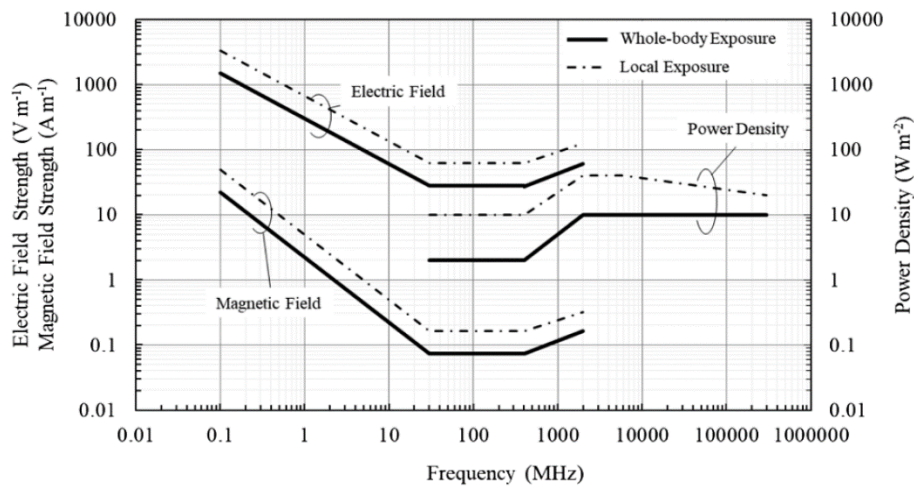
The set of basic restrictions regarding the SAR is shown in Table 4.1:

Parameter	Freq. Range	Spatial Exposition	Time Exposition	ΔT	SAR for Occupational	SAR for General public
Whole body	100 kHz – 300 GHz	Whole body average	30 min	1 °C	0.4 W/kg	0.08 W/kg
Local (Head/Torso)	100 kHz – 6 GHz	10 g of cubic mass	6 min	2 °C	10 W/kg	2 W/kg
Local (Limbs)	100 kHz – 6 GHz	10 g of cubic mass	6 min	5 °C	20 W/kg	4 W/kg

Table 4.1 - Restrictions for electromagnetic field exposure from 100 kHz to 300 GHz, for averaging intervals > 6min.

Concerning the physical quantities of electric/magnetic fields, and power density, they are represented in the following graphs Figure 4.2:

General Public



Occupational

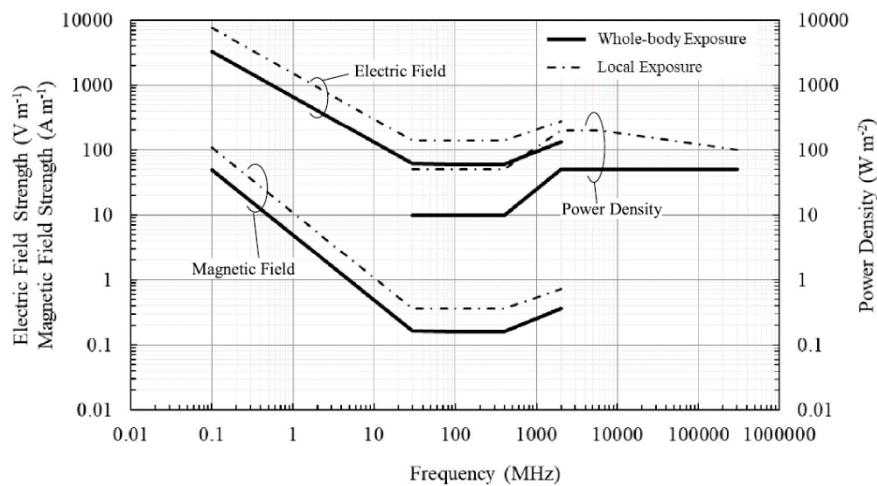


Figure 4.2 – Reference levels for time averaged general public and occupational exposition of > 6 min, to electromagnetic fields from 100 kHz to 300 GHz (unperturbed rms values) [7].

It is noted that radiofrequency basic restrictions and reference levels are based on the lowest radiofrequency exposure levels that may cause an adverse health effect. Since the health effects are related to the temperature rises caused by the exposure, the limits are determined by the energy or power of the radiofrequency exposure.

In the future chapters, these limitations will be further discussed, and applied to the MagnetoElectric devices, studied in this thesis.

5. Conclusion

Designing an implantable electronic system demands several general requirements, such as minimal size, and weight, low power consumption, good reliability, high biocompatibility, long lifetime, and minimal toxicity. In addition, smaller, and lighter devices result less invasive to the body of the patients, causing less pain, and discomfort to the host during healing, and use [7]. The excessive size and weight are highly restrictive, in terms of the normal level of human activity, thus afford a low quality of life to the patients, and they may be detrimental by putting pressure on the adjacent tissues, causing inflammatory processes.

The power source and encapsulation components remain the major contributors to the overall weight, and size of the device, whereas the electric circuitry components, have decreased dramatically with the advancements in MEMS, and nanotechnology [7].

To guarantee the device's hermeticity, and biocompatibility in long term, the metallic encapsulations are preferred over the polymeric ones, as described in paragraph 3.2; however, in terms of volume density, a metallic casing can achieve a density until three orders more than a polymeric capsule.

Furthermore, from the point of view of power consumption, the most employed energy source is the single-use batteries. Nonetheless, to ensure the longevity of the implants, it is necessary for the replacement of the discharged battery, which requires a costly, and invasive surgical procedure. To overlap these issues different techniques have been tested, as described in paragraph 3.4.

In terms of collected density of power, the Wireless Power Transfer technique results the most efficient. Acoustic, and electromagnetic WPT systems have been recently investigated for use in IMDs. The advantage of the acoustic transmission consists of a low attenuation in soft tissue, and short wavelengths (compared to electromagnetic wavelengths), which increases the efficiency of very small receivers [38]. However, acoustic power transfer systems are complicated by poor transmission through bone, and the need for the transmitter to be in direct contact with the skin, paragraph 3.4.2.

From the point of view of electromagnetic WPT systems, they can be either Inductive Power Transfer (IPT) if the coupling is in the near field, or Radio Frequency (RF) if the coupling is in the mid-field (i.e., transition region) or far-field. Inductive coupling techniques appear to be the most advanced for powering implants. Inductive coupling utilizes a pair of coils that must be physically close, and well-aligned to allow an efficient energy transfer. Subsequently, the power transmission is highly dependent on the size, orientation, and distance between the coils [38]. Ultimately, these dependencies make this form of WPT more difficult for IMDs (such as pacemakers), where the depth of the implant is relatively shallow, and the alignment of the coils cannot be well controlled.

Unlike acoustic and inductively coupled systems, alignment is not as critical for RF WPT systems because receivers do not need to be tightly coupled to the transmitter. However, as the size of receivers decreases, the operating frequency must increase to a level where tissue tends to absorb and attenuate the transmitted signal [38]. This attenuation is not only inefficient because it could cause an incorrect functioning of the device, but it is potentially hazardous for the associated tissue heating, due to Eddy's currents. For biomedical applications, the electromagnetic fields must match the IEEE human tissue exposure standards.

A technology that could make efficient the use of low-frequency electromagnetic power transfer at a distance, without the need for specific orientation, is the MagnetoElectric transducer (ME). The innovation of this device is based on the coupling phenomenon between electric, and magnetic fields, through mechanical deformation of the matter. Due to the physical properties of a ME system, it could be an efficient receiver of orders of magnitude smaller than the classical inductive, and RF WPT systems. With this purpose, the potentialities of a ME system are analyzed and studied in the following chapters.

A general overview of the most common AIMDs has been done for their physiological functionalities, employed materials for the packaging, and their power consumption. All the examples, before described, have been summarized in Table 5.1.

Energy source	Type implant	Distance	Operating frequency	Power Consumption	Size of receiver	Packaging	Received Power	Transfer efficiency
Radiative Inductive coupling [18]	Neural stimulator	3 mm	150 kHz	750 mW	56 x 42 x 9 mm ³	Ti enclosure with a sapphire window	460 mW	57.8%
Ultrasound wave [32]	Neural stimulator	5 cm depth	1 MHz	2 mW	8.8 x 11 x 5.2 mm ³	PVDF transducer	15.81 mW	-26.6 dB
Infrared Light [33]	Cardiac Pacemaker	3 mm depth	400 THz	60 μW	1000 mm ³	Polymeric external coating	2.1 mW/cm ²	16.5%
Piezoelectric harvester [5]	Cardiac pacemaker	In the heart chamber	1.5 Hz	10 μW	282 mm ³	To fill	3 mJ/cm ³ /cycle	-
Biofuel cells [35]	Brain Machine Interface	-	-	40 μg of immobilized guest	5 x 7 mm ²	Nafion	2.18 mW/cm ²	-

Table 5.1 – Summary of analyzed AIMDs.

6. Bibliography

1. marketsandmarkets.com/Market-Reports/european-medical-devices-market-241277169.html
2. Jiang G, Zhou DD. *Technology advances, and challenges in hermetic packaging for implantable medical devices*. In: Zhou DD, Greenbaum ES, editors. *Implantable neural prostheses 2: techniques, and engineering approaches*. Berlin: Springer; 2010. p. 28-61.
3. ISO 13485:2016. *Medical devices – Quality management systems – Requirements for regulatory purposes*. Available from [iso.org/obp/ui/#iso:std:iso:13485:ed-3:v1:en](https://www.iso.org/obp/ui/#iso:std:iso:13485:ed-3:v1:en).
4. Johnson JA. *FDA regulation of medical devices*. Congressional research service, June 25, 2012 [Internet]. Washington, DC: Federation of American Scientists; c2013 [cited 2013 Jul 13]. Available from: fas.org/sgp/crs/misc/R42130.pdf.
5. Deterre M., *Toward an energy harvester for leadless pacemakers*, October 2013, theses.fr/2013PA112114
6. sganalytics.com/blog/winning-in-implantable-medical-devices-market-pharmas-next-frontier/
7. Bazaka K., and Jacob M.V., *Implantable Devices: Issues, and Challenges*, doi: 10.3390/electronics2010001
8. W. H. Maisel, *Transvenous implantable cardioverter-defibrillator leads: The weakest link*, *Circulation*. 2007.
9. Europace. *Cardiovascular Diseases Statistics*, date 15/01/2017, available at ec.europa.eu/eurostat/statistics-explained/index.php/Cardiovascular_diseases_statistics#Further_Eurostat_information
10. Albatat M., Bergsland J., Arevalo H., Odland H.H., Bose P., Halvorsen P.S., Balasingham I., *Technological, and Clinical Challenges in Lead Placement for Cardiac Rhythm Management Devices*, doi: 10.1007/s10439-019-02376-0
11. Maldari M., Amara K., Rattlino I., Jabbour C., Desgreys P., *Human Body Communication Channel Characterization for Leadless Cardiac Pacemakers*, 2018 25th IEEE International Conference on Electronics, Circuits, and Systems (ICECS), 185-188, 2018
12. Palaksha D., and Rizzo G., Nocua R., Lefeuvre E., Kansanen K., *Load Modulation For Leadless Pacemaker Synchronization in a Dual Chamber Pacemaker System*
13. *Cancer fact sheets: Colorectal cancer*, online at gco.iarc.fr/today/fact-sheets-cancers?cancer=6&type=0&sex=0
14. Umav I., Fidan B., Barshan B.n, *Localisation, and tracking of Implantable Biomedical Sensor*
15. *Wireless Capsule Endoscopy*, doi: 10.1016/j.gie.2013.06.02
16. Mahmood S., Schurr M.O., Schostek S., *Predictive Tilt Compensation for Robot Assisted Magnetic Capsule Endoscope*, doi: 10.1109/EMBC.2019.8857294
17. Noorda R., Nevarez A., Colomer A., Naranjo V., Pons Beltran V., *Automatic Detection of Intestinal Content to Evaluate Visibility in Capsule Endoscopy*, doi: 10.1109/ISMICT.2019.8743878
18. Yin M., Borton D., Aceros J., Patterson W., and Nurmikko A., *A 100-Channel Hermetically Sealed Implantable Device for Chronic Wireless Neurosensing Applications*, doi/ 10.1109/TBCAS.2013.2255874
19. K. E. Jones, P. K. Campbell, and R. A. Normann, *A glass/silicon composite intracortical electrode array*, *Ann. Biomed. Eng.*, vol. 20, no. 4, pp. 423–437, Jul. 1992
20. Greenhouse H., Lowry R., Romenesko B., *Hermeticity of Electronic Packages*, Second Edition
21. Williams, *The Williams Dictionary of Biomaterials*, Liverpool University Press, 1999
22. Davis J.R., *Handbook of materials for medical devices*, ASM International, Materials Park, OH
23. Khan W., Muntimadugu E., Jaffe M., and Domb A.J., *Focal Controlled Drug Delivery*, Ch.2 *Implantable Medical Devices*, Ed. 2014
24. Callister W., *Fundamentals of Materials Science, and Engineering*, Edition 6
25. Amar A.B., Kouki A.B. 1, and Cao H., *Power Approaches for Implantable Medical Devices*, doi:10.3390/s151128889
26. Mallela V.S., Ilankumaran V., Rao N.S., *Trends in cardiac pacemaker batteries*, *Indian Pacing Electrophysiol J.* 2004; 4(4):201-12

27. Lee J., Jungwoo J., Yoon-Kyu Song, *A review on Wireless Powering Schemes for Implantable Microsystems in Neural Engineering Application*
28. Montgomery KL., Yeh AJ., HO JS., TSAO V., Iyer SM., Grosenick L., Ferenczi EA., Tanabe Y., Deisseroth K., Delp S., and Poon A., *Wirelessly powered, fully internal optogenetics for brain, spinal, and peripheral circuits in mice*, doi: 10.1038/nmeth.3536
29. Denisov A., and Yeatman E., *Ultrasonic vs Inductive Power Delivery for Miniature Biomedical Implants*, 2010 International Conference on Body Sensor Networks
30. Seward JB, Hagker DJ., Mair DD., Lie JT., *Two-dimensional real-time ultrasonic imaging of the heart, and great vessels. Technique, image orientation, structure identification, and validation*. Mayo Clinic Proc., 1978; 53(5):271-303
31. Arra S., Leskinen J., Heikkila J., Vanhala J., *Ultrasonic power, and data link for wireless implantable applications*, Conf Proc Int Symp Wirel Pervasive Comput. 2007; 1:567-571
32. Tsai JY., Huang KH., Wang JR., Liu SL., Li PC., *Ultrasonic Wireless Power, and Data Communication for Neural Stimulation*, doi: 10.1109/ULTSYM.2011.0258
33. Saha A., Iqbal S., Karmaker M., Zinnat SF., and Ali MT., *A Wireless Optical Power System for Medical Implants Using Low Power Near-IR Laser*, 2017 39th Annual International Conference of the IEEE Engineering in Medicine, and Biology Society (EMBC)
34. R F Drake, B K Kusserow, S Messinger, and S Matsuda, *A tissue implantable fuel cell power supply*, *Transactions - American Society for Artificial Internal Organs*, 16 (1970), no. 1, 199–205.
35. Rapoport Bl., Kedzierski JT., Sarpeshkar R., *A glucose fuel cell for implantable brain-machine interfaces*, PLoS One. 2012; 7(6):e38436
36. Kwon CH., Lee SH., Choi YB., Lee JA., Kim SH., Kim HH., Spinks GM., Wallace GG., Lima MD., Kozlov ME., Baughman R., Kim SJ., *High-power biofuel cell textiles from woven bistructured carbon nanotube yarns*. Nat Comm. 2014; 5:3928
37. Zebda A., Alcaraz J.P., Vadgama P., Shleev S., Minteerd S F., Cinquin P., Martina D.K., *Challenges for successful implantation of biofuel cells*, doi: 10.1016/j.bioelechem.2018.05.011
38. Rupp T., Truong B.D., Williams S., and Roundy S., *Magnetolectric Transducer Designs for Use as Wireless Power Receivers in Wearable, and Implantable Applications*, *Materials* 2019, 12, 512; doi:10.3390/ma12030512
39. Cordero R., *Subcutaneous Monitoring of Cardiac Activity for Chronically Implanted Medical Devices*, theses.fr/2020UPASS020
40. *ICNIRP GUIDELINES for limiting exposure to electromagnetic fields (100 kHz to 300 GHz)*, *Health Phys* 118(5):483-524;2020

7. List of figures

FIGURE 1.1 - TREND OF EUROPEAN MEDICAL DEVICES [1].	19
FIGURE 2.1 – EXAMPLES OF IMDs [6].	20
FIGURE 3.1 – FIGURE A) REPRESENTS AN IMPLANTED CARDIAC PACEMAKER. FIGURE B) REPRESENTS A LEADLESS CARDIAC PACEMAKER. FIGURE 2C SHOWS THE DIFFERENT SIZES OF LEADLESS PACEMAKER (IN THE LEFT HAND), AND AN OLD-GENERATION PACEMAKER (IN THE RIGHT HAND) [39].	22
FIGURE 3.2 – FIGURE 3A REPRESENTS THE SCHEME OF A WIRELESS CAPSULE ENDOSCOPE. FIGURE 3B REPRESENTS THE ENDOSCOPY PROCESS, WITH A PAIN-LESS WIRELESS CAPSULE ENDOSCOPE [14].	23
FIGURE 3.3 – PHOTOGRAPHS (ON THE LEFT), AND SCHEME (ON THE RIGHT) OF THE 100-CH FULLY IMPLANTABLE WIRELESS NEUROSENSING DEVICE [18].	24
FIGURE 3.4 - PERMEABILITY CHART FOR COMMON CLASSES OF PACKAGING MATERIALS [20].	25
FIGURE 3.5 - MECHANICAL COMPARISON OF MATERIALS, BASED ON [24].	26
FIGURE 3.6 – EXAMPLE OF IMD POWERED BY BATTERY, AND THEIR LIFETIME [25].	29
FIGURE 3.7 – SCHEMATIC TRANSCUTANEOUS WIRELESS ENERGY TRANSFER CONCEPT: AN EXTERNAL DEVICE TRANSMITS POWER TO THE IMPLANTABLE DEVICE THROUGH RF WAVES, INFRARED LIGHT, AND ULTRASOUNDS [5].	30
FIGURE 3.8 – INDUCTIVE COUPLING OVERVIEW [5].	31
FIGURE 3.9 – WORKING PRINCIPLE OF THE OPTICAL WPT SYSTEM AS INTENDED FOR A CARDIAC PACEMAKER, AND OTHER IMDs [33].	32
FIGURE 3.10 – EXAMPLES OF ENERGY IN HUMAN BODY [37].	33
FIGURE 3.11 – SCHEMATIC OF A BIO-FUEL CELL [25].	34
FIGURE 4.1 – ELECTROMAGNETIC SPECTRUM [40].	35
FIGURE 4.2 – REFERENCE LEVELS FOR TIME AVERAGED GENERAL PUBLIC AND OCCUPATIONAL EXPOSITION OF > 6 MIN, TO ELECTROMAGNETIC FIELDS FROM 100 KHZ TO 300 GHZ (UNPERTURBED RMS VALUES) [7].	37

8. List of tables

TABLE 3.1 – COMPARISON BETWEEN WCE SYSTEMS.....	23
TABLE 3.2 - COMPARISON OF CHARACTERISTICS, AND MECHANICAL PROPERTIES OF METALLIC IMPLANTS MATERIALS [21].....	27
TABLE 3.3 – EXAMPLES OF POLYMERS, AND THEIR APPLICATIONS IN IMDs [23].	28
TABLE 3.4 - TYPICAL IMPLANTS POWER REQUIREMENTS [25].	28
TABLE 3.5 – SCHEME OF THE DIFFERENT TECHNOLOGIES, USED TO CHARGE AN AIMD.	34
TABLE 4.1 - RESTRICTIONS FOR ELECTROMAGNETIC FIELD EXPOSURE FROM 100 KHZ TO 300 GHZ, FOR AVERAGING INTERVALS > 6MIN.....	36
TABLE 5.1 – SUMMARY OF ANALYZED AIMDS.	39

Chapter 2

Model and Application of a MagnetoElectric transducer

Table of Contents

Chapter 2 Model and Application of a MagnetoElectric transducer	45
1. Introduction	47
2. Magnetic Materials	48
2.1 Principles, and structures.....	49
2.2 Fundamental Equations	51
2.3 Magnetostriction	54
2.3.1 Piezomagnetism.....	55
2.3.2 Magnetostrictive materials.....	56
2.4 Applications.....	57
3. Piezoelectric Materials.....	59
3.1 Principles, and Structures	60
3.2 Fundamental Equations	62
3.3 Oscillation modes/Dynamic Behavior	63
3.4 Type of piezoelectric materials	65
3.5 Applications.....	66
4. MagnetoElectric Composites	68
4.1 Principles, and structures.....	69
4.2 Fundamental Equations	71
4.2.1 Magnetostrictive Constitutive Equations	72
4.2.2 Piezoelectric Constitutive Equations.....	72
4.2.3 MagnetoElectric Constitutive Equations.....	73
4.3 Equivalent circuit model	74
4.3.1 Static Regime.....	76
4.3.2 Dynamic Regime	78
4.3.3 Output Power, and Optimal Electrical Load.....	79
4.3.4 Model with Rectifier	80
4.4 Considered Materials.....	82
4.4.1 Magnetostrictive material	82
4.4.2 Piezoelectric material.....	84
4.4.3 Description of the MagnetoElectric Samples.....	85
4.4.4 FEM analysis of radial resonance modes	86
4.5 Application	88
5. Conclusion.....	90
6. Bibliography	91
7. List of figures.....	94
8. List of tables	95

1. Introduction

To better understand the potentialities of a MagnetoElectric transducer for low-frequency electromagnetic power transfer, this chapter is dedicated to the explanation of the theory behind this technology. It describes the magnetolectric device from the point of view of the physics, materials, and potential applications in the biomedical field.

The current chapter is structured into three parts. The first part is dedicated to the magnetic materials, describing the fundamental relationships between the internal magnetization, and the external magnetic field. From this class of materials, the magnetostrictive ones are highlighted. In particular, the phenomena of piezomagnetism, and the magnetostriction are considered to describe the coupling between the magnetic field, and mechanical deformation, presented in a magnetolectric composite.

The second part is focused on the piezoelectric materials, and their coupling between the electric field, and mechanical deformation of the matter. The physics of the piezoelectricity is described, considering the influence of the sample's shape on the vibration modes, resonance frequencies, and electric potentials. Some examples of the most used piezoelectric materials are reported. Due to their low energy consumption, and low cost, piezoelectric devices can be very versatile. For this reason, just a few, but interesting, examples of applications in the biomedical field are cited.

The third part is dedicated to the magnetolectric systems. Starting from the theory previously considered, the effect of the union of the magnetostrictive, and the piezoelectric materials is described. In this new composite, some properties follow the physics of the single phases, others not. From these anomalies, a microscopic description is conducted. The explanation of the physical laws, which govern this type of system, is followed by an equivalent circuit model, to study the device from an electrical point of view. Furthermore, some examples of the most used materials and their characteristics are reported. From this comparison, the choice of the materials for this thesis is apported. Finally, some examples of the potentialities of magnetolectric transducers are highlighted.

2. Magnetic Materials

Magnetism includes all the physical phenomena which take place inside, and around a magnetic material; in specific, magnetism can be proper of the material or induced from another field (electric or magnetic). The word magnetism derives from the Greek μαγνήτις (magnētis) λίθος (lithos), "the Magnesian stone".

The origin of magnetism is very ancient. The first traces of the subject, in the Occidental world, were attributed to a scientific conversation between Aristotle, and the philosopher Thales of Miletus (600 BC). In ancient China, one of the earliest literary references lies in 2nd-century BC annals, about "the lodestone attracts iron". The 11th-century Chinese scientist Shen Kuo was the first person to write of the magnetic needle compass, and the improved accuracy of navigation by employing the astronomical concept of true north. However, the first scientific study of magnetism was associated with the British William Gilbert, who published *De Magnete* in the XVII century; a work dedicated to the permanent magnets, and Earth's magnetic field [1]. Only in 1820, the relationship between electricity, and magnetism was discovered by Hans Christian Ørsted, a professor at the University of Copenhagen, who found that an electric current can induce a magnetic field [1]. After this landmark, several other experiments followed; André-Marie Ampère in 1820 discovered that the magnetic field circulating in a closed-path was related to the current flowing through a surface enclosed by the path; Jean-Baptiste Biot, and Félix Savart, both of whom in 1820 came up with the Biot–Savart law giving an equation for the magnetic field from a current-carrying wire; Michael Faraday, who in 1831 found that a time-varying magnetic flux through a loop of wire induced a voltage. James Clerk Maxwell synthesized, and expanded these insights into Maxwell's equations, unifying electricity, magnetism, and optics into the field of electromagnetism. In 1905, Einstein used these laws in motivating his theory of special relativity, requiring that the laws be held in all inertial reference frames. Electromagnetism has continued to develop into the 21st century, being studied into the more fundamental theories, and with application in several fields (Figure 2.1): communications, biomedical, electronics, mechanical, transports.



Figure 2.1 – Different applications of magnetism in the contemporary society.

2.1 Principles, and structures

The macroscopic manifestation of magnetism is expressed by the attractive or repulsive force between two permanent magnets. This effect is the largescale result of a microscopic phenomenon.

Each atom has two magnetic moments: the orbital $\vec{\mu}_L$, and the spin $\vec{\mu}_S$. The first one is defined as the angular moment of an electron, due to its movement around the atom's nucleus. The second contribution is linked to the intrinsic state of the electron. This characteristic was proved for the first time by Otto Stern, and Walther Gerlach in 1921, and is strictly linked to Pauli's exclusion principle, about the unicity of electrons within the same quantum system. The spin-orbital moments create an elementary magnetic moment $\vec{\mu}_{el}$, which contributes to the total magnetization \vec{M} of the material (2.I), defined as the volume density of magnetic moments [1].

$$\vec{M} = \frac{\sum \vec{\mu}_{el}}{Volume} \quad (2.I)$$

In general, the magnetization of a material depends on its internal structure, but it may be induced or varied under the application of an external magnetic field \vec{H} . The relationship between the magnetization, \vec{M} , and the external magnetic field is defined as magnetic susceptibility χ (2.II):

$$\vec{M} = \chi \cdot \vec{H} \quad (2.II)$$

From the value and sign of the magnetic susceptibility, it is possible to define different orders of magnetic materials, and different responses to an applied magnetic field.

- *Diamagnetism*, $-10^{-6} < \chi_{dia} < -10^{-3}$. It arises, at the microscopic materials' structures, from the electronic orbitals. Due to the negative sign of χ , it could be expressed as the tendency of the material to oppose itself to the penetration of the magnetic field. It does not depend on the temperature or applied magnetic field, and it appears in all materials. (e.g. Bi or graphite).
- *Paramagnetism*, $10^{-8} < \chi_{para} < 10^{-4}$. It comes from partially filled orbitals or delocalized electrons. Due to the positive sign of χ , and to its small value, paramagnetism can be expressed as a weak phenomenon. In fact, in absence of an applied magnetic field, a paramagnetic material has not a spontaneous magnetization; for the thermal motion, each magnetic moment takes a random direction, and the total moment results zero. On the contrary, under an applied magnetic field, the magnetic moments of material are aligned with the external field and assume a total magnetic moment. χ_{para} is not dependent on the applied field [1]. There are two cases of paramagnetism: the first one is called *Pauli paramagnetism*, χ is temperature independent, and it has a weak value, of the order of 10^{-5} . The second case is called *Curie paramagnetism*, χ depends on the temperature, and scales with $1/T$ (2.III). Only certain materials give rise to paramagnetism: metals or insulators with localized moments [4]. (e.g. Al or Ti).
- *Ferromagnetism*, $10^0 < \chi_{ferro} < 10^6$. Each magnetic moment interacts with the adjacent ones, leading to the phenomenon of magnetic ordering at finite temperature, and zero fields. The magnetic moments are, then, coupled through a positive exchange interaction, which favors the parallel alignment of microscopic moments, and occurs a spontaneous magnetization. In ferromagnetic materials, the susceptibility depends on the external field and the working temperature. In fact, for a high applied magnetic field, all the moments result parallel to it, the magnetization achieves the saturation, and χ decreases. From the point of view of temperature, ferromagnetic materials present these characteristics at or below the Curie temperature; above this limit, the thermal motion results predominant over the exchange interaction, and the material becomes paramagnetic. The dependency of χ from the temperature is expressed by Curie-Weiss law (2.III):

$$\chi = \frac{C}{T - T_c} \quad (2.III)$$

where C is the Curie constant, and T_c is the Curie temperature. Once the Curie temperature is passed, the material loses its magnetization also in case of return at the room temperature. The

same principle is applied to the high applied magnetic field. Only three pure elements are ferromagnetic at room temperature Fe, Ni, and Co.

- **Antiferromagnetism**, $10^{-5} < \chi_{\text{antiferro}} < 10^{-2}$. As for the ferromagnetism, each magnetic moment interacts with the adjacent ones, over the phenomenon of magnetic ordering at finite temperature, and zero fields. In this case, the exchange interaction results negative, favoring the antiparallel alignment of neighboring moments, and leading to zero the net magnetization of the system. The susceptibility is dependent on the temperature, and it achieves its maximum value at the Néel temperature. After this point, the thermal motion, and the paramagnetic nature of the material become predominant. (e.g. chromium oxide). The Néel temperature is defined as the point of the change.
- **Ferrimagnetism**, $10^0 < \chi_{\text{ferri}} < 10^4$. It comes, such as for antiferromagnetism, from the negative exchange coupling between moments of different magnitude. The difference consists of the net magnetization of the material, which is not zero for ferrimagnetics. The susceptibility depends on the temperature and the applied magnetic field. Some ferrites belong to this class of materials. (e.g. cobalt or nickel ferrites).

They are schematized in the following Table 2.1, based on their properties, and configurations.

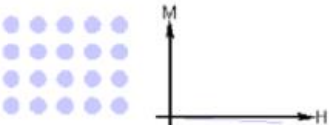
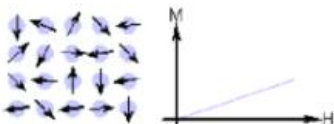
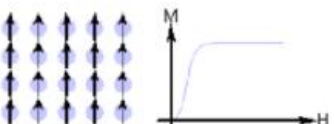
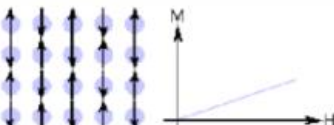
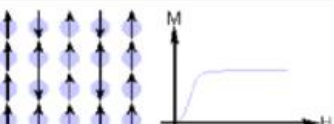
Type of magnetism	Magnetic susceptibility, χ	Atomic / Magnetic Behavior	Temperature dependence	Examples and comments
Diamagnetic	Negative and small, Au: -2.74×10^{-6} Cu: -0.77×10^{-6}		Temperature independent	The shells of the atoms are closed as in the case of covalent solids such as Ge, Si, and metals such as Au, Cu, Ag, etc.
Paramagnetic	Positive and small, β -Sn: 0.19×10^{-6} Pt: 21.04×10^{-6} Mn: 66.10×10^{-6} $10^{-5} - 10^{-4}$		Temperature independent	Atoms have randomly oriented magnetic moments as in alkali and transition metals
	Positive and small		Follows Curie or Curie-Weiss law: $\chi = \frac{C}{T - \theta}$	Atoms constituting the material have a permanent magnetic moment as in ferromagnets (Fe), antiferromagnets (Cr), ferrimagnets (Fe_2O_3) at high temperatures
Ferromagnetic	Positive and large, function of applied field, microstructure dependent Fe: $\sim 100,000$		Ferromagnetic below Curie temperature and paramagnetic above it	Atoms have parallel aligned magnetic moments, possesses large permanent magnetization even without external magnetic field as in some transition metals and rare earths such as Fe, Co, Ni, Gd, Dy
Antiferromagnetic	Positive and small, Cr: 3.6×10^{-6}		Antiferromagnetic below the Néel temperature and paramagnetic above it	Atoms have mixed parallel and anti-parallel aligned magnetic moments. Primarily oxides and salts of transition metals such as MnO, NiO, MnF_2 .
Ferrimagnetic	Positive and large, function of applied field, microstructure dependent, Ba ferrite: ~ 3		Ferrimagnetic below the Curie temperature and paramagnetic above it	Atoms have anti-parallel aligned magnetic moments, possesses large magnetization even without external magnetic field

Table 2.1 - Classification of materials, based on the amplitude of their magnetic susceptibility, χ [5].

2.2 Fundamental Equations

The magnetic material can be imagined as an assembly of permanent magnetic moments, of quantum-mechanical origin. The simplest situation is an ideal paramagnet, where the elementary moments do not interact with each other, but they are independently shaken by thermal agitation. Therefore, they take random orientations in space, which gives zero net magnetization in any macroscopic piece of material [2]. However, a nonzero magnetization can be induced by an external field \vec{H} . This field gives rise to potential energy, defined as the field energy or Zeeman energy [3]:

$$E_z = -\mu_0 \vec{M} \cdot \vec{H} \quad (2.IV)$$

An appreciable net magnetization component along the field is obtained when the field energy is at least comparable in order of magnitude to the thermal energy, which means $E_z \sim k_B T$. At room temperature, fields of the order of 10^2 [A/m] should be insufficient to overcome thermal agitation and produce any appreciable magnetization, that is why the paramagnetic materials have a small susceptibility and no remanent magnetization. In 1907, Weiss suggested the ferromagnetic materials could exhibit a large spontaneous magnetization, even at low fields, because the elementary magnetic moments are strongly coupled by an internal field proportional to the magnetization itself [2]. Weiss explained this phenomenon through the magnetic domains' theory. He postulated a ferromagnetic material is subdivided into regions, the domains; in each of them the magnetization is largely uniform, but the local orientation can vary from one region to another. So, when an external magnetic field is applied, the magnetization favors domains magnetized in the direction of the applied field. When \vec{H} varies in time, the energy balance of the system is altered, and it causes rearrangements of the domain structures, through the motion of the interface layers, known as domain walls, separating adjacent domains [2]. The domains with magnetization in the direction of the external field expand and incorporate the surrounding regions. At high fields, the material is completely occupied by one big domain and magnetized in the direction of \vec{H} . When the field is reversed, regions of reversed magnetization are formed. They progressively increase in size through domain wall motion, until a single big domain of reversed magnetization is formed. This mechanism is represented through the hysteresis loop, as shown in (Figure 2.2).

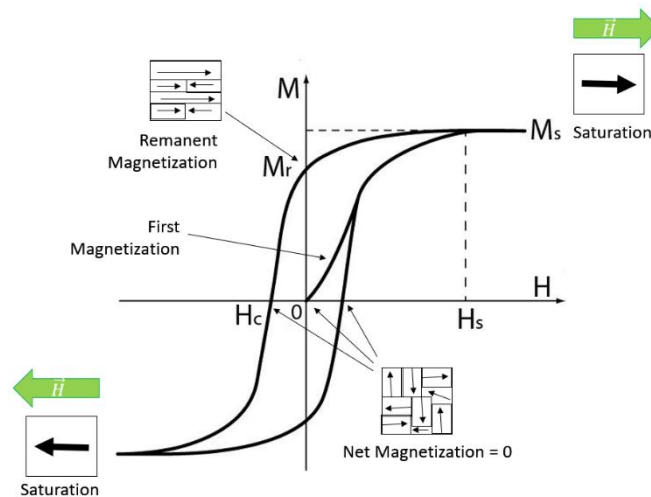


Figure 2.2 – Hysteresis loop of a ferromagnetic material [2].

The Hysteresis loop represents the relationship between the material's magnetization and an external magnetic field. It may take many different shapes and give prime characterization about the material's properties. The curve presents a centrosymmetric, which reflects the time-reversal symmetry of Maxwell's equation ($H \rightarrow -H$, and $M \rightarrow -M$) [3]. From the graph, two main quantities can be estimated, the *remanent magnetization*, M_r , and the *coercive field*, H_c . The remanence or remanent magnetization represents the obtained magnetization after the material exposition to a high magnetic field. It explains why ferromagnet can

be spontaneously magnetized, even in absence of external actions. The order of magnitude of M_r is the same as the spontaneous magnetization. The coercive field represents the necessary field to bring the magnetization from the remanent value to zero. Furthermore, the coercivity measures the field that must be applied to a material, to reverse its magnetization [2].

At first, the magnetic material does not show any magnetization ($\vec{M} = 0$, and $\vec{H} = 0$), the moments are randomly oriented for the thermal motion, and the sum of all magnetic moments results zero, to minimize the magnetostatic energy. Applying an external magnetic field, the domains with the same direction of the field tend to expand. This process continues, increasing the field, until the moment when the material is entirely occupied by a unique big domain, so it reaches a state of saturation. The *first magnetization curve* represents the material's behavior from the demagnetized state to a saturated state (Figure 2.2). From this graph, it is possible to estimate the susceptibility of the material, as the slope of the curve between two points, comprised between the zero, and the saturation limit, knowing the polarization field H_0 :

$$\chi_{diff} = \left. \frac{dM}{dH} \right|_{H_0} \quad (2.V)$$

A second time, when \vec{H} decreases, the inverse process starts. Other domains appear and start to move in a discontinuous way, defined as the Barkhausen effect, creating "jumps" in the magnetic flux. The discontinuity is due to the defects of the crystal lattice and causes losses of energy, hysteresis losses. From the magnetization point of view, this process implies that part of the magnetic moments keeps the same orientation, even if the field decreases. The pinning of magnetic moments signs the irreversibility of the magnetization, and it is defined as the remanent magnetization M_r (Figure 2.2). When the applied field decreases until becoming zero, a certain magnetization remains in the material, which is called M_r [1]. The necessary field, able to cancel this magnetization is the coercive field, H_c . Higher is H_c , and higher will be the needed field to demagnetize the material. From the values of H_c , it is possible to classify the soft or hard magnetic materials.

Soft magnetic materials are easy to magnetize, destined to applications where a low coercive field is a prime requirement. The coercive field is of the order of 50-100 A/m in non-oriented Si-Fe alloys and decreases to 10 A/m in grain-oriented Si-Fe alloys, employed in transformer cores. This is also the typical coercivity in Mn-Zn and Ni-Zn ferrites. Extremely soft materials, obtained from approximately 80% Ni, and 20% Fe, are known as permalloys. An additional parameter in the characterization of soft materials is the *power loss*, proportional to the area of the hysteresis loop [2]. *Hard magnetic materials* are used for their stability, and permanent source of the magnetic field, insensitive to external actions. The coercive field can exceed 1000 kA/m in rare-earth magnets of Sm-Co or Nd-Fe-B type [2].

If the applied magnetic field is an alternative field (\vec{H}_{AC}), with a pulsation of $\omega = 2\pi\nu$, and value of h not negligible:

$$H_{AC}(t) = H_0 + h \cdot \cos(\omega t) \quad (2.VI)$$

the magnetization will not be linear as in the previous case, but it will be dependent on the pulsation:

$$M(t) = M_0 + m(\omega) \cdot \cos(\omega t - \theta) \quad (2.VII)$$

where M_0 is the induced magnetization with a static magnetic field H_0 , $m(\omega)$ is the amplitude of dynamic magnetization, θ is the delay of magnetization $M(t)$ due to the AC field $H_{AC}(t)$ (Figure 2.4). As consequence, the susceptibility of the material will be estimated as:

$$\chi' = \frac{m(\omega) \cdot \cos\theta}{h} \quad \chi'' = \frac{m(\omega) \cdot \sin\theta}{h} \quad (2.VIII)$$

which are respectively index of the magnetic dispersion, and absorption of the material [3].

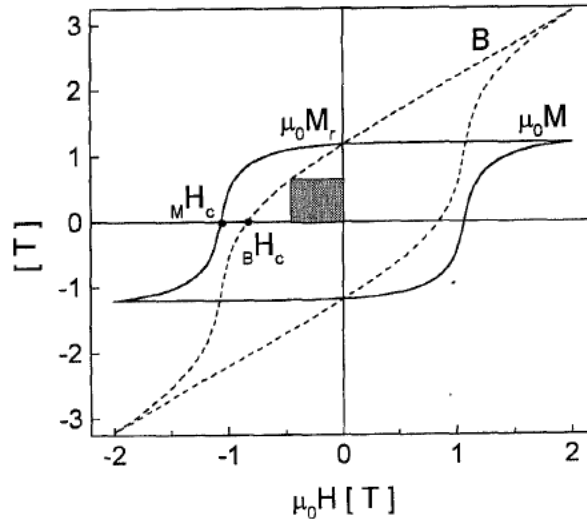


Figure 2.3 – $B(H)$, and $M(H)$ hysteresis loops in hard magnets. The shaded rectangular area represents the energy associated with a given point of the $B(H)$ curve [2].

A hysteresis loop can be represented in terms of magnetization, $M(H)$, but also by the magnetic induction, $B(H)$, as shown in (Figure 2.3).

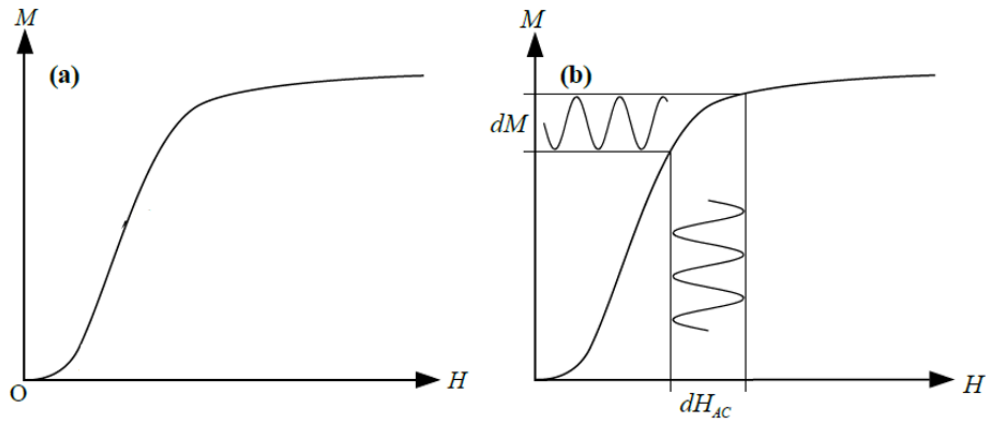


Figure 2.4 – Curves of first magnetization, a) for a DC field, and b) for an AC field [1].

The relationship between magnetization and induction derives from Maxwell's equation, considering as two different ensembles the free electric charges, and the bound electric charges plus spins, contributing to magnetization. The relation is governed by the formula:

$$\vec{B} = \mu_0(\vec{H} + \vec{M}) \tag{2.IX}$$

where μ_0 is the magnetic permeability in free space, $\mu_0 = 4\pi \cdot 10^{-7}$ H/m.

2.3 Magnetostriction

The magnetostriction is a magnetoelastic phenomenon, linked to the spin-orbit effect, which causes a deformation of the material in response to a change of its magnetization. The change of magnetization or magnetic polarization \vec{M} , can be caused either by a variation of temperature or by the application of an external magnetic field. The process is reversible; the inverse phenomenon, called the *Villari effect*, consists of a change of the magnetic properties, like susceptibility χ or permeability μ_R , as a response of applied mechanical stress.

The magnetostriction was firstly observed in an iron sample by James P. Joule in 1842 [6], as a magnetomechanical coupling arising from the dependency of magnetic moment orientation with interatomic spacing. A breakthrough in magnetostrictive materials occurred in 1963 with the discovery of the largest-known magnetostriction in the rare earth elements terbium, and dysprosium, with a strain of the order of $10000 \cdot 10^{-6}$ at cryogenic temperatures. Later, the temperature limitation brought to the combination of the magnetostrictive rare-earth (R) elements with the magnetic transition metals nickel, cobalt, and iron by direct compound synthesis, and by rapid sputtering into amorphous alloys. In contrast to the normal Curie temperature behavior of the R-Ni, and R-Co compounds, the R-Fe compounds exhibit an increase in the Curie temperature with increasing rare earth element concentration. Consequently, huge room temperature magnetostriction of up to $3000 \cdot 10^{-6}$ was achieved in the specific compound of $TbFe_2$ [7].

In general, all materials are elastic. The strain response to stress in a solid derives from the energies associated with stretching, compressing, or bending the bonds between atoms. On the contrary, magnetism occurs for an unusual imbalance in the elementary magnetic moments of material. When the imbalance occurs, the electrons can order in such a way that the net magnetic moment is oriented, lowering the crystal symmetry [8]. This phenomenon is called magnetocrystalline anisotropy, and the associated anisotropy energy, K_1 , is defined as the amount required to rotate the magnetic moments away from their preferred direction. The crystal anisotropy energy and the linear magnetostriction are closely related. Indeed, if the anisotropy is independent of the state of the strain, there will be no magnetostriction [11]. In the rare earth elements, for instance, the large strains are a direct consequence of the huge strain dependence of the magnetic anisotropy [12]. Under the action of a magnetic field, measurable strains result from the deformations of the crystal lattice, to minimize the energy state of the material [7]. Two manifestations of magnetostriction, due to a magnetic field \vec{H} are shown (Figure 2.5): (a) a linear deformation with increasing field magnitude, and (b) a rotating deformation caused by changing the direction of a field of fixed magnitude.

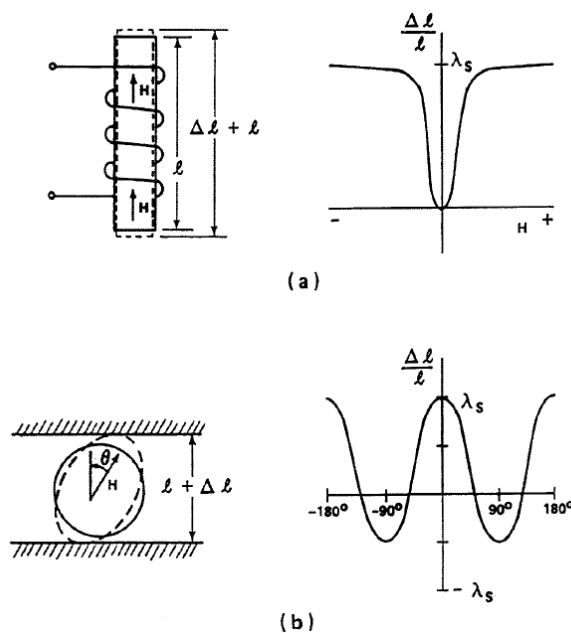


Figure 2.5 – Joule magnetostriction caused by (a) application of a magnetic field, and (b) rotation of a saturating magnetic field [8].

The magnetostriction corresponds to a relative deformation, expressed in m/m or ppm (part per million), characterized by the magnetostriction coefficient:

$$\lambda = \frac{\Delta l}{l} = \frac{l_H - l_0}{l_0} \quad (2.X)$$

where l_H represents the length of material under an applied field \vec{H} , and l_0 is the length of material at $\vec{H} = 0$. If the coefficient results negative, the material will shrink, otherwise, the material will elongate. When the magnetization achieves the saturated value, the magnetostriction arrives at saturation too, λ_s [7]:

$$\lambda = \frac{3}{2} \lambda_s \cdot \left(\frac{M}{M_s}\right)^2 \quad (2.XI)$$

The magnetic answer of magnetostrictive material is linked to its anisotropy and the magnetostriction. In (Figure 2.6) it is represented the changes of a hysteresis loop, depending on these two quantities:

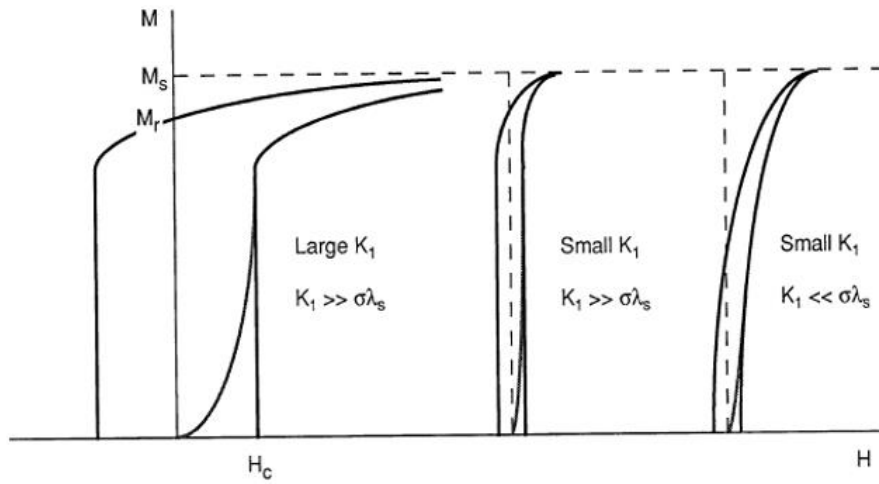


Figure 2.6 – Hysteresis loop as function of the anisotropy, K_1 , and the internal deformation $\sigma\lambda_s$ [13].

2.3.1 Piezomagnetism

Piezomagnetism is one of the consequences of the magnetoelastic coupling. The piezomagnetic effect is based on the excitation of the magnetostrictive material with AC, and DC magnetic field, which gives a dynamic deformation of the system in phase with the exciting AC field. Etienne du Tremolet de Lacheisserie defined piezomagnetism as the induced oscillating deformation of the material, due to an \vec{H}_{AC} , and knowing the polarizing field \vec{H}_{DC} [6]. This contribution can be expressed as:

$$q = \left(\frac{\partial \lambda_{AC}}{\partial H_{AC}}\right)_{H_{DC}} \quad (2.XII)$$

where q is the piezomagnetic coefficient, H_{AC} is the amplitude of the alternative magnetic field, and λ_{AC} is the dynamic magnetostriction, for a polarizing continuous field H_{DC} . The dynamic deformation can be defined as:

$$\lambda_{AC} = \frac{\Delta l_{AC}}{l_H} \quad (2.XIII)$$

where Δl_{AC} is the dynamic deformation, and l_H is the static deformation, due to the polarizing field \vec{H} [1]. The piezomagnetism is a dynamic phenomenon, linked to the dynamic susceptibility (2.VIII), which influences the hysteresis loop as shown in (Figure 2.7).

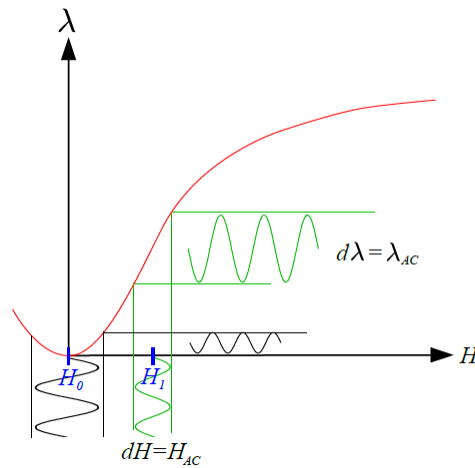


Figure 2.7 – Piezomagnetic curve at $H_0 = 0$, and $H_1 \neq 0$ [1].

2.3.2 Magnetostrictive materials

Since the discovery of magnetostrictive effects in iron by Joule in 1842, magnetostrictive materials had been researched within transition metals, e.g. Nickel (Ni), Cobalt (Co), and Permalloy (Ni-Fe-Co). Only in the second half of the XX century, highly magnetostrictive properties were associated with rare earth elements, principally to Samarium (Sm), Terbium (Tb), and Dysprosium (Dy). Later, they were combined with the magnetic transition metals, to gain over the temperature limitation. Huge room temperature magnetostrictions were achieved for TbFe₂ compound. However, because the magnetostriction originates in the strain-anisotropy dependency, the large magnetostriction of this compound was obtained at the expense of large anisotropies. This poses a technological limitation for the necessary large fields of over 2 MA/m to achieve saturation.

Partial substitution of dysprosium with terbium in the TbFe₂ compound resulted in an improvement of magnetostriction, and anisotropy properties [7]. In 1971, the US Naval Ordnance Laboratory fabricated an alloy of Tb, Dy, Fe, which exhibits giant magnetostriction up to 2000 ppm at room temperature, at a moderate saturation field of 0.16 MA/m. The stoichiometry of the compound can be represented as Tb_{0.3}Dy_{0.7}Fe_{1.9-1.95}, and since the 1980s it has commercialized under the name Terfenol-D (**Ter** = terbium, **Fe** = iron, **N** = Naval, **O** = Ordnance, **L** = Laboratory, **D** = Dysprosium). A second new magnetostrictive material, based on amorphous metal was introduced in 1978, produced by the rapid cooling of iron, nickel, and cobalt alloys with elements of silicon, boron, and phosphorus. These alloys are commercially known as Metglas (metallic glass) and are commonly produced in thin-ribbon geometries. Furthermore, in 1999 a new alloy of iron, and gallium was created with the name of Galfenol, Fe_{81.6}Ga_{18.4}. In Table 2.2, a brief scheme of the physical properties of the main magnetic, and magnetostrictive materials is reported.

Material	$3/2 \lambda_s (10^{-6})$	$\rho (g/cm^3)$	$B_s (T)$	$T_c (^\circ C)$	$E (GPa)$	k
Fe	-14	7.88	2.15	770	285	-
Ni	-50	8.9	0.61	358	210	0.31
Co	-93	8.9	1.79	1120	210	-
Tb	3000 (-196 °C)	8.33	-	-48	55.7	-
Dy	6000 (-196 °C)	8.56	-	-184	61.4	-
TbFe ₂	2630	9.1	1.1	423	-	0.35
Terfenol-D [14]	1620	9.25	1	380	90	0.77
Galfenol [15]	400	7.8	1.5	670	80	0.65
Metglas	60	7.32	1.65	370	25 - 200	0.92

Table 2.2 – Magnetoelastic properties of some magnetostrictive materials [7]. λ_s is the saturated magnetistraction, ρ is the material's density, B_s is the saturation flux density, T_c is the Curie temperature, E is the Young's modulus, and k is the magnetomechanical coupling factors.

2.4 Applications

By the growing number of publications, and patents, magnetostrictive materials are being employed in a wide variety of technological applications. In this paragraph, four examples of designs are reported, such as magnetostrictive sensor, actuator, motor, and hybrid transducer.

Magnetostrictive sensors

In the overview reported by [7], the term *sensor* is used to indicate the attributes of magnetostrictive materials which generate electrical signals in response to mechanical excitations such as force, strain, and torque, or magnetic excitations such as magnetic fields. By the properties of the magnetomechanical coupling, changes in the magnetoelastic state produce measurable changes in the magnetization anisotropy. To complete the sensing mechanism, a pick-up coil is often wrapped around the magnetostrictive material to detect the magnetization changes [8]. The principle that links the magnetization in the material with the voltage V , generated across a pick-up coil, is the Faraday-Lenz law of electromagnetic induction:

$$V = -N A \frac{dB}{dT} \quad (2.XIV)$$

in which N , and A , are respectively the number of turns, and constant cross-sectional area of the coil and B is the magnetic induction, which quantifies the magnetization state through the relation (2.IX). A position sensor is taken as an example of a magnetostrictive application. The sensor responds to the changes in the permeability of the magnetostrictive material, connected to the magnetomechanical coupling. A position detector can be made with a magnetostrictive material, employed as an acoustic waveguide. It is formed by a permanent magnet, connected to the target, and rides along the length of the waveguide, an emitter/receiver head, which sends, and receives either an acoustic or current pulse down the waveguide and a damper, which prevents unwanted wave reflections. The scheme of the sensor is represented in Figure 2.8.

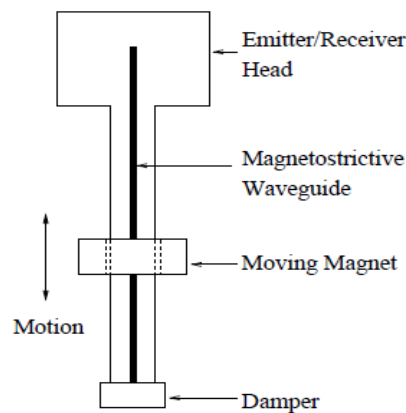


Figure 2.8 – Magnetostrictive waveguide position sensor [8].

The operating principle consists of the interaction of the permanent magnet with the magnetostrictive waveguide, and on the local change of material properties. These material properties changes can be detected in different ways. In one version, the stiffness discontinuity, produced by the magnet, partially reflects an acoustic pulse, sent by the emitter. In a second version, the emitter sends a continuous current pulse down the waveguide which produces a circumferential magnetic field, that interacts with the axial field from the magnet. In both versions, the transit times of the original, and reflected pulses provide a measure of the location of the magnet along the waveguide [8].

Magnetostrictive actuators

The number of actuator applications, based on magnetostrictive materials, mainly Terfenol-D, is continuously increasing as a consequence of the high energy density, high force, broad frequency bandwidth, and fast response that these materials can provide [8]. Magnetostrictive actuators are designed for different applications: sonar, high precision micropositioning, borehole seismic sources, geological tomography, etc.

Sonar actuators must produce high mechanical power at low frequencies, often with the additional constraint of a broad frequency bandwidth or equivalently. Although nickel was widely employed in sonar applications during the Second World War; it features a low magneto-mechanical coupling coefficient of $k = 0.30$, which typically demands a high Q , to achieve good efficiencies [8]. In contrast, the giant magnetostrictive materials have a much higher coupling coefficient of over $k = 0.70$, which makes it possible to simultaneously operate the actuator at low Q and attain high power outputs [8]. For example, a Terfenol-D Tonpilz actuator can produce a bandwidth of 200 Hz at a resonance frequency of 2 kHz ($Q = 10$), and a source-level of 200 dB [9].

Motors applications

From the point of view of motors, one example is Kiesewetter motor, reported in Figure 2.9, which displaces loads beyond the maximum strain normally achievable with Terfenol-D rod [8]. The direct coupling between the load and magnetostrictive element implies the net load-displacement will be limited by the magnetostriction.

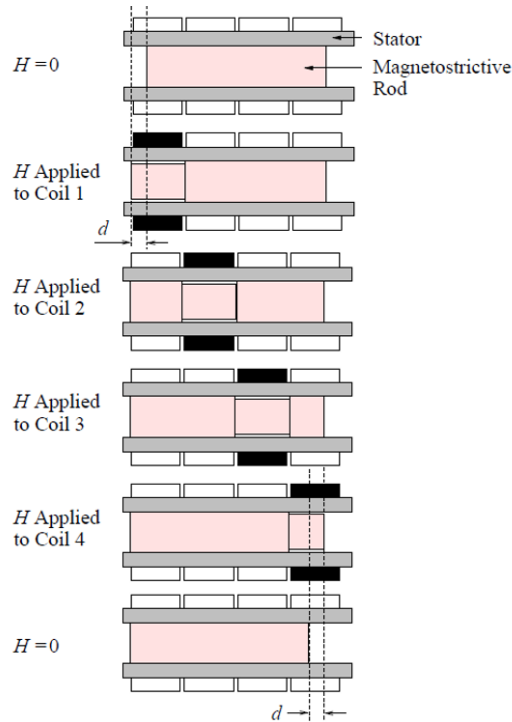


Figure 2.9 – Kiesewetter inchworm motor [8].

Kiesewetter motor consists of a cylindrical Terfenol-D rod, which fits inside a stiff stator tube when no magnetic field is applied. Several short coils surround the stator to produce a magnetic field to sweep the Terfenol-D. Once, the section of the rod is directly exposed to the magnetic field, it stretches, and shrinks. As the field is removed, the rod clamps itself inside the stator, but at a distance d to the left of the original position, and so on for the resting coils. The direction of motion is changed by inverting the sequence in which the coils are energized. From a design perspective, the total displacement is limited only by the length of the Terfenol-D rod, whereas the speed of motion is proportional to the sweeping frequency, and the rod's magnetostriction. A proof-of-concept of Kiesewetter motor has been presented in [10].

Magnetostrictive transducer

From the technological interest of this thesis, the hybrid smart material transducer can be considered in a separated class, because magnetostrictive materials are inductive, and piezoelectric elements are capacitive. It results in advantageous to combine both types of materials in the same device, to produce a resonant electric circuit. When driven at resonance, this type of device behaves like a purely resistive load, and only the energy effectively converted to mechanical motion or lost to inner losses needs to be supplied externally. This greatly simplifies amplifier design and helps for attaining high efficiencies [8]. An example of a hybrid magnetostrictive/piezoelectric device is presented in the following paragraphs.

3. Piezoelectric Materials

Piezoelectricity represents the relationship between mechanical deformation and electricity; in specific, it qualifies the coupling behavior between mechanical strain, and electrical field in some specific polarized materials (e.g. crystals, and certain ceramics). The word piezoelectricity comes from the Greek πιέζειν (piezein), which means “to press/to squeeze”, and ἤλεκτρον *ēlektron* (amber), the ancient source of electric charge.

The first demonstration of the piezoelectric effect was achieved by French physicists Jacques, and Pierre Currie in 1880, followed by Lippmann in 1881 who proved the reversibility of the phenomenon from the fundamental thermodynamic principles [16]. However, the piezoelectric phenomenon found its first practical application during World War I with the ultrasonic submarine detector, invented by Paul Langevin [17]. The first sonar was built as a mosaic of thin quartz crystals, with the resonant frequency of about 50 kHz, glued between two steel plates, and mounted in a housing suitable for submersion. Thanks to the return echo, the timing between the generated, and reflected acoustic waves, they were able to measure the depths, and distances from other underwater objects. The success of sonar stimulated intense development activity on all kinds of piezoelectric devices, both resonating, and non-resonating, and mainly based on ultrasonic waves generation or high precision measurements. In fact, after World War I, most of the classic piezoelectric applications were conceived and reduced to practice, such as microphones, accelerometers, ultrasonic transducers, bender element actuators, signal filters, etc. During World War II, and the Cold War, advances in materials science brought to the discovery new family of piezoelectric materials, and to improve their properties. In the U.S., Japan, and the Soviet Union, different research groups discovered ceramic materials exhibiting dielectric constants up to 100 times higher than common cut crystals, such as perovskite, and later the lead zirconate titanate family, with an easy fabrication. Meanwhile, they focused their attention on the correspondence of the crystal structure to the electro-mechanical activity, and the possibility to dope both families with metallic impurities (e.g. Ni, Bi, Sb, Nb) to achieve the same properties. This capability allows tailoring the materials to a specific application. In contrast to the competitive, and secrecy policy practiced among U.S. piezoceramic manufacturers, several Japanese companies, and universities formed a cooperative association, which brought Japan to dominate the market of the piezoelectric industry in the second half of XX century.

Nowadays, piezoelectric crystals are used in different domains, and with different applications, such as sensors, actuators, transducers, and energy harvesters (Figure 3.1).

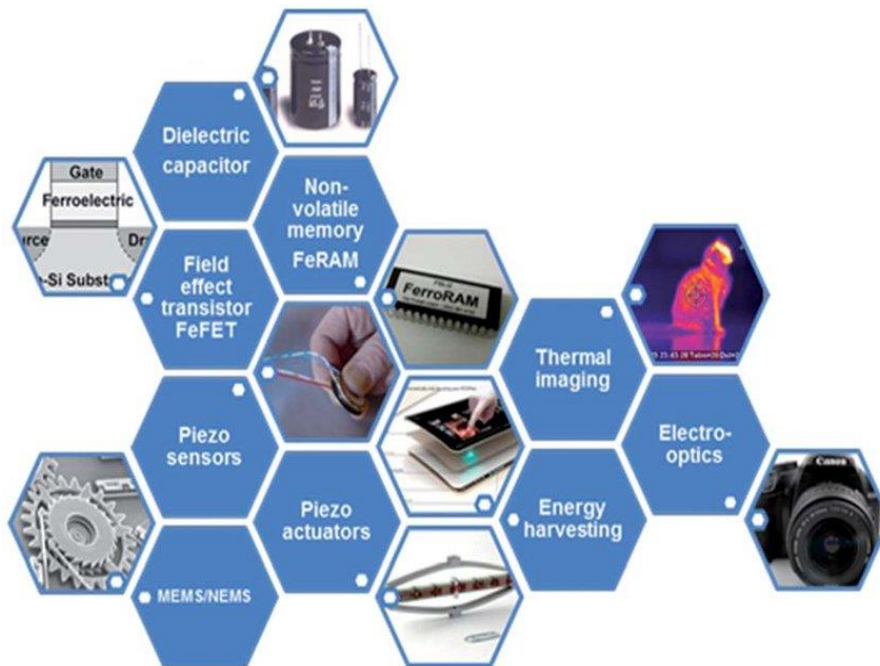


Figure 3.1- Different applications of piezoelectric materials [18].

3.1 Principles, and Structures

Piezoelectricity is an electromechanical phenomenon, dependent on the crystal structure of materials, and demonstrated through two macroscopic effects (Figure 3.2). The *direct piezoelectric effect* is based on a mechano-electric conversion. Mechanical stresses, arising from an external force that acts on the piezoelectric body, induce displacements of the electrical dipoles. This generates an electric field, which produces a corresponding electric voltage. The direct piezoelectric effect is also called a sensor or generator effect. On the contrary, the *indirect piezoelectric effect* is based on an electromechanical conversion. When an electric voltage is applied to a piezoelectric component, free of mechanical constraints, it causes a geometric modification of its internal structure. The achieved deformation directly depends on the device's polarity, the direction of the polarization, and the applied voltage. This effect is frequently also called the actuator or motor effect [19].

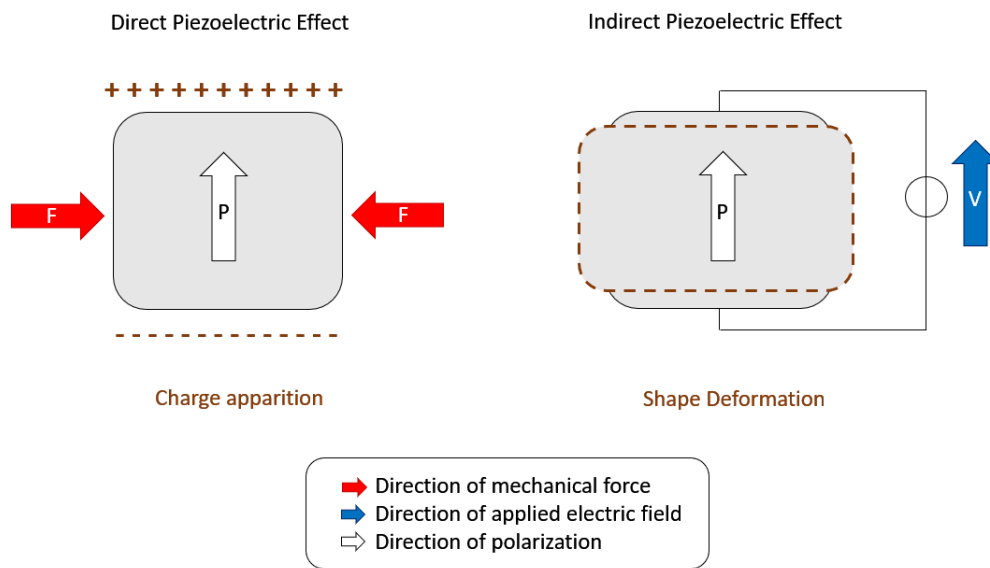


Figure 3.2 - Direct, and Indirect Piezoelectric Effects [2].

From the microscopic point of view, piezoelectricity was demonstrated by the Curie brothers, studying the crystal structure of quartz. In this configuration, the center of positive charges is not the same as negative ones. So, when a mechanical force is applied to the material, the two electrical centers tend to move away, creating an internal asymmetry, and a consequent polarization inside the mesh. The quartz was just the starting point for the discovery of piezoelectric materials; later, the attention was focused on oxide ceramics with a crystal structure of perovskite-type (general formula $A^{2+}B^{4+}O^{3-}$). In particular, the most employed piezoelectric material started to be the Lead-Zirconate-Titanium (PZT), which exhibits large displacements, and large induced electric voltages.

Among the 32 crystal classes of materials, 20 are piezoelectric, and some of them have further pyroelectric, and ferroelectric properties (Figure 3.3). Any material develops a dielectric polarization when an electric field is applied, but a material, which has a natural charge separation, even in the absence of a field, is called polar material; it is due to its crystal structure, and the working temperature. All polar crystals are pyroelectric. Pyroelectricity can be described as the ability of certain materials to generate a temporary voltage when they are heated or cooled. Among the pyroelectrics, there are ferroelectric materials.

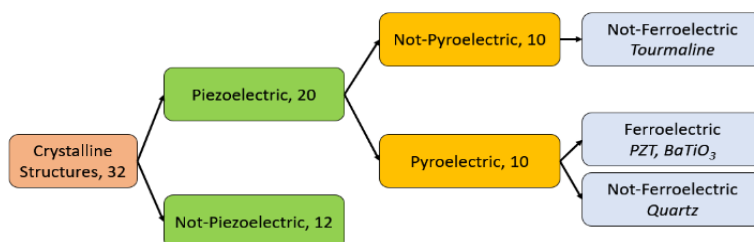


Figure 3.3 - Scheme of different crystal classes [1].

The ferroelectric phenomenon is directly linked to three elements, the applied electric field, the mechanical strain, and the temperature, which plays the main role in its crystal structure. From the points of view of the electric field, and mechanical strain, the reactions of ferroelectric materials are represented in (Figure 3.4), through the ideal polarization, and butterfly hysteresis loops. Ferroelectric materials, in the absence of an electric field, and a mechanical strain, do not exhibit a *remanent polarization* (P_R). It means all the dipoles are not uniformly oriented, so the total electric moment is zero. However, upon the application of an electric field or external pressure, of enough magnitude, the crystal becomes permanently polarized until saturation (P_S). The *coercive field* E_c is defined as the strength of the electric field at which the macroscopic polarization of the ferroelectric material disappears.

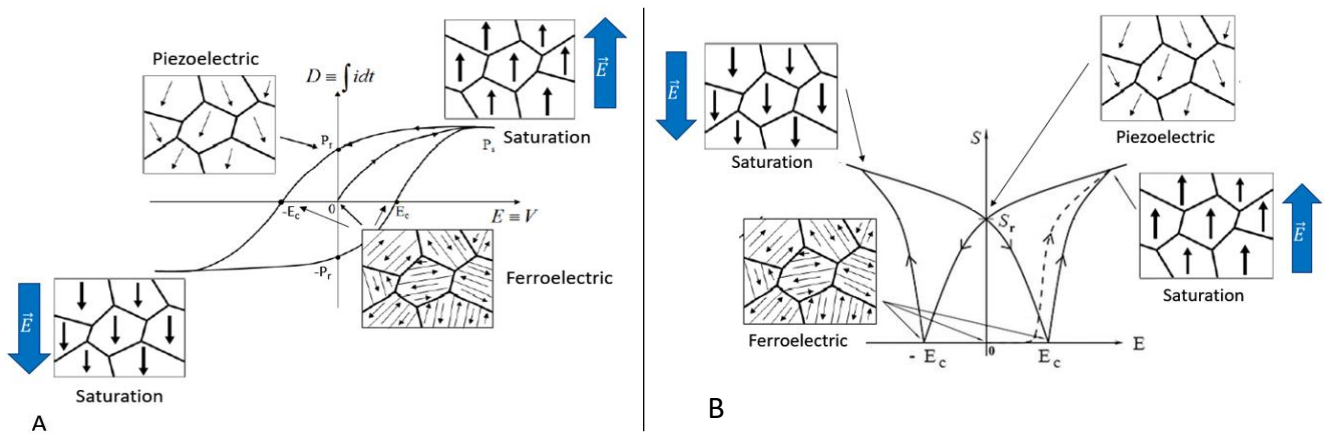


Figure 3.4 – (A) Hysteresis Cycle of a ferroelectric material. (B) Butterfly curve of a ferroelectric material [45].

From the point of view of temperature, as shown in (Figure 3.5), at high temperature, a ferroelectric material appears without electric asymmetry, and any piezoelectric properties, even in presence of external mechanical pressure. On the contrary, at low temperatures, its structure presents an electrical asymmetry and a consequent internal polarization; so, it can be defined as a ferroelectric material. The temperature, which shows this change of properties, is called *Curie Temperature* (T_c).

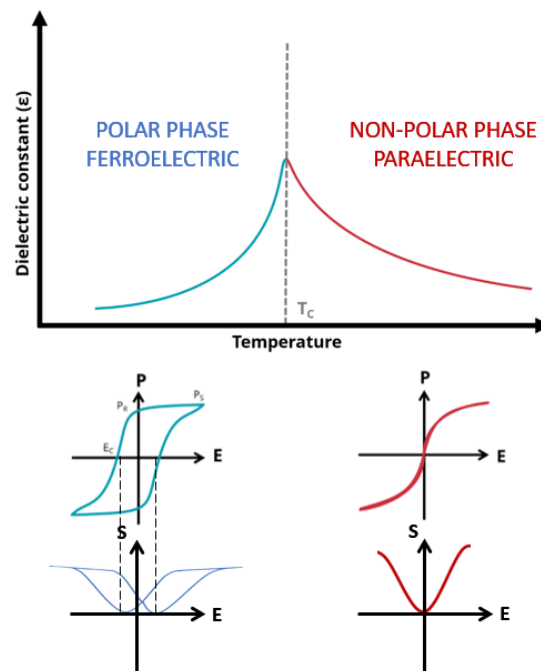


Figure 3.5 – Dependency of dielectric constant to the temperature. In the ferroelectric state the field-dependent electric polarization, and strain exhibits hysteresis [1].

In general, the ferroelectric materials are divided into two groups, referring to the mobility of the dipoles or domains, and hence to the polarization, and depolarization behavior. The *soft* group has a high domain's mobility, and easy to polarize. The *hard* group can be subjected to high electrical, and mechanical stresses. Their properties do not change too much under these conditions, and this makes them particularly ideal for high-power applications.

3.2 Fundamental Equations

Under Curie temperature, the piezoelectric phenomenon is governed by the interactions between electric, and mechanical properties (Figure 3.6). To understand, and study polarized piezoelectric materials, it is necessary to describe these two effects through physical quantities.

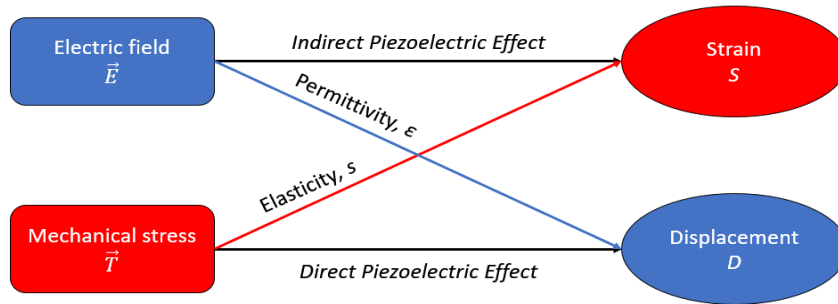


Figure 3.6 – Scheme of piezoelectric effects.

In simplified form, the basic relationships between the electrical, and mechanical properties can be respectively obtained starting from the constitutive law for the electric field (3.I), and Hooke's law (3.III):

$$\vec{D} = \epsilon \vec{E} + \vec{P} \quad (3.I)$$

where D is the electric displacement field, ϵ is the absolute permittivity, E is the electric field, and P is the electric polarization of the sample. In the case of a piezoelectric material, the polarization of the sample can vary as a consequence of applied pressure, so it can be linked to a mechanical component as follow, (3.II):

$$D_i = P_i = d_{ij} T_j \quad (3.II)$$

where P_i is the induced polarization along i -direction, T_j is the elastic stress along j -direction, and d_{ij} is defined as a piezoelectric coefficient. It is defined as the induced electric charge per unit to the applied mechanical stress.

From the mechanical point, Hooke's law expresses the cause-effect relationship between the mechanical deformation of a material, due to an applied external force:

$$S_\alpha = s_{\alpha\beta} T_\beta \quad (3.III)$$

where S_α is the mechanical strain, measured along α -direction, T_β the mechanical stress along β -direction, and $s_{\alpha\beta}$ the elastic compliance coefficient, defined as the produced strain along $\alpha\beta$ -direction per unit of stress. The often-used elasticity or Young's modulus corresponds in the first approximation to the reciprocal value of the corresponding elasticity coefficient. In a piezoelectric material, the induced elastic strain can be caused by an applied electric field, so it can be associated with the electrical component through the following formula (3.IV):

$$S_\alpha = d_{i\alpha} E_i \quad (3.IV)$$

where S_α is the induced strain along α -direction, $d_{i\alpha}$ is defined as a piezoelectric coefficient, and E_i is the applied electric field along i -direction. In this case, the piezoelectric coefficient is defined as the mechanical strain obtained per unit of the electric field applied.

In conclusion, the *Direct Piezoelectric Effect* can be represented through the formula (3.V):

$$D_i = \varepsilon_{i\beta} E_\beta + d_{ij} T_j \quad (3.V)$$

and the *Indirect Piezoelectric Effect* with (3.VI):

$$S_\alpha = d_{ij} E_i + s_{\alpha\beta} T_\beta \quad (3.VI)$$

3.3 Oscillation modes/Dynamic Behavior

Piezoelectric elements are widely used as emitters, sensors, resonators, filters, and actuators to convert electrical to mechanical energy, and vice versa. In general, a piezoelectric transducer can be regarded as a two-port network; at the input port, an alternating electric signal is applied, and a consequent mechanical vibration is produced at the output. The vibration modes of a transducer can be different, on the base of its geometries, polarization, and the applied electric field. Here is a brief scheme (Table 3.1) on the possible types of vibrations, associated with shapes, and boundary conditions:

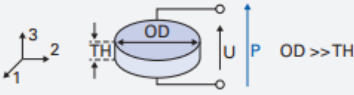


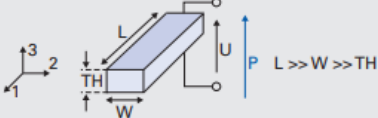
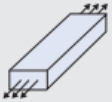
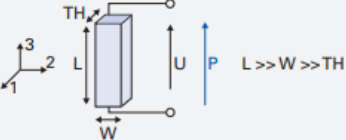

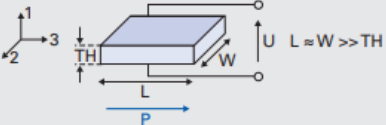
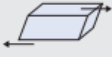
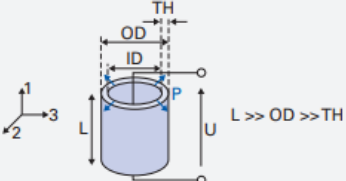


Shape	Oscillations	
	Type	Mechanical deformation
Thin disk 	radial	
	thickness	
Plate 	transverse	
Rod 	longitudinal	
Shear plate 	thickness shear	
Tube 	transversal	
	thickness	

Table 3.1 - Scheme of vibration modes of different piezoelectric transducers. OD is the external diameter, and ID the internal one, TH the thickness, W the width, and L the length. P represents the electrical polarization, and U the electric voltage [21].

In general, piezoelectric transducers are resonant devices. When they operate at the resonance frequency, the output mechanical or acoustical power and the energy conversion efficiency reach the maximum values. Near the resonance frequency, the piezoelectric transducer can be represented by a lumped electromechanical equivalent circuit as shown in (Figure 3.7).

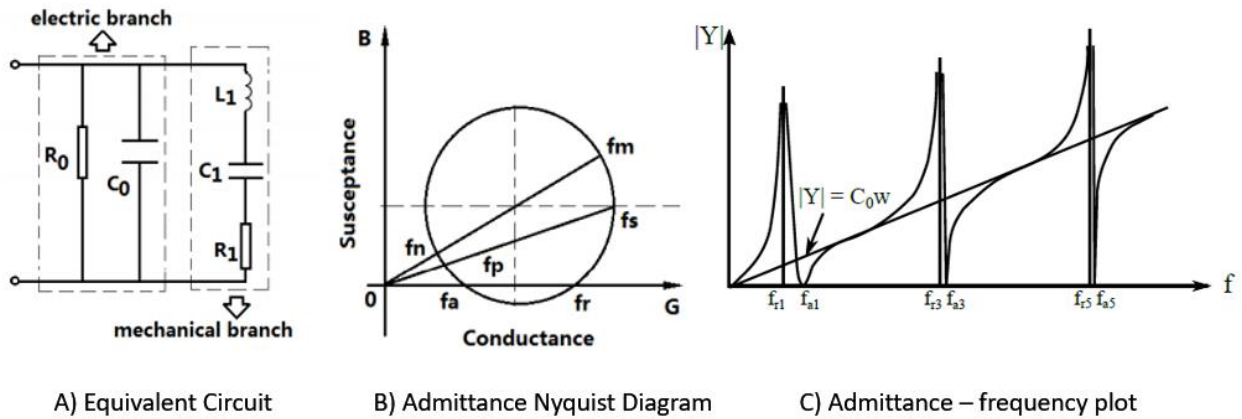


Figure 3.7 – (A) Lumped electromechanical equivalent circuit, and (B) admittance circle diagram of a piezoelectric transducer at resonance [22]. (C) Plot of the admittance, and frequency for a piezoelectric transducer [23].

The equivalent circuit can be divided into two parts: the electric, and mechanical branches. In Figure 3.7.A, R_0 , and C_0 represent the dielectric loss resistance and the clamped capacitance of the piezoelectric transducer. On the contrary, the mechanical branch (R_1 , L_1 , and C_1) describes the change in the mechanical properties, such as elastic deformation, effective mass (inertia), and mechanical losses resulting from internal friction. R_1 is composed of two parts, one is the internal mechanical loss of the transducer, the other is the load mechanical resistance. From the lumped electromechanical equivalent circuit of a piezoelectric transducer, the input electric admittance, and its characteristics frequencies are obtained (Figure 3.7.B):

- f_m = max admittance freq. f_p = parallel resonance freq. f_r = resonance freq.
- f_n = min admittance freq. f_s = series resonance freq. f_a = antiresonance freq.

However, when the loss resistances and the load are ignored, these frequencies correspond with a good approximation to $f_m = f_s = f_r$, and $f_n = f_p = f_a$ [49]. These frequencies are not unique, as shown in Figure 3.7.C, but they correspond to each oscillating state of the piezoelectric element. Oscillation states or modes, resonant frequency, and the deformation are decided by the geometry of the element, its elastic properties, and by the orientations of the electric field, and the polarization. Before proceeding with the specific cases, it is better to schematize the useful electromechanical quantities.

Type	Symbol	Physical Quantity	Definition	Units
Electrical	D	Dielectric displacement	$D = \epsilon^T E + dT$	C/m ²
	E	Electric field		V/m
	ϵ^T	Relative permittivity for T = const.		
Mechanical	S	Mechanical strain	$S = dE + s^E T$	N/m ²
	T	Mechanical stress		
	s^E	Elastic Coefficient for E = const.		
Piezoelectric	d_{ij}	Piezoelectric Coefficient	The ratio of induced electric charge to the mechanical stress or of the achievable mechanical strain to an applied electric field (T = constant).	C/N or m/V
	g_{ij}	Piezoelectric Voltage Coefficient	The ratio of the induced electric field E to the effective mechanical stress T.	V·m/N
	N_i	Frequency Coefficient	It describes the relationship between the body's geometry, and the corresponding (series) resonance frequency.	

	k_{ij}	Coupling Factor	It describes the ability of piezoelectric material to convert electrical energy into mechanical energy, and vice versa.	
	Q_m	Quality Factor	It characterizes the “resonance sharpness” of a piezoelectric body or resonator.	

Table 3.2 – Scheme of piezoelectric quantities.

Starting from data given in Table 3.1, it is possible to estimate the resonance frequencies, mechanical displacements, and electrical voltages for each piezoelectric geometry, and vibration type. In the following Table 3.3, they are represented:



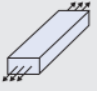

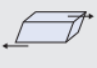


Type	Oscillations		Electrically induced displacement (small signal)	Mechanically induced voltage (small signal)
	Mechanical deformation	Series resonance frequency		
radial		$f_s = \frac{N_p}{OD}$	$\Delta OD = \frac{d_{31} OD}{TH} U$	
thickness		$f_s = \frac{N_t}{TH}$	$\Delta TH = d_{33} U$	$U = -\frac{4g_{33} TH}{\pi OD^2} F_3$
transverse		$f_s = \frac{N_l}{L}$	$\Delta L = \frac{d_{31} L}{TH} U$	$U = -\frac{g_{31}}{W} F_1$
longitudinal		$f_s = \frac{N_3}{L}$	$\Delta L = d_{33} U$	$U = -\frac{g_{33} L}{W TH} F_3$
thickness shear		$f_s = \frac{N_5}{TH}$	$\Delta L = d_{15} U$	$U = -\frac{g_{15} TH}{LW} F_3$
transversal		$f_s = \frac{N_l}{L}$	$\Delta L = \frac{d_{31} L}{TH} U$	
thickness		$f_s = \frac{N_t}{TH}$	$\Delta TH = d_{33} U$	

Table 3.3 – Oscillation states for different piezoelectric geometries [2291].

3.4 Type of piezoelectric materials

The piezoelectric materials can be divided into different families, on the base of their crystal lattices. Four classes can be identified: monolithic crystals, ceramics, polymers, and composites.

Monolithic crystal

Monolithic crystals are solid materials, formed by a unique single crystal, repeated in the lattice. They can be presented in nature, like the quartz, and LiNbO_3 , or be synthesized. The ferroelectric monocrystals have one direction of polarization, which corresponds to one of the crystallographic axes, and they have the characteristic to not be porous, the relative density of 100%, which gives them good characteristics at high frequencies. Examples of monolithic crystals are PZNR, PZN-PT, and PMN-PT [2].

Ceramics

Ceramics are synthesized materials, sintered from a starting powder or paste, with a polycrystalline configuration. The conformation of the internal grains influences the properties of the entire material. Some examples of these ceramics are BaTiO_3 , and PZT [2].

Polymers

Polymeric piezoelectric materials, such as PVDF, have the advantage to be flexible, easy to integrate into the composites, and lightweight. They usually have a lower coupling coefficient, compared to monocrystals, and ceramics, and low relative permittivity, which limits their applications.

Composites

The composites are materials, formed by piezoelectric elements incorporated in an insulating polymeric material. An example is the MFC (Macro Fibre Composite), developed by NASA in 1999. The MFC is constituted by piezoelectric rods in resin layers, electrodes, and polyimide film [2].

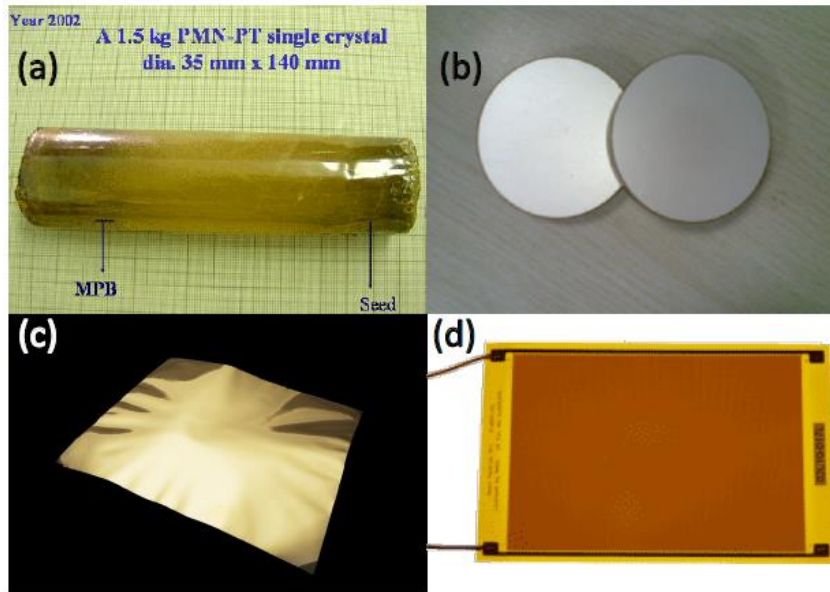


Figure 3.8 – (a) Monocrystal of PMN-PT, (b) Ceramic PZT, (c) PVDF film, and (d) MFC [2].

3.5 Applications

From mechanical engineering or production technology through to semiconductor technology, they benefit from the piezoelectric characteristics of the components. Due to their low energy consumption, reliability, precision, small dimension, and low-cost, piezoelectric devices can be very versatile.

In specific, the medical engineering, and biotechnology industry employ piezoelectric devices in many applications for example in imaging for medical diagnostics, such as radiography, magnetic resonance imaging (MRI), computed tomography (CT), elastography, photoacoustic imaging, and ultrasound, etc. Furthermore, they could be used in therapy for the treatment of pain, for monitoring liquids, such as the detection of air bubbles in dialysis, or also a drive for micropumps.

Ultrasound imaging

In ultrasound Imaging, the big advantage of sonography is the harmlessness of the sound waves, which is why the method is widely used. The ultra-sonic transmitter contains a piezo element, which generates ultrasonic waves, and detects them back. The ultrasonic transmitter emits short, directional sound wave pulses which are reflected, and scattered by the tissue layers to different degrees. By measuring the propagation time, and the magnitude of the reflection an image of the structure under investigation is produced. For propagation time measurements the piezoelectric transducer operates outside the medium to be measured as both transmitter, and receiver. It emits an ultrasonic pulse in the air which is reflected by the content. The propagation time required is a measure of the distance traveled in the empty part of the container. This allows non-contact measurements whereby the level of liquids, and solids, can be measured. The resolution or accuracy depends on how well the ultrasonic pulse is reflected by the respective surface [22].

Bubble sensor

As a piezoelectric sensor, the ultrasonic bubble sensor provides reliable control of liquid transport in tubes. The sensor undertakes non-contact detection of the air, and gas bubbles in the liquid through the tube wall, and thus allows continuous quality monitoring. The application possibilities are in the medical, pharmaceutical, and food technology fields. The sensors are used to monitor dialysis machines, infusion pumps, or transfusions. Industrial applications include control technology, such as the monitoring of dosing, and filling machines, for example [22].

Energy harvester

As an energy harvester, as described in Chapter 1, a piezo-electric device was implanted in moving parts of the body, to convert vibration or mechanical energy to electrical energy, that activates electronic circuits in the AIMD. They specifically worked on the development, and design of an energy harvesting device to power supply a miniaturized leadless pacemaker without battery, directly placed in heart chambers. The piezoelectric characteristics are very promising and versatile. In this thesis, they will be explored in association with magnetostrictive properties.

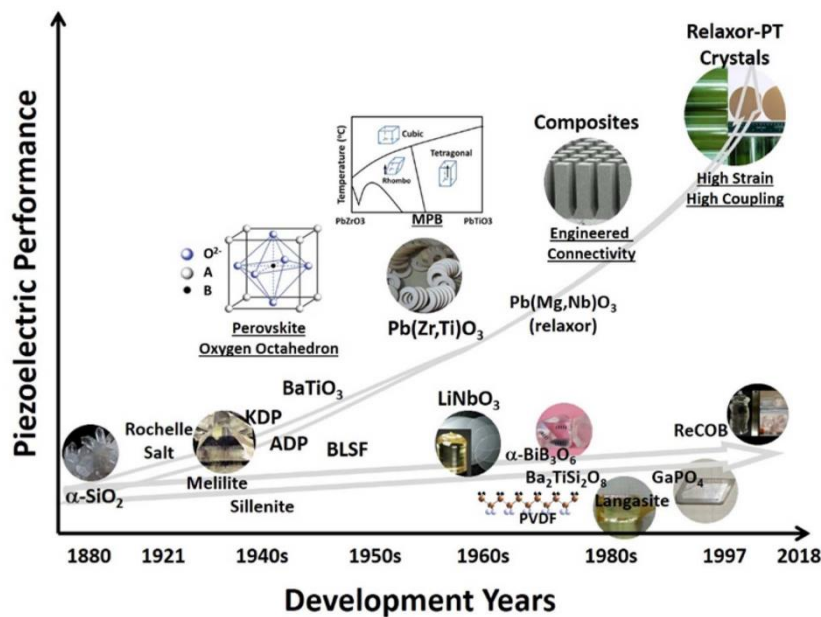


Figure 3.9 - Development of piezoelectric materials with milestones/ breakthroughs [48].

The piezoelectric characteristics are versatile and very effective for energy conversion. In this thesis, these materials will be studied in association with magnetostrictive materials, in the form of magnetoelectric composites.

4. MagnetoElectric Composites

The magnetolectricity denominates the coupling phenomenon between electric, and magnetic fields in the matter [25]. In specific, the magnetolectric (ME) effect is defined as the variation of the material's electric polarization, induced by an applied magnetic field (direct effect) or, conversely, a change of magnetization for an applied electric field (indirect effect).

Historically, two independent events marked the birth of the ME effect. In 1888 Röntgen discovered that a moving dielectric, subjected to an electric field, became magnetized [26]. Later, in 1894, Curie pointed out the possibility of intrinsic ME behavior of (non-moving) crystals, based on symmetry considerations [16]. The term *magnetolectric* was coined by Debye [25] a few years after the first (unsuccessful) attempts to an experimental demonstration of the static ME effect. Many decades passed until it was realized that the ME response is only allowed in time-asymmetric media. Such violation of time-reversal symmetry can extrinsically occur through the application of an external magnetic field [27] or movement, as in the historical experiment conducted by Röntgen, or intrinsically in the form of long-range magnetic ordering. In 1960, Dzyaloshinskii [28] was the first to show the violation of time-reversal symmetry for a specific system (antiferromagnetic Cr_2O_3), which was soon followed by experimental confirmation of an electric-field-induced magnetization, and a magnetic-field-induced polarization in Cr_2O_3 [25], both linear in the applied field. The experiments on Cr_2O_3 constituted a breakthrough in research on the ME effect. Ten years later, Van Suchetelenele, a researcher at Philips, proposed the concept of magnetolectric effect, as an intermediate coupling between the ferroelectric, and the ferromagnetic phases [1].

In general, the magnetolectric effect could be intrinsic or extrinsic. In the first case, the material presents one single phase, with an order of ferroelectric/ferrielectric/antiferroelectric jointly with an order of ferromagnetic/ferrimagnetic/antiferromagnetic, which is rare [1]. In this case, the ME effect is due to the local interaction between the magnetic, and ferromagnetic orders within the crystal lattice [29]. Nowadays, the most employed intrinsic magnetolectric material is the bismuth ferrite (BiFeO_3), for its good ME behavior at room temperature [30]. The second type of magnetolectric effect, defined as extrinsic, results from an intermediate coupling (generally mechanical) between the ferromagnetic phase, and the ferroelectric phase. Concerning this type of effect, which is investigated in this thesis, the magnetostrictive material is mechanically coupled to a piezoelectric material, generating an artificial ME behavior [8].

Scott et al. [32], gives an overview of magnetolectric, and multiferroic materials through Venn diagram, Figure 4.1. The larger circle contains antiferromagnets, antiferroelectrics, ferrimagnets, and in general magnetically or electrically ordered crystals (violet circle). The upper left circle contains ferrimagnetic materials (black circle), whereas the upper right has ferroelectric materials (green circle). The upper left oval contains antiferromagnetic materials (blue oval), whereas the upper right has antiferroelectric materials (green oval). The overlap is multiferroic, which is neither necessary nor sufficient for magnetolectricity (red-hatched region).

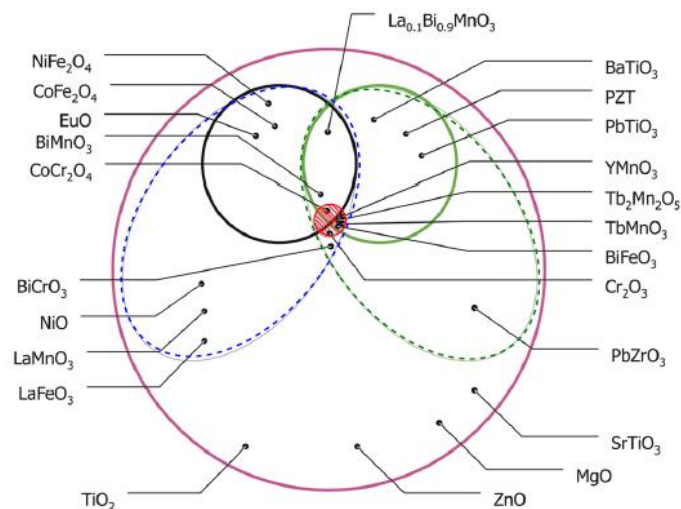


Figure 4.1 – Venn diagram for magnetolectric, and multiferroic materials [3231].

4.1 Principles, and structures

Magnetolectric (ME) materials, which exhibit coupling between magnetic properties, and dielectric properties, have raised great interest during the last decades, due to their potential use in smart electronic applications [25]. As previously described, the *direct magnetolectric effect* is a polarization response to an applied magnetic field \vec{H} . The two physical entities are linked through the *magnetolectric coefficient* α_{ME} :

$$\vec{E} = \alpha_{ME} \vec{H} \quad (4.I)$$

which is expressed in (V/m)/(A/m) in SI unit or (V/(cm·Oe)) in the American system. On the contrary, the *indirect magnetolectric effect* is referred to as a change of magnetization for an applied electric field \vec{E} , through the *indirect magnetolectric coefficient* α_{ME}^T :

$$\vec{M} = \alpha_{ME}^T \vec{E} \quad (4.II)$$

Due to the rarity of the intrinsic magnetolectric materials, in this thesis, only the direct extrinsic magnetolectric effect will be analyzed, as the result of the coupling of three different phenomena: piezomagnetic, mechanical, and piezoelectric.

In Figure 4.2, the direct magnetolectric mechanism is represented with two schemes. Referring to the scheme on the right, an external alternating magnetic field is applied to the system, to excite the sample (*phase 1*). An additional DC field can be used to bias the system, and work in a condition of linear magnetostriction (*phase 2*). The magnetostrictive part reacts to the magnetic excitation with a mechanical deformation at the same frequency of the AC field, defined as a piezomagnetic mechanism (*phase 3*). Due to the mechanical coupling, the strain is transferred to the piezoelectric part, which starts oscillating. The induced vibrations cause a change of the internal polarization, and a consequent electric field at the boundaries of the piezoelectric material (Chapter 2, Paragraph 3). So, the mechanical strain is transformed into electric voltage, through the piezoelectric coupling (*phase 4*). In general, the magnetolectric coefficient is strongly dependent on the intrinsic properties of the composite, and the mechanical coupling at the interface between magnetostrictive, and piezoelectric materials.

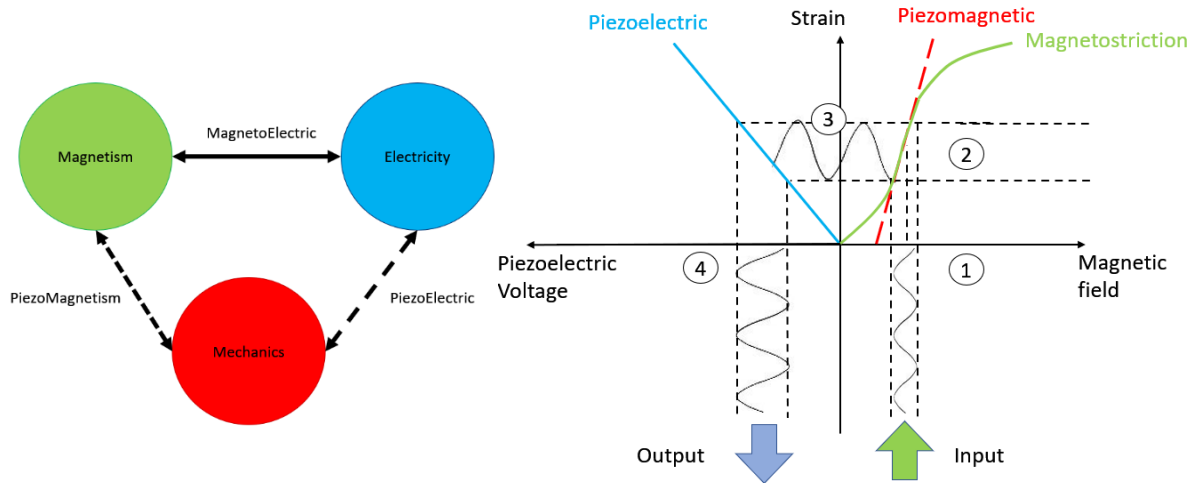


Figure 4.2 – Representation of the Direct Extrinsic MagnetoElectric Effect [2].

As described by Scott et al. [32], the extrinsic magnetolectric effect results from an intermediate interaction between the ferromagnetic phase, and the ferroelectric phase. In 1978, Newham proposed different categories of geometric structures, considering the coupling between the constituent phases [32]. Most of the fabrication processes are based on an initial mixing of starting powders, followed by e.g. pressing, sintering, densification, and solidification until reaching a net shape [34]. Newham's classification refers to the volume fraction of one constituent phase in the entire final composite, called 0-3, 2-2, and 1-3 (Figure 4.3).

The type 0-3 is usually formed by a magnetic oxide (electric insulator), represented by the green particles, isolated in a piezoelectric matrix. This structure requires a homogeneous mixing of the two phases to obtain a good polarization, which leads to several limitations on the reproducibility, and reliability of the composite. The specific issues are linked to the chemical reactions, which are difficult to prevent due to the sintering process at high temperature, the dielectric breakdown of magnetostrictive phase, during the polling process for the piezoelectric phase, and the presence of mechanical defects as cracks, pores, etc. resulting in poor elastic bonding between constituent phases [33]. Due to the difficulty in obtaining a good 0-3 composite, the study of this thesis will be focused on 2-2 structures.

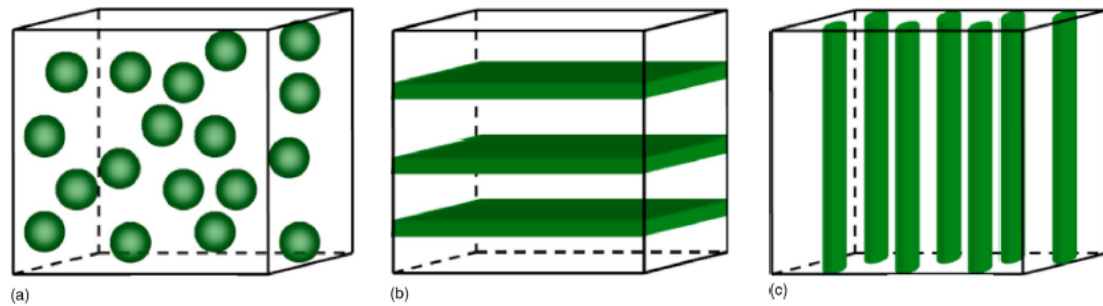


Figure 4.3 – Schematic configurations for different connectivity types of two-phase composite materials. a) 0-3, b) 2-2, c) 1-3 [34].

The 2-2 category is referred to the laminate composite, which presents a series of layers of the two different phases. Four bimorph configurations exist for these structures, which allow working with different vibrating modes. The laminate orientation combinations are defined as *L-T*, *T-T*, *L-L*, and *T-L* modes, indicating the relative directions of the magnetostriction, and polarization; L stays for longitudinal, and T for transversal to the length of the sample. In this case, the conductivity of the magnetic phase does not impact the polarization of the piezoelectric material. This advantage allows having better properties than 0-3 composites, due to their easier manufacturing control, and accurate volume fraction tuning (Table 4.1). Nevertheless, the co-sintering or adhesive bonding between each laminate composite inevitably leads to defaults in the interface, which involves mechanical losses [33]. In his thesis [2], Aubert reports a comparison of the ME effects between the first two structures, measured with the indicated exciting H_{AC} , and frequencies for the 0-3 category, and in quasi-static condition for the 2-2 one:

0-3 structure				2-2 structure		
Composition	α (V/A)	H_{AC} (mT)	f (kHz)	Composition	α (V/A)	Forme (mm)
0.4 CoFe ₂ O ₄ - 0.6 BTO*	0.062	2	60	Terfenol-D/PZT	7.38	Disque ($t=1/0.5/1$ $\varnothing=10$)
0.2 CoFe ₂ O ₄ - 0.8 BTO	3.175	0.5	160	Terfenol-D/PMN-PT	12.88	Disque ($t=1/0.5/1$ $\varnothing=10$)
0.2 CoFe ₂ O ₄ - 0.8 PZT	0.038	0.2	80	NiFe ₂ O ₄ /PZT	1.88	? ($t=0.04/0.04$ (10x))
0.5 CoFe ₂ O ₄ - 0.5 PMN-PT	0.018	1.6	0.1	Co _{0.6} Zn _{0.4} Fe ₂ O ₄ /PZT	0.312	? ($t=0.04/0.04$ (10x))
0.5 CoFe ₂ O ₄ - 0.5 BTO	0.225	—	—	NiCoZnFe ₂ O ₄ /PZT	0.55	Disque ($t=0.5/0.5/0.5$ $\varnothing=10$)
0.4 NiFe _{1.98} O ₄ - 0.6 BTO	0.315	0.1	0.1	NiCoZnFe ₂ O ₄ /PZT	2	Tore ($t=2/0.25$ $\varnothing=5/10$)
0.2 NiFe ₂ O ₄ - 0.8 PZT	0.244	0.1	1	NiCuZnFe ₂ O ₄ /PZT	1	Disque ($t_{tot}=3.25$ $\varnothing=10$)
0.3 NiFe ₂ O ₄ - 0.7 PZT	0.00063	—	1	MnZnFe ₂ O ₄ /PZT	3.25	Tore ($t=2/1$ $\varnothing=5/10$)
0.4 Ni _{0.8} Zn _{0.2} Fe ₂ O ₄ - 0.6 PZT	16.25	0.1	300	Metglas/PVDF	26.88	Pavé ($t=0.025/0.025$ $l=30x15$)
0.5 NCCF* - 0.5 NBT [†]	0.829	1	—	Galfenol/PZT	8.75	? ($t=20/400$ mm)
0.5 Ni _{0.5} Zn _{0.5} Fe _{1.9} O ₄ - 0.5 NBT	0.0011	—	—			

*BTO : BaTiO₃; *NCCF : Ni_{0.83}Co_{0.15}Cu_{0.02}Fe_{1.9}O_{4- δ} ; [†]NBT : Na_{0.5}Bi_{0.5}TiO₃

Table 4.1 – Summary of Magnetolectric coefficients for different laminate composites [2].

The third, and last structure, defined as 1-3, contains an array of piezoelectric materials (in form of a square rod, cylinder, etc.) embedded in continuous magnetic phases or magnetic/epoxy mixture matrix. This structure can be fabricated using a dice-and-fill technique, which allows controlling the volume ratio of the piezoelectric phase modifying the periodicity of the rod array [33]. This type of composite is usually employed in the fibers of nanocomposites, and present a high ME coefficient, as the 2-2 category.

4.2 Fundamental Equations

In magnetolectric composites, the magnetolectric effect is due to the magneto-mechanical-electric transform, induced by the mechanical coupling between the magnetostrictive, and piezoelectric layers. Dong et al., and Zhai J. [38 - 41] published a series of papers on the design, and modeling of bimorph laminate ME transducers. Their work created model subsets for each of the four possible coupling configurations within the ME structure. Several prototypes of rectangular and disk types of three-layer composites were designed, fabricated, and tested to validate the model [41]. The rectangular configuration is considered as a reference. These combinations are represented in Figure 4.4, indicating the longitudinal, and transversal orientations of the polarization, and magnetization in the bimorph composites.

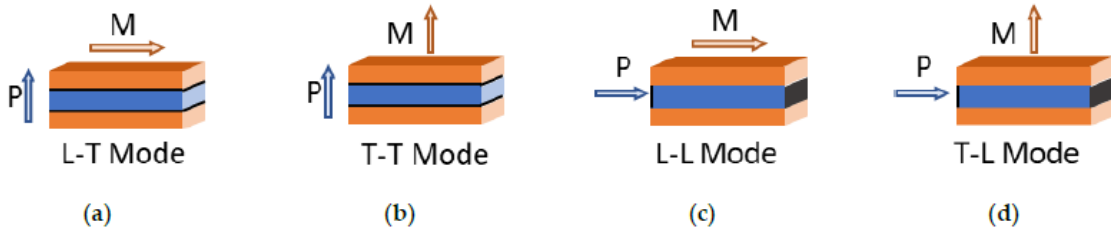


Figure 4.4 – Four relative orientations of the magnetization (M), and polarization (P), in laminate ME bimorph structure. Orange indicates the magnetostrictive materials (MS), blue the piezoelectric (PE), and black the location of the piezoelectric electrodes. Additionally, the letters in the mode names, T for transverse, and L for longitudinal respect to the MS, and PE materials. a) L-T mode, b) T-T mode, c) L-L mode, d) T-L mode [44].

In these papers, the ME energy transducer has been studied at a frequency much lower than the resonant frequency ($\omega \ll f_r$) and considering a uniform deformation under the external constraints [41]. Zhai J. et al [40] rank the four ME laminate configurations in descending order of the magnetolectric voltage coefficient as L-L, L-T, T-L, T-T. The magnetolectric voltage coefficient is expressed in [V/(A/m)] defined as:

$$\alpha_{MEV} = \frac{dV_{ME}}{dH} \quad (4.III)$$

where V_{ME} is the magnetolectric voltage, measured on the piezoelectric electrodes, and \vec{H} is the excitation magnetic field. For this thesis, the L-T structure was chosen, because of the materials' availability, and good coupling of piezoelectric-magnetostrictive configuration.

Due to the complexity of the multi-physics problem of a ME laminated energy transducer, a finite element method (FEM) in 2D is employed. A trilayer magnetostrictive/piezoelectric/magnetostrictive system is considered for the model with an external circuit. The system is excited from an external magnetic field, perpendicular to the polarisation direction, along the length of the sample, as showed in Figure 4.5.

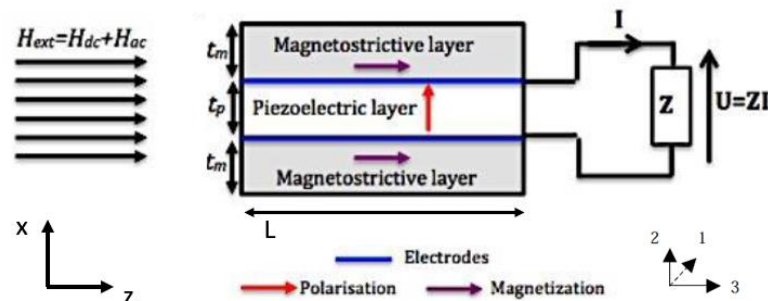


Figure 4.5 – Illustration of the 2D trilayer MPM composite in L-T mode [34].

In this case, both longitudinal, 33, and transverse, 31, magnetostrictive vibration modes are excited. However, due to the long length of the transducer, $L \gg (t_m + t_p + t_m)$, the 33-vibration mode becomes the fundamental mode, and the transversal one can be neglected. Since the layers of the laminate are stress coupled, the piezoelectric layer undergoes force oscillation along the z-direction, and a voltage is induced

between the electrodes in the x-direction. So the L-T ME effect occurs, when \vec{H} is parallel applied to the longitudinal vibration direction of the laminate, and the induced voltage, V , is perpendicular. To express the coupling links between the magneto-mechanical-electric parameters of the composite, it needs to correlate the electromagnetic (2.IX), electro-mechanical (3.V), and the magneto-mechanical (2.XII) constitutive laws, through two sets of linear equations [41].

4.2.1 Magnetostrictive Constitutive Equations

The magnetostrictive layer, excited by the external magnetic field \vec{H} , reacts with mechanical deformation. The induced strain, S , is directly proportional to the magnetic input, $S = \lambda H^2$, through two factors: the magnetostrictive coefficient λ (2.X), and the piezomagnetic coefficient q (2.XII). The two values are maximal at the inflection point of the quadratic S-H curve, showed in Figure 4.6. To work in this condition, the sample can be biased by an external DC field.

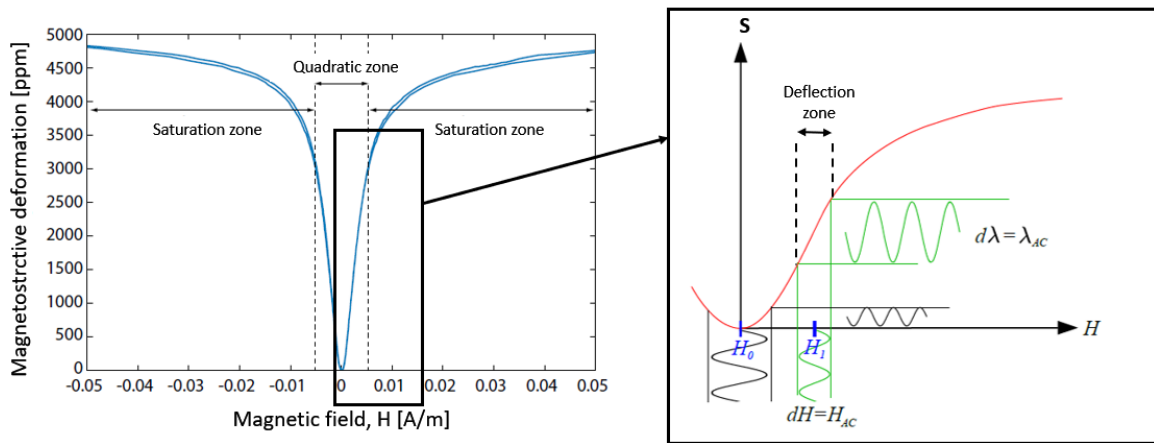


Figure 4.6 – Magnetostrictive deformation due to an applied magnetic field, in a magnetostrictive material [2].

When the magnetic field is applied parallel to the z-direction, a longitudinal strain is created ($S_1 = S_2 = 0$), and a magnetic field flux density B_3 is measured inside the magnetostrictive layer. The governing physics equations are presented as follows:

$$S_{3m} = d_{33m}H_3 + s_{33}^H T_{3m} \quad (4.IV)$$

$$B_3 = \mu_{33}^T H_3 + d_{33m} T_{3m} \quad (4.V)$$

where H_3 is the magnetic field along z, s_{33}^H , d_{33m} , and μ_{33}^T are respectively the elastic compliance at constant H , the longitudinal piezomagnetic constant, and the magnetic permeability at constant stress in the magnetostrictive layers [41].

4.2.2 Piezoelectric Constitutive Equations

The piezoelectric layer is polarized in its thickness direction, as represented in Figure 4.7, and the stress is imposed by the magnetostrictive layers in the length direction (principal strain), independently of the external \vec{H} direction of application.

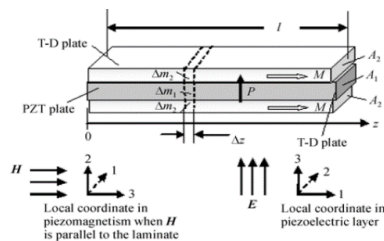


Figure 4.7 – L-T laminate composite representation [39].

Accordingly, the piezoelectric constitutive equations for this model are [39]:

$$D_3 = \varepsilon_{33}^T E_3 + d_{31p} T_{1p} \quad (4.VI)$$

$$S_{1p} = d_{31p} E_3 + s_{11}^E T_{1p} \quad (4.VII)$$

where D_3 is the electric displacement, ε_{33}^T is the permittivity under constant stress, s_{11}^E is the elastic compliance of the piezoelectric material under constant E , d_{31p} is the transverse piezoelectric constant, T_{1p} , and S_{1p} are the stress, and strain in the length direction of the piezoelectric layer, imposed by the magnetostrictive layer.

4.2.3 MagnetoElectric Constitutive Equations

Previous analysis of magnetostrictive/piezoelectric laminates has linearly combined the magnetostrictive, and piezoelectric constitutive equations, which do not account for loss components and supposed a uniform deformation. However, significant nonlinearities in both piezoelectric, and magnetostrictive materials are known to exist. To not neglect these losses, a harmonic approximation is added to the above relationships [39].

Assuming a harmonic motion in the z -direction, each small mass unit in the laminate can be considered to have the same displacement $u(z)$, and correspondingly strain:

$$S(x) = \frac{\partial u}{\partial z} \quad (4.VIII)$$

According to Newton's Second Law, it is possible to express an equation of motion to couple the piezoelectric, and magnetostrictive constitutive laws [39]:

$$(\Delta m_1 + 2\Delta m_2) \frac{\partial^2 u}{\partial t^2} = \Delta T_{1p}(A_1) + \Delta T_m(2A_2) \quad (4.IX)$$

where $\Delta m_1 = \rho_p A_1 \Delta z$, $\Delta m_2 = \rho_m A_2 \Delta z$, and ρ_p , and ρ_m are respectively the mass densities of the piezoelectric, and magnetostrictive layers, and A_1 , and A_2 the cross-sectional areas of the two layers. The equation of motion can be rewritten as [39]:

$$\bar{\rho} \frac{\partial^2 u}{\partial t^2} = n \frac{\partial T_{i,m}}{\partial z} + (1 - n) \frac{\partial T_{1,p}}{\partial z} \quad (4.X)$$

where $n = \frac{2A_2}{A} = 2t_m/(2t_m + t_p)$ is a geometric factor, and $\bar{\rho} = \frac{\rho_p A_1 + \rho_m 2A_2}{A}$ is the average mass density of the laminated composite. At this point, substituting in (4.X) the constitutive piezoelectric, and magnetostrictive laws, under harmonic oscillations, it is possible to simplify the motion equation to [39]:

$$\frac{\partial^2 u}{\partial z^2} + k^2 u = 0 \quad (4.XI)$$

where k^2 is the wavenumber defined as $k = \omega/v_{LT}$, ω is the system pulsation, and v_{LT} is the sound velocity, expressed as:

$$v_{LT}^2 = \left(\frac{n}{s_{11}^H} + \frac{1-n}{s_{11}^E} \right) / \bar{\rho} \quad (4.XII)$$

4.3 Equivalent circuit model

Design and analysis of a magneto-electric transducer is a complex multi-physics problem related to mechanics, materials science, and electronics. An equivalent circuit can be used to model a magneto-elastic-electric composite, starting from an extension of Mason's model for piezoelectric material [40]. The combination of the magneto-mechanical coupling with the mechano-electrical coupling was recently employed in literature [38 - 43], to investigate the ME transducer with its load for different modes, in static, and dynamic regimes.

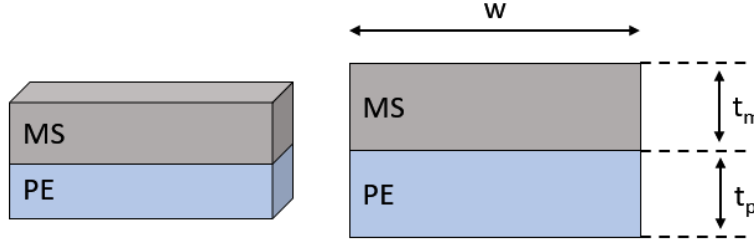


Figure 4.8 – Geometry layout of a ME transducer, formed by a layer of magnetostrictive material (MS), and a layer of piezoelectric material (PE).

The equivalent circuit is presented in Figure 4.9, where it is possible to identify three main blocks: magnetic (green), mechanical (red), and electrical (blue) blocks.

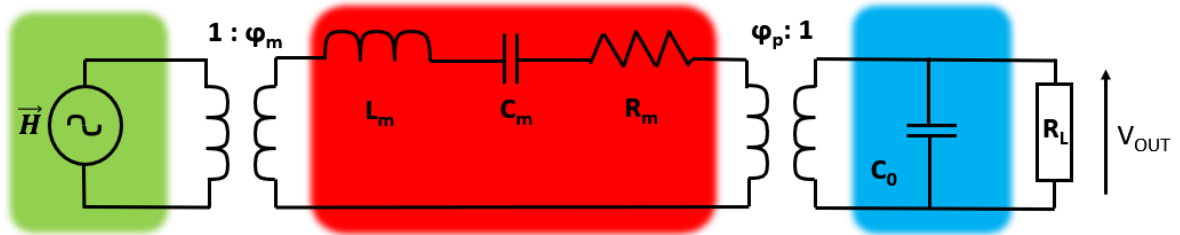


Figure 4.9 – Equivalent circuit model for magnetolectric transducer [34, 38]. Green for magnetic block, red for mechanical part, and blue for the electric one.

The equivalent generator represents the stress force, at which the ME laminate composite is subjected due to the external magnetic field \vec{H} . The applied magnetic field consists of a strong bias DC field, and a small AC field. Given H_0 as the peak-value of the AC magnetic field, the magnitude of \vec{H} can be expressed as:

$$H = H_{AC} + H_{DC} = H_0 e^{i\omega t} + aH_0 = H_0 (e^{i\omega t} + a) \quad (4.XIII)$$

The magnetic field is transmitted to MS layer, which causes a mechanical deformation of its structure. The MS transduction is modeled through the *magneto-elastic* or *magnetostrictive coupling*, φ_m . Consequently, the PE layer reacts to the mechanical strain through a mechano-electric transformation. In the model, the PE transduction is theoretically defined by the *elasto-electric* or *piezoelectric coupling*, φ_p . The two coefficients are dependent on the materials' properties, such as the elastic compliance, the piezomagnetic and piezoelectric coefficients, and the transducer's dimensions [44].

However, the mechano-electric blocks are based on the application of a piezoelectric energy harvester model to the ME case. Figure 4.10 represents the model from physical and electrical points of view. C_0 is defined as the clamped capacitance of the piezoelectric element, C_m identifies the mechanical stiffness of the system, L_m the equivalent dynamic mass, and R_m the mechanical losses of the system through a mechanical damper [42]. The respective relationships are reported in the following formulas (4.XIV):

$$\begin{aligned} C_m &= 1/K \\ L_m &= M \\ R_m &= D \end{aligned} \quad (4.XIV)$$

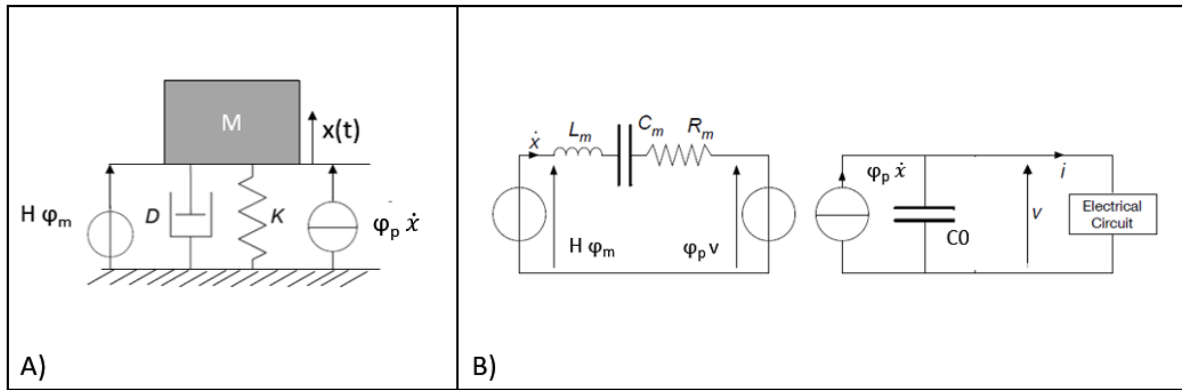


Figure 4.10 – Scheme of a transducer energy harvester. A) Physical point of view. B) Electrical point of view [42].

Consequently the discretization in finite elements of the coupled system, using the magnetolectric equation (4.XI), and Kirchoff's law for the electrical block, takes the form of the following matrix systems [34, 42]:

$$\begin{aligned}
 [M]\{\ddot{X}\} + [D]\{\dot{X}\} + [K]\{X\} + [\varphi_p]\{V\} &= [\varphi_m]\{H\} \\
 \{I\} &= [\varphi_p]\{\dot{X}\} - [C_0]\{V\}
 \end{aligned}
 \tag{4.XV}$$

where $[M]$, $[D]$, $[K]$, $[C_0]$, and $[\varphi_p]$ represents respectively the electro-mechanical mass, damping, stiffness, clamped capacitance, and elasto-electric coupling matrices. The vectors $\{X\}$, and $\{H\}$ represent respectively the unknown position, and excitation vector, due to the external magnetic field, $\{I\}$, and $\{V\}$ are the current, and voltage in the electric block.

This model was here developed considering the LT mode of a rectangular ME composite plate, but it could be further applied to other modes and geometries of the ME composite. The main assumptions are the linearity of the material properties and their time invariance.

4.3.1 Static Regime

In a static regime, it is possible to estimate the system's parameters through the measurements of the transducer's output impedance [42]. In this case, the *static regime* is defined as an operating condition, under which the transducer is biased through a DC magnetic field. The equivalent circuit can be simplified as in Figure 4.11:

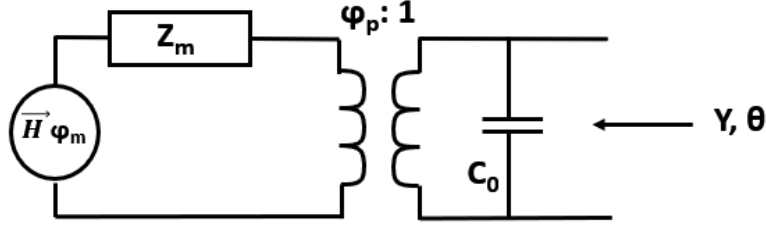


Figure 4.11 - Adapted equivalent circuit model for ME transducer in open circuit condition [34].

Following the equivalent circuit model, to calculate the output impedance or admittance of the transducer, it is possible to short-circuit the system's generator, represented by the external DC magnetic field. Then, the circuit impedance can be represented by two parts, one mechanical, Z'_m , and one electrical, Z_0 . To estimate the first component, the impedance of the mechanical block Z_m is transferred to the electric part of the circuit with the piezoelectric coupling factor φ_p , through the following relationships:

$$\begin{aligned} L'_m &= L_m / \varphi_p^2 \\ C'_m &= C_m \cdot \varphi_p^2 \\ R'_m &= R_m / \varphi_p^2 \end{aligned} \quad (4.XVI)$$

So, the two parts of the impedance can be calculated as:

$$Z'_m = j\omega L'_m + \frac{1}{j\omega C'_m} + R'_m \quad (4.XVII)$$

$$Z_0 = \frac{1}{j\omega C_0} \quad (4.XVIII)$$

and the final systems admittance results as:

$$\begin{aligned} Y_{eq} &= \frac{1}{Z_{eq}} = \frac{1}{Z_0} + \frac{1}{Z'_m} = j\omega C_0 + \frac{\varphi_p^2}{j\omega L_m + \frac{1}{j\omega C_m} + R_m} \\ Y_{eq} &= \frac{(j\omega)^3 L_m C_m C_0 + (j\omega)^2 C_m R_m C_0 + (j\omega)(\varphi_p^2 C_m + C_0)}{(j\omega)^2 L_m C_m + (j\omega) C_m R_m + 1} \end{aligned} \quad (4.XIX)$$

Under these conditions, it is possible to estimate the parallel (open-circuit resonance), ω_p , and series (short-circuit resonance), ω_s , resonance pulsations of the system, the mechanical quality factor, Q_m , and the effective electromechanical coupling coefficient, k_{ee} .

k_{ee}^2 describes the effectiveness of the quasi-static energy conversion between electrical, and mechanical forms. For a system subjected to quasi-static stress in an open-circuit configuration, it is equal to the electrostatic energy divided by the total energy of the system [42]. The previous parameters can be evaluated through the following formulas [34, 42, 49]:

$$\omega_s = \frac{1}{\sqrt{L_m C_m}} \quad (4.XX)$$

$$\omega_p = \frac{1}{\sqrt{L'_m \frac{C'_m \cdot C_0}{C'_m + C_0}}} = \frac{\sqrt{\varphi_p^2 C_m + C_0}}{\sqrt{L_m C_m C_0}} \quad (4.XXI)$$

$$k_{elasto-electric}^2 = \frac{\omega_p^2 - \omega_s^2}{\omega_p^2} = \frac{\varphi_p^2}{\varphi_p^2 + K C_0} \quad (4.XXII)$$

$$Q_m = \frac{\omega_s L_m}{R_m} \quad (4.XXIII)$$

There are several methods to calculate the circuit's parameters, based on fitting the theoretical and experimental admittance behaviors on the spectrum of frequencies. In the case of this thesis, as further described in Chapter 3 Paragraph 2.2.1, the adopted method consists to set a priori the value of the equivalent dynamic mass, L_m , and to experimentally measure the values of resonance and antiresonance frequencies.

From these three known values, it has been possible to determine the unknown parameters (C_m , R_m , C_0 , Q , k_{ee} , φ_p), fitting the experimental behavior of the complex admittance with the theoretical one (4.XIX), minimizing the error between them.

4.3.2 Dynamic Regime

After having identified the system's parameters, it is possible to extend the analysis of the ME transducer to the dynamic regime. In this case, the *dynamic regime* is defined as an operating condition, under which the transducer is excited through an AC magnetic field of small magnitude, superposed to the DC field.

Frequency-domain analysis of the equivalent circuit (Figure 4.12) yields a direct relationship between the applied magnetic field, and the output voltage. In this regime, firstly it has been possible to estimate the ME transfer function of the complete system. Secondly, it has been possible to determine the output ME voltage, and power of a loaded ME transducer.

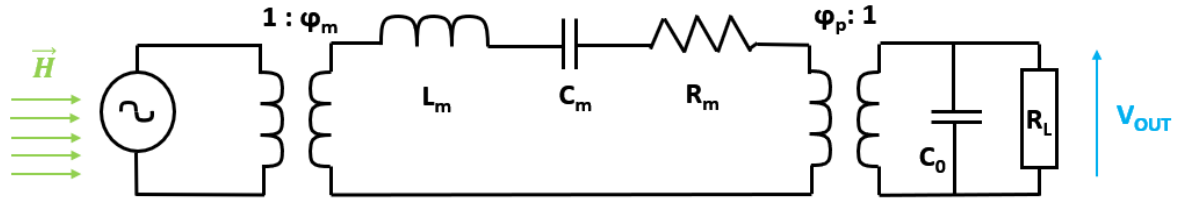


Figure 4.12 – Equivalent circuit for ME transducer in dynamic regime.

Through a first measurement in an open circuit configuration, the magnetolectric voltage coefficient has been measured. The effective magnetolectric voltage coefficient, α_{MEV} , defines the proportionality between the electrical output, and the magnetic input. The equivalent circuit, taken as reference, is the same reported in Figure 4.11. The difference between the static and dynamic regime models consists of the input magnetic field. In the static regime, \vec{H} represents the DC magnetic field. In this case, the \vec{H} represents the superposition of an AC and DC magnetic fields.

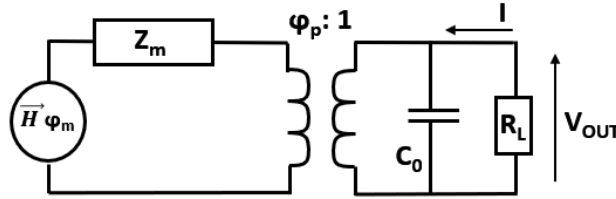


Figure 4.13 – Adopted equivalent circuit model for ME transducer in dynamic regime.

In the open-circuit condition, the induced current $I = 0$ and the system's general formulas (4.XV) become as:

$$\begin{aligned} [M]\{\dot{X}\} + [D]\{\dot{X}\} + [K]\{X\} + [\varphi_p]\{V\} &= [\varphi_m]\{H\} \\ [\varphi_p]\{\dot{X}\} &= [C_0]\{V\} \end{aligned} \quad (4.XXIV)$$

Assembling the two expressions, the effective magnetolectric voltage coefficient, α_{MEV} , can be theoretically approximated, under small magnetic field excitation, as [3439]:

$$\alpha_{MEV} = \left| \frac{dV}{dH} \right| = \frac{\varphi_p \varphi_m}{j\omega C_0 Z'_m + \varphi_p^2} \quad (4.XXV)$$

High magnetoelastic coupling and high electromechanical coupling are important contributing factors to the design of a high ME voltage coefficient. The equivalent circuit's parameters (Z'_m , C_0 , φ_p) are already known from the previous study in static regime, apart from φ_m , which is still undefined. The magnetoelastic coupling and the magnetolectric voltage coefficient have been determined by fitting the theoretical (4.XXV) and experimental behaviors on the spectrum of frequencies.

Once the two parameters are identified, the output ME voltage can be estimated as [34]:

$$V_{OUT} = \frac{R_L}{R_L + Z_{eq}} (\alpha_{MEV} H_{IN}) \quad (4.XXVI)$$

Z_{eq} is the equivalent impedance, previously estimated through (4.XIX), \vec{H} is the applied magnetic field (4.XIII), transformed through the magnetostrictive and piezoelectric coupling coefficients, and the effective magnetoelectric coefficient.

To validate the model, the expected values of ME voltage have been compared with the ones experimentally obtained during the characterization tests. This next step will be presented and further discussed in Chapter 3 Paragraph 2.2.2.

4.3.3 Output Power, and Optimal Electrical Load

The deliverable power can be calculated with the output current I_{out} (4.XXVII), using Norton equivalent model represented in Figure 4.14:

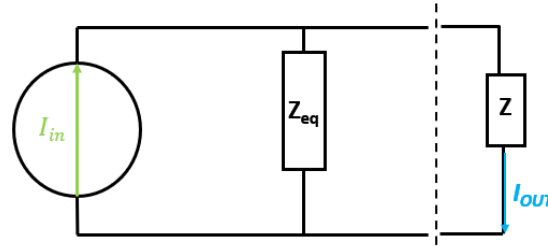


Figure 4.14 – Norton equivalent model for MagnetoElectric transducer.

$$I_{out} = \frac{Z_{eq}}{Z_{eq} + Z} I_{in}$$

(4.XXVII)

where Z_{eq} is the equivalent impedance, previously estimated through (4.XIX). If the load is a complex impedance $Z = R_L + jX_L$, the deliverable output power is given by:

$$P = R_L \frac{I_{out}^2}{2} = \left| \frac{R_{eq} + jX_{eq}}{R_{eq} + jX_{eq} + R_L + jX_L} \right|^2 \cdot \frac{R_L \cdot I_{in}^2}{2}$$

(4.XXVIII)

In this case, the deliverable power is maximal when the load is the complex conjugate of the source impedance $Z = R_{eq} - jX_{eq}$:

$$P_{max} = (R_{eq}^2 + X_{eq}^2) \cdot \frac{I_{in}^2}{8R_{eq}}$$

(4.XXIX)

If the load is resistive, $Z = R_L$, the deliverable output power results:

$$P = R_L \frac{I_{out}^2}{2} = \frac{(R_{eq}^2 + X_{eq}^2)}{(R_{eq} + R_L)^2 + X_{eq}^2} \cdot \frac{R_L \cdot I_{in}^2}{2}$$

(4.XXX)

Consequently, the optimal resistive load is estimated solving the first derivative of the power equal to zero:

$$\frac{\partial P}{\partial R_L} = \frac{(R_{eq}^2 + X_{eq}^2)(R_{eq}^2 + X_{eq}^2 - R_L)}{((R_{eq} + R_L)^2 + X_{eq}^2)^2} \cdot \frac{I_{in}^2}{2} = 0$$

(4.XXXI)

and obtaining that:

$$R_{L_optimal} = \sqrt{R_{eq}^2 + X_{eq}^2} = |Z_{eq}|$$

(4.XXXII)

4.3.4 Model with Rectifier

The final application of the studied magnetoelectric transducer is powering an implantable medical device, through the charge of its battery or internal accumulator. Since the magnetoelectric element generates an AC voltage, while the electrochemical battery needs a stabilized DC voltage, it requires an additional circuit to ensure electrical compatibility. A classical AC/DC rectifier and DC/DC converter are usually necessary to precede the battery. Here reported an example of a possible real WPT system, employing the ME transducer, Figure 4.15.A.

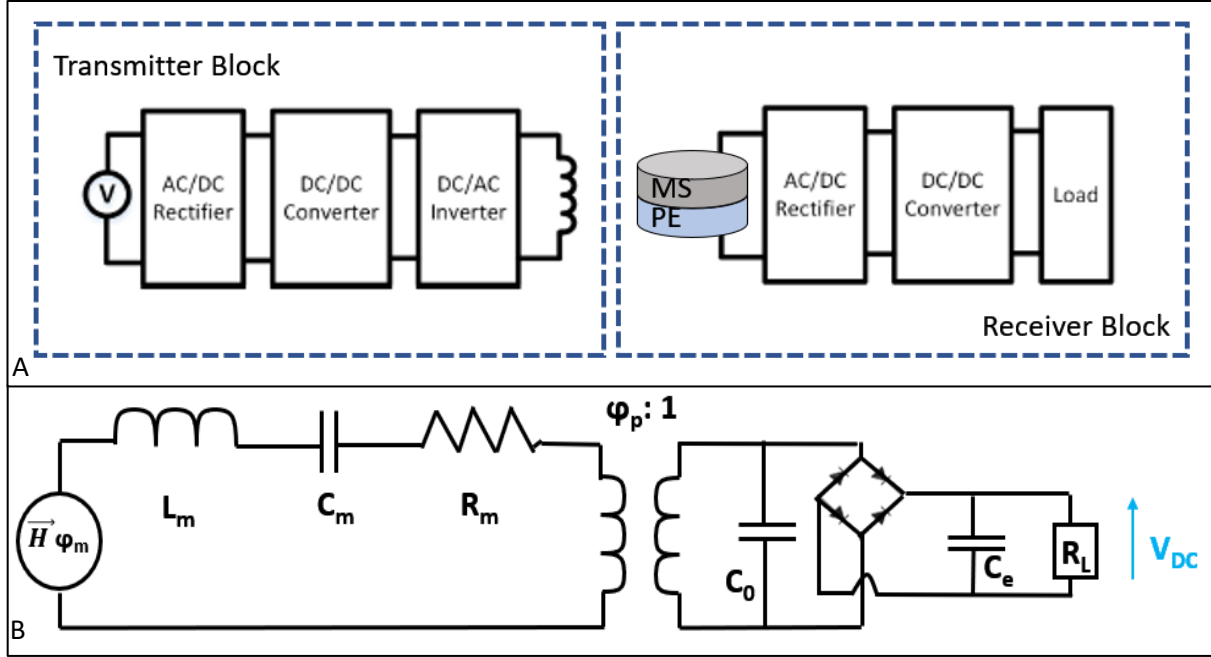


Figure 4.15 – A) Example of WPT system. B) Equivalent circuit of the ME receiver block using the classical rectifier circuit.

In Figure 4.15.B the equivalent circuit of the receiver block is reported. For this thesis, the additional circuit is represented by an AC/DC rectifier, followed by a filtering capacitance C_e to smooth the DC voltage. The circuit is shown in Figure 4.15, where R_L represents the equivalent input resistance of the device to be supplied. The transduced power is then calculated as the power dissipated over R_L .

As studied in detail by Shu, and Lien in [47], the rectifying bridge is open-circuited if the voltage across the transducer, $|V_{OUT}|$, is smaller than the rectified voltage V_{DC} . As a result, the current flowing into the circuit vanishes. On the other hand, when $|V_{OUT}|$ reaches V_{DC} , the bridge conducts, and the transducer voltage is kept equal to the rectified voltage, i.e. $|V_{OUT}| = V_{DC}$. Finally, the conduction in the rectifier diodes is blocked again when the absolute value of the transducer voltage starts decreasing in time. As most applications require, the output DC voltage V_{DC} needs to be stable, the common approach to achieve this objective is to assume that the smoothing capacitor C_e is large enough, so that the output voltage V_{DC} is essentially constant [47].

As described by Badel and Lefeuvre in [42], sinusoidal ambient accelerations around the resonance frequency of the transducer are considered, and it is assumed that the filtering capacitor is large enough to neglect the ripple value of V_{DC} . So, the behavior of V_{DC} can then be obtained as a function of the magnitude x_M of the dynamic mass relative displacement:

$$V_{DC} = \frac{\varphi_p \omega R_L}{\omega C_0 R_L + \pi/2} x_M$$

(4.XXXIII)

Because of the nonlinear behavior of the full-wave rectifier, the output voltage results periodically but not sinusoidal. However, since only its fundamental harmonic frequency is close to the resonance frequency of the transducer, it can be assumed that only this fundamental component V_1 , given in the frequency domain by

Eq.(4.XXXIV), impacts the displacement of the transducer dynamic mass, which is represented in a normalized form through \bar{x} , [42].

$$V_1 = \frac{\varphi_P}{C_0} (V + jv)\bar{x}$$

$$\text{with } \begin{cases} V = \frac{\omega R_L C_0}{\omega R_L C_0 + \pi/2} \\ v = \frac{2\omega R_L C_0}{(\omega R_L C_0 + \pi/2)^2} \end{cases} \quad (4.XXXIV)$$

It can be seen from the previous equation that v is comprised between 0, and 1, and the resonance frequency of the transducer between the open-circuit, and short-circuit resonance frequency, ω_P , and ω_S , Eq. (4.XX)-(4.XXI). So, the estimation of the harvested power can be obtained [47] as:

$$P = \frac{V_{DC}^2}{R_L} = \frac{\varphi_P^2 \omega^2 R_L}{(\omega C_0 R_L + \pi/2)^2} (x_M)^2 \quad (4.XXXV)$$

For the model of Badel and Lefeuvre [42], the expression of the displacement is linked to the dynamic mass and the acceleration of the system. In this case, the external stimulating force is represented by the applied magnetic \vec{H} field. So the expression to calculate the displacement in the frequency domain becomes:

$$x = \frac{H \varphi_m}{\frac{1}{C_m} - L_m \omega^2 + \frac{\varphi_P^2}{C_0} v + j(C_0 \omega + \frac{\varphi_P^2}{C_0} v)} \quad (4.XXXVI)$$

where the equivalent dynamic mass is expressed through the sample's mass, and a corrective factor:

$$L_m = m/1.4 \quad (4.XXXVII)$$

The nature of this correction links one of the circuit's parameters to the physical properties of the device. This dependency, reported by Serrate, Vasic, and Costa [49], will be described in detail in Chapter 3 Paragraph 2.2.1. Furthermore, in Chapter 3 Paragraph 2.5.2, the displacement of the dynamic mass, and V_{bc} have been determined with the experimental values. An optical direct measurement of the transducer's displacement has been tested. Due to the set-up sensibility and transducer resonance frequency, the optical measurements were not conclusive. Therefore, the total displacement has been finally estimated, starting from the applied magnetic \vec{H} field and the magnetoelastic coupling, experimentally evaluated in the dynamic regime study of the transducer.

4.4 Considered Materials

Magnetolectric composites refer to a branch of active materials that can couple the ferromagnetic behavior to the ferroelectric one. As described by Scott et al. [32], there are two types of magnetolectric effects, intrinsic, and extrinsic. In this thesis, only the extrinsic magnetolectric effect is considered. The samples used to convert energy between magnetic, and electric forms, are composites of piezoelectric, and magnetostrictive materials. In Table 4.2, they are compared to different physical points of view.

Properties	Magnetostrictive Material	Piezoelectric Material
Mechanics	Deformation: [0.1 - 0.6] % Forces: [500 – 5000] N	Deformation: [0.1 - 0.6] % Forces: [500 – 30000] N
Thermic	Curie Temperature $\approx 400^\circ\text{C}$	Curie Temperature $\approx 300^\circ\text{C}$
Energetic	Energy Density $\approx 200 \text{ kJ/m}^3$ Consumption: low Coupling: Magneto-Elastic Magnetic Field $\approx 200 \text{ kA/m}$	Energy Density $\approx 1 \text{ kJ/m}^3$ Consumption: very low Coupling: Electro-Elastic Electric Field $\approx 1 - 2 \text{ kV/m}$

Table 4.2 - Comparison between Magnetostrictive, and Piezoelectric materials [45].

4.4.1 Magnetostrictive material

Concerning the magnetostrictive layer (MS), the Terfenol-D was chosen for the giant magnetostriction, up to 2000 ppm at room temperature, due to the anisotropic properties of its cubic crystallographic structures [33]. As already described in paragraph 2.3.2, the Terfenol-D is one of the most employed magnetostrictive materials with Galfenol, and MetGlas [45]. The choice of using Terfenol-D was motivated by the availability of this material in different shapes and dimensions; big freedom compared to the MetGlas, which is fabricated in a thin ribbon of few μm -thickness. The choice between Galfenol and Terfenol was based on the magnetostrictive properties (strain, energy density, and magnetomechanical coupling factor), which result in a higher in Terfenol-D. The tested samples present a disk shape, chosen to avoid secondary magnetic effects at the angles of the device, with diameters of 10 mm, and 16 mm, and thickness 1 mm (Figure 4.16). They are produced by TdVib LLC.

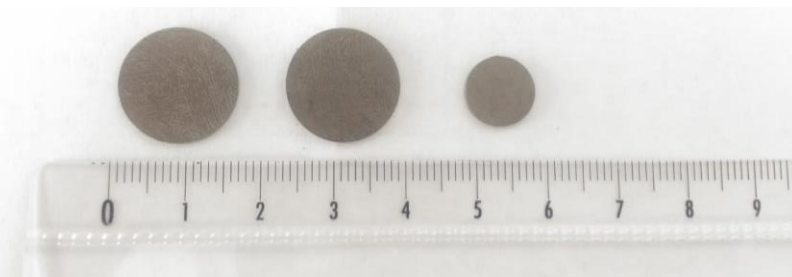


Figure 4.16 – Magnetostrictive samples of Terfenol-D, diameters of 10 mm, and 16 mm, thickness 1 mm.

Properties of Terfenol-D

Composition	Tb _{0.3} Dy _{0.7} Fe _{1.92}		
Bulk Modulus	90 GPa	Density	9250 kg/m ³
Young's modulus	55 GPa	Poisson's ratio	0.5
Elastic compliance s₃₃^H	38 pm ² /N	Saturation Flux Density	1 T
Melting Point	1240 °C	Relative Permeability	2 – 10
Curie Temperature	380 °C	Electrical resistivity	60 10 ⁻⁸ Ω·m
Magnetomechanical coupling factor	0.7 – 0.8	Piezomagnetic coefficient q₃₃^m	8.5 nm

Table 4.3 – Properties of Terfenol-D, full datasheet in Annex II.

The anisotropic, and not-linear properties of Terfenol-D are shown in the following graphs (Figure 4.17), provided by TdVib LLC. In the first graph, the relationship between the magnetic field, and the magnetostriction is presented for different mechanical stresses. The second graph represents the material's hysteresis loop. The third one shows the dependency of the magnetostriction to the temperature, for different compositions of Terfenol-D.

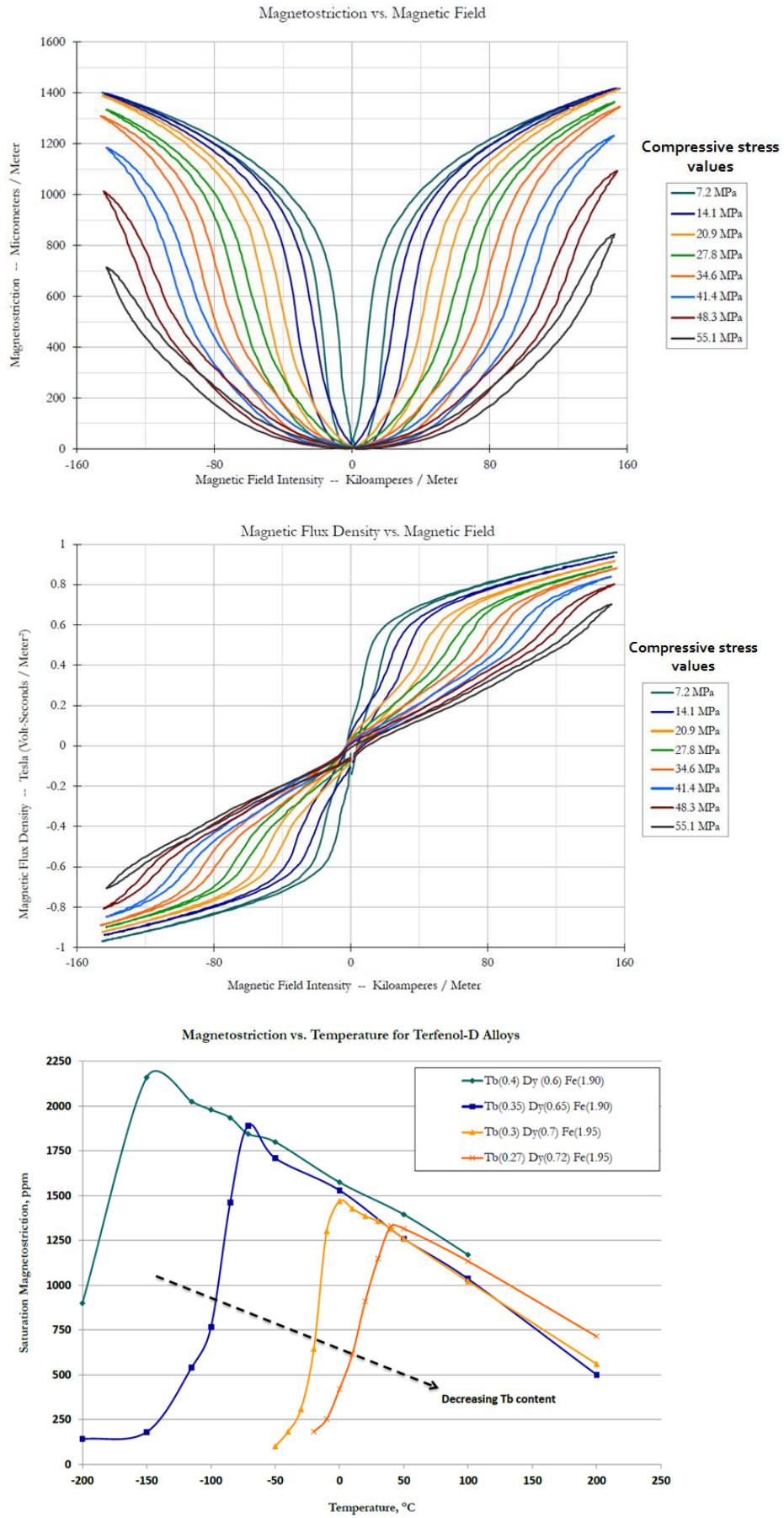


Figure 4.17 – Properties of Terfenol-D [15].

In the first graph, the non-linear dependency of magnetostriction to the magnetic field is presented. With the increment of magnetic field intensity, the magnetostriction increases until the saturation state. For higher values of compressive stress, the saturated magnetostriction results lower. As explained in Paragraph 2, under the action of a magnetic field, and measurable mechanical compression, the crystal lattice tends to re-order itself to minimize the energy state of the material. For higher fields and stresses, the saturated state is reached at a smaller value of magnetostriction.

Since the magnetostriction and magnetization are directly correlated, Eq. (2.XI), the same behavior appears in the second graph. The hysteresis loop depends on the material's anisotropy, and internal deformation, as already explained through (Figure 2.6). At higher internal deformations, the curve will tend to saturate faster, consuming less energy (internal area of the curve).

In the third graph, it is represented the influence of the temperature on the saturated magnetostriction for temperatures lower than Curie temperature. It is interesting to notice the decrement of the limit-state for higher temperatures, so for higher internal energy.

4.4.2 Piezoelectric material

From the point of view of the piezoelectric part (PE), the PZT ceramic PIC181 was chosen for the high mechanical quality factor, high electromechanical coupling, and stability in a time of the dielectric, and elastic properties. This hard-piezoelectric Lead-Zirconate-Titanate ceramic presents optimal performances in terms of energy conversion in radial resonance mode. The used samples have a disk-shape of diameters 10 mm, and 16 mm, to be adapted to the Terfenol-D samples, with a thickness of 1 mm, and 2 mm. The sample is axially polarised and used in a radial deformation mode (Figure 4.19). These samples are manufactured by PI Piezoelectric Technologies, [22].

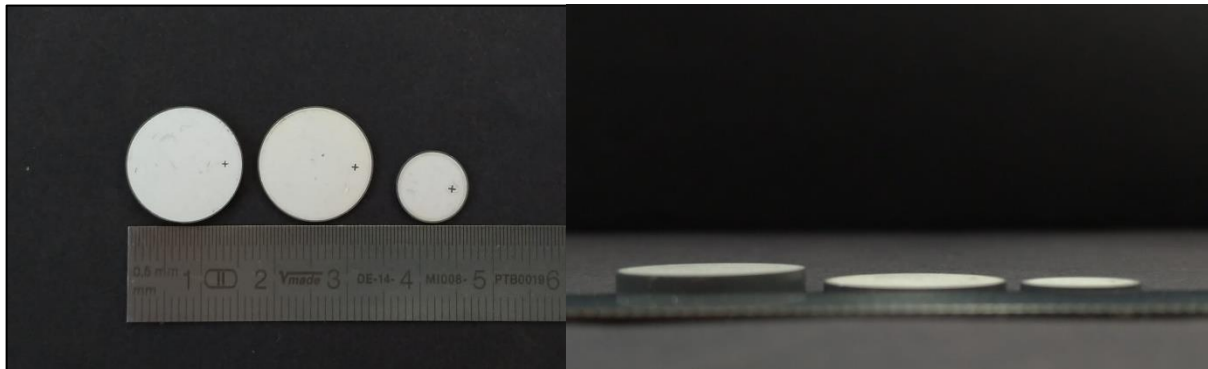


Figure 4.18 - Piezoelectric samples of PIC181, diameters of 10 mm, and 16 mm (vertical view on left side), thickness 1 mm, and 2 mm (lateral view on the right side).

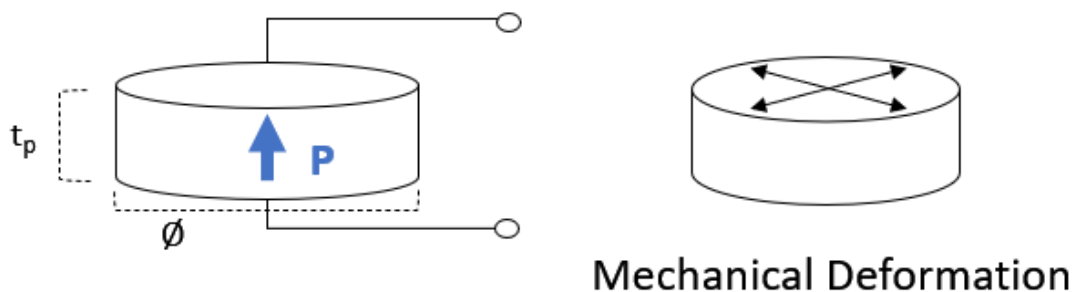


Figure 4.19 – Piezoelectric sample representation. On the left the representation of its polarization, and on the right side the mechanical deformation in radial direction.

Properties of PIC181

Density	7850 kg/m ³	Poisson ratio (σ)	0.35
Quality factor Qm	2200	Coupling factor k _p	0.55
Curie Temperature	330 °C	Coupling factor k _t	0.46
Relative permittivity ϵ_{33}^S	624	Piezoelectric coefficient d ₃₃	2.530E-10 m/V
Elastic compliance s ₃₃ ^E	7.9630E-12 m ² /N	Frequency coefficient N _p	2265

Table 4.4 – Properties of PIC181, full datasheet in Annex II.

4.4.3 Description of the MagnetoElectric Samples

For this thesis, 6 different transducers were made, and tested. The fabricated samples have a disk shape, with diameters of 10 mm, and 16 mm, and thickness from 2 mm to 5 mm, depending on the number of layers. The different layers are assembled with a bicomponent-epoxy (EPOTECNY 608566-250), and electrodes attached to the external layers through a conductive-Ag glue (G3790).

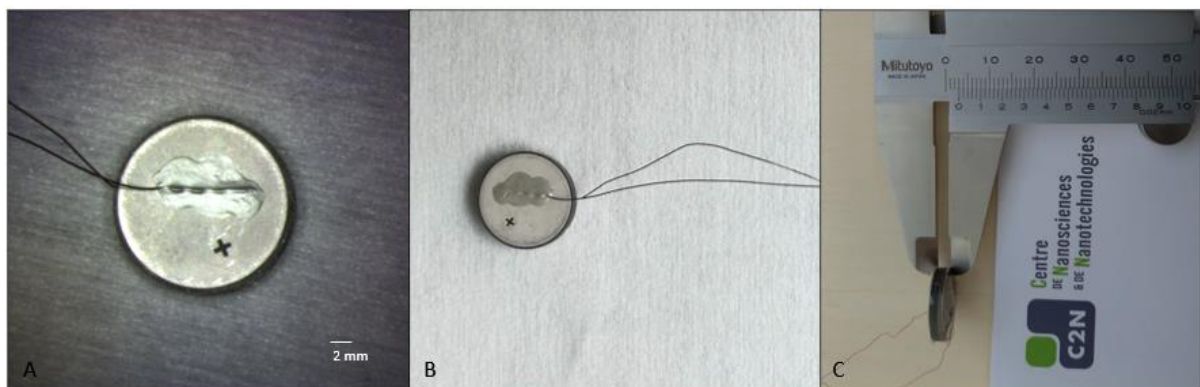
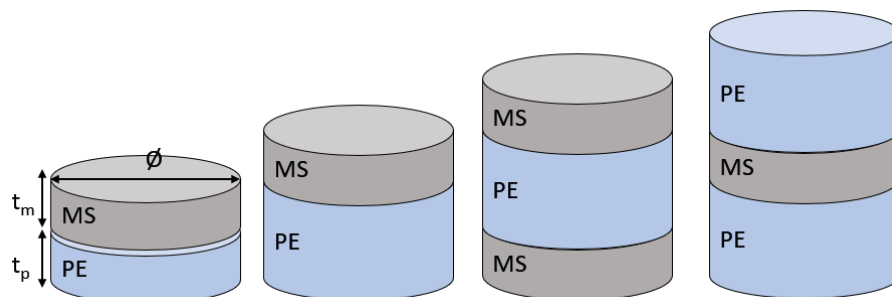


Figure 4.20 – Photos of a MagnetoElectric sample, assembled, and tested for this thesis. A) View through the optical microscope, B) vertical view of sample A (Table 4.5). C) Lateral view of the sample with a caliper.



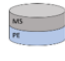
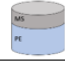
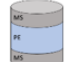
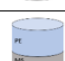
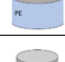
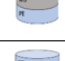
Sample	# layers	ϕ [mm]	tp [mm]	tm [mm]	m (g)
A) 	2 layers	16	1	1	3.7
B) 	2 layers	16	2	1	5.16
C) 	3 layers (M-P-M)	16	2	1 and 1	6.97
D) 	3 layers (P-M-P)	16	2 and 2	1	8.41
E) 	2 layers	10	1	1	2.53
F) 	3 layers	10	1 and 1	1	4.03

Table 4.5 - ME transducer with different thicknesses, and masses of piezoelectric, and magnetostrictive layers, studied in this thesis.

4.4.4 FEM analysis of radial resonance modes

A first mechanical analysis of the samples has been conducted to study the respective vibration modes and eigenfrequencies. The platform COMSOL Multiphysics 5.3a has been used for the finite element analysis. The samples have been represented by a single layer of the piezoelectric material of diameter 10mm and 16mm with different thicknesses, under free boundary conditions, and no applied electrodes. In this case, the physics simulation considers just the piezoelectric part and aims to give a first overview of the radial resonance modes and the respective eigenfrequencies of the transducer.

The characteristics of the employed material are reported in detail in Appendix II. The devices have been studied with the *Shell* physics and *Eigenfrequency* study. Figure 4.21 shows the example of sample C, a transducer with a diameter of 16 mm, and a thickness of 4 mm, studied in the range of frequency comprised in [100 – 200] kHz.

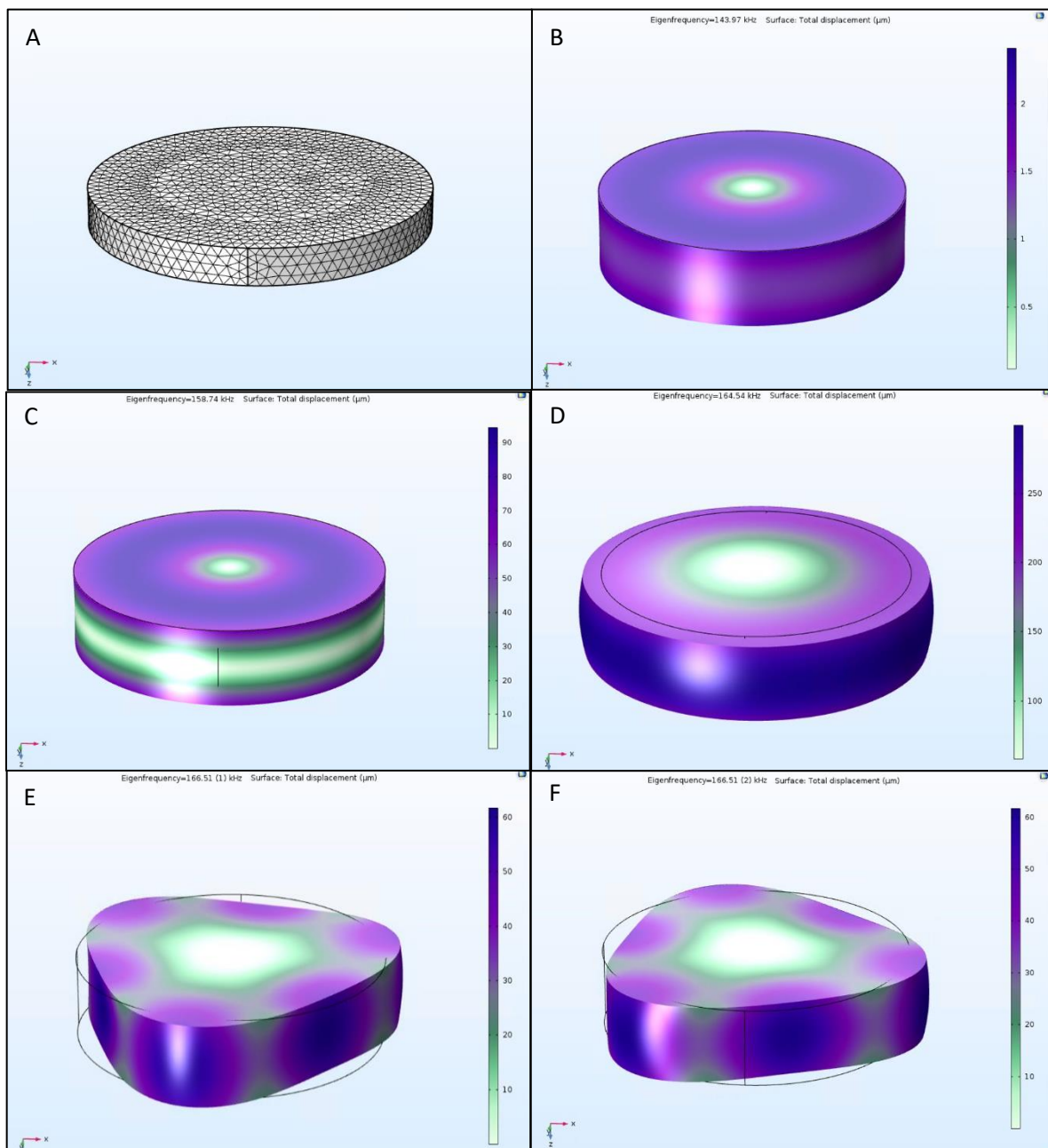


Figure 4.21 – Vibration modes, and Eigenfrequency of piezoelectric transducer. Figure A) represents the FEM study. Figure B) represents the vibration mode for the eigenfrequency of 143.97 kHz. Figure C) represents the vibration mode for the eigenfrequency of 158.7 kHz. Figure D) represents the vibration mode for the eigenfrequency of 164.5 kHz. Figure E), and F) represent respectively the vibration modes of first, and second order for the eigenfrequency of 166.5 kHz.

The figure represents the total displacement (in μm) of the transducer's surface at the resonance frequencies. In this case, the simulation calculates several fundamental eigenfrequencies (figures B, C, and D), respectively at 143.97 kHz, 158.7kHz, and 164.5 kHz, linked to the radial deformation of the structure. Among them, the principal mode is the one at 164 kHz, which causes a higher mechanical deformation of the material.

In general, the resonance frequency is linked to the material characteristics, but it could be modified by external forces, for example, an external magnetic field, as described in Chapter 3, paragraph 2.2.1. Moreover, the fabrication process of the transducer could influence it. When the piezoelectric material is assembled to a magnetostrictive layer, part of the respective properties could be lost and new properties can appear, first of all, the magnitude of the deformation at the resonance and the value of the frequency, as described in Chapter 2 Paragraph 4.1.

Furthermore, the simulation reports some resonance frequency associated with vibration modes of a higher order than the fundamental, as figure E), and F) which represent the vibration mode of first, and second order for the eigenfrequency of 166 kHz. In this case, these modes could not be considered since they could not be coupled with the magnetostrictive and the piezoelectric layers. The mechanical deformation of the ME transducer should be radial to be coupled and maximized by the entire composite.

This first simulation allowed to have an overview of the vibrational modes of the sample, the type of deformation, and the range of the resonance frequency. Further considerations and analysis have been added in Chapter 3, to achieve a theoretical model for the ME transducer.

4.5 Application

Nowadays, advances in microfabrication, and bio/chemical engineering technology are enabling a large variety of miniaturized electronic devices. The progress made in the field of magnetoelectric laminate composites allows potential high-performance applications such as magnetic field sensors [49], current sensors [50], gyrators [52], more recently, memory devices [54], and energy transducer [38].

In the domain of magnetic field and current sensors, magnetoelectric composites show many advantages, such as high performances, low cost, power supply free, galvanic isolation, and simplified electronic circuits [54]. Different types of magnetoelectric AC current sensors have been reported in the literature. For example, in the case of the current sensor for electronic device applications, the main goal is to obtain high-performance sensors (sensitivity, linearity, resolution) with large frequency bandwidth. This is achieved in a ring-type sensor, slice-type sensor, and packaged current sensor [55]. From the point of view of the gyrator, it is defined as a network element that could be used in circuit design, to convert impedance, or also current, and voltage. The construction of the gyrator is based on the coupling of ferroelectric, and ferromagnetic materials. In the case of the ME gyrator, it reaches a high conversion efficiency (until 85% [52]) at the resonance frequency, due to the characteristic coupling between magnetic, and electric fields.

The most recent application of ME systems is in the memory devices. The magnetoelectric random access memories (MERAM) employs the magnetoelectric coupling to switch the magnetization of the ferromagnetic layer, by using a voltage [57]. In other words, the electric field control of magnetism can dramatically enhance the performance of magnetic memory devices in terms of switching energy efficiency and switching speed. The development of such an energy-efficient and ultrafast memory has the potential to change the paradigm of a hierarchical memory system in conventional computer architecture. By combining speed, low power, and high density, electric-field-controlled magnetic memory merges features of multiple separate memory technologies used in today's memory hierarchy [54].

However, in this thesis, an application of ME transducer is developed for the biomedical field. It is proposed as a solution to the major problems of the wireless powering technique. Wireless power transmission (WPT) techniques could be classified in Inductive Power Transfer if the coupling is in the near field, or Radio Frequency (RF) if the coupling is in the mid-field (i.e., transition region) or far-field (Chapter 1, Paragraph 3.4). Inductive coupling techniques appear to be well suited for powering implants, which supplies the implantable devices through an external transmitter. The entire system consists of two main blocks, an out-body source, and an in-body receiver, which usually has more constraints in terms of size, and position. The transmitter and receiver coils must be physically close, and well-aligned to enable the efficient transfer of power. Subsequently, the power transfer is highly dependent on the size, orientation, and distance between the two coils. On the contrary, for RF WPT systems the alignment between the transmitter, and receivers does not constitute an issue. However, as the size of receivers decreases, the operating frequency must increase to a level where tissue tends to absorb, and high-power transmission could be potentially hazardous because of associated tissue heating [44].

The ME technology is studied here to investigate the possibility to make more efficient the wireless power transfer at low frequency for deep small implantable systems. Despite the application of ME transducers in biomedical WPT is still little explored, some examples of this technology are already presented in the literature. Yang [34] developed in his thesis a tri-layer ME energy transducer, made of Terfenol-D/PZT-5A/Terfenol-D, working at 75 kHz of frequency and 0.1 mT of B_{AC} . In his thesis, he studied the performances of four rectangular ME composites (LT, TL, LL, and TT modes), with a length of 14 mm, a thickness of 3 mm, and a width of 6 mm, at the resonance frequency. The systems were connected to an AC/DC converter and analyzed in terms of output power over a matched resistive load. Among them, the L-T mode was the most efficient configuration, able to deliver a ME output power of 800 μ W, for an optimal load of 18 k Ω and a 75.3 kHz of frequency, Figure 4.22.

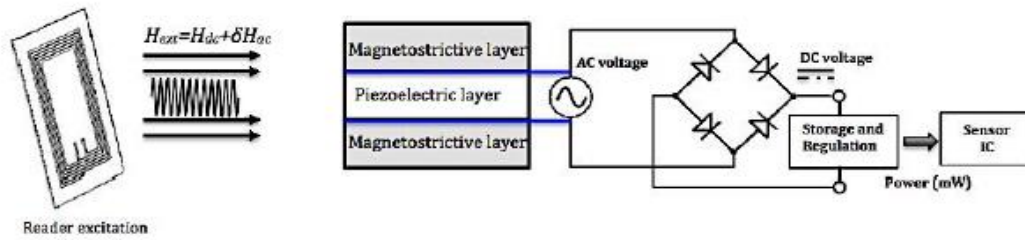


Figure 4.22 – Example of ME energy transducer structure presented by Yang [34].

Malleron [58] was equally focused on the ME composite performances in his studies. He reported, in the cited paper, a comparison between several structures of ME energy transducers, adding to the layer of Terfenol-D a thin layer of the magnetostrictive Metglas. He took as reference a bi-layered system of Terfenol-D/PZT-5H, with a length of 14 mm, width 10 mm, and thickness of 1 mm for the magnetostrictive layer and length of 20 mm, width 10 mm, thickness 1 mm for the piezoelectric layer, Figure 4.233. The studied system could deliver about 380 μW for a resonant frequency of 70 kHz and an AC magnetic field of 0.6 mT, measuring the highest magnetoelectric coefficient. Furthermore, he investigated a similar structure with an additional 35 μm layer of Metglas. In this last configuration, he measured the highest value of output power, close to 600 μW at 68 kHz.

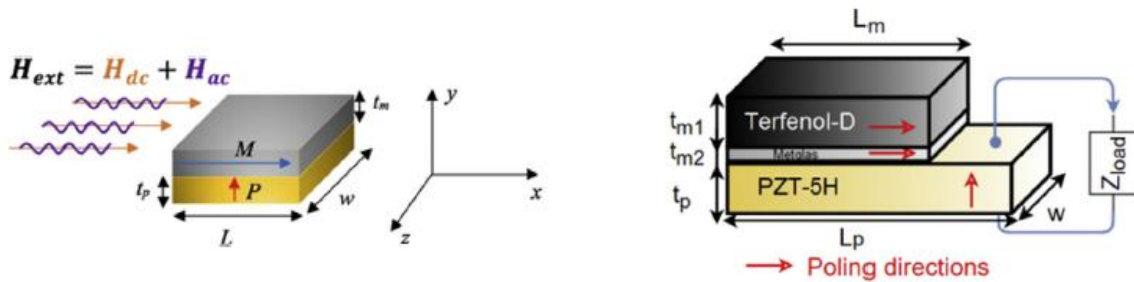


Figure 4.23 – Example of ME energy transducer presented by Malleron [58].

Furthermore, Rupp [44] investigated the potentialities of ME composites, made with alternative magnetostrictive materials, such as Galfenol and Metglas. Rupp developed a structure of Galfenol/PZT-5A, resonant at 70.7 kHz, and a structure of Metglas/PVDF, resonant at 100 kHz, for an overall size constrain of 2mm^3 . In the experimental measurement with the first configuration, he obtained the highest value of output power around 5 mW. With the optimized ME devices, he estimated to produce 42.7 mW ($21.35\text{ mW}/\text{mm}^3$) and 62.6 μW ($31.3\text{ }\mu\text{W}/\text{mm}^3$) under the IEEE and ICNIRP standard, respectively.

Finally, much work still needs to be done to implement transducers of this size and performance level, but these results are very promising in the context of being able to wirelessly power miniaturized biomedical implants.

5. Conclusion

In this chapter, the technology, and potentialities of the MagnetoElectric transducer have been presented. Starting from a general description of the physics, and properties of the magnetic materials, the magnetostriction phenomenon has been introduced. The great advantage of the magnetostrictive materials consists of showing a mechanical deformation under a magnetic-field excitation. From all this family of materials, the Terfenol-D has been chosen for its high magnetostriction at room temperature, and excellent magnetoelastic properties, which makes it one of the most employed magnetostrictive materials.

These characteristics, coupled with the piezoelectricity, allowed to develop a MagnetoElectric Transducer. From the point of view of piezoelectrics, their great ability consists of the generation of electric energy as consequence of elastic deformation. They have been described from a physical point of view, explaining the relationship between the resonance-behavior, and oscillation modes with the sample's dimensions. In this case, among all the piezoelectric materials, the ceramic PIC181 has been chosen for its high mechanical quality factor.

The combination of magnetostrictive and piezoelectric properties is the focus of this thesis. A new group of hybrid materials, called MagnetoElectric materials, have raised a great interest during the last decades, due to their potentialities in smart electronic applications [25]. In this thesis, a MagnetoElectric composite has been developed in the context of wireless power transmission for active implantable medical devices. Here the ME transducer is proposed as an alternative energy receiver to the usual receiver coil. The expected advantage of this technology consists of a less sensitivity to the alignment between the transmitter source and receiver block.

Fundamentally, a magnetolectric transducer can convert energy from the magnetic domain to the electric domain, and vice versa. The electromagnetic wave is converted to a mechanical acoustic wave before being transduced to electricity. Here, the ME composite has been described from macroscopic, and microscopic points of view. An analysis of the magnetostrictive properties and piezoelectric characteristics has been reported, explaining the physics of the two coupled phenomena and the behavior at the resonance frequency. The two materials could have different properties, but once they are embedded, they can show new ones. The methodology of the fabrication process and the made ME samples are described. In this thesis, the ME samples present a disk shape, chosen to avoid secondary magnetic effects at the angles of the device. The most efficient performances of the system are reported at the resonance frequency, at which a fundamental radial mode well-coupled is shown. The magneto-mechanic-electric coupling effects have been then modeled using an equivalent circuit model. The multi-physics system has been studied in open circuit configuration and with an associated electronics interface circuit to optimize its working conditions and make it compatible with an active medical device. Finally, an overview of some examples of ME transducers is reported in the context of the wireless power transmission for the biomedical field. In specific, for this thesis the developed ME transducer wants to be compared to a coil-coil system, maintaining the same boundary conditions, such as working frequency, and dimensions of the receiver.

The experimental performances and the characterizations of the ME sample are extensively presented in the following chapter, opening the comparison with the physical response, and the theoretical models here presented.

6. Bibliography

1. Gilbert W., *De Magnete*, Peter Short, London, 1600
2. Aubert A., *Synthèse, caractérisation et modélisation de matériaux multiferroïques (magnétoélectriques) composites massifs*, October 2018, theses.fr/2018SACLN036
3. Bertotti G., *Hysteresis in magnetism: for physicists, materials scientists, and engineers*, Academic Press, 1998
4. Fruchart O., *Lecture Notes on Nanomagnetism*, version 20/04/2015, <http://perso.neel.cnrs.fr/olivier.fruchart/lectures/nanomagnetism-2015-04-20.pdf>
5. Skomski R., *Simple models of magnetism*, Oxford, 2008
6. Özgüri U., Alivov Y., and Morkoç H., *Microwave ferrites, part 1: Fundamental properties*, Journal of Materials Science Materials in Electronics, September 2009, doi: 10.1007/s10854-009-9923-2
7. Du Trémolet de Lacheisserie E., *Magnetostriction: Theory, and Applications of Magnetoelasticity*, CRC Press, Inc., Boca Raton, 1993
8. Dapino M.J., *Magnetostrictive Materials: Their Use in Smart Structure Applications*, July 2002, doi:10.1002/0471216275.esm051
9. G.A. Steel, *A 2-kHz Magnetostrictive transducer*, in *Transducers for Sonics, and Ultrasonics*, pp. 250-258, Mancaster, PA. Technomic, Inc., 1993
10. L. Kiesewetter, *The application of Terfenol in linear motors*, Proc. 2nd Inter. Conf. Giant Magnetostrictive Alloys, Marbella, Spain, Oct. 12-14 1988
11. Engdahl G., *Handbook of Giant Magnetostrictive Materials*, Academic Press, New York, 2000
12. Bozorth R.M., *Ferromagnetism*, D. Van Nostrand, Inc., 1968
13. Lindgren E.A., Poret J.C., Whalen J.J., Martin L.P., Rosen M., Wun-Foglr M., Restorff J.B., Clark A.E., and Lindberg J.F., *Development of Terfenol-D transducer material*. IN US Navy Workshop on Acoustic Transduction Materials, and Devices, State College, PA, 13-15 April 1999
14. Dionne G.F., *Magnetic Oxides*, Springer US, 2010
15. TdVib LLC, *Terfenol datasheet*, tdvib.com/terfenol-d/
16. TdVib LLC, *Galfenol datasheet*, tdvib.com/galfenol/
17. Lippmann G., *Principe de la conservation de l'électricité*, 1881
18. Chilowsky C., and Langevin P., *Production of submarine signals, and the location of submarine objects*, US1471547A, 19 May 1917, Clarendon Press, 1985
19. Varghese, J., Whatmore, R. W., & Holmes, J. D., *Ferroelectric nanoparticles, wires, and tubes: synthesis, characterisation, and applications*, Journal of Materials Chemistry 2013, doi:10.1039/c3tc00597f
20. Ikeda T., *Fundamentals of piezoelectricity*, Oxford University Press, 1990
21. Dragan Damjanovic, *Hysteresis in Piezoelectric, and Ferroelectric Materials*, The Science of Hysteresis, Volume 3 – Chapter 4; I. Mayergoyz, and G.Bertotti (Eds.); Elsevier (2005)
22. *Datasheet of PI Piezo Technologies*, static.piceramic.com/
23. Lin S., and Xu J., *Effect of the Matching Circuit on the Electromechanical Characteristics of Sandwiched Piezoelectric Transducers*, Sensors 2017, 17, 329; doi:10.3390/s17020329
24. Royer D., and Dieulesaint E., *Ondes élastiques dans les Solides (Tome 1)*. Masson, 1996
25. E. Du Tremolet de Lacheisserie, *Magnetostriction: Theory, and Applications of Magnetoelasticity*, Boca Raton, FL, USA: CRC Press, 1993
26. Fiebig M., *Revival of the magnetoelectric effect*, Journal of Physics D : Applied Physics, volume 38, R123 (2005), doi:10.1088/0022-3727/38/8/R01
27. Röntgen W C, 1888 Ann. Phys. 35 264
28. Van Vleck J H, *The Theory of Electric, and Magnetic Susceptibilities*, London: Oxford University Press, 1932
29. Dzyaloshinskii I E 1959 Sov. Phys.—JETP 10 628
30. Hill, N. A., *Why Are There so Few Magnetic Ferroelectrics?*, The Journal of Physical Chemistry B, 104(29), 6694–6709. doi:10.1021/jp000114x
31. Sando, D., Xu, B., Bellaiche, L., & Nagarajan, V., *A multiferroic on the brink: Uncovering the nuances of strain-induced transitions in BiFeO3*, Applied Physics Reviews, 3(1), 011106. doi:10.1063/1.4944558

32. Scott, J. F., *Applications of magnetoelectrics*, Journal of Materials Chemistry, 22(11), 4567. doi:10.1039/c2jm16137k
33. Newnham R.E., Skinner D. P., and Cross L.E., *Connectivity, and piezoelectric-pyroelectric composites*, Materials Research Bulletin, 13(5):525-536, 1978
34. Yang G., *Contribution to modelling of magnetoelectric composites for energy harvesting*, theses.fr/2016PA066731
35. Nan C.W., Bichurin M.I., Dong S., Viehland D., and Srinivasan G., *Multiferroic magnetoelectric composites: Historical perspective, status, and future directions*, Journal of Applied Physics, 2008, 103(3):031101
36. Lam K.H., Lo C.Y., Chan H.L.W., *Frequency response of magnetoelectric 1-3 type composites*, Journal of Applied Physics, 2010, 107,093901
37. Talleb. H., Gensbittel A., Ren Z., *Finite element modelling of magnetoelectric laminate composites in considering nonlinear, and load effects for energy harvesting*, Journal of Alloys, and Compounds, 2014, 615(5), 65–74, doi: 10.1016/j.compstruct.2015.11.001
38. Dong S., Li J.F., Viehland D., *Magnetoelectric coupling efficiency, and voltage gain effect in piezoelectric-piezomagnetic laminate composites*, Journal of Materials Science, 41(1), 97–106. doi:10.1007/s10853-005-5930-8
39. Dong S., and Zhai J., *Equivalent circuit method for static, and dynamic analysis of magnetoelectric laminated composites*, Chinese Science Bulletin, 2008, vol. 53, no. 14, 2113-2123
40. Zhai J., Xing Z., Dong S., Li, J., Viehland D., *Magnetoelectric Laminate Composites: An Overview*, Journal of the American Ceramic Society, 2008, 91(2), 351–358. doi:10.1111/j.1551-2916.2008.02259.x
41. Dong S., Li J.F., Viehland D., *Longitudinal, and Transverse Magnetoelectric Voltage Coefficients of Magnetostrictive/Piezoelectric Laminate Composite: Theory*, Transactions on Ultrasonics, Ferroelectrics, and Frequency Control, 2003, 50(10), 1253–1261. doi:10.1109/tuffc.2003.1244741
42. Badel A., and Lefeuvre E., *Nonlinear Conditioning Circuits for Piezoelectric Energy Harvesters*, Nonlinearity in Energy Harvesting Systems, Springer (2016), doi:10.1007/978-3-319-20355-3_10
43. Yang, F., Wen, Y. M., Li, P., Zheng, M., & Bian, L. X., *Resonant magnetoelectric response of magnetostrictive/piezoelectric laminate composite in consideration of losses*, Sensors, and Actuators A: Physical, 141(1), 129–135. doi:10.1016/j.sna.2007.08.004
44. Rupp T., Truong B.D., Williams S., and Roundy S., *Magnetoelectric Transducer Designs for Use as Wireless Power Receivers in Wearable, and Implantable Applications*, Materials 2019, 12, 512; doi:10.3390/ma12030512
45. Nguyen T.T., *Modélisation par éléments finis de matériaux composites magnéto-électriques*, theses.fr/2011PA112271
46. Malleron K., *Modelisation multiphysique, caractérisation et conception de transducteurs magnetoelectriques pour l'alimentation de capteurs biomédicaux autonomes*, theses.fr/2018SORUS203
47. Shu, Y. C., & Lien, I. C., *Analysis of power output for piezoelectric energy harvesting systems*, Smart Materials, and Structures, 2006, 15(6), 1499–1512. doi:10.1088/0964-1726/15/6/001
48. Zhang S., Li F., Yu F., Jiang X., Lee H.Y., Luo J., Shrout T.R., *Recent Developments in Piezoelectric Crystals*, Journal of the Korean Ceramic Society 2018; 55(5): 419-439, doi:10.4191/kcers.2018.55.5.12
49. Sarraute E., Vasic D., Costa F., *Transformateurs piezoelectriques*, Ref. D3015 V1
50. C. Fang, J. Jiao, J. Ma, D. Lin, H. Xu, X. Zhao, H. Luo, *Significant reduction of equivalent magnetic noise by in-plane series connection in magnetoelectric Metglas/Mn-doped Pb(Mg 1/3 Nb2/3)O3-PbTiO3 laminate composites*, J. Phys. D: Appl. Phys. 48(46), 465002 (2015)
51. Y. Guo, T. Wang, D. Shi, P. Xiao, Q. Zheng, C. Xu, K.H. Lam, D. Lin, *Strong piezo-electricity, and multiferroicity in BiFeO3-BaTiO3-NdCoO3 lead-free piezoelectric ceramics with high curie temperature for current sensing application*, J. Mater. Sci. Mater. Electron. 28(7), 5531 (2017)
52. C.M. Leung, X. Zhuang, D. Friedrichs, J. Li, R.W. Erickson, V. Laletin, M. Popov, G. Srinivasan, D. Viehland, *Highly efficient solid state magnetoelectric gyrators*, Appl. Phys. Lett. 111(12), 122904 (2017)
53. C.E. Ciomaga, O.G. Avadanei, I. Dumitru, M. Airimioaei, S. Tascu, F. Tufescu, L. Mitoseriu, *Engineering magnetoelectric composites towards application as tunable microwave filters*, J. Phys. D: Appl. Phys. 49(12), 125002 (2016)

54. Kang L., Lee H., Amiri P.K., Magnetolectric Random Access Memory-Based Circuit Design by Using Voltage-Controlled Magnetic Anisotropy in Magnetic Tunnel Junctions, doi:10.1109/TNANO.2015.2462337
55. Aubert A., Loyau V., Chaplier G., Mazaleyrat F., Lobue M, Enhanced magnetolectric voltage in ferrite/PZT/ferrite composite for AC current sensor application, hal.archives-ouvertes.fr/hal-01841115
56. Y. Zhou, S. Priya, in Composite Magnetolectrics, Woodhead Publishing Series in Electronic, and Optical Materials (Woodhead Publishing, 2015), p. 209
57. Bibes M., and Barthélémy A., *Towards a magnetolectric memory*, Nature Materials 7, 425–426(2008)
58. Malleron K., Gensbittel A., Talleb H., Ren E., *Experimental study of magnetolectric transducers for power supply of small biomedical devices*, doi: 10.1016/j.mejo.2018.01.013

7. List of figures

FIGURE 2.1 – DIFFERENT APPLICATIONS OF MAGNETISM IN THE CONTEMPORARY SOCIETY.	48
FIGURE 2.2 – HYSTERESIS LOOP OF A FERROMAGNETIC MATERIAL [2].	51
FIGURE 2.3 – $B(H)$, AND $M(H)$ HYSTERESIS LOOPS IN HARD MAGNETS. THE SHADED RECTANGULAR AREA REPRESENTS THE ENERGY ASSOCIATED WITH A GIVEN POINT OF THE $B(H)$ CURVE [2].	53
FIGURE 2.4 – CURVES OF FIRST MAGNETIZATION, A) FOR A DC FIELD, AND B) FOR AN AC FIELD [1].	53
FIGURE 2.5 – JOULE MAGNETOSTRICTION CAUSED BY (A) APPLICATION OF A MAGNETIC FIELD, AND (B) ROTATION OF A SATURATING MAGNETIC FIELD [8].	54
FIGURE 2.6 – HYSTERESIS LOOP AS FUNCTION OF THE ANISOTROPY, K_1 , AND THE INTERNAL DEFORMATION σ/λ_s [13].	55
FIGURE 2.7 – PIEZOMAGNETIC CURVE AT $H_0 = 0$, AND $H_1 \neq 0$ [1].	56
FIGURE 2.8 – MAGNETOSTRICTIVE WAVEGUIDE POSITION SENSOR [8].	57
FIGURE 2.9 – KIESEWETTER INCHWORK MOTOR [8].	58
FIGURE 3.1- DIFFERENT APPLICATIONS OF PIEZOELECTRIC MATERIALS [18].	59
FIGURE 3.2 - DIRECT, AND INDIRECT PIEZOELECTRIC EFFECTS [2].	60
FIGURE 3.3 - SCHEME OF DIFFERENT CRYSTAL CLASSES [1].	60
FIGURE 3.4 – (A) HYSTERESIS CYCLE OF A FERROELECTRIC MATERIAL. (B) BUTTERFLY CURVE OF A FERROELECTRIC MATERIAL [45]. .	61
FIGURE 3.5 – DEPENDENCY OF DIELECTRIC CONSTANT TO THE TEMPERATURE. IN THE FERROELECTRIC STATE THE FIELD-DEPENDENT ELECTRIC POLARIZATION, AND STRAIN EXHIBITS HYSTERESIS [1].	61
FIGURE 3.6 – SCHEME OF PIEZOELECTRIC EFFECTS.	62
FIGURE 3.7 – (A) LUMPED ELECTROMECHANICAL EQUIVALENT CIRCUIT, AND (B) ADMITTANCE CIRCLE DIAGRAM OF A PIEZOELECTRIC TRANSDUCER AT RESONANCE [22]. (C) PLOT OF THE ADMITTANCE, AND FREQUENCY FOR A PIEZOELECTRIC TRANSDUCER [23].	64
FIGURE 3.8 – (A) MONOCRYSTAL OF PMN-PT, (B) CERAMIC PZT, (C) PVDF FILM, AND (D) MFC [2].	66
FIGURE 3.9 - DEVELOPMENT OF PIEZOELECTRIC MATERIALS WITH MILESTONES/ BREAKTHROUGHS [48].	67
FIGURE 4.1 – VENN DIAGRAM FOR MAGNETOELECTRIC, AND MULTIFERROIC MATERIALS [31].	68
FIGURE 4.2 – REPRESENTATION OF THE DIRECT EXTRINSIC MAGNETOELECTRIC EFFECT [2].	69
FIGURE 4.3 – SCHEMATIC CONFIGURATIONS FOR DIFFERENT CONNECTIVITY TYPES OF TWO-PHASE COMPOSITE MATERIALS. A) 0-3, B) 2-2, C) 1-3 [34].	70
FIGURE 4.4 – FOUR RELATIVE ORIENTATIONS OF THE MAGNETIZATION (M), AND POLARIZATION (P), IN LAMINATE ME BIMORPH STRUCTURE. ORANGE INDICATES THE MAGNETOSTRICTIVE MATERIALS (MS), BLUE THE PIEZOELECTRIC (PE), AND BLACK THE LOCATION OF THE PIEZOELECTRIC ELECTRODES. ADDITIONALLY, THE LETTERS IN THE MODE NAMES, T FOR TRANSVERSE, AND L FOR LONGITUDINAL RESPECT TO THE MS , AND PE MATERIALS. A) L-T MODE, B) T-T MODE, C) L-L MODE, D) T-L MODE [44].	71
FIGURE 4.5 – ILLUSTRATION OF THE 2D TRILAYER MPM COMPOSITE IN L-T MODE [34].	71
FIGURE 4.6 – MAGNETOSTRICTIVE DEFORMATION DUE TO AN APPLIED MAGNETIC FIELD, IN A MAGNETOSTRICTIVE MATERIAL [2]. ...	72
FIGURE 4.7 – L-T LAMINATE COMPOSITE REPRESENTATION [39].	72
FIGURE 4.8 – GEOMETRY LAYOUT OF A ME TRANSDUCER, FORMED BY A LAYER OF MAGNETOSTRICTIVE MATERIAL (MS), AND A LAYER OF PIEZOELECTRIC MATERIAL (PE).	74
FIGURE 4.9 – EQUIVALENT CIRCUIT MODEL FOR MAGNETOELECTRIC TRANSDUCER [34, 38]. GREEN FOR MAGNETIC BLOCK, RED FOR MECHANICAL PART, AND BLUE FOR THE ELECTRIC ONE.	74
FIGURE 4.10 – SCHEME OF A TRANSDUCER ENERGY HARVESTER. A) PHYSICAL POINT OF VIEW. B) ELECTRICAL POINT OF VIEW [42].	75
FIGURE 4.11 - ADAPTED EQUIVALENT CIRCUIT MODEL FOR ME TRANSDUCER IN PEN CIRCUIT CONDITION [34].	76
FIGURE 4.12 – EQUIVALENT CIRCUIT FOR ME TRANSDUCER IN DYNAMIC REGIME.	78
FIGURE 4.13 – ADOPTED EQUIVALENT CIRCUIT MODEL FOR ME TRANSDUCER IN DYNAMIC REGIME.	78
FIGURE 4.14 – NORTON EQUIVALENT MODEL FOR MAGNETOELECTRIC TRANSDUCER.	79
FIGURE 4.15 – A) EXAMPLE OF WPT SYSTEM. B) EQUIVALENT CIRCUIT OF THE ME RECEIVER BLOCK USING THE CLASSICAL RECTIFIER CIRCUIT.	80
FIGURE 4.16 – MAGNETOSTRICTIVE SAMPLES OF TERFENOL-D, DIAMETERS OF 10 MM, AND 16 MM, THICKNESS 1 MM.	82
FIGURE 4.17 – PROPERTIES OF TERFENOL-D [15].	83
FIGURE 4.18 - PIEZOELECTRIC SAMPLES OF PIC181, DIAMETERS OF 10 MM, AND 16 MM (VERTICAL VIEW ON LEFT SIDE), THICKNESS 1 MM, AND 2 MM (LATERAL VIEW ON THE RIGHT SIDE).	84

FIGURE 4.19 – PIEZOELECTRIC SAMPLE REPRESENTATION. ON THE LEFT THE REPRESENTATION OF ITS POLARIZATION, AND ON THE RIGHT SIDE THE MECHANICAL DEFORMATION IN RADIAL DIRECTION.	84
FIGURE 4.20 – PHOTOS OF A MAGNETOELECTRIC SAMPLE, ASSEMBLED, AND TESTED FOR THIS THESIS. A) VIEW THROUGH THE OPTICAL MICROSCOPE, B) VERTICAL VIEW OF SAMPLE A (TABLE 4.5). C) LATERAL VIEW OF THE SAMPLE WITH A CALIBER.	85
FIGURE 4.21 – VIBRATION MODES, AND EIGENFREQUENCY OF PIEZOELECTRIC TRANSDUCER. FIGURE A) REPRESENTS THE FEM STUDY. FIGURE B) REPRESENTS THE VIBRATION MODE FOR THE EIGENFREQUENCY OF 143.97 KHZ. FIGURE C) REPRESENTS THE VIBRATION MODE FOR THE EIGENFREQUENCY OF 158.7 KHZ. FIGURE D) REPRESENTS THE VIBRATION MODE FOR THE EIGENFREQUENCY OF 164.5 KHZ. FIGURE E), AND F) REPRESENT RESPECTIVELY THE VIBRATION MODES OF FIRST, AND SECOND ORDER FOR THE EIGENFREQUENCY OF 166.5 KHZ.....	86
FIGURE 4.22 – EXAMPLE OF ME ENERGY TRANSDUCER STRUCTURE PRESENTED BY YANG [34].	89
FIGURE 4.23 – EXAMPLE OF ME ENERGY TRANSDUCER PRESENTED BY MALLERON [58].	89

8. List of tables

TABLE 2.1 - CLASSIFICATION OF MATERIALS, BASED ON THE AMPLITUDE OF THEIR MAGNETIC SUSCEPTIBILITY, χ [5].	50
TABLE 2.2 – MAGNETOELASTIC PROPERTIES OF SOME MAGNETOSTRICTIVE MATERIALS [7]. λ_s IS THE SATURATED MAGNETOSTRICTION, ρ IS THE MATERIAL’S DENSITY, B_s IS THE SATURATION FLUX DENSITY, T_c IS THE CURIE TEMPERATURE, E IS THE YOUNG’S MODULUS, AND k IS THE MAGNETOMECHANICAL COUPLING FACTORS (4.XXVI).	56
TABLE 3.1 - SCHEME OF VIBRATION MODES OF DIFFERENT PIEZOELECTRIC TRANSDUCERS. OD IS THE EXTERNAL DIAMETER, AND ID THE INTERNAL ONE, TH THE THICKNESS, W THE WIDTH, AND L THE LENGTH. P REPRESENTS THE ELECTRICAL POLARIZATION, AND U THE ELECTRIC VOLTAGE [21].	63
TABLE 3.2 – SCHEME OF PIEZOELECTRIC QUANTITIES.	65
TABLE 3.3 – OSCILLATION STATES FOR DIFFERENT PIEZOELECTRIC GEOMETRIES [22].	65
TABLE 4.1 – SUMMARY OF MAGNETOELECTRIC COEFFICIENTS FOR DIFFERENT LAMINATE COMPOSITES [2].	70
TABLE 4.2 - COMPARISON BETWEEN MAGNETOSTRICTIVE, AND PIEZOELECTRIC MATERIALS [45].	82
TABLE 4.3 – PROPERTIES OF TERFENOL-D, FULL DATASHEET AT ANNEX II.	82
TABLE 4.4 – PROPERTIES OF PIC181, FULL DATASHEET AT ANNEX II.	85
TABLE 4.5 - ME TRANSDUCER WITH DIFFERENT THICKNESSES, AND MASSES OF PIEZOELECTRIC, AND MAGNETOSTRICTIVE LAYERS, STUDIED IN THIS THESIS.	85

Chapter 3

Experimental measurements of a MagnetoElectric transducer

Table of Contents

Chapter 3 Experimental measurements of a MagnetoElectric transducer	97
1. Introduction	99
2. Characterization test.....	100
2.1 Measurement Set up	100
2.2 Circuit Model.....	103
2.2.1 Static regime	103
2.2.2 Dynamic regime	108
2.2.3 Output power.....	111
2.3 MagnetoElectric Samples.....	115
2.4 Characterization Method	116
2.5 Results, and Discussion	119
3. Medical Regulatory Compatibility.....	131
4. In-vitro Test.....	132
4.1 Measurement Set up	133
4.2 Tested Samples	134
4.3 Method.....	136
4.4 Results, and Discussion	137
5. Phantom Test	144
5.1 Measurement Set up	144
5.2 Tested Samples	145
5.3 Method.....	146
5.4 Results, and Discussion	147
6. Conclusion.....	149
7. Bibliography	151
8. List of figures.....	152
9. List of tables	155

1. Introduction

This chapter proposes an experimental perspective of the MagnetoElectric composites as energy transducers for low-frequency wireless power transfer. This part is dedicated to the practical study of ME technology, and its potentialities for biomedical applications. As described in the previous chapter, 6 devices have been fabricated to evaluate, and compare the performances of the different ME transducers concerning their dimensions, and the volume-ratio of the magnetostrictive, and piezoelectric parts.

The current chapter is structured into four parts. The first part consists of the characterization of the ME transducers. The samples have been stimulated with a DC magnetic field, to set their magnetostrictive working point, and with an AC magnetic field to study their performances at different frequencies. The responses of the ME samples have been measured in terms of ME voltage, and power, with different magnitude, and orientations of the input magnetic field. The aim was to test the efficiency of the device with different boundary conditions. The employed test bench has been described, and the experimental results have been compared with the theoretical models presented in Chapter 2.

The second part talks about the medical regulatory, which is applied to the ME transducer, once inserted in an active implantable medical device. This paragraph aims to give an overview of the control, and the limits imposed by the ICNIRP, the commission that determines the exposure limits for electromagnetic fields. These medical regulatory must be considered for practical applications of wireless power transfer in the human body, because they may limit the system performances.

In the third part, a series of in-vitro tests were reported. A comparative set of measurements have been effectuated, testing the performances of a coil-coil system, coil-coil with the ferrite core system, and ME-coil system. For these tests, a mechanical robot was employed to precisely displacing the devices from an external charger. These measurements aimed to study the effect of the alignment, between the transmitter source, and the receiver device, over the system's efficiency for different boundary conditions.

Finally, the last part reports a set of experiments in a phantom environment. The tests aimed to record the performances of the ME devices, through a medium, close to human tissue (duck meat), in terms of efficiency, and orientation sensitivity. For these measurements, the devices were inserted in a polymeric capsule, to preserve the ME resonator characteristics, and avoid any influence of the environment on their mechanical vibration.

2. Characterization test

To estimate the biomedical potentialities of the ME composites as energy transducers, a series of characterization tests were performed. The samples have been stimulated with a DC magnetic field, to set their magnetostrictive working points in the static regime, and with an AC magnetic field of smaller magnitude, to measure their performances in the dynamic regime.

A new test bench has been specifically developed for this series of tests, to guarantee the reliability, and reproducibility of the results. The bench helped to simultaneously control an AC magnetic field, generated by a copper-coil, and a DC magnetic field, generated by a pair of permanent magnets. The final aim was the stimulation of the ME sample through different input source parameters, to observe the maximum reachable performances in terms of ME voltage, and power density.

Firstly, the ME transducers have been studied under different magnetic fields excitations, and with different orientations of the sample in the magnetic field. In a second time, the measurements have been repeated connecting the transducer to a rectifier circuit. Rectification is usually the first step in an electronic interface circuit enabling to maximize the output power of the transducer and to get DC output voltage, compatible with the rechargeable battery of the implant. Based on these measurements, the ME samples have been compared among them, in terms of power, and power density, to investigate the effect of the volume ratio between the piezoelectric, and the magnetostrictive parts.

The ME characteristics were finally studied, comparing the output responses, previewed by the theoretical models, and reported in Chapter 2, with the experimental performances. This last test aims to estimate the accuracy of the chosen model, and its ability to predict the system performances.

2.1 Measurement Set up

The characterization tests aim to stimulate the ME samples, with different AC and DC magnetic fields, and to study their responses. The used test bench is represented in the following scheme (Figure 2.1). An input signal from a waveform generator (Keysight 33600A Series), amplified by the power amplifier (HAS 4101, voltage gain x10), supplies the coil, which generates the AC magnetic field. The DC magnetic field is generated through a pair of permanent magnets. The sample is inserted in these two fields and it is connected to the oscilloscope, which measures the ME voltage over the sample's electrodes and the delivered output power. A PC controls the waveform generator, the oscilloscope, and the load, through an automated measurement code. The code allows piloting the instruments to automatize the measurements over a spectrum of frequencies and loads and assure their repeatability.

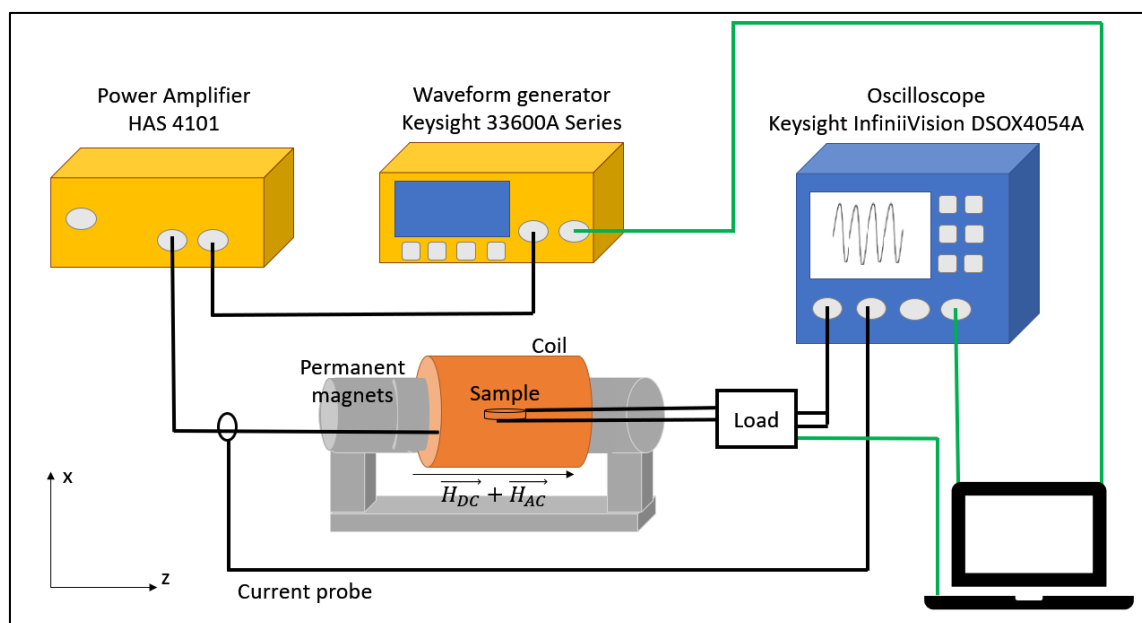


Figure 2.1 – Scheme of the test bench for the characterization tests.

In the setup, the sample is placed at the center of a pair of permanent magnets and the coil. The holder is shown in Figure 2.2. In the higher figure, there is the scheme of the system, made with SolidWorks®. In the lower part, there is a photo of the real holder, from a vertical view.

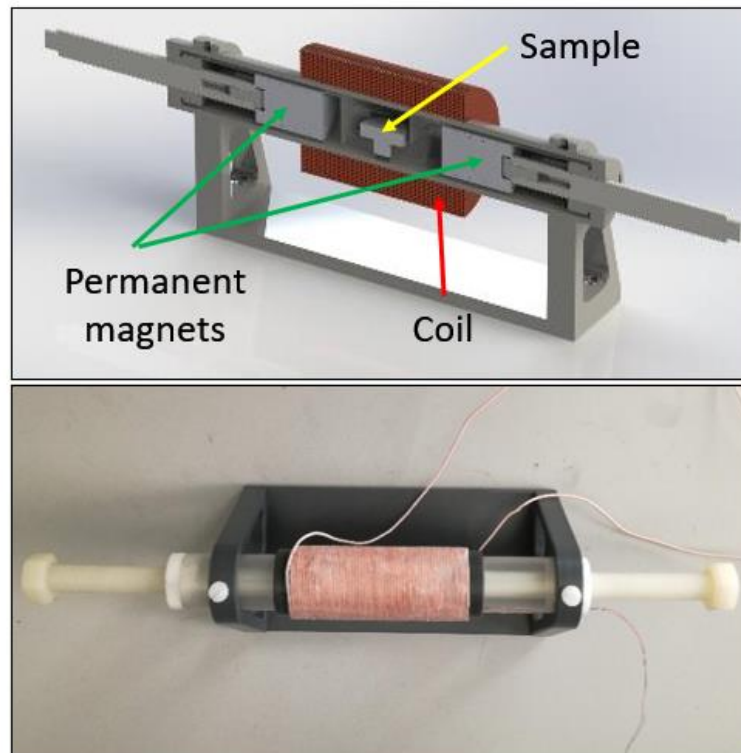


Figure 2.2 - Photos of the sample's holder. In the left picture, there is the holder with permanent magnets, and the sample. The photo on the right is the holder with coil, from a vertical view.

The permanent magnets are 8 in total, made with neodymium (also known as NdFeB). They have a cylindrical shape with a radius of 7.5 mm, and a height of 5 mm each. A group of 4 magnets is placed per each side of the sample. The system's holder is movable, so it is possible to modify the distances between magnets, to change the biasing DC field. The minimum distance is 3cm, to leave sufficient space for the sample, until 8.2 cm. Here reported a graph (Figure 2.3) of the z-component of the DC field, measured at the center of the sample's holder, with a Gaussmeter (GM08 Hirst Magnetic Instruments Ltd).

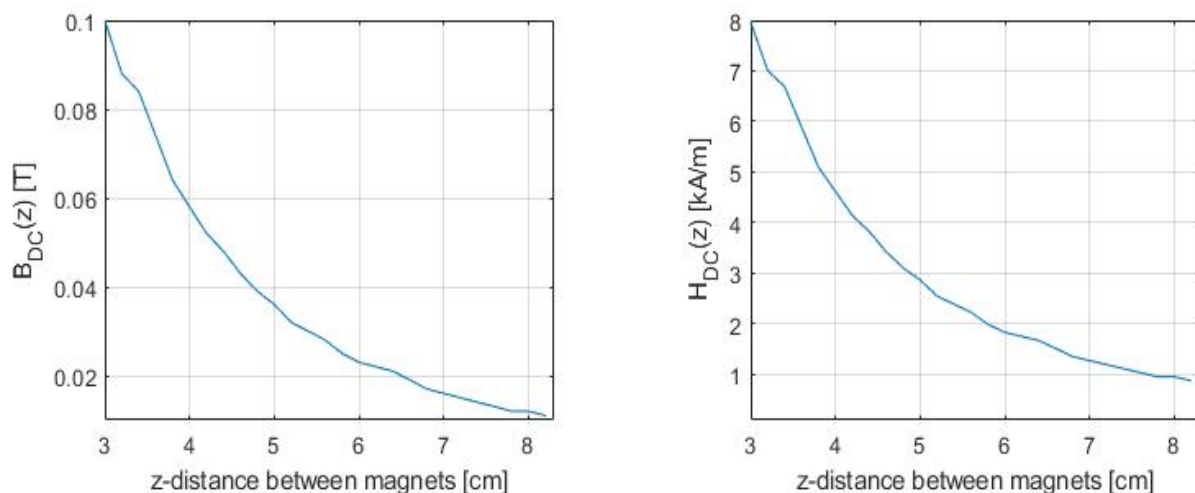


Figure 2.3 - Trend of DC magnetic field, varying the distance between permanent magnets.

The magnets are surrounded by a coil, which excites the sample through an AC field. The solenoid is made with litz wire. It has 60 turns, a length of 68 mm, an external diameter of 26 mm, and a wire's radius of 0.57 mm. The coil is supplied by the signal of the waveform generator and the power amplifier. The current through the coil is controlled with a contactless current probe (HIOKI CT6700), connected to the oscilloscope (Keysight InfiniiVision DSOX4054A). The estimation of the AC magnetic field is calculated through the formula:

$$B_{AC} = \mu_0 \frac{N}{l} i_{AC} \quad (2.1)$$

where N is the number of coil's turns, l is the length of the coil, i_{AC} is the RMS value of the coil current measured with the probe, and μ_0 is the vacuum permeability ($\mu_0 = 4 \pi 10^{-7}$ T m/A). In this case, the influence of the neodymium magnet in the coil-core is considered negligible for the magnetic field estimation, due to the value of its relative permeability equals 1.05 [3].

The sample is connected to a load resistor, over which the ME voltage, and power are measured with the oscilloscope. To perform a set of measurements with different load resistance values, an electronic card is used instead of a simple resistance. The card has, in parallel, three series of 8 resistances (values from 1 Ω to 1E7 Ω), and it is controlled through a computer and a python code. Furthermore, the generated code controls the waveform generator, and the oscilloscope, to automatize the measurements, and improve their reproducibility.

The test bench was, firstly, used to measure the output impedance of the ME samples. In this way, the equivalent circuit parameters of the transducers could be estimated, as described in Chapter 2. Once the equivalent circuit model has been evaluated, the set-up could be employed to characterize the ME transducer, in terms of output ME voltage, and power density.

2.2 Circuit Model

The equivalent circuit represents the nonlinear ME system through three main blocks, connected by two phenomena, the magneto-mechanical, and electro-mechanical couplings. The model, showed in Figure 2.4, represents the magnetic part in green, mechanical in red, and electrical in blue, strictly linked through the transformer ratios, φ_m , and φ_p , symbolizing respectively the *magneto-elastic*, and the *elasto-electric couplings*.

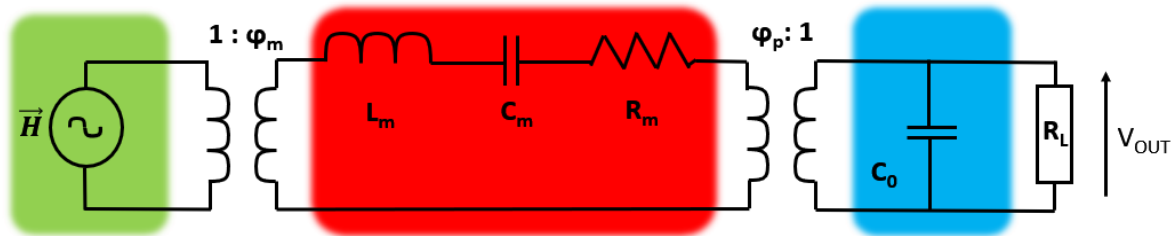


Figure 2.4 – Equivalent circuit model for magnetoelastic transducer [8, 9]. Green for magnetic block, red for mechanical part, and blue for the electric one.

The magnetic field is transmitted to the magnetostrictive layer, which causes a mechanical deformation of its structure. Consequently, the piezoelectric layer reacts to the mechanical strain through a mechano-electric transformation, creating a voltage across its electrodes.

Applying the theoretical equivalent circuit model to the fabricated samples, it has been possible to estimate the circuit parameters for each of the 6 configurations presented in Table 4.5 of Chapter 2.

2.2.1 Static regime

The *static regime* is defined as an operating condition, under which the transducer is biased through a DC magnetic field. The first aim of this phase is the estimation of the equivalent circuit model to represent the ME samples. A measurement of the output impedance allows the calculation of the circuit parameters. Starting from this configuration (Figure 2.5), the theoretical behavior of the ME transducer has been fitted with the experimental one.

Following the equivalent circuit model, to calculate the output impedance or admittance of the transducer, it is possible to short-circuit the system's generator, represented by the external DC magnetic field. Then, the circuit impedance can be represented by two parts, one mechanical, Z'_m , and one electrical, Z_θ . To estimate the first component, the impedance of the mechanical block Z_m is transferred to the electric part of the circuit with the piezoelectric coupling factor φ_p . The theoretical admittance (4.XIX) was fitted with the experimental one, measured with the impedance analyzer (HIOKI IM3570).

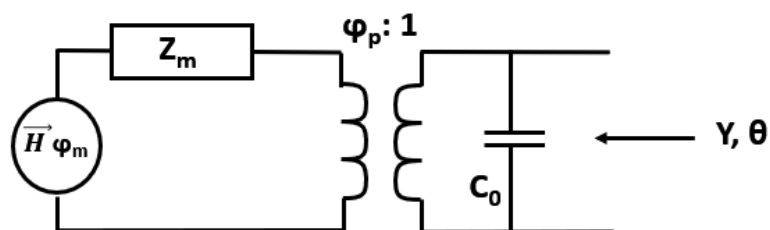


Figure 2.5 - Adapted equivalent circuit model in open circuit conditions [8].

There are several methods to calculate the circuit's parameters, based on fitting the experimental behaviors, and minimization of the error. In general, to estimate all parameters from the admittance measurements (L_m , C_m , R_m , C_0 , Q , k_{ee} , φ_p), it is better to set a priori at least one of the parameter values to maintain the physical meaning of the identified parameters.

In this case, the value of L_m , representing the dynamic mass, was chosen as a fixed parameter, due to its link with the physical mass of the device. As reported by Serrate, Vasic, and Costa [149], for the first radial mode

of vibration, the equivalent dynamic mass is linked to the real mass of the sample through the following equation:

$$L_m = \frac{\rho_m \pi (r)^2 t}{1.4} \quad (2.11)$$

where ρ_m is the volumic mass density [kg/m³], r is the sample's radius [m], and t is its thickness [m]. This choice was motivated by the interest to have a value with the physical meaning of L_m . Ali Koteiche, Alexis Brenes, and Kevin Malleron, for example, explored another methodology, based on the imposition of C_0 . This parameter was measured independently from the admittance measurement [2]. For this thesis, this methodology led to identifying values of L_m very different from the physical value of the dynamic mass. Conversely, setting the value of the physical dynamic mass L_m led to identifying values of C_0 very close to the actual capacitance of the piezoelectric disks. Therefore, this last identification method was adopted.

Secondly, from the experimental measurements, it has been possible to determine the values of resonance and antiresonance frequencies. From these three known values (L_m , f_r , f_a), the unknown parameters could be calculated (C_m , R_m , C_0 , Q , k_{ee} , φ_p), fitting the experimental behavior of the complex admittance with the theoretical one (4.XIX).

In the following figures, the admittance diagrams are reported, measured in the static regime ($H_{AC} = 0$), and the admittance diagrams obtained with the model and the identified parameters. The measurements were performed without DC magnetic field (Figure 2.6) and under a DC magnetic field of 0.1 T (Figure 2.7).

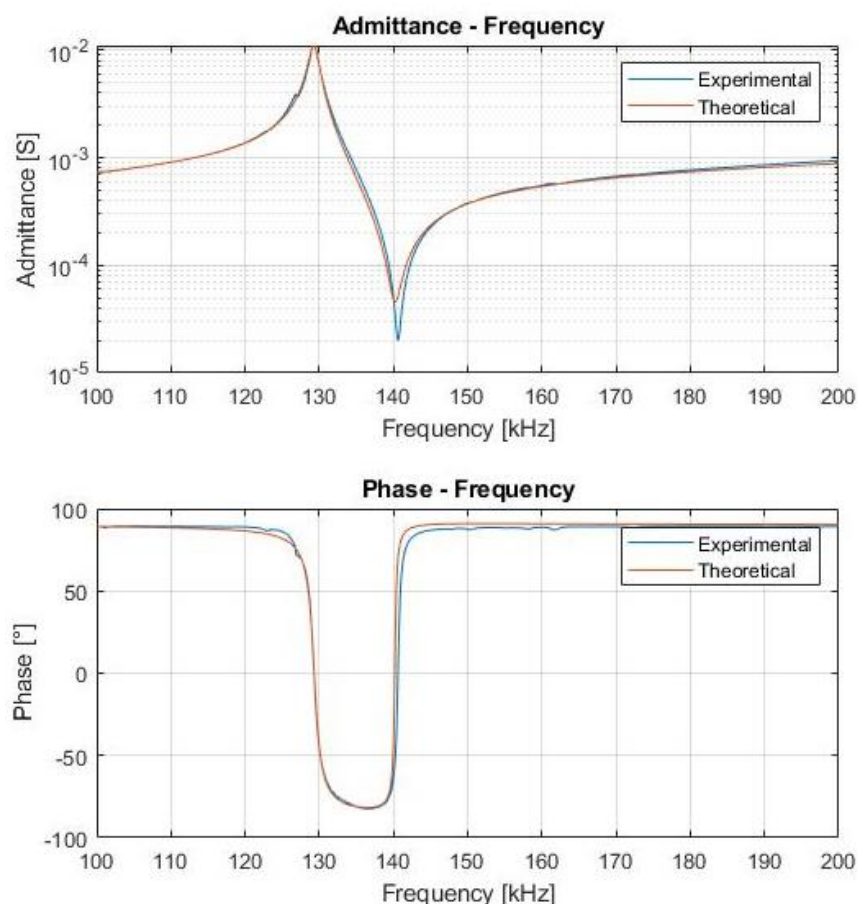


Figure 2.6 - Experimental, and theoretical behaviour of a ME transducer in static regime, with $H_{AC} = 0$. Sample C.

This methodology was adopted to determine the model parameters of all the samples (Appendix III). In this case, the sample C (diameter of 16 mm, and tri-layer M-P-M) is considered. From these graphs, it is possible to

notice that the DC magnetic field plays a role in the resonance frequency and the peaks of resonance and antiresonance are right-shifted in the presence of the DC magnetic field.

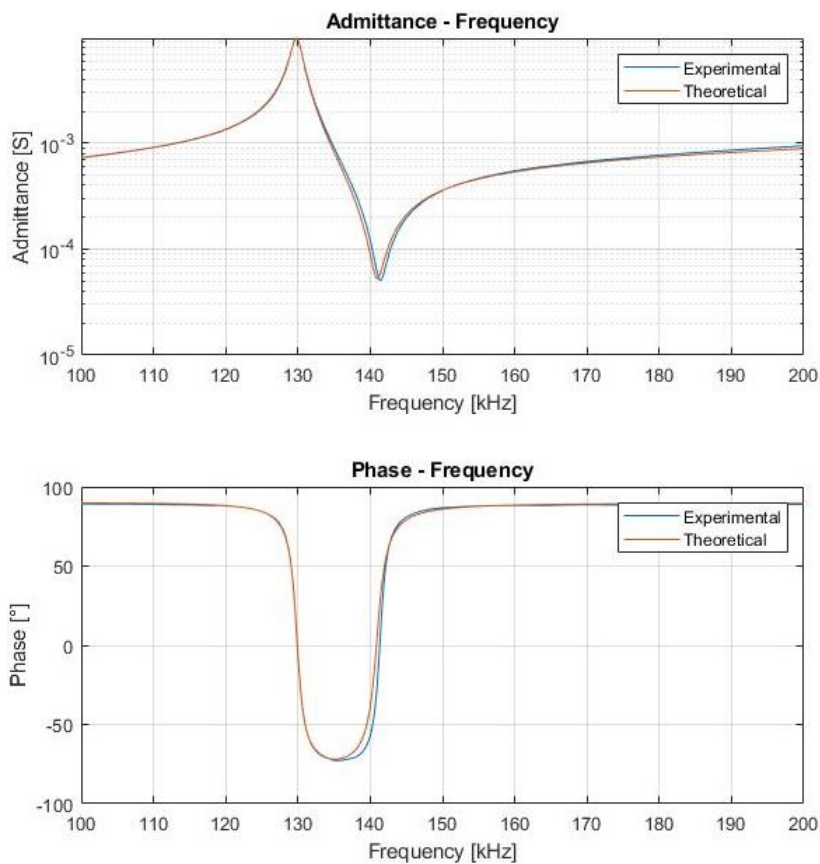


Figure 2.7 - Experimental, and theoretical behaviour of a ME transducer in static regime, under a bias field H_{DC} of 0.1 T. Sample C.

In Table 2.1, the circuit parameters are reported under the two static-regime conditions, 0-field, and 0.1 T fields. One can note that the most influenced parameter is the motional resistance (R_m). When the DC field is applied, the value of R_m is increased, indicating an increment of the mechanical losses.


Sample	B_{DC} [T]	m [g]	L_m [mH]	C_m [nF]	R_m [Ω]	C_0 [nF]	Fr res [kHz]	Fr antir [kHz]	$ Y_{max} $ [ms]
	0	6.97	4.98	0.3	42.19	0.8	129.28	140.63	11.02
	0.1	6.97	4.98	0.3	48.97	0.81	129.84	141.36	9.8

Table 2.1 - Model parameter values for static regime measurements, without, and with DC field for tri-layers composite. Sample C.

Under the DC magnetic field, tensile mechanical stress is induced in the magnetoelectric transducer by the magnetostrictive layer of the composite in the direction of the magnetic field. So, this mechanical deformation is at the origin of the observed increment of the mechanical damping and the resonance and antiresonance frequencies.

Changing the distance between the permanent magnets enables to change the magnitude of the DC magnetic field, as shown in Figure 2.3. The admittance Bode diagram of the tri-layer device MPM was measured under different values of the DC magnetic field, ranging from 0.012 T to 0.1 T, as reported in Figure 2.8.

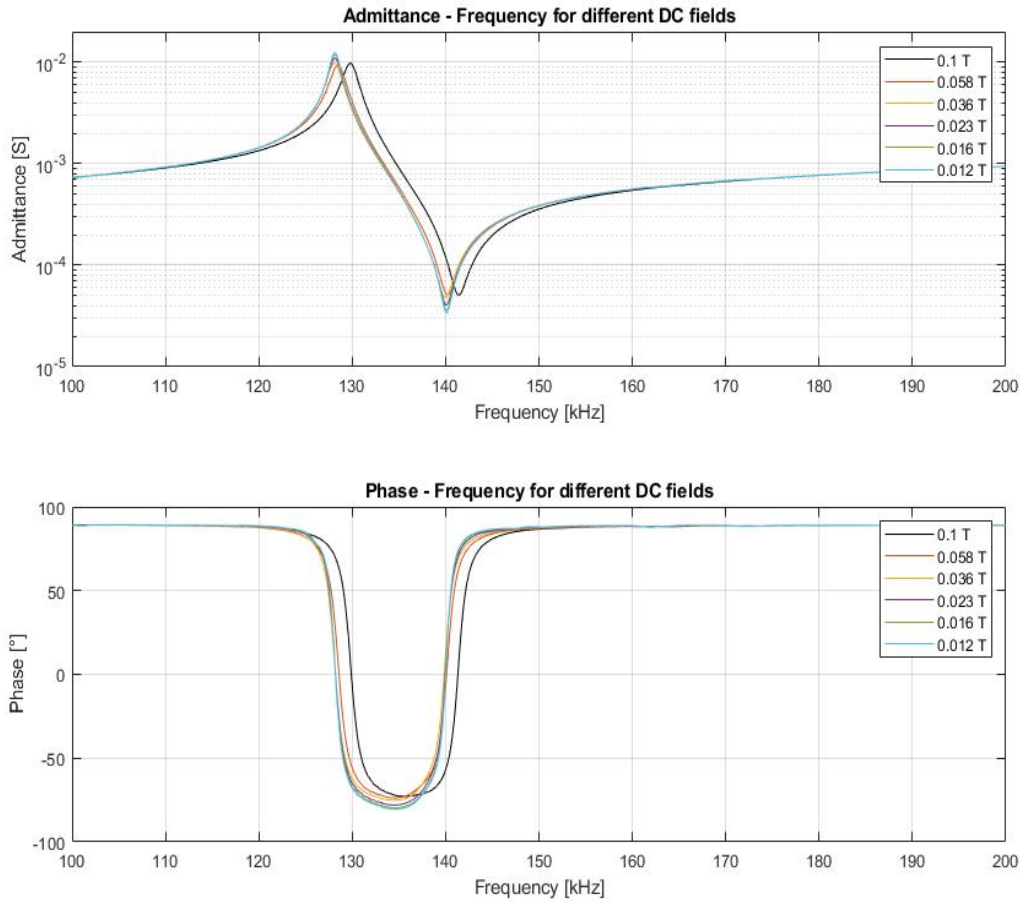


Figure 2.8 – Admittance and phases of MPM sample for different bias fields. Sample C.

The frequency shift effect is more visible for the highest value of the DC magnetic field (0.1 T), and the peak modulus of admittance results higher for lower fields. This measurement procedure was repeated for all the samples. In Table 2.3, all the equivalent circuit parameters are reported. The circuit parameters are presented at varying DC-magnetic fields, 6 values of excitation are considered.

As discussed before, L_m is assumed constant, and dependent only on the sample’s mass. Furthermore, the parameter C_m , representing the mechanical stiffness of the system, is moderately influenced by the external DC magnetic field. On the contrary, R_m , which represents the mechanical damping, significantly varies with the external DC magnetic field. In general, it results highest for 0.058 T field, and it tends to decrease for lower and higher magnetic fields. This value of the DC magnetic field also corresponds to the highest output power, as it will be shown in the following measurements (Figure 2.23).

Furthermore, C_0 represents the clamped capacitance of the electro-mechanical block. The obtained values of C_0 for the ME devices are very close to the values of C_0 of the single piezoelectric layer. This point has been verified by determining the equivalent circuit parameters of the single piezoelectric layers from output admittance measurements (Table 2.2).

Piezoelectric Sample	L_m (mH)	C_m (nF)	R_m (Ω)	C_0 (nF)
$\varnothing = 10$ mm - t = 1 mm	0.44	1.11	2.29	0.71
$\varnothing = 16$ mm - t = 1 mm	1.12	1.13	1.33	1.63
$\varnothing = 16$ mm - t = 2 mm	2.25	5.62	1.69	0.79

Table 2.2 – Circuit parameters of single piezoelectric layer.

As described in Chapter 2, when the ME transducer is assembled, it loses some properties from the piezoelectric, and magnetostrictive materials, creating new ones. In this case, it is possible to consider that the transducer keeps the dependency of C_0 from the original piezoelectric characteristics. So, one may consider that C_0 is only dependent on the physical properties of the PIC181 material. For sample D, with two piezoelectric layers of 2 mm-thickness, it is possible to consider C_0 as the parallel of two piezoelectric capacitances.

From the point of view of the resonance frequency, it depends mainly on the sample's dimensions, and on the diameter, but it is further influenced by the DC magnetic field; it results higher for smaller-diameter samples, as predicted by theory. The elasto-electric coupling coefficient k_{ee}^2 results dependent on the properties of the piezoelectric disk and the elastic properties of the magnetostrictive layer. Overall, a very small change of the elasto-electric coefficient is observed, indicating a very moderate effect of the DC magnetic field over the elastic properties of the magnetostrictive layer. It is interesting to notice the samples A and C, which have the same diameter and same percentage of magnetostrictive material, 50% of the total volume, report the same value of k_{ee} . This could explain the dependence on the physical properties of the magnetostrictive layer.

On the contrary, the quality factor seems highly dependent on the magnetic fields. Especially the quality factor results in higher for the configurations of tri-layers composites (PMP), which also correspond to the sample with lower magnetostrictive volume ratio.

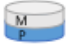
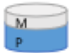
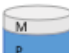
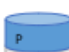


Sample	Size	B_{DC} (T)	L_m (mH)	C_m (nF)	R_m (Ω)	C_0 (nF)	φ_p	k_{ee}^2	Q
 A	\varnothing 16 mm t_m 1 mm t_p 1 mm	0.1	2.64	0.56	36.14	1.62	0.72	0.15	117
		0.058		0.58	46.48	1.63	0.71	0.15	91.2
		0.036		0.59	45.7	1.62	0.7	0.15	94.32
		0.023		0.6	36.84	1.58	0.69	0.15	119.53
		0.016		0.6	34.57	1.58	0.69	0.15	127.02
		0.012		0.6	33.63	1.58	0.69	0.15	130.78
		0.012		0.6	33.63	1.58	0.69	0.15	130.78
 B	\varnothing 16 mm t_m 1 mm t_p 2 mm	0.1	3.69	0.39	52.66	0.84	0.65	0.16	139.35
		0.058		0.4	66.7	0.98	0.64	0.14	112.35
		0.036		0.4	82.12	1.03	0.63	0.14	92.45
		0.023		0.4	79.12	1.03	0.62	0.13	101.3
		0.016		0.4	81.7	0.97	0.58	0.12	111.79
		0.012		0.4	50.65	0.94	0.57	0.12	187.5
		0.012		0.4	50.65	0.94	0.57	0.12	187.5
 C	\varnothing 16 mm t_m 1+1 mm t_p 2 mm	0.1	4.98	0.3	48.97	0.81	0.69	0.15	173.15
		0.058		0.31	49.94	0.8	0.68	0.15	172.38
		0.036		0.31	46.84	0.79	0.68	0.15	185.75
		0.023		0.31	41.37	0.79	0.68	0.15	211.45
		0.016		0.31	38.09	0.78	0.68	0.15	230.11
		0.012		0.31	36.59	0.78	0.68	0.15	239.34
		0.012		0.31	36.59	0.78	0.68	0.15	239.34
 D	\varnothing 16 mm t_m 1 mm t_p 2+2 mm	0.1	6.01	0.25	27.14	0.41	0.65	0.21	429.48
		0.058		0.26	27.87	0.4	0.64	0.21	421.35
		0.036		0.26	27.79	0.4	0.64	0.21	422.77
		0.023		0.26	26.04	0.4	0.64	0.21	450.62
		0.016		0.26	24.55	0.39	0.64	0.21	481.4
		0.012		0.26	23.25	0.4	0.64	0.21	512.34
		0.012		0.26	23.25	0.4	0.64	0.21	512.34
 E	\varnothing 10 mm t_m 1 mm t_p 1 mm	0.1	1.81	0.43	60.65	0.66	0.49	0.14	139.85
		0.058		0.44	53.96	0.66	0.48	0.13	166.64
		0.036		0.44	48.00	0.68	0.48	0.13	186.2
		0.023		0.43	43.46	0.68	0.48	0.13	204.63
		0.016		0.45	33.2	0.70	0.44	0.11	304.7
		0.012		0.45	32.54	0.7	0.44	0.11	314.4
		0.012		0.45	32.54	0.7	0.44	0.11	314.4
 F	\varnothing 10 mm t_m 1 mm t_p 1+1 mm	0.1	2.88	0.22	40.06	0.31	0.58	0.19	266.46
		0.058		0.22	37.66	0.29	0.58	0.2	287.51
		0.036		0.22	33.85	0.29	0.57	0.2	326.39
		0.023		0.22	30.47	0.28	0.57	0.21	363.5
		0.016		0.22	28.33	0.27	0.57	0.21	389.77
		0.012		0.22	27.75	0.27	0.57	0.21	394.57
		0.012		0.22	27.75	0.27	0.57	0.21	394.57

Table 2.3 - Circuit parameters (L_m , C_m , R_m , C_0), elasto-electric coupling coefficient k_{ee} , quality factor Q, and resonance frequency for 6 different ME transducers.

2.2.2 Dynamic regime

The *dynamic regime* is defined as an operating condition, under which the transducer is excited through an AC magnetic field of small magnitude, superposed to the DC field. For the study in a dynamic regime, the response of the sample has been measured with an additional external AC magnetic field of 0.7 mT. The process described here was adopted to study all the samples (Annex III). In this case, the sample C (diameter of 16 mm, and tri-layer M-P-M) is considered.

To understand the influence of this alternating field, two types of measurements were performed over the ME composite, the first one in an open circuit (OC), and the second one with an output resistive load. The first measurement allows the calculation of the ME coefficient, which is not possible to obtain through the impedance measurement in a static regime. Thanks to the ME transfer function, the ME model results complete. So, now it is possible to estimate the output ME voltage, and power of a loaded ME transducer. In this case, the second measurement aims to compare the expected ME output with the experimental one.

As described in Paragraph 4.1 of the previous chapter, the magnetolectric transfer function is experimentally measured in open circuit configuration, as:

$$\alpha_{ME} = \frac{E}{H_{AC}} = \frac{V_{OUT}}{H_{AC} t_p} \quad (2.III)$$

The ME transfer function of sample C is reported for an external DC magnetic field of 0.1 T in Figure 2.9. V_{OUT} represents the output magnetolectric voltage of the transducer, H_{AC} is the AC magnetic field, and t_p is the thickness of the piezoelectric layer [2]. As shown in the figure, the highest value of the magnetolectric coefficient is reported at the resonance, with a consequent change of phase.

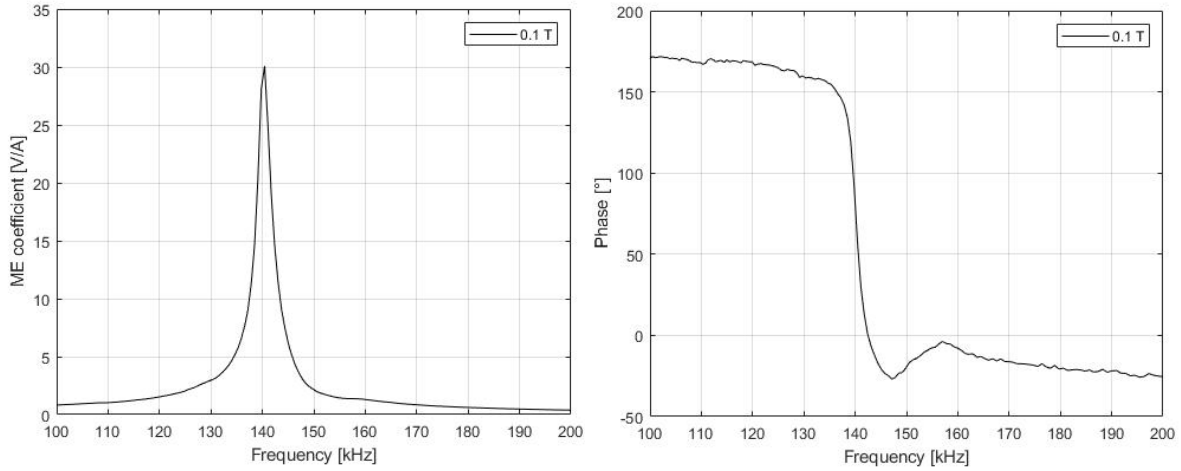


Figure 2.9 - Trend of the complex α_{ME} for the sample C for different frequencies with a bias field of 0.1 T.

Once the magnetolectric transfer function is calculated from the measurement in OC, the experimental V_{OUT} of the closed system can be predicted through the equations:

$$V_{OUT} = \frac{R_L}{R_L + Z_{eq}} (\alpha_{ME} t_p H_{IN}) \quad (2.IV)$$

where R_L is the output load, and Z_{eq} is the internal impedance of the equivalent circuit, calculated from the identified parameters (Table 2.3) as:

$$Z_{eq} = \frac{(j\omega)^2 L_m C_m + (j\omega) C_m R_m + 1}{(j\omega)^3 L_m C_m C_0 + (j\omega)^2 C_m R_m C_0 + (j\omega)(\varphi_p^2 C_m + C_0)} \quad (2.V)$$

To estimate the behavior of the ME coefficient, and ME voltage at a specific bias magnetic field, the optimal resistive load is considered. As described in Chapter 2, Paragraph 4.3.3, the optimal value of the load resistance varies over the frequency spectrum, and for the external DC magnetic field. In this case, the maximum value corresponds to 10 k Ω for a DC magnetic field of 0.1 T.

So, the second measurement of ME responses was conducted for a charge of 10 k Ω . Figure 2.10 shows the trend of the ME voltage and its phase. In a red curve the theoretical ME voltage, calculated from the circuit's parameters, and the ME coefficient measured in the OC circuit, is presented. In a blue curve, the experimental ME voltage is reported, measured over a load of 10 k Ω .

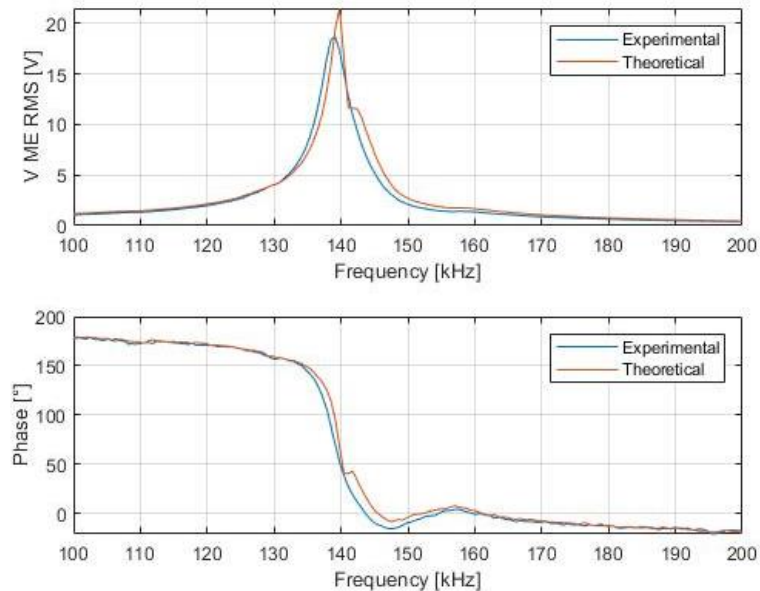


Figure 2.10 - The ME voltage of a tri-layer transducer (MPM) is reported at the varying frequency for a bias field of 0.1 T, and over a load of 10 k Ω . The measured V_{OUT} is represented with the blue curve, and the estimated V_{OUT} with the red one.

In Figure 2.10, at a first view, the estimated output voltage magnitude and phase exhibit more irregularities than the experimental ones, due to the experimental calculation of α_{ME} in open circuit condition. Furthermore, it is possible to notice the presence of the second peak of resonance, less accentuated at the right side of the resonance frequency. The maximum ME voltage is overestimated by around 13%, indicating that the ME model parameters also depend on the operating point determined by the load. Among those parameters, the magneto-elastic coupling is likely to exhibit significant change, due to the nonlinearities of the magnetostriction curve and the influence of the load on the vibration magnitude of the transducer.

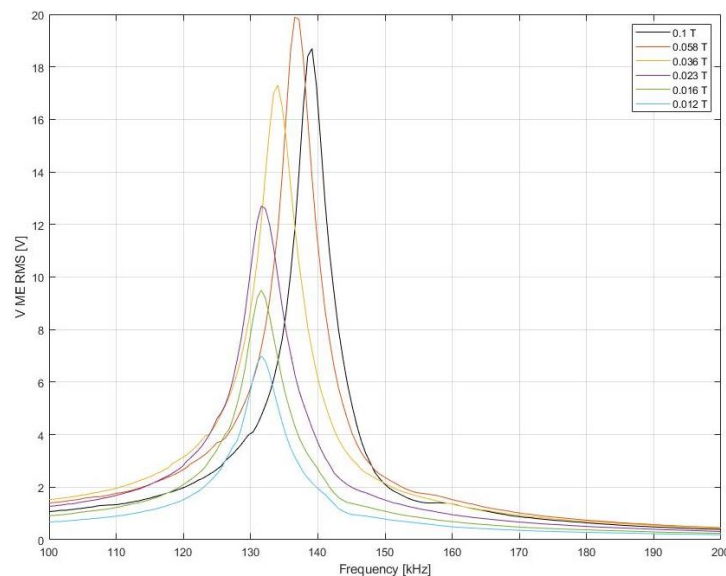


Figure 2.11 – Measurements of the ME voltage for different DC magnetic fields.

Figure 2.11 shows the measured ME voltage for different biasing magnetic fields, ranging from 0.012 T to 0.1 T and with a load resistance of 10 k Ω . These curves show that the value of the ME voltage increases with higher DC magnetic field until the value of 0.058 T. As described in Paragraph 2.2.1 and shown in Figure 4.2 of Chapter 2, for the magnetostrictive material there is an optimal working zone, defined as the quadratic region, where the slope of the magnetostriction is linear. Above this region, the sample enters in a saturation zone, where the magnetostrictive deformation tends to saturate at the increase of the magnetic field \vec{H} (Figure 4.6 of Chapter 2). The superposition of the DC, and AC magnetic fields has the role to define the working boundaries of the ME sample. So, in this case, the 0.058 T corresponds to the optimal DC magnetic field for the quadratic zone, and the 0.1 T reveals the beginning of the saturation one.

Furthermore, the resonance frequencies tend to left-shift at lower biasing fields. In general, the resonance frequency with load resistance is comprised between the open-circuit, and short-circuit resonances, which are inversely proportional to the circuit parameters L_m , C_m , and C_0 . As shown in Table 2.3, the value of these parameters may exhibit small change as a function of the DC magnetic fields, but they are not sufficient to explain the left-shift of the resonance frequency at lower magnetic fields, showing obvious limitations of this model.

Despite its imprecision, the considered model gives useful information on the global behavior of the ME transducer. Once all the parameters of the equivalent circuit model have been identified, it has been possible to study the ME composite as a power transducer. In the following paragraph, an evaluation of the achieved output power is reported. As a DC output voltage is required for the considered application of wireless battery charging, classical AC/DC rectifier circuits have been added to the ME circuit and studied in comparison with the ME system with the load resistance.

2.2.3 Output power

From the need to power and recharge active implantable medical devices, the interest to study the magnetolectric transducer with additional electric interfaces was born. In the first step, the ME transducer was connected to a resistive load and the output AC voltage and power were measured. Secondly, since the electrochemical battery needs a stabilized DC voltage, the ME transducer was studied with an additional circuit to ensure electrical compatibility. A classical AC/DC rectifier, which usually precedes the battery in the medical device, was connected to the system.

To better understand the output characteristics of the system, the equivalent circuit model of the ME transducer was implemented with SPICE-based software (SPICE: Simulation Program with Integrated Circuit Emphasis). This study aims to simulate the ideal behavior of the energy transducer.

The equivalent circuit model in the dynamic regime and with a resistive load was reproduced using the parameters of Table 2.3 for each sample. Here reported the scheme for sample C (diameter of 16 mm, and tri-layer M-P-M), Figure 2.12. The input voltage, representing the system excitation due to the external magnetic field, has been estimated starting from a 0.1 T DC magnetic field and the experimental value of φ_M , as described by the formula (4.XXIV) of Chapter 2. The working conditions have been studied for an interval of frequencies comprised between 100 kHz and 200 kHz. In this case, the electrical circuit is represented by the resistive load R_L of 10 k Ω , determined as the optimal value for this circuit configuration. The output AC voltage, theoretically calculated through the equation (4.XXVI) of Chapter 2 and the output power, calculated as:

$$P_{AC} = \frac{V_{OUT}^2}{R_L} = \frac{R_L}{(R_L + Z_{eq})^2} (\alpha_{MEV} H_{IN})^2 \quad (2.VI)$$

are compared to the values of the LTSpice simulation.

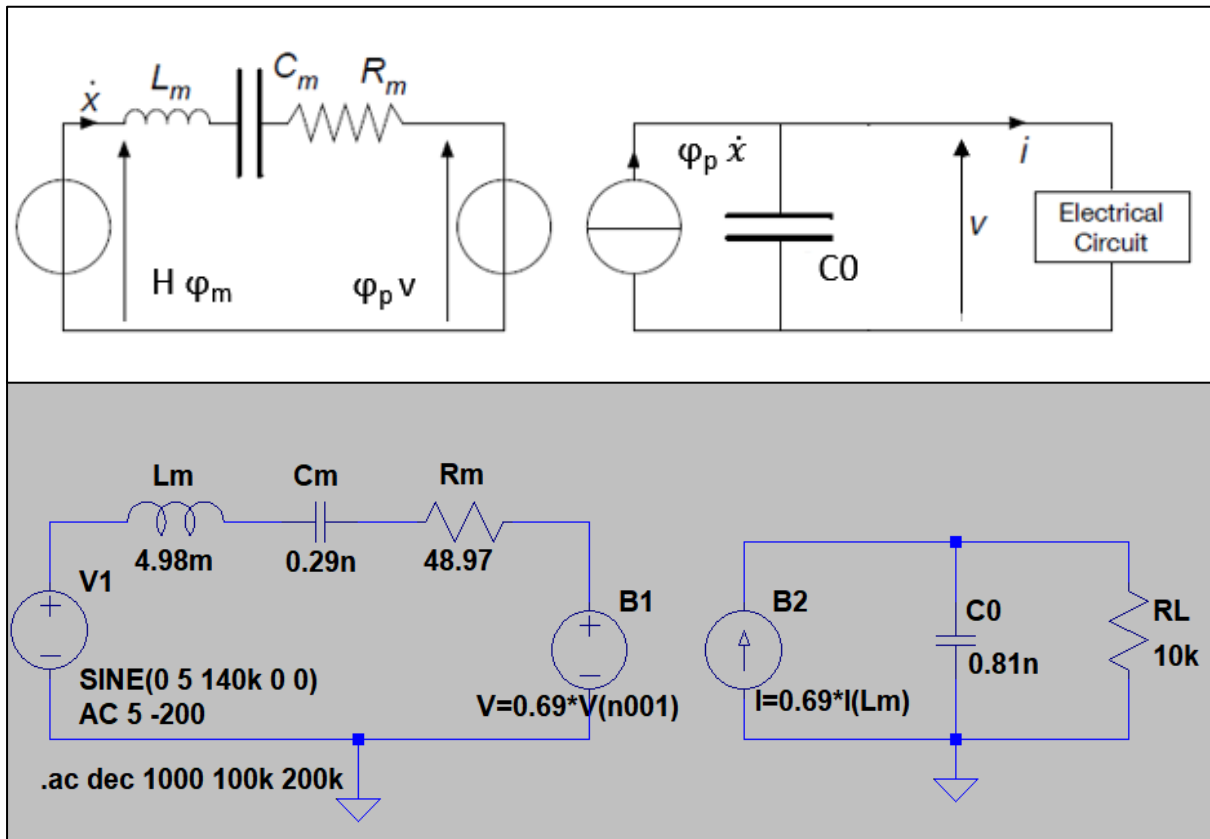


Figure 2.12 – Equivalent circuit model of a tri-layer transducer (MPM) in dynamic regime, for 0.1 T DC magnetic field.

The ME voltage RMS (green curve), and ME power RMS (red curve) are reported in Figure 2.13. Comparing the ME voltage previously showed in Figure 2.10 at the resonance, the “experimental” ME voltage results 17% lower than the value obtained with the LTSpice simulation, and the “theoretical” ME voltage results 2.5% lower than the LTSpice value.

In the model for the dynamic regime, the “theoretical” voltage was estimated, over the spectrum of frequency, through the equation (2.IV). It is called “theoretical”, but it depends on the magnetoelectric coefficient α_{MEV} , which represents the transfer function of the system experimentally determined. On the contrary, the “experimental” ME voltage was uniquely obtained through the characterization measurements.

For these values of error, the studied equivalent circuit model seems acceptable, and the 17% of error, estimated at resonance, is linked to the real losses of the system.

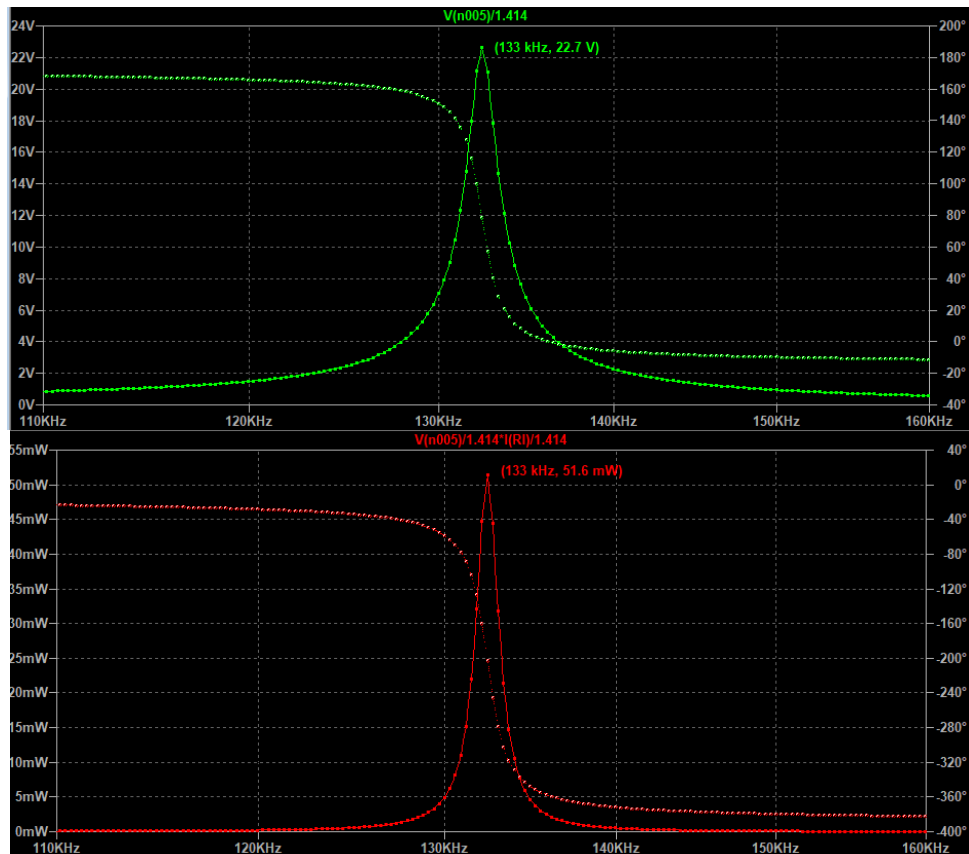


Figure 2.13 – ME transducer performances of a trilayer composite (\varnothing 16 mm, and t 4 mm), sample C. The green curve represents the ME voltage RMS over R_L 10 k Ω , with a maximum value of 22 V at resonance. The red curve represents ME power RMS over R_L 10 k Ω , with a maximum value of 51 mW at resonance.

The same procedure has been followed, inserting an AC/DC rectifier at the resistive load place. Indeed, the AC output voltage of the magnetostrictive transducer must be rectified to power the electronics of the medical implant, and to recharge its electrochemical battery. A classical AC/DC rectifier and DC/DC converter are usually used to stabilize the output DC characteristics.

The equivalent circuit model in the dynamic regime with the rectifier was reproduced using the parameters of Table 2.3 for each sample. In the following simulations, the sample C (diameter of 16 mm, and tri-layer M-P-M) has been taken as an example. As in the previous case, the input voltage has been estimated starting from a 0.1 T DC magnetic field and the experimental value of φ_M , as described by the formula (4.XXIV) of Chapter 2. The working conditions have been studied for an interval of frequencies comprised between 100 kHz and 200 kHz. In this case, the electrical circuit is represented by a half-bridge and a full-bridge rectifier.

The output DC voltage is theoretically calculated through the equation (4.XXXIII) of Chapter 2 and the output power through the equation:

$$P = \frac{V_{DC}^2}{R_L} = \frac{\varphi_p^2 \omega^2 R_L}{(\omega C_0 R_L + \pi/2)^2} (x_M)^2 \quad (2.VII)$$

where the value of the displacement, Eq. (4.XXXVI) of Chapter 2, is linked to the value of the experimental value of the applied magnetic field and φ_M . The example of the equivalent circuit model with the full-bridge rectifier is reported in Figure 2.15 and with the half-bridge rectifier in Figure 2.14.

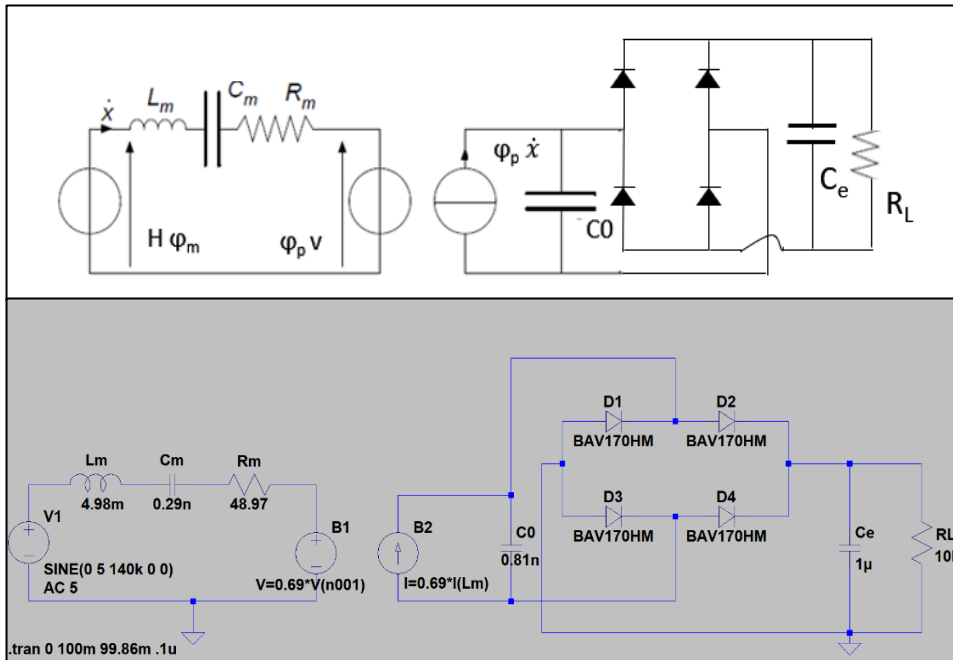


Figure 2.15 - Equivalent circuit model of a tri-layer transducer (MPM) in dynamic regime, for 0.1 T DC magnetic field, followed by a full bridge rectifier. Sample C.

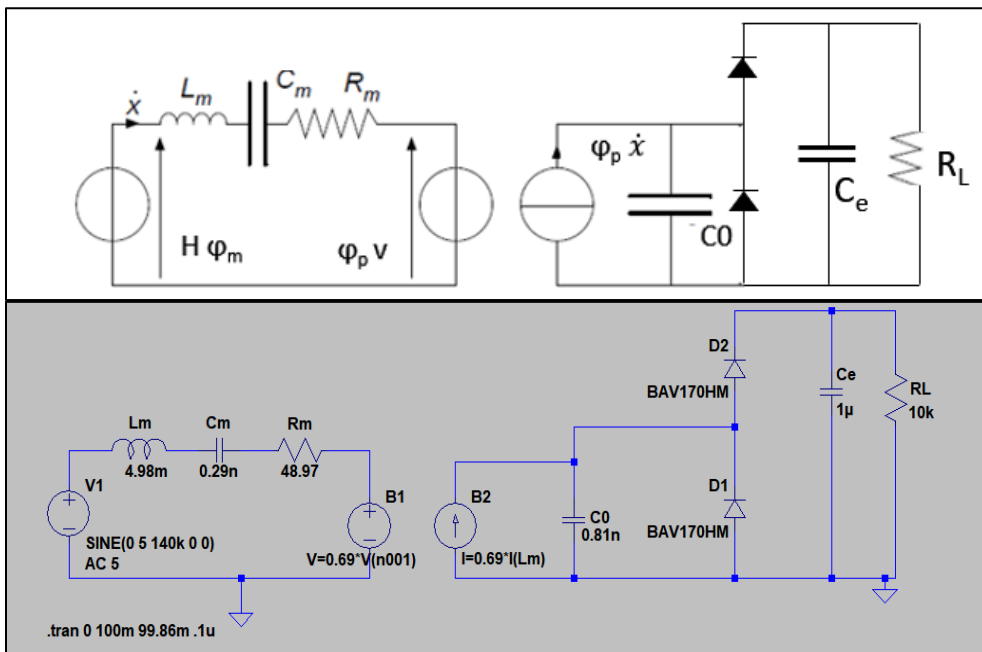


Figure 2.14 - Equivalent circuit model of a tri-layer transducer (MPM) in dynamic regime, for 0.1 T DC magnetic field, followed by a half bridge rectifier. Sample C.

The output response of the circuit with a full bridge rectifier is shown in Figure 2.16. It is possible to notice that the output DC voltage and DC power result a little bit lower than the AC RMS voltage, and power, that may be due to the diodes, and the accumulation over the capacitor.

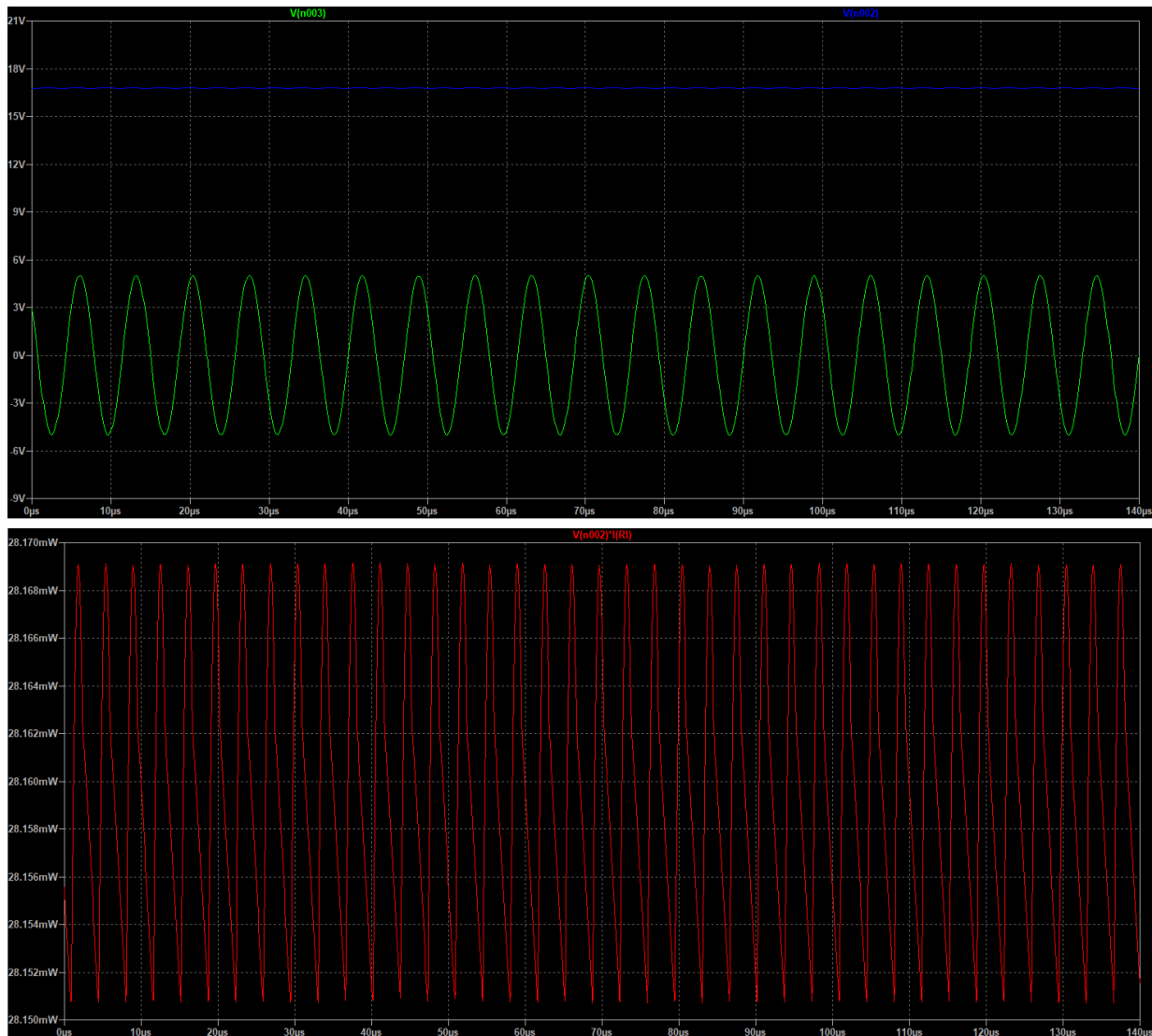


Figure 2.16 - ME transducer performances of a trilayer composite ($\varnothing 16$ mm, and $t 4$ mm). The green curve represents the Input voltage (V1). The blue curve is the output voltage over RL, and the red curve is the power over RL.

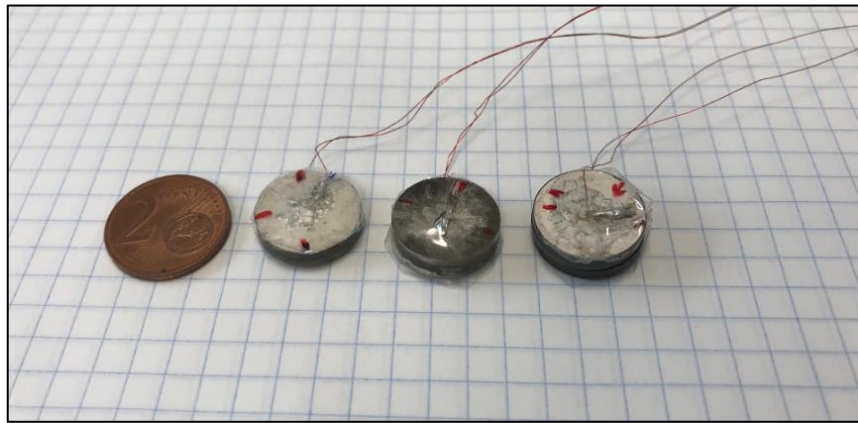
The SPICE simulation wanted to give an overview of the ideal behavior of the ME energy transducer, at specific conditions of the dynamic regime. The obtained theoretical values have been compared with the experimental ones, obtained during the characterization tests, in Paragraph 34.12.6.12.5.2.

2.3 MagnetoElectric Samples

As described in Chapter 2, Paragraph 4.4.3, the fabricated ME transducers have a disk shape with diameters of 10 mm, and 16 mm, and thickness from 2 mm to 5 mm, depending on the number of layers. They have been assembled with bicomponent epoxy glue, and the electrodes have been attached with conductive glue.

In total, 6 samples have been characterized. Four samples with the biggest diameter (16 mm) have been fabricated to compare the power density for different structures and volume ratio of the piezoelectric, and magnetostrictive materials.

In Table 2.4, the tested samples are reported, with their characteristics in terms of diameter ϕ , the thickness of the piezoelectric part t_p , the thickness of the magnetostrictive part t_m , total mass m , and the volume ratio, which is the ratio of the volume of the magnetostrictive part to the total volume of the transducer.



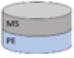
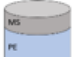

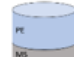
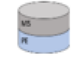
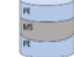
Sample	# layers	ϕ [mm]	t_p [mm]	t_m [mm]	m (g)	Volume ratio of M.
A) 	2 layers	16	1	1	3.7	0.5
B) 	2 layers	16	2	1	5.16	0.33
C) 	3 layers (M-P-M)	16	2	1 and 1	6.97	0.5
D) 	3 layers (P-M-P)	16	2 and 2	1	8.41	0.2
E) 	2 layers	10	1	1	2.53	0.5
F) 	3 layers	10	1 and 1	1	4.03	0.33

Table 2.4 – List the ME samples, and photo of the sample A, C, and D.

2.4 Characterization Method

The objective of this section is to detail the methodology followed to characterize the ME transducer in terms of output voltage, and output power. These characteristics mainly depend on the magnetic field which stimulates the ME sample, as:

- The DC magnetic field value
- The AC magnetic field magnitude, and frequency
- The orientation of the ME transducer respect to the magnetic field direction.

The temperature of the ME transducer also influences its characteristics. The main effect which has been observed is the variation of the resonant frequency at the change of the sample temperature. This phenomenon has not been studied in detail in the framework of this thesis. For the considered application, the ME transducer temperature is supposed to be very close to body temperature, which is relatively stable. In practice, wireless power transfer devices usually include a resonant frequency tracking system to solve the issues related to resonance frequency drift.

To examine in details the influence of the DC, and AC magnetic fields, two types of experiments were mainly conducted:

- Experiments varying the DC magnetic fields with a constant magnitude of the AC magnetic field.
- Experiments varying the AC magnetic fields with a constant DC magnetic field.

The experiments were performed with, and without a rectifier, to compare the reachable AC, and DC output powers. All these tests were first performed at the best orientation of the sample. A specific characterization test was conducted with the sample B (2 layers device, and $\varnothing = 16$ mm), to analyze its response at a different alignment inside the sample's holder.

Figure 2.17 shows a picture of the test bench developed for characterizing the 6 samples.

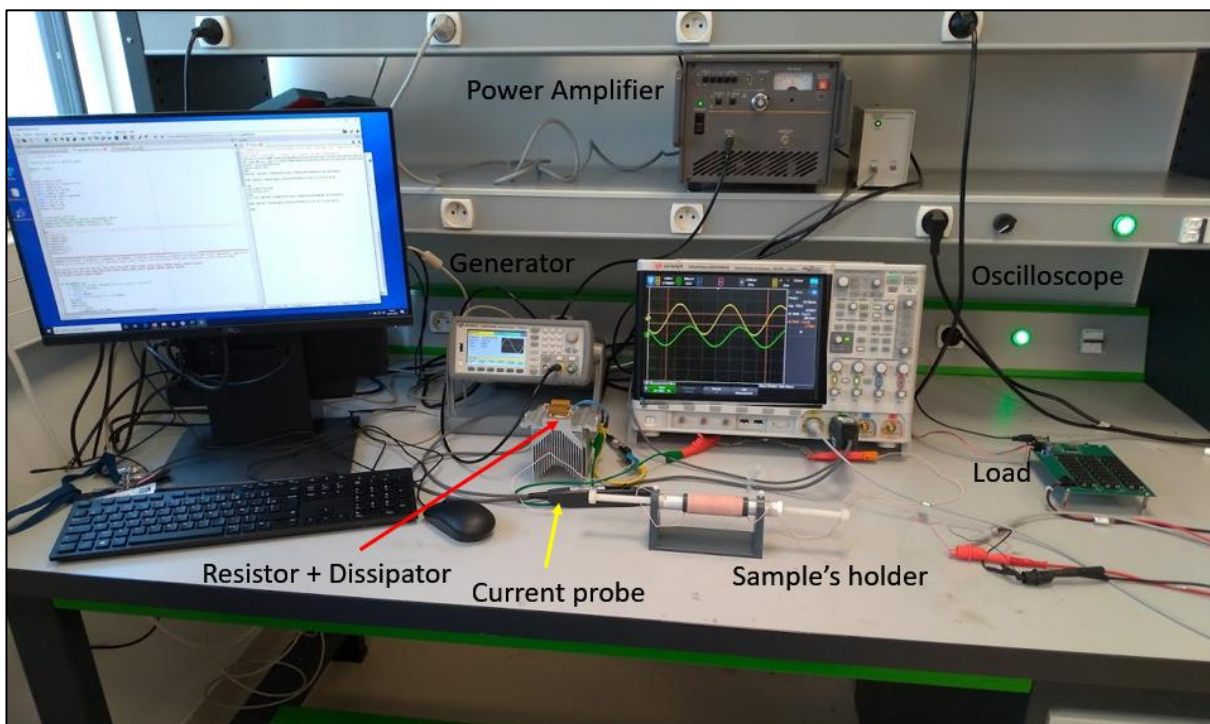


Figure 2.17 – Employed test bench for the characterization tests.

2.4.1 Experiments with different DC magnetic fields

For the first type of test, the sample was inserted at the center of the holder, and excited with a bias magnetic field, from the permanent magnets, and with an AC magnetic field, through the coil. To quantify the effect of a bias field on the ME transducer, the sample was excited with different DC fields. For this type of stimulation, the magnets were symmetrically moved in 6 different positions (d), obtaining 6 different bias fields:

$$B_{DC} = [0.1 \text{ T}, 0.058 \text{ T}, 0.036 \text{ T}, 0.023 \text{ T}, 0.016 \text{ T}, 0.012 \text{ T}]$$
$$d = [3 \text{ cm}, 4 \text{ cm}, 5 \text{ cm}, 6 \text{ cm}, 7 \text{ cm}, 8 \text{ cm}]$$

The value of B_{DC} has been measured through a Gaussmeter. Figure 2.3 shows the relationship between the distances of the magnets and the value of the magnetic field. The waveform generator was set with an input sinus wave of 10 Vpp, the maximum allowed for the used amplifier.

The range of working frequency was, firstly, searched manually, and in a second time controlled by the automated measurement code, on the base of the sample's resonance frequency:

$$\text{Sample A, B, C, and D (with } \varnothing = 16 \text{ mm) } \rightarrow \text{freq} = [100 \text{ to } 200] \text{ kHz}$$
$$\text{Samples E, and G (with } \varnothing = 10 \text{ mm) } \rightarrow \text{freq} = [150 \text{ to } 250] \text{ kHz.}$$

The current, injected in the coil, was maintained constant for all the measurements, to have the same value of current, and B_{AC} field at the resonance, such as:

$$\text{Sample A, B, C, and D (with } \varnothing = 16 \text{ mm) } \rightarrow i_{RMS} = (0.75 \pm 0.5) \text{ A}$$
$$\text{Samples E, and G (with } \varnothing = 10 \text{ mm) } \rightarrow i_{RMS} = (0.65 \pm 0.5) \text{ A.}$$

The ME voltage and ME power were measured over an output load, controlled by the automated measurement code. The spectra of ME voltage and power were collected for an interval of loads comprises between 10 Ω until 500 k Ω . The same procedure was repeated, connecting a full bridge rectifier, and a half-bridge rectifier to the sample, to determine the reachable DC output power. In this case, the rectifiers were connected to the electronic card of loads, and the ME voltage was measured over the card.

2.4.2 Experiments with different AC magnetic fields

For the second type of test, the sample was equally inserted at the center of the holder, and excited with a DC magnetic field, from the permanent magnets, and with an AC magnetic field, through the coil.

Maintaining fixed the DC magnetic field, the samples were excited with different AC magnetic fields, to study the ME output power at the resonance frequencies. For this study, the samples were connected to the respective optimal loads, defined from the experiment described in Paragraph 2.4.1. In this case, the measurements were performed manually, without the automated measurement code. The resonance frequency was searched manually, and the current in the coil was also manually adjusted through the amplitude of the sinusoidal signal of the waveform generator. The measurements were repeated for different DC magnetic fields:

$$B_{DC} = [0.1 \text{ T}, 0.058 \text{ T}, 0.036 \text{ T}, 0.023 \text{ T}, 0.016 \text{ T}, 0.012 \text{ T}].$$

The same procedure was repeated, connecting a full bridge rectifier, and a half-bridge rectifier to the sample, to determine the reachable DC output power.

2.4.3 Experiments with a different sample's orientation

As described in the paragraph about the magnetostriction phenomenon (Chapter 2, Paragraph 2.3), the measured strain on a magnetostrictive material is linked to its magnetocrystalline anisotropy. Due to this microscopic characteristic, the sample can generate different ME responses, depending on its orientations respectively with the magnetic field lines. In this case, the ME composite was turned in-plane inside the holder. The experiments were performed at the best, and worst orientations of the device.

The sample was tested maintaining fixed the magnitude of the AC magnetic field at the resonance, and varying 6 DC magnetic fields, and with the following ranges of working frequency, and output load:

$B_{DC} = [0.1 \text{ T}, 0.058 \text{ T}, 0.036 \text{ T}, 0.023 \text{ T}, 0.016 \text{ T}, 0.012 \text{ T}]$

Freq = [110 to 180] kHz

Load = [10 Ω to 500 k Ω]

The sample's holder is reported in Figure 2.18.



Figure 2.18- Top view of the sample's holder with the ME composite.

2.5 Results, and Discussion

The objective of this section is to present and to comment the results of the characterization tests, whose procedure has been presented in the previous subsections. The ME transducer has been characterized in terms of output voltage, and output power in three main sets of experiments:

- Experiments varying the DC magnetic fields with a constant magnitude of the AC magnetic field
- Experiments varying the AC magnetic fields with a constant DC magnetic field.
- Experiment varying the orientation of the ME transducer respect to the magnetic field direction.

For each group of tests, the results of one sample are considered as example. The data of the other ME samples are reported in Annex III.

2.5.1 Experiments with different DC magnetic fields

For the first type of measurement, the sample was excited with different DC magnetic fields, from the permanent magnets, and with a constant AC magnetic field, through the coil. For this type of stimulation, the magnets were symmetrically moved in 6 different positions, obtaining 6 different bias fields:

$$B_{DC} = [0.1 \text{ T}, 0.058 \text{ T}, 0.036 \text{ T}, 0.023 \text{ T}, 0.016 \text{ T}, 0.012 \text{ T}]$$

In this case, the responses of sample C (diameter of 16 mm, and tri-layer M-P-M) are reported here, to compare the experimental results with the theoretical ones, previously discussed in Paragraph 2.2.2. The ME transducer was stimulated with a 0.1 T DC magnetic field and a 0.8 mT AC magnetic field.

In Figure 2.19, and Figure 2.20 the ME RMS voltage, and power are shown. The maximum ME RMS voltage results 35.7 V for a load of 500 k Ω , the highest measured value, and the closest to the open-circuit configuration. The maximum ME RMS power results 0.035 W, for 10 k Ω load resistance, before calculated as the optimal load.

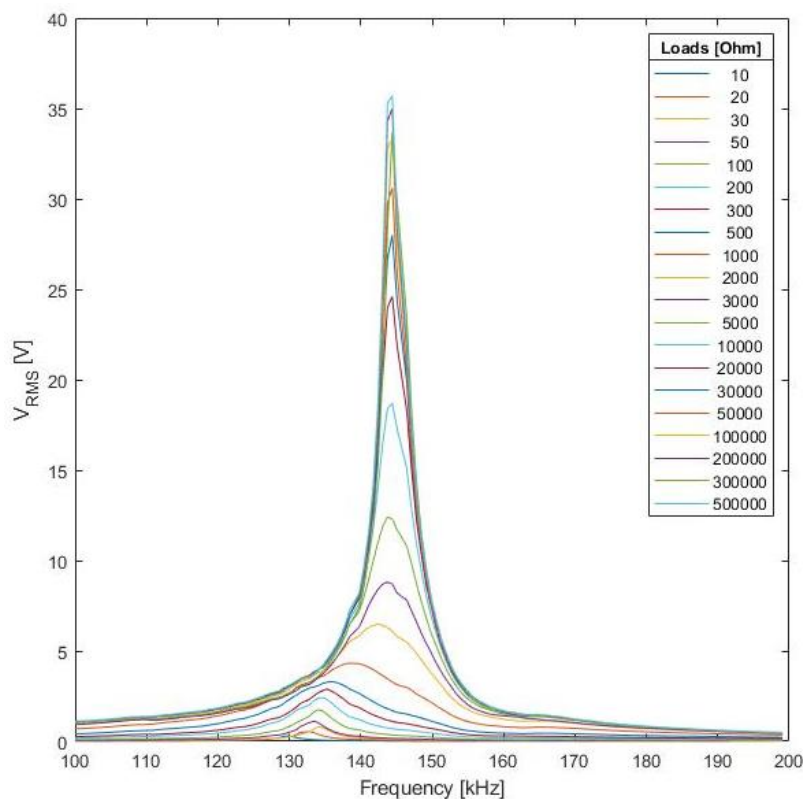


Figure 2.19 – ME RMS voltage of the ME transducer (diameter of 16 mm, and tri-layer M-P-M) measured over different loads, in a frequency spectrum between 100 kHz, and 200 kHz. Sample stimulation with 0.1 T of DC magnetic field, and 0.8 mT of AC magnetic field.

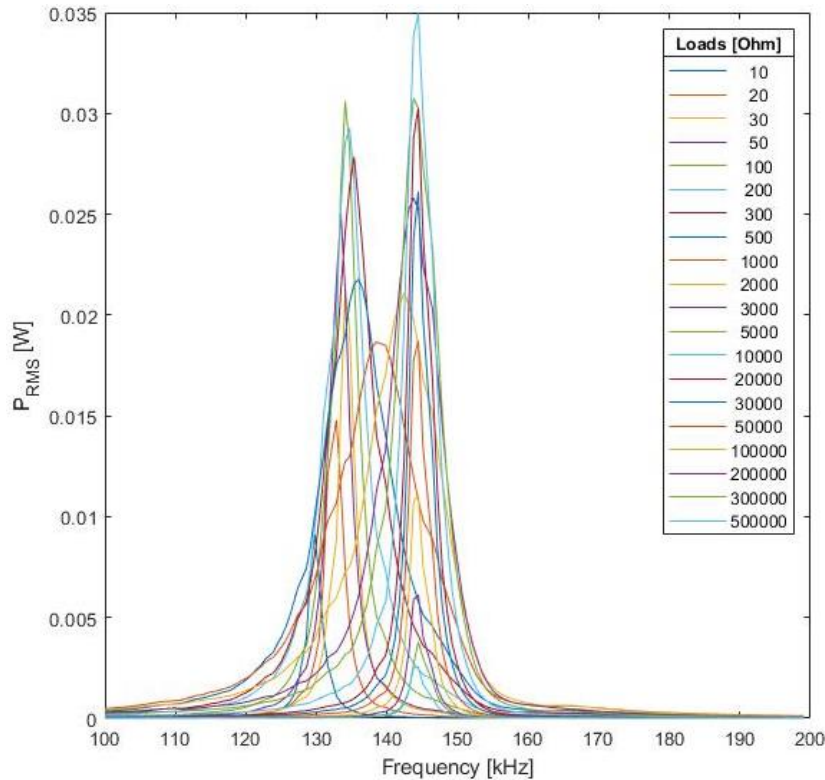


Figure 2.20 - ME RMS power of the ME transducer (diameter of 16 mm, and tri-layer M-P-M) measured over different loads, in a frequency spectrum between 100 kHz, and 200 kHz. Sample stimulation with 0.1 T of DC magnetic field, and 0.8 mT of AC magnetic field.

At this point it results possible to compare the experimental values with the theoretical ones, before discussed in Paragraphs 2.2.2, and 2.2.3. Taking as example the ME response for a load of 10 k Ω , the maximum value of the output RMS voltage is around 18 V, a smaller value compared to the semi-theoretical model using the experimental transfer function α_{ME} (difference of 13 %), and the theoretical model implemented using MATLAB and LTSpice model (difference of 17 %). This may be due to the real magnetoelastic, and electromechanical losses of the system.

In Figure 2.20, two main peaks of power are shown, associated with the resonance frequency of different loads. As described in the theoretical model of Paragraph 2.2, the transducer resonance frequency, obtained from the equivalent circuit, is comprised between the short-circuit, and the open-circuit resonance frequencies. The variation of the system's resonance frequency (including the load) is inversely proportional to the system's global quality factor, which is inversely dependent on the load resistance. So, at higher loads, the deviation of the resonance frequency from the short-circuit resonance frequency is expected bigger.

The theoretical model (Paragraph 2.2.3) was used to estimate the maximum output power over the spectrum of frequency. Starting from the parameters of Table 2.3, the following parameters were slightly modified to fit better with the measurements, k_{ee}^2 (0.14 instead of 0.15), φ_p (0.68 instead of 0.69), and Q (187 instead of 173). The value of φ_m , which represents the magneto-elastic coupling, was also adjusted to fit with the measurements.

As shown in Figure 2.21, the maximum power given by the model using these parameters lightly overestimates the real performances of the transducer. The model gives two peaks with the same maximum power, whereas in practice, the second peak associated with the bigger load (10 k Ω), achieves a higher value of power than the first one (100 Ω). The power difference between the peaks is 4 mW, so it cannot be considered negligible. The explanation could be associated with the non-linear behaviour of the magnetostrictive material under the magnetic field, but it opens a good point of reflection for future investigations.

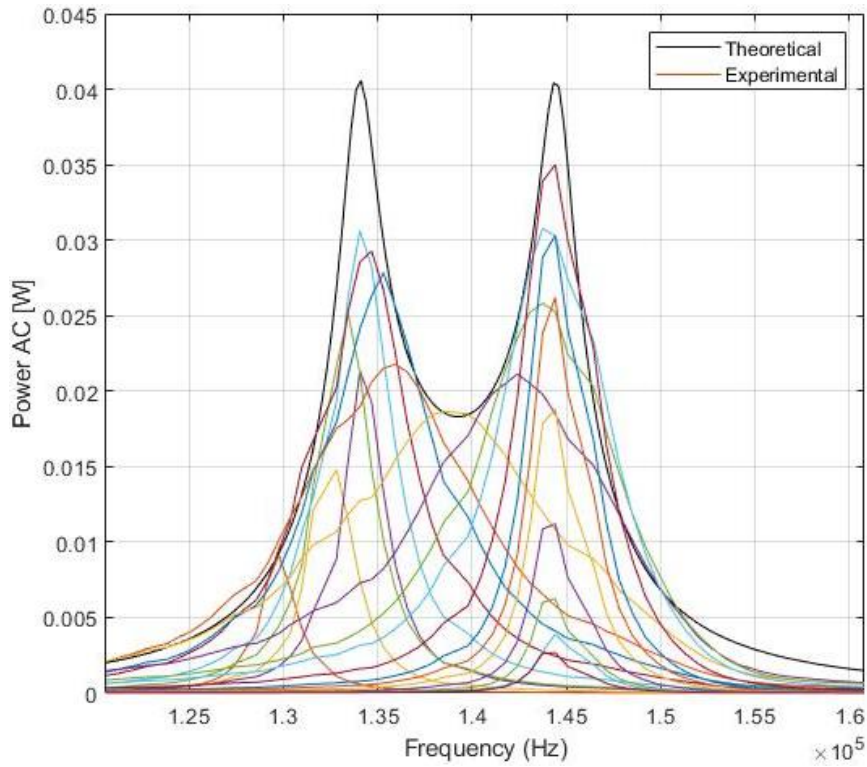


Figure 2.21 - ME RMS power of the ME transducer (diameter of 16 mm, and tri-layer M-P-M) measured over different loads, in a frequency spectrum between 100 kHz, and 200 kHz. Sample stimulation with 0.1 T of DC magnetic field, and 0.8 mT of AC magnetic field. The black curve represents the maximum RMS power from the theoretical model.

The same approach was adopted for a lower DC magnetic field. The same sample was stimulated with an external DC magnetic field of 0.058 T, Figure 2.21, and Figure 2.22.

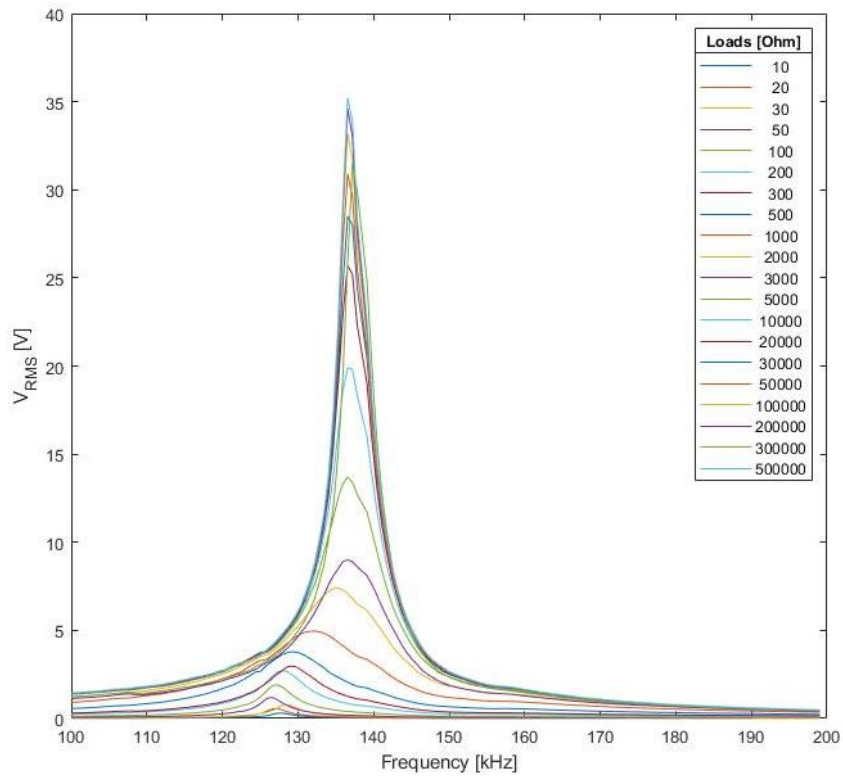


Figure 2.22 - ME RMS power of the ME transducer (diameter of 16 mm, and tri-layer M-P-M) measured over different loads, in a frequency spectrum between 100 kHz, and 200 kHz. Sample stimulation with 0.058 T of DC magnetic field, and 0.8 mT of AC magnetic field.

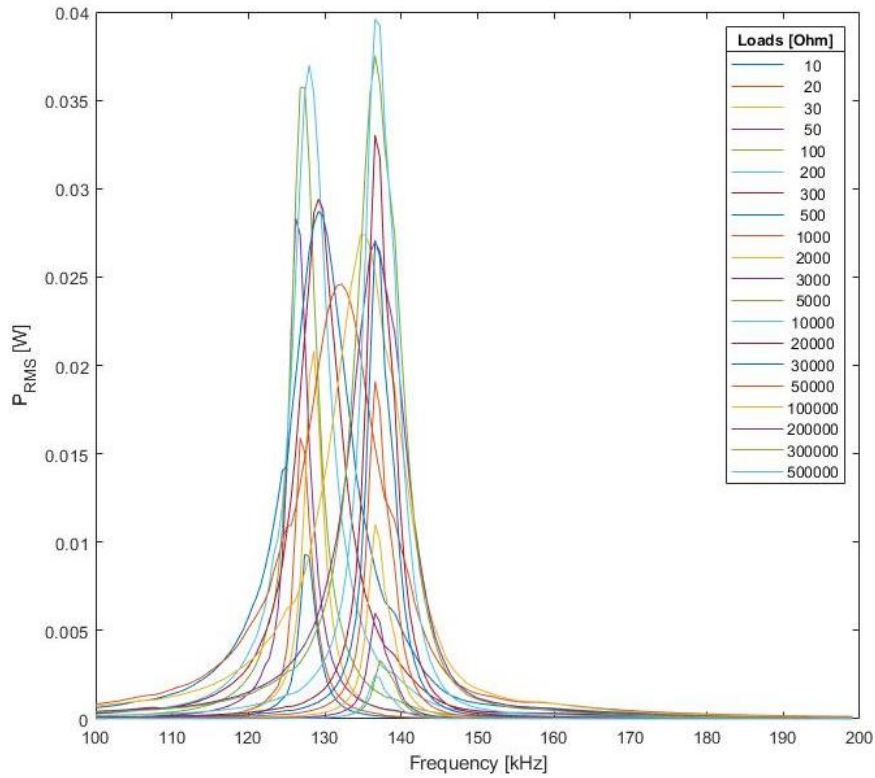


Figure 2.22 - ME RMS power of the ME transducer (diameter of 16 mm, and tri-layer M-P-M) measured over different loads, in a frequency spectrum between 100 kHz, and 200 kHz. Sample stimulation with 0.058 T of DC magnetic field, and 0.8 mT of AC magnetic field.

In this case the maximum value of RMS voltage, and power are slightly higher (35.2 V and 40 mW), and the resonance frequency is left-shifted. In terms of power, there is an increase of 12%, which reflects the dependence of the dynamic magneto-elastic effect with the DC magnetic field.

To complete this analysis, the maximum output power characteristics of sample C are plotted in Figure 2.23 for 6 different values of the DC magnetic field as a function of the load resistance (for each value of the load, the

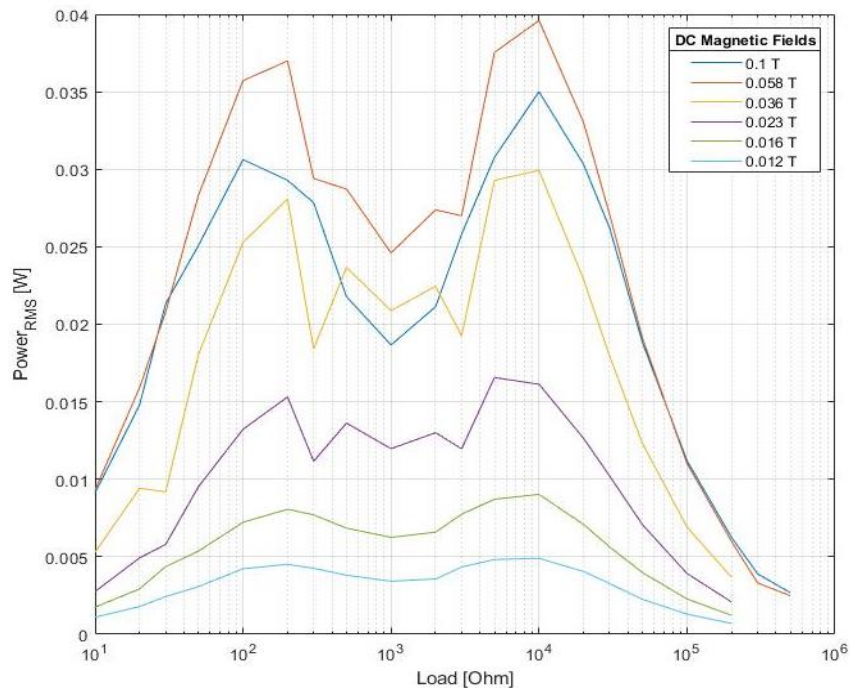


Figure 2.23 - ME RMS power of the ME transducer (diameter of 16 mm, and tri-layer M-P-M) measured over different loads stimulation with different DC magnetic field, and 0.8 mT of AC magnetic field.

maximum value of the RMS power was taken). According to these results, the best power performance was obtained for the 0.058 T DC magnetic field.

To summarize the ME behaviors at the varying of the loads, the maximum power is reported for different ME transducers. The four samples (A, B, C, and D) have the same diameter, but different amount of magnetostrictive material, referring to Table 2.4. In Figure 2.24 and Figure 2.25, the samples were excited with 0.058 T of DC magnetic fields, which leads to the best performances in each case, and 0.8 mT of the AC magnetic field.

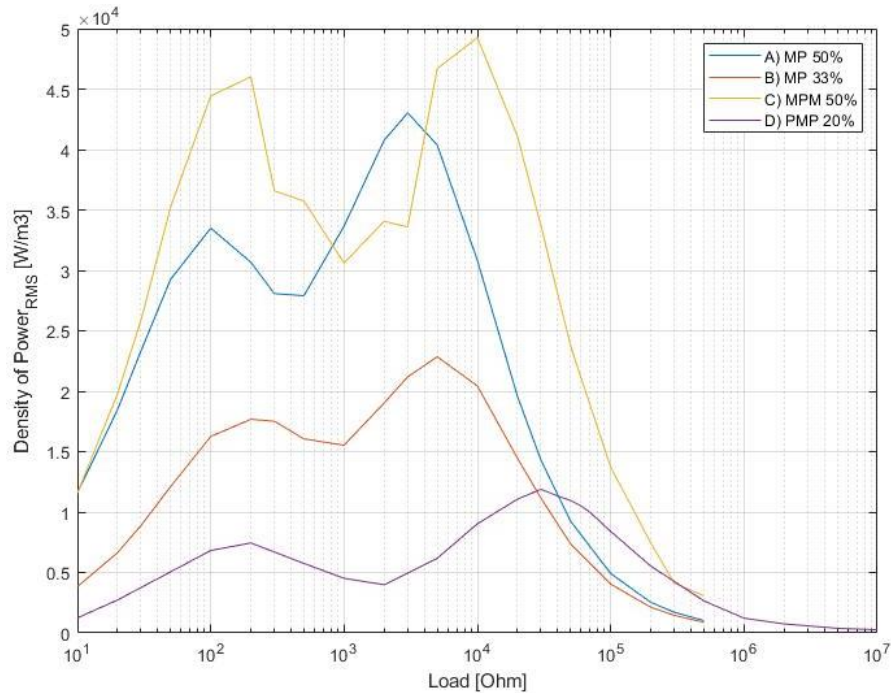


Figure 2.25 - ME density of power at varying of the magnetostrictive volume ratio, for the excitation fields of 0.058 T DC magnetic field, and 0.8 mT AC magnetic field.

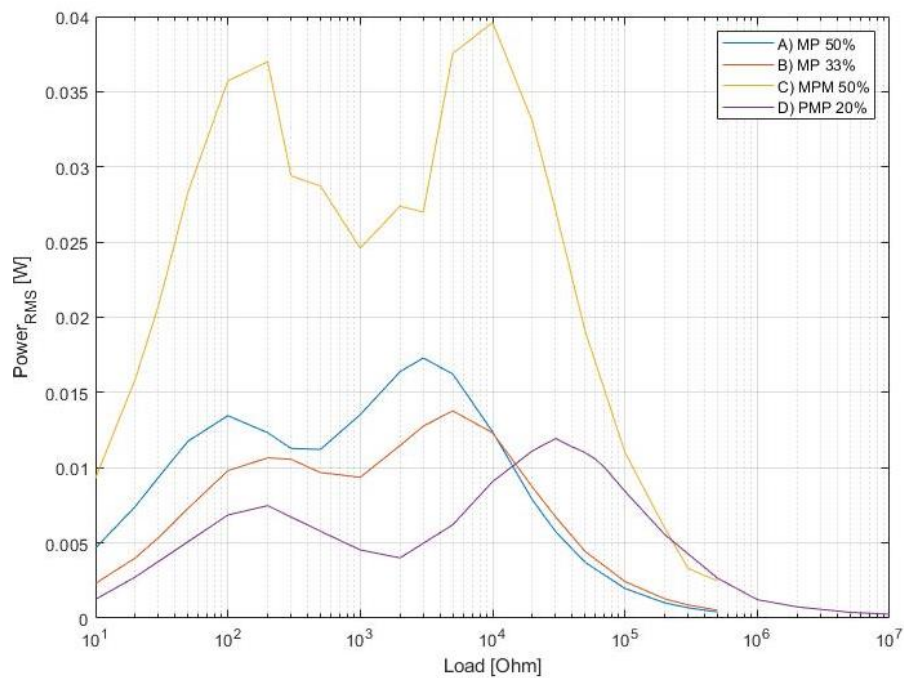


Figure 2.24 – ME RMS power at varying of the magnetostrictive volume ratio, for the excitation fields of 0.058 T DC magnetic field, and 0.8 mT AC magnetic field.

From the point of view of the magnetostrictive volume ratio, it is interesting to notice the best performances in terms of power density are obtained with the samples composed of 50% magnetostrictive materials. Indeed, the samples with 33% and 20% magnetostrictive material exhibit much lower power density. The optimal volume fraction leading to the maximum power density is presumably not attained amongst the tested samples. Indeed, increasing the volume ratio of magneto-electric material would simultaneously increase the input mechanical power, decrease the piezo-elastic electromechanical coupling, and reduce the mechanical quality factor according to the trends observed in Table 2.3. Consequently, the problem of power density optimization, which is the way to miniaturize ME transducers, is relatively complex.

Table 2.5 summarizes the ME output responses of the tested samples. Several physical quantities have been analyzed during the characterization tests. In this case, a focus on the relationship between the percentage of magnetostrictive material, the resonance frequencies, the optimal loads, the maximum value of output ME power, and the maximum value of output ME power density are reported. As shown in the table, and previously described, the resonance frequency is strongly related to the diameter dimension of the sample. Furthermore, the maximum ME power is obtained for a bigger sample (sample C), and a smaller sample with a high percentage of the magnetostrictive material.

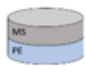
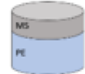
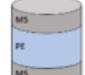
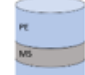
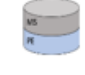
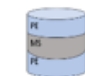
Sample	Dimensions	Percentage of Magnetostrictive Material	Freq. resonance	Optimal Load	Max power RMS	Power density
A) 	2 layers Ø 16 mm t 2 mm	50%	130 kHz	100 Ω	13.46 mW	0.034 mW/mm ³
			140 kHz	3000 Ω	17.3 mW	0.043 mW/mm ³
B) 	2 layers Ø 16 mm t 3 mm	33%	132 kHz	200 Ω	10.66 mW	0.018 mW/mm ³
			141 kHz	5000 Ω	13.78 mW	0.023 mW/mm ³
C) 	3 layers MPM Ø 16 mm t 4 mm	50%	131 kHz	200 Ω	37 mW	0.046 mW/mm ³
			139 kHz	10 kΩ	40 mW	0.049 mW/mm ³
D) 	3 layers PMP Ø 16 mm t 5 mm	20%	129 kHz	200 Ω	7.5 mW	0.008 mW/mm ³
			144 kHz	30 kΩ	12 mW	0.012 mW/mm ³
E) 	2 layers Ø 10 mm t 2 mm	50%	195 kHz	300 Ω	1.6 mW	0.01 mW/mm ³
			197 kHz	2000 Ω	3.8 mW	0.024 mW/mm ³
F) 	3 layers Ø 10 mm t 3 mm	33%	191 kHz	200 Ω	11.6 mW	0.05 mW/mm ³
			198 kHz	10 kΩ	0.18 mW	0.0008 mW/mm ³

Table 2.5 – Summary of the ME output responses for the tested samples at the 0.058 T of DC magnetic field. The biggest samples (A, B, C, and D) have been stimulated with a constant AC magnetic field of 0.8 mT, and the smallest ones (E, and F) with an AC field of 0.7 mT.

In this case, an AC output voltage has been measured over the ME sample. In the following test, an AC/DC converter has been connected to the transducer to get a DC output voltage.

2.5.2 Experiments with different DC magnetic fields with Rectifier

The same modus operandi was used, connecting a full-bridge, and half bridge rectifiers to the magnetoelectric transducers. Figure 2.26 reports the scheme of the equivalent circuit model of a ME energy transducer, connected to the analyzed AC/DC rectifiers.

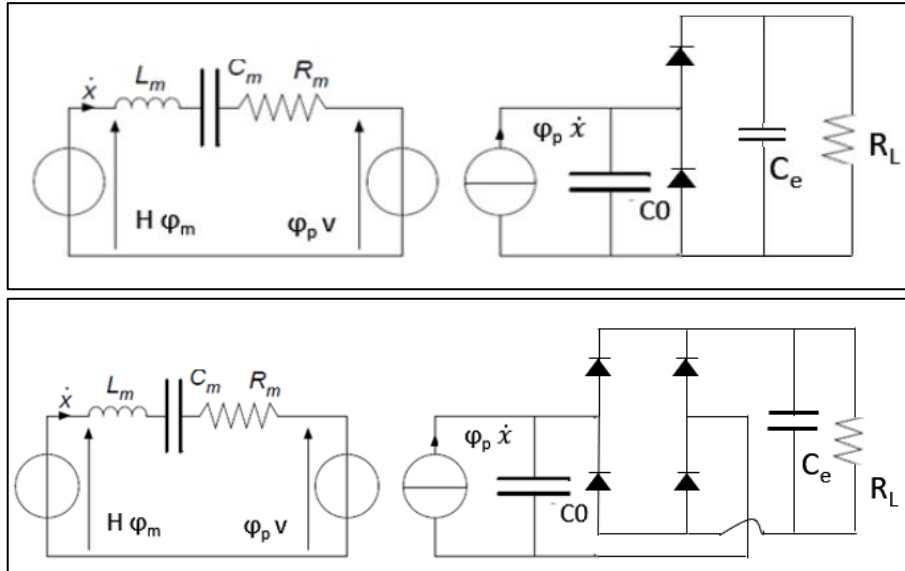


Figure 2.26 – Equivalent circuit model of ME transducer with half-bridge rectifier (in the upper scheme), with full-bridge rectifier (in the lower scheme).

The samples were tested with different DC magnetic fields, varying loads, and over a spectrum of frequency between 100 kHz, and 200 kHz. In the presented case, the sample C (diameter 16 mm, and tri-layers M-P-M) is considered. In the two figures, Figure 2.27 and Figure 2.28, there are reported the best configurations for the ME transducer, with excitation magnetic fields of 0.058 T DC field, and 0.8 mT RMS AC field.

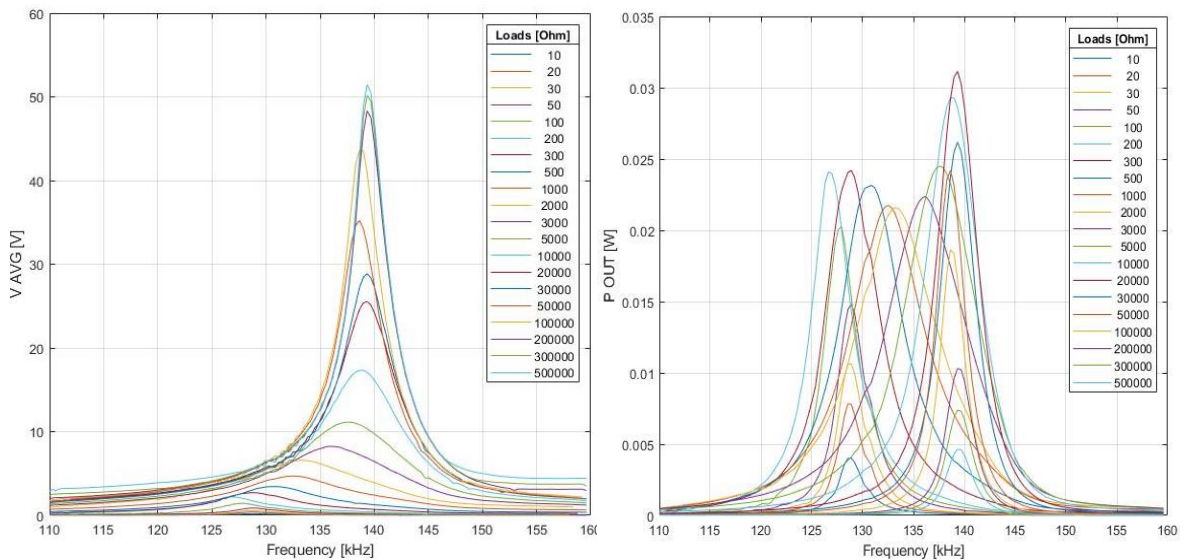


Figure 2.27 – ME DC output voltage, and power are represented for the ME transducer (diameter of 16 mm, and tri-layer M-P-M) connected to a full bridge rectifier. The output measured over different loads, in a frequency spectrum between 100 kHz, and 200 kHz. Sample stimulation with 0.058 T of DC, and 0.8 mT of AC magnetic field.

In terms of power, the performances of the ME transducers are quite similar in both cases. In terms of output voltage, the half-bridge output is larger than the full-bridge one, due to the voltage doubling effect of the half-bridge configuration. Since the transducer voltage is higher and the number of diodes is lower, the power lost in the diodes is lower in the half-bridge configuration. The resonance frequency is not expected to be significantly changed with or without rectifier, in half-bridge or full-bridge configuration. However, the half-bridge configuration presents an unexpected left shift of the frequencies, which may be due to the sample heating during the measurements. In terms of output power, the achieved values are a bit lower than the without-rectifier case (34 mW compared to 40 mW). This power drop is due to the diodes. It is interesting to notice that compared to the AC case, the first peak is relatively small compared to the second one. Actually, the first peak corresponds to a much lower voltage than the second one. Therefore, the power loss due to the voltage drop across the diodes is more visible in this case. As explained by Brenes et al. [6], the half-bridge rectifier configuration can reach the same power of the full-bridge case, but with an optimal resistance 4 times larger. In our case, the peak of power is obtained for 20 k Ω and 100 k Ω load resistance for the full-bridge and half-bridge rectifiers respectively. So, the observed trend is consistent with the theory.

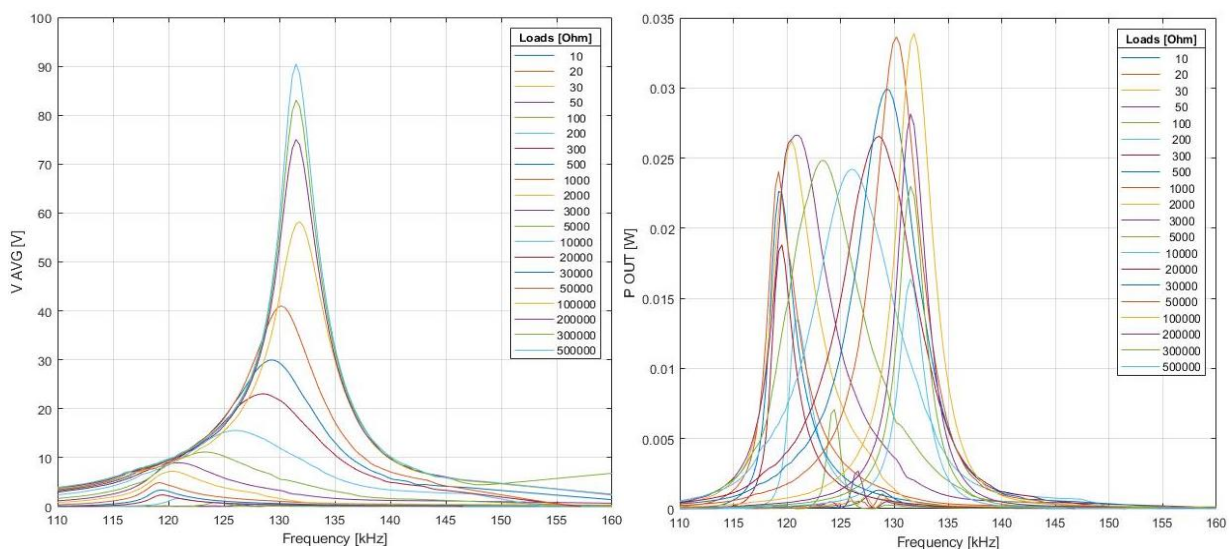


Figure 2.28 - ME DC output voltage, and power are represented for the ME transducer (diameter of 16 mm, and tri-layer M-P-M) connected to an half bridge rectifier. The output measured over different loads, in a frequency spectrum between 100 kHz, and 200 kHz. Sample stimulation with 0.058 T of DC, and 0.8 mT of AC magnetic field.

Using the theoretical model, presented in paragraph 4.3.4 of Chapter 2 and paragraph 2.2.3 of Chapter 3, the theoretical power was compared to the experimental data.

In order to follow the previous consideration, sample C was characterized by a full-bridge rectifier under a DC magnetic field of 0.1 T, and an AC magnetic field of 0.8 mT. The output behavior is reported in Figure 2.29. In the right graph, the theoretical power has been compared with the experimental values. The black curve represents the maximum power given by the formula (2.VII). In the left graph, the experimental powers have been normalized with the maximum theoretical power, over the spectrum of frequency.

As already mentioned in the case of the single load resistance, the model also lightly overestimates the real performances of the transducer with the rectifier. The theoretical model was estimated, starting from the circuit's parameters of Table 2.3, with a small variation of the k_{ee}^2 (0.14 instead of 0.15), φ_p (0.68 instead of 0.69), and Q (187 instead of 173). The excitation input (H , φ_m) was adapted to fit the real curves, as explained in Paragraph 2.2.2. For example, for a load of 10k Ω , the output power calculated through the SPICE simulation is estimated at 28 mW and for the experimental value, reported in Figure 2.29, it results 22.5 mW.

Furthermore, as the diodes' losses are not taken into account in this model, the two peaks of maximum power are identical. On the contrary, in the experimental measurements, the second peak is much higher than the first one. This behavior is accentuated in the normalized power in Figure 2.29. However, regarding the output power at the second peak, the experimental estimation is close to the theoretical value, with a difference of 7%.

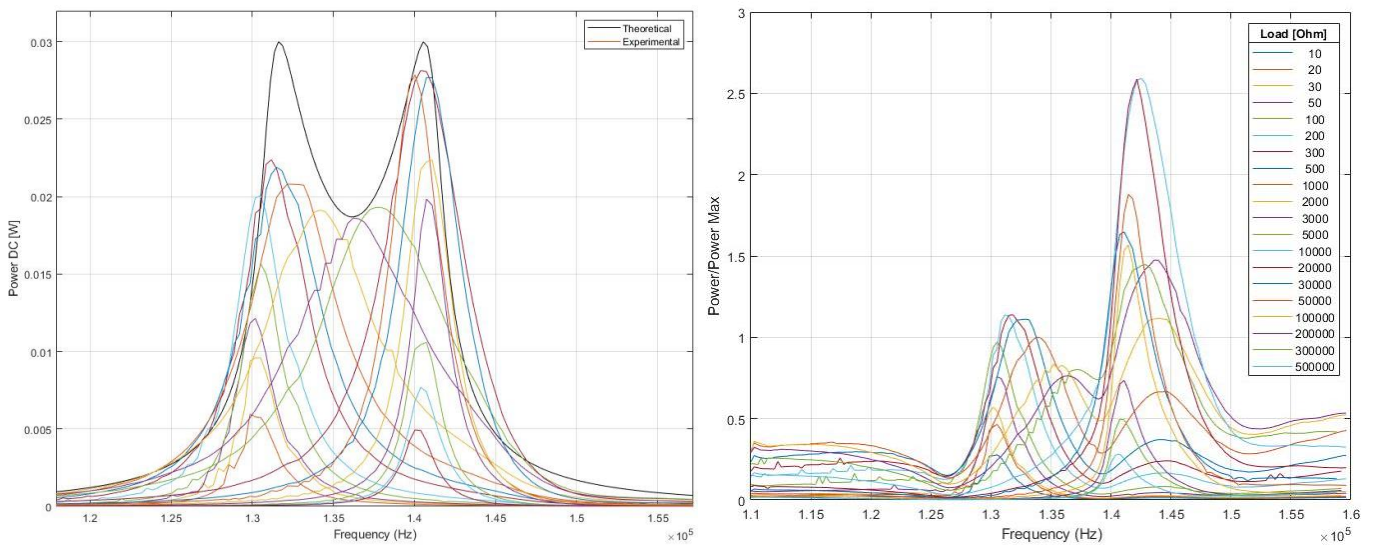


Figure 2.29 - ME output power is represented for the ME transducer (diameter of 16 mm, and tri-layer M-P-M) connected to full-bridge rectifier, and measured over different loads, in a frequency spectrum between 100 kHz, and 200 kHz. Sample stimulation with 0.1 T of DC magnetic field, and 0.8 mT of AC magnetic field. The black curve represents the maximum power from the theoretical model.

Overall, the theoretical model can describe the power response of the ME transducer in an acceptable way, in terms of “frequency bandwidth” but with some imprecisions in terms of power. Further developments are still necessary, to integrate all the non-linearities of the ME transducer in the model, and in specific the influence of the temperature and Eddy’s currents.

2.5.3 Experiments with different AC magnetic fields

For the second type of test, the sample was also inserted at the center of the holder, and excited with a bias magnetic field, generated by the permanent magnets, and with an AC magnetic field, generated by the coil surrounding the sample. This set of experiments aims to determine the influence of the magnitude, and frequency of the external AC magnetic field over the ME transducer.

So, maintaining fixed the DC magnetic field, the samples were excited with different AC magnetic fields, to study the ME output power at the resonance frequency.

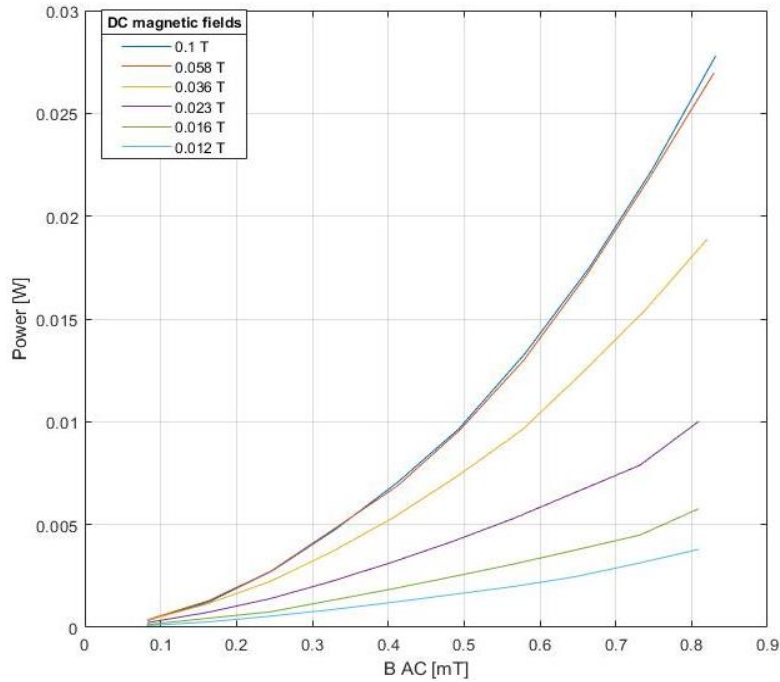


Figure 2.30 – ME RMS power is represented for the ME transducer (diameter of 16 mm, and tri-layer M-P-M) measured over 10 k Ω -load, and stimulated with different DC, and AC magnetic fields.

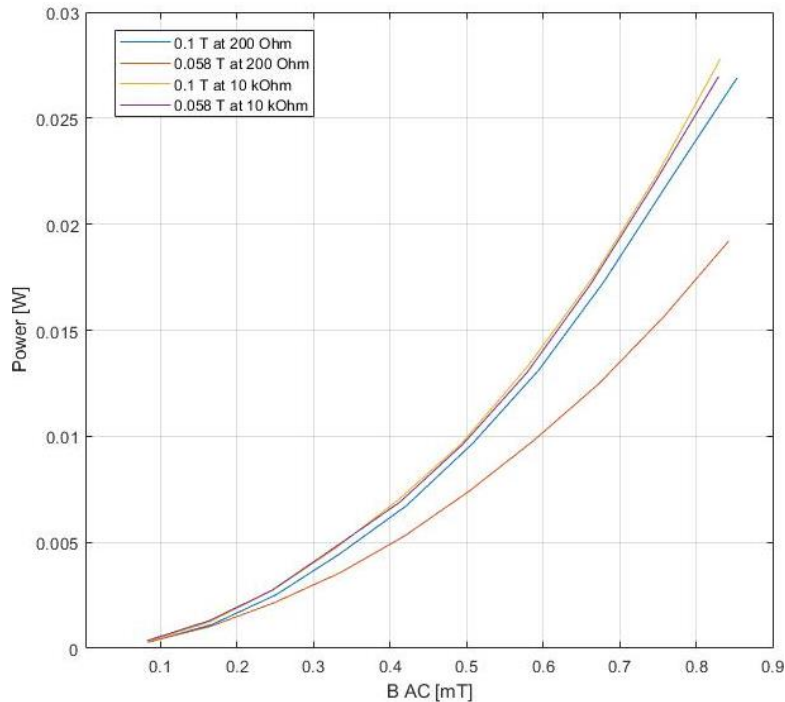


Figure 2.31 - ME RMS power is represented for the ME transducer (diameter of 16 mm, and tri-layer M-P-M) measured over 200 Ω , and 10 k Ω loads, and stimulated with different DC, and AC magnetic fields.

The samples were connected to the respective optimal loads, defined from the previous experiment, Paragraph 2.4.1. In this case, the samplings were performed manually, so without the automated measurement code. The resonance frequency was searched manually for each measurement and the current in the coil was adjusted to get the desired value of the AC magnetic field.

In this case, sample C was considered, measuring the output over the corresponding loads of the two main peaks, 200 Ω , and 10 k Ω . In Figure 2.30, and Figure 2.31 the output power is reported at varying the DC, and AC magnetic fields.

The output power increases at higher DC and AC magnetic fields with a quadratic dependency. As said in previous cases, the reached power at 0.1 T, and 0.058 T DC fields are very close for the 10 k Ω , for 200 Ω the difference is more accentuated. Furthermore, the output power for 10 k Ω is close to the power for 200 Ω , at 0.1T DC field, for the smaller field the asymmetry between the peaks increases.

In Figure 2.32, the behavior of the maximum power with, and without rectifier is represented, and the trend is similar.

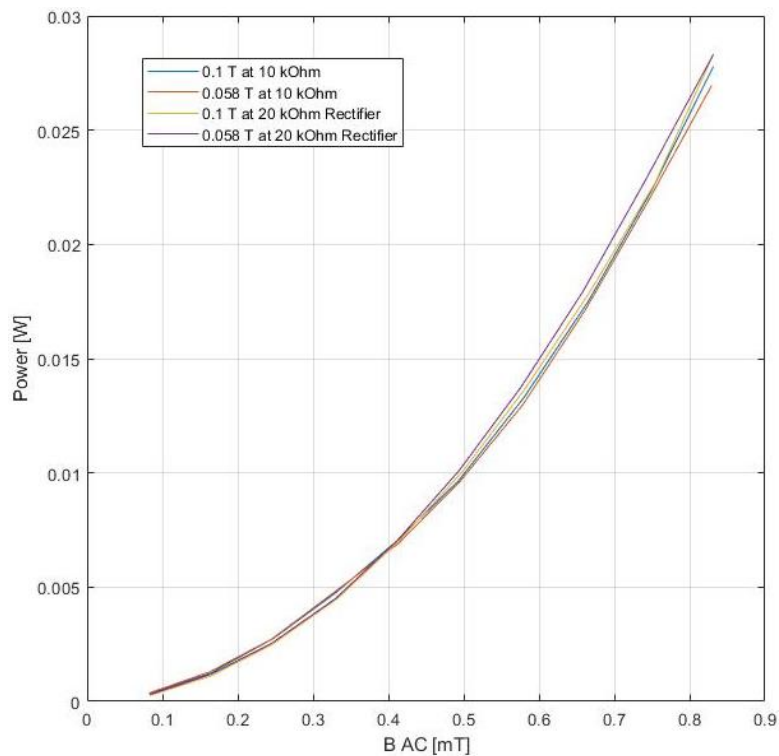


Figure 2.32 - ME output power of the ME transducer (diameter of 16 mm, and tri-layer M-P-M) measured over 10 k Ω , and 20 k Ω loads, with, and without rectifier, stimulated with different DC, and AC magnetic fields.

In conclusion, the output responses of the ME transducers are strongly dependant on the DC and AC components of the excitation magnetic field. The applied DC magnetic field acts on the sample by setting the operating point on the static magnetostriction characteristic of the sample. The output ME power increases with the increase of the magnetic field until the optimal point is reached. Then, the ME power starts decreasing with the beginning of the magnetic saturation of the magnetostrictive material. According to the presented results, the optimal magnetic field is close to 0.058 T. The AC magnetic field, superposed to the continuous field and with a lower magnitude, induces the sample to dynamically deform its structure from the static operating point. The quadratic dependence of the output power with the AC magnetic field can be explained by the theoretical model. Indeed, according to this model, the power is proportional to the magnetostrictive force squared, and this force is proportional to the AC magnetic field magnitude. The maximum reached output RMS power is around 40 mW, a similar value to the configuration with the rectifier. This value has been achieved at 0.058 T of DC field for all configurations.

Once the optimal magnitude and frequency of external magnetic fields have been fixed, the behavior of the ME sample has been analyzed changing its orientation to the external fields, as presented in the next section.

2.5.4 Experiments with different sample's orientation

The third and last experiment of the characterization tests consisted of studying the ME transducer's response to different orientations of the sample. As described in Chapter 2, Paragraph 4.2, the measured strain on a magnetostrictive material is linked to its magnetocrystalline anisotropy. Due to this microscopic characteristic, the magnetoelectric response of the sample depends on its orientation respect to the magnetic field direction.

The ME samples were turned in-plane inside the holder, to find the best and worst orientations of the device, corresponding respectively to the highest and lowest magnetoelectric response. A picture of the setup with the ME sample in two different orientations (worst and best) is shown in Figure 2.33.

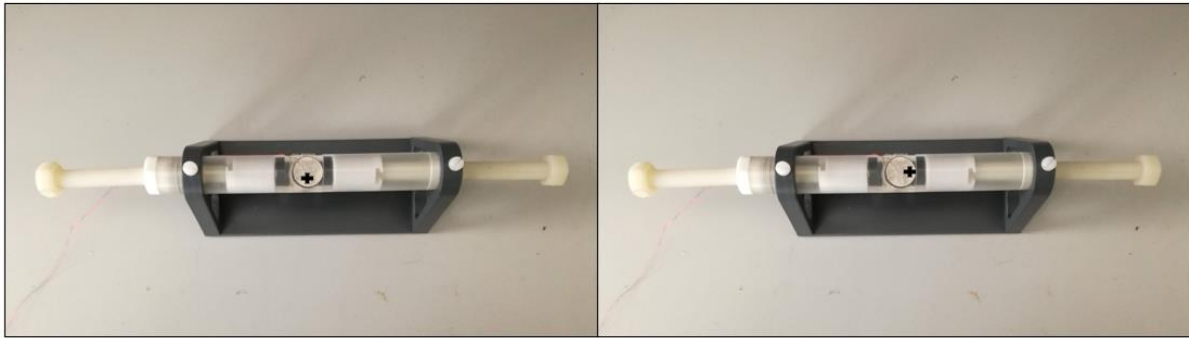


Figure 2.33 – Photo of the set up in the best, and worst orientation, using the sign over the piezoelectric face as a reference.

Once the two orientations were individuated, the sample was characterized with the automated test bench at a constant AC magnetic field, of 1.1 mT, and for different DC magnetic fields, and loads.

In Figure 2.34, the RMS power of sample A (16 mm diameter, 2 layers) is reported for the two orientations. In the worst orientation, the ME transducer can create an RMS output power slightly lower than the case of best position, with around 35% difference. Furthermore, comparing the peaks of maximum power for the same DC fields, it is possible to notice they are shifted to the load resistance.

In conclusion, in the worst orientation, the ME transducer can provide enough power, smaller than the one in the best alignment, but still efficient. Furthermore, the resonance frequency (not represented here) and the optimal load resistance are affected by the magnetic field orientations.

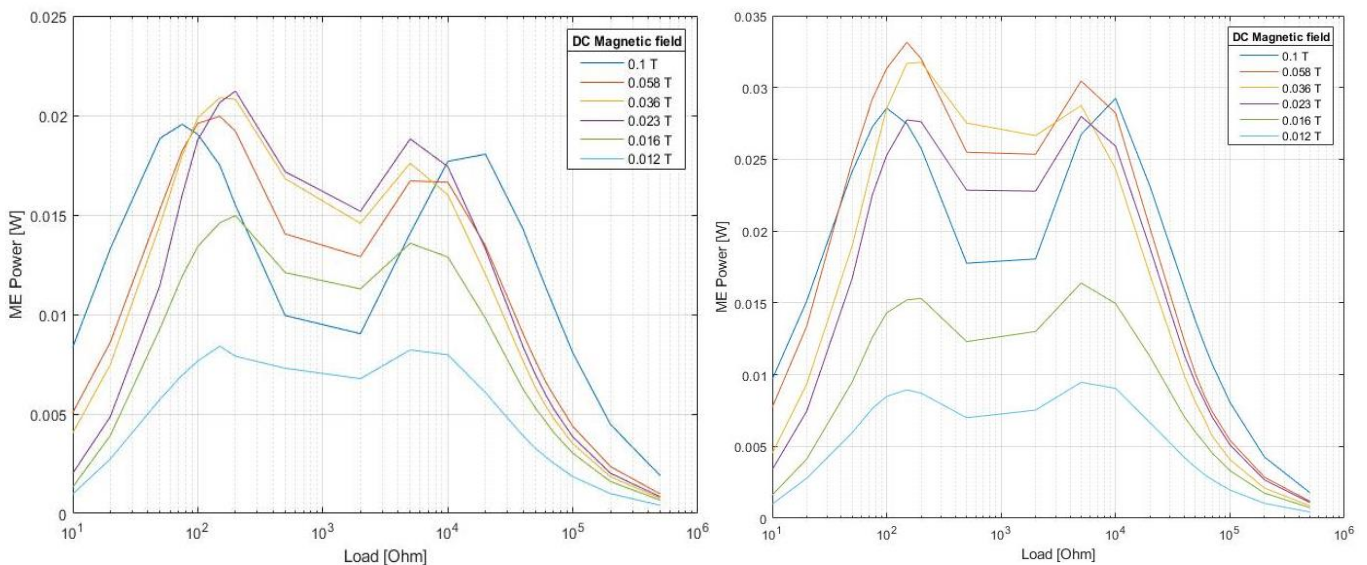


Figure 2.34 – ME RMS power of the transducer A (diameter of 16 mm, and bi-layer M-P) measured over different loads, stimulated with different DC magnetic field and a 1.1 mT AC magnetic field. The left graph corresponds to the worst orientation and the right one the best orientation.

3. Medical Regulatory Compatibility

The ME transducer studied here is aimed to be part of a biomedical device. Therefore, it results useful to have an overview of the medical regulatory, which must be considered for practical applications of WPT in the human body, because they may have an impact on the system performances.

As described previously in Chapter 1, Paragraph 4, the guidelines are generally interested in how much EMF is absorbed by the human body and its penetration depths through the tissues [7]. From a health risk perspective, the physical quantities used to specify the restrictions, mostly concern specific absorption rate (SAR), incident magnetic field (H), an electric field (E), current density (J), and power density (U).

Concerning this thesis and the range of working frequency, it could be useful to focus the attention on the incident magnetic fields. A brief scheme is reported with the values, and the range of frequencies, inherent to this thesis (Table 3.1):

Physical quantity	Frequency	Spatial Exposition	Time Exposition	Occupational	General public
Incident E-field strength (V/m)	100 kHz – 30 MHz	Local exposure	6 min	1504/ f_M	671/ f_M
Incident E-field strength (V/m)	100 kHz – 30 MHz	Whole body	30 min	660/ f_M	300/ f_M
Incident H-field strength (A/m)	100 kHz – 30 MHz	Local exposure	6 min	10.8/ f_M	4.9/ f_M
Incident H-field strength (A/m)	100 kHz – 30 MHz	Whole body	30 min	4.9/ f_M	2.2/ f_M
Incident power density (W/m ²)	100 kHz – 30 MHz	Local exposure	6 min	Not Applicable	Not Applicable
Incident power density (W/m ²)	100 kHz – 30 MHz	Whole-body	30 min	Not Applicable	Not Applicable
Electric current (mA)	100 kHz – 110 MHz	Any limb	6 min	100	45
Induced E-field (V/m)	100 kHz – 10 MHz	2 mm x 2 mm x 2 mm	-	$2.7 \cdot 10^{-4} \cdot f$	$1.35 \cdot 10^{-4} \cdot f$

Table 3.1 – Restriction values related to any region of the body, and to rms-EMF values. With f is intended the working frequency in [Hz], f_M the frequency expressed in [MHz], [7].

Considering the range of frequency of 100 kHz, and 200 kHz used in this thesis, the limit of the incident field for a local exposure of 6 min for general public results:

$$H_{\max-100\text{kHz}} = 4.9/(f_M) = 4.9/0.100 = 49 \text{ A/m}$$

$$B_{\max-100\text{kHz}} = \mu H = 4 \cdot \pi \cdot 10^{-7} \cdot H_{\max-100\text{kHz}} = 0.06 \text{ mT}$$

$$H_{\max-200\text{kHz}} = 4.9/(f_M) = 4.9/0.200 = 24.5 \text{ A/m}$$

$$B_{\max-200\text{kHz}} = \mu H = 4 \cdot \pi \cdot 10^{-7} \cdot H_{\max-200\text{kHz}} = 0.03 \text{ mT}$$

The highest values of the magnetic field employed in this thesis are higher than the one admitted from the medical regulatory. The final purpose was to test the maximum achievable power for the range of frequencies comprised between 100 kHz and 200 kHz. Considering 0.06 mT RMS as a maximum value for B_{AC} , the ME transducer (sample C) can achieve 1 mW of output power and 1.24 kW/m³ of power density (Figure 2.32). This amount of power can supply several active implantable devices, such as new generation pacemakers. Increasing the power density at a smaller RMS AC magnetic field would therefore extend the applicability of ME transducers to other types of implants with higher power consumption.

4. In-vitro Test

The ME technology has been studied to make more efficient wireless power transfer at low frequency. In this thesis, the ME transducer has been proposed as an alternative energy receiver than the usual receiver coil. Firstly, the response of the ME transducer has been characterized under different controlled inputs, to examine the influence of the external magnetic fields over the ME composite, and to determine its potentialities, and limits. Once the sample working conditions have been identified, the ME transducer has been measured in an in-vitro context.

During this set of experiments, the ME transducer has been studied through a new test bench, to test its behavior in a realistic wireless power transmission configuration. The in-vitro tests reproduce a real application of wireless power transmission, between an out-body transmitter block, and an in-body receiver one. In this case, the transmitter block consists of a coil system over a ferritic layer, with two permanent magnets, to provide both DC and AC excitation magnetic fields.

As a matter of comparison, three different types of receivers with the same outer dimensions have been studied:

- a coil, made with copper wire
- a coil, made with copper wire, and a core of ferrite
- a ME transducer.

The main objective of this test was to compare the coil-ME transducer system with the classical coil-coil configuration, maintaining the same boundary conditions, such as working frequency, and receiver's dimensions.

For these experiments, a mechanical robot was employed to precisely displacing the devices from the external charger. The necessity of study the samples' performances for different orientations to the magnetic field is linked to the difficulty in tracing the real-time position of an implanted device.

In fact, in a real application, the receiver block is supposed to be placed in-body. In this case, the samples have been measured in the air. In the following experiment, Paragraph 5, a phantom test is proposed to observe the effect of the wireless ME power transmission in a medium similar to the human body environment.

4.1 Measurement Set up

The in-vitro tests aim to study the performances of the ME device in a configuration close to a real application. The measurements consist of exciting samples with AC and DC magnetic fields, in different orientations. The test bench, used to measure the ME voltage over the samples, is represented in Figure 4.1. In this case, the automated code has not been used to perform the samplings over the spectrum of frequencies. The devices were tested at the resonance and the resonant frequency was searched manually.

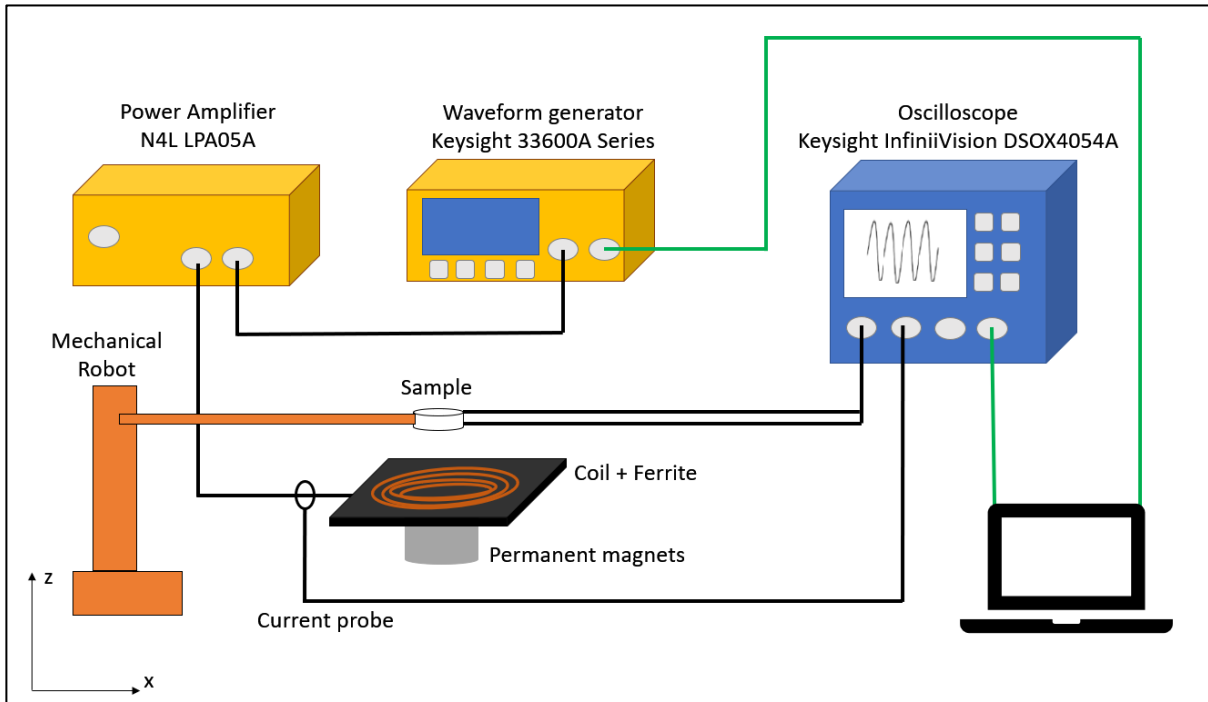


Figure 4.1 – Scheme of the test bench for the in-vitro tests.

In this setup, the sample has been excited with a magnetic source, made with a layer of ferrite, with a 20-turns coil in litz wire, and 2 permanent neodymium magnets. It is supplied by the waveform generator (Keysight 33600A Series), and power amplifier (N4L LPA05A). The DC magnetic field is created through two neodymium magnets, and the AC magnetic field through the coil controlled simultaneously with the current probe. Figure 4.2 reports two photos of the employed transmitter.

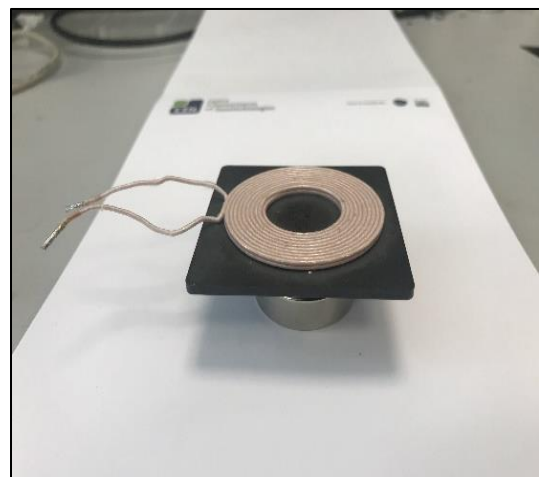
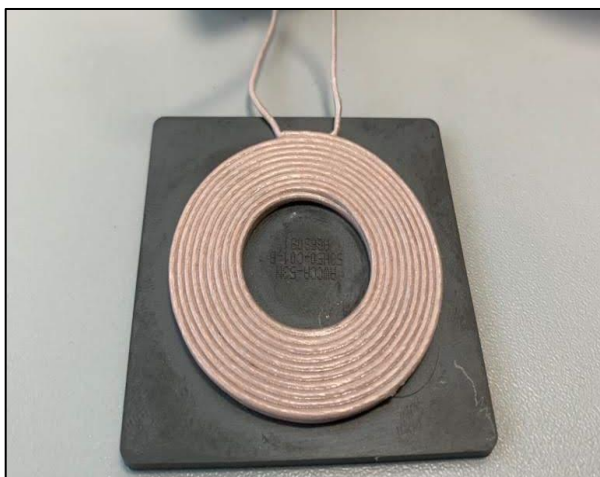


Figure 4.2 – Magnetic source for in-vitro tests.

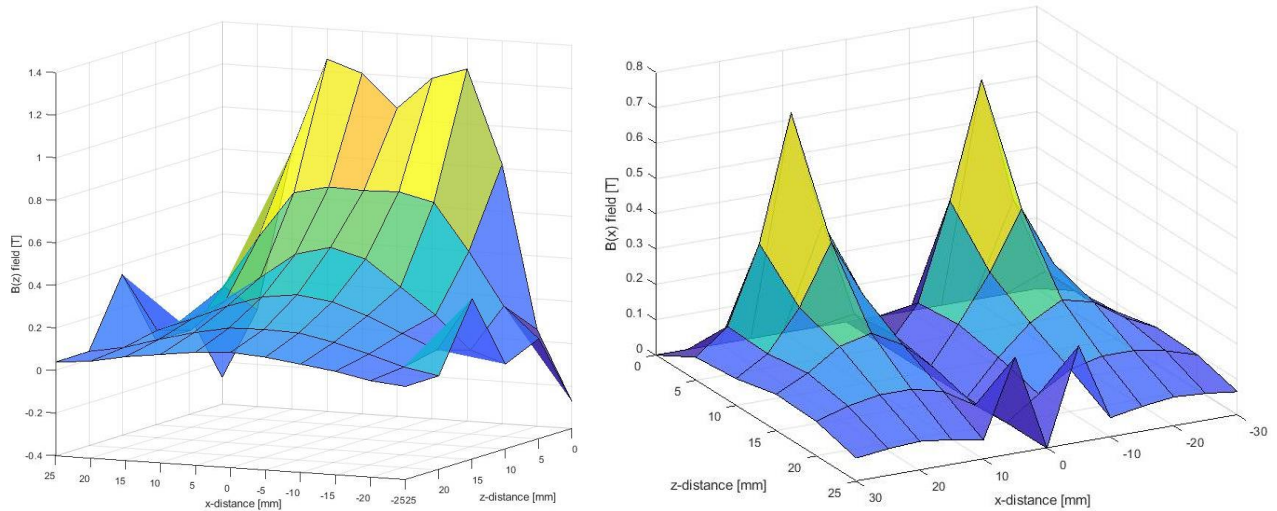


Figure 4.3 – Component z of the magnetic flux density in the left graph, and component x of the magnetic flux density in the right graph, along x, and z-directions

In Figure 4.3, the components x, and z of the DC magnetic flux density, along x, and z-directions, are reported, and measured at the center of the sample’s holder, with a Gaussmeter (GM08 Hirst Magnetic Instruments Ltd). The plane XZ is reported in Figure 4.1 as a reference.

4.2 Tested Samples

As described in Chapter 2, Paragraph 4.4.3, the fabricated ME transducers have a disk-shape with diameters of 10 mm, and 16 mm, and thickness from 2 mm to 5 mm, depending on the number of layers. The chosen sample for the in-vitro tests, shown in Figure 4.4, is a ME transducer with 16 mm-diameter, and a thickness of 3 mm for the bi-layer one (sample B), Table 2.4.

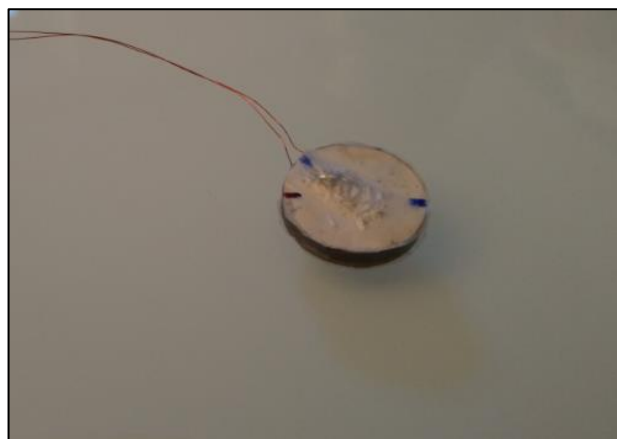


Figure 4.4 – Used ME transducers in the in-vitro tests. Photo of the bi-layer composite, with diameter of 16 mm, and thickness of 3 mm.

To compare the ME efficiency with the classical coil-to-coil system, the two other samples have been fabricated. The first one is a classical coil, made of 120 turns of copper wire of 0.17 mm diameter. The sample has an external diameter of 16.09 mm, an internal diameter of 9.25 mm, and a thickness of 4.25 mm. The objective was to get the same outer dimensions as the ME transducer. A photograph of the coil is reported in Figure 4.5.

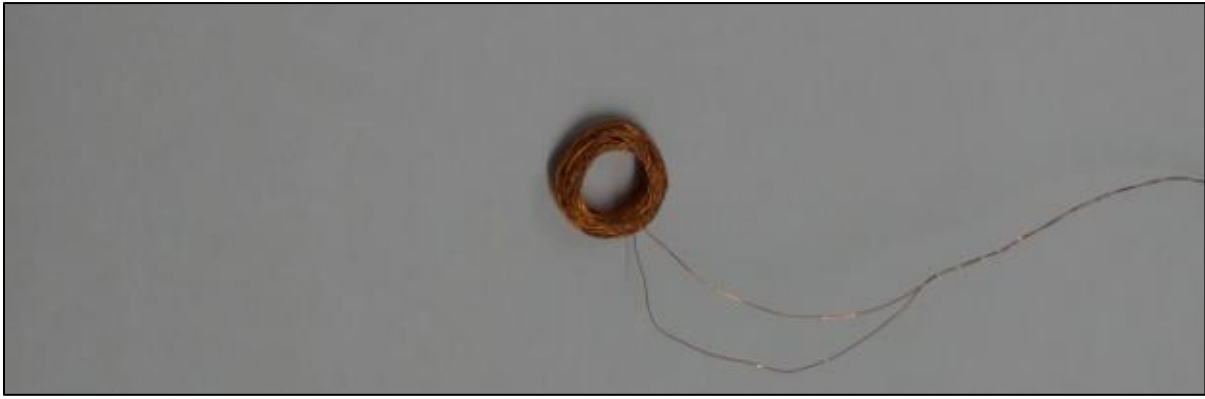


Figure 4.5 - Coil-sample for the in-vitro tests, made with copper wire, external diameter of 16 mm, internal diameter of 9.25mm, thickness of 4.25 mm, and 120 turns.

The second sample has been fabricated after a qualitative study of the effect of the ferrite core in the solenoid. Since the ferritic cores can modify the magnetic field lines, a new copper coil was made to compare the efficiency of the samples. The sample, reported in Figure 4.6, is a classical coil, made of 120 turns in copper wire, wire's diameter of 0.17 mm, with a ferrite core (Ref. 210-3387). The sample measures an external diameter of 15 mm, an internal diameter of 10 mm, and a thickness of 4.35 mm.

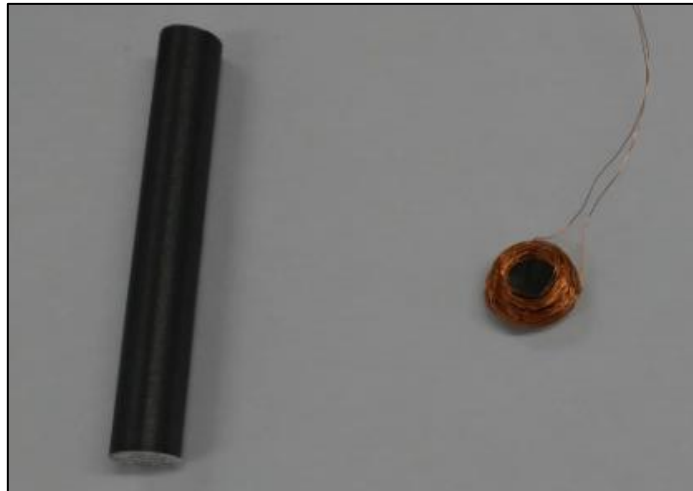


Figure 4.6 – Photograph of the sample, ferrite-core coil used for the in-vitro tests, made with copper wire, external diameter of 15 mm, internal diameter of 10mm, thickness of 4.35 mm, 120 turns, and ferrite core.

4.3 Method

For the in-vitro tests, three types of measurements were mainly conducted:

- Experiments with the sample aligned in parallel orientation to the axis of the emitter-coil
- Experiments with the sample aligned in perpendicular orientation to the axis of the emitter-coil
- Experiments with the sample aligned in α -orientation to the axis of the emitter-coil.

The output voltage was measured over the three samples, employing the test bench shown in Figure 4.7. The experiments were performed moving the samples along two axes, so stimulating them with different DC magnetic fields and a constant AC magnetic field, generated by a current of 17 A in the coil. The resonance frequency was manually searched for each of the tested positions:

z-position = [0 to 50] mm

x-position = [0 to 50] mm.

The map of the intensity of the DC magnetic field is showed in Figure 4.3.

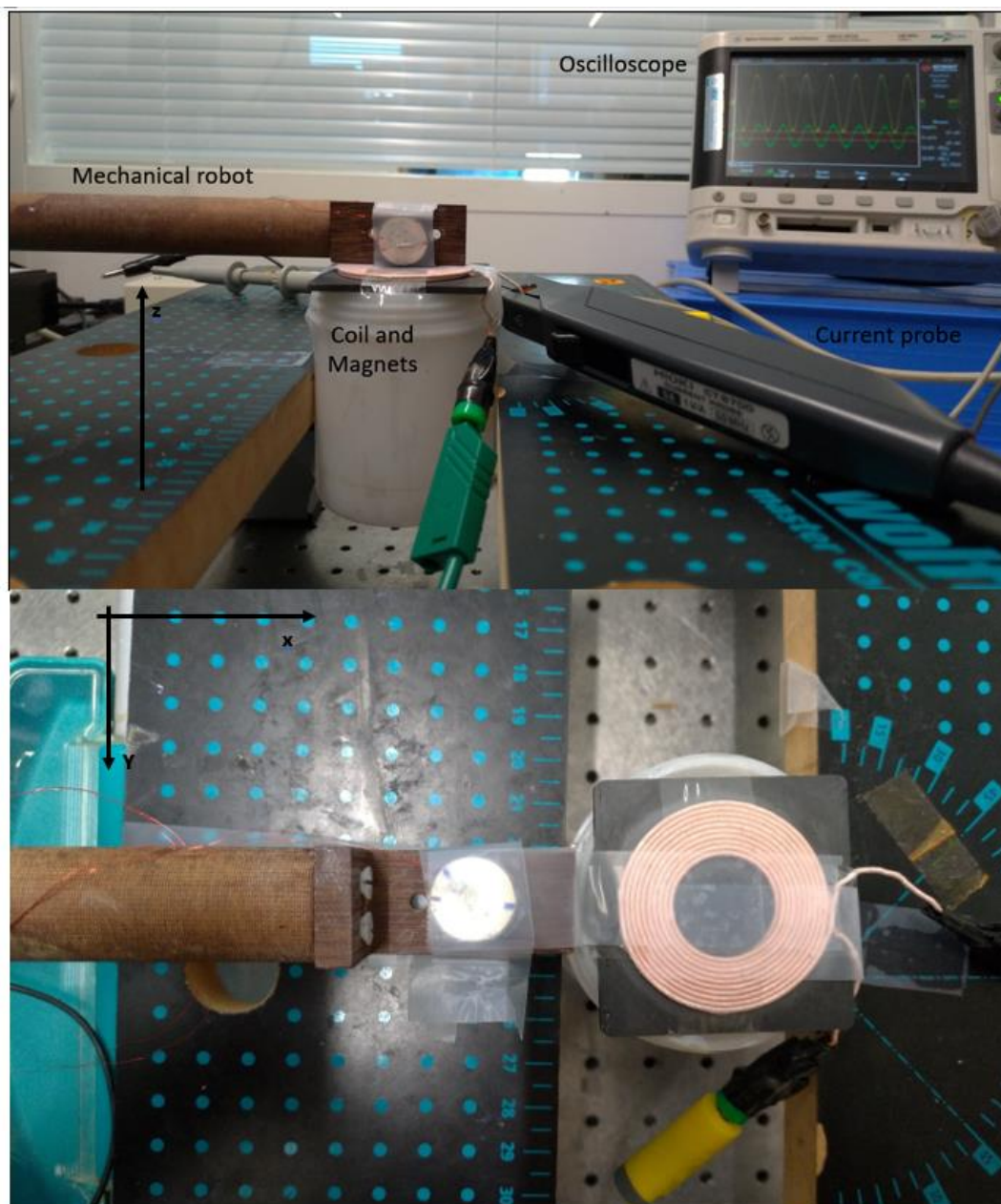


Figure 4.7 – Test bench employed for the in-vitro tests.

4.4 Results, and Discussion

The in-vitro experiments consist of the study of a WPT system, in terms of output voltage over the receiver block. Three main experiments are analyzed in the following paragraphs.

4.4.1 Experiments in the parallel orientation

For the first type of test, the three samples have been tested at different displacements, from the center of the transmitter-coil. The samples have been moved along the x and z-axis, counted from the center of the sample. Changing the sample distances means to change the DC magnetic field, received by the receiver block. In this case, the lower parts of the samples were parallelly aligned to the coil, as shown in Figure 4.8.

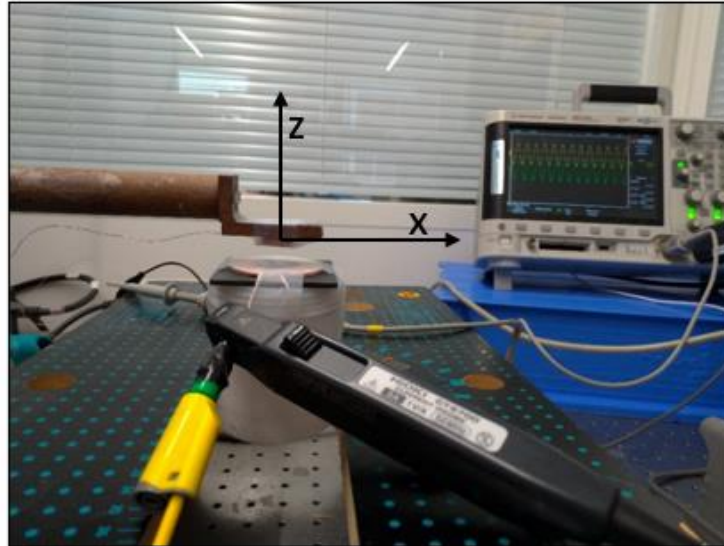


Figure 4.8 – Experiment in parallel orientation

In this configuration, since the cross-section of the transmitter, and receiver coils are faced up, the sample can receive the maximum magnetic flux. On the contrary, the ME transducer represents its worst orientation. For the coil, and coil configuration, the output RMS voltage at the varying of z, and x-positions is reported in Figure 4.9:

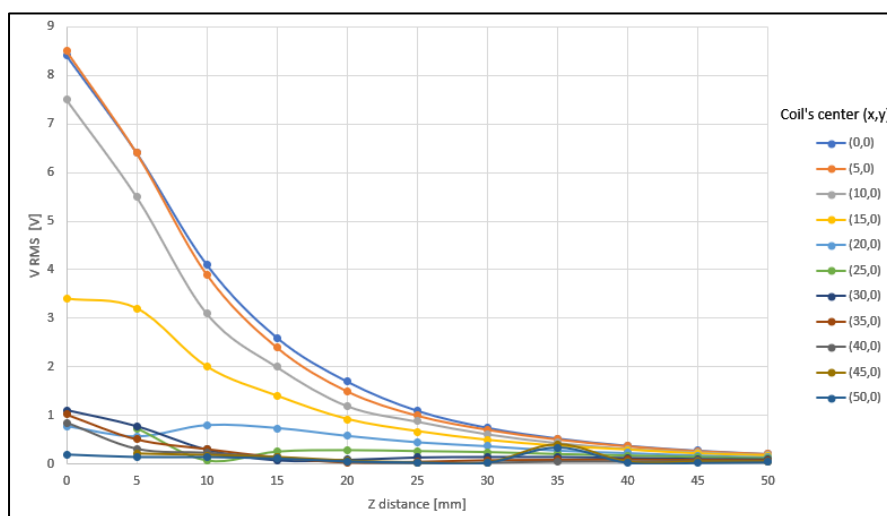


Figure 4.9 – RMS Voltage from the coil-sample, at varying of z, and x positions, in parallel orientation.

For the coil, and coil+ferrite configuration, the output RMS voltage at the varying of z, and x-positions is reported in Figure 4.10:

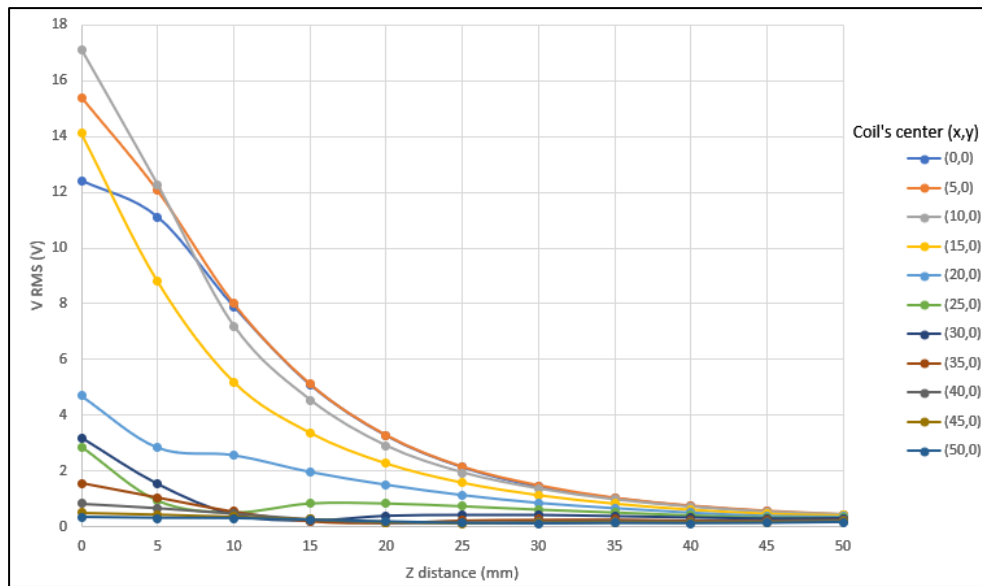


Figure 4.10 – RMS Voltage from the sample, coil with ferrite, at varying of z, and x positions, in parallel orientation.

For the coil, and ME transducer configuration, the output RMS voltage at the varying of z, and x-directions is reported in Figure 4.11:

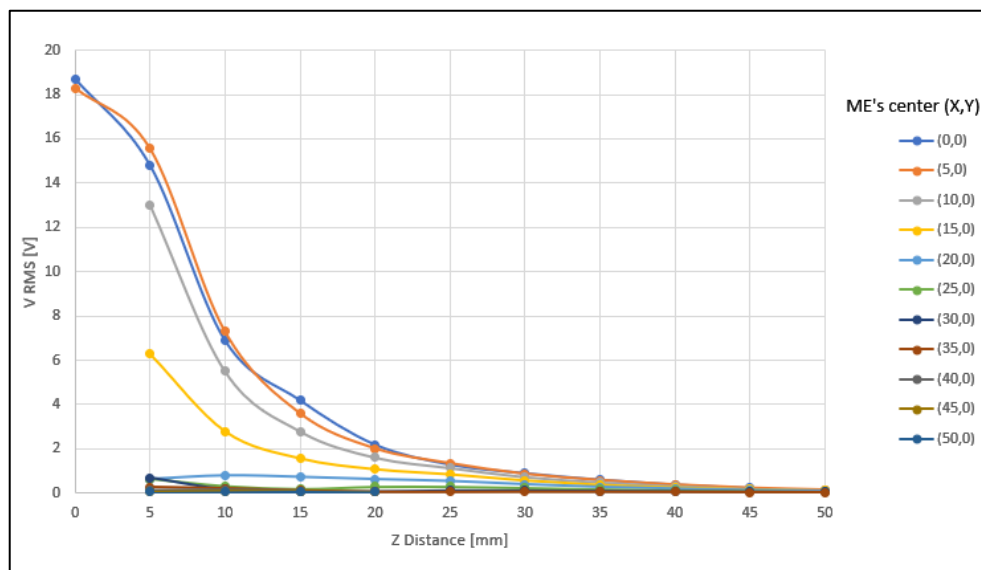


Figure 4.11 - RMS Voltage from the ME transducer, at varying of z, and x positions, in parallel orientation.

In this case, the ME transducer and coil+ferrite are the most efficient configurations. However, the ME sample can achieve sufficient voltage until 20 mm of displacement. Counting 20 mm from in z and x position, the ME transducer can produce 1V of output. On the contrary, the coil+ferrite sample can achieve the same amount of output voltage at 25 mm of displacement.

4.4.2 Experiments in the perpendicular orientation

For the second type of test, the three samples were tested at different displacements along x, and z-axis. In this case, the base of the sample was perpendicularly aligned to the coil and the z-position was counted from the lower part of the sample, as showed in Figure 4.12.

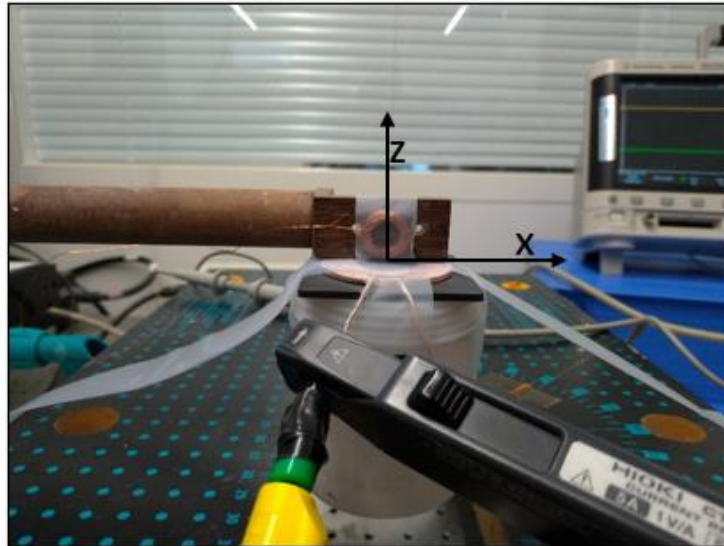


Figure 4.12 – Experiment in perpendicular orientation.

In this configuration, since the cross section of the transmitter, and receiver coils are perpendicular, the sample receives the minimum magnetic flux. On the contrary, for the ME transducer, it represents the best configuration. For the coil, and coil configuration, the output RMS voltage at the varying of z, and x-positions is reported in Figure 4.13:

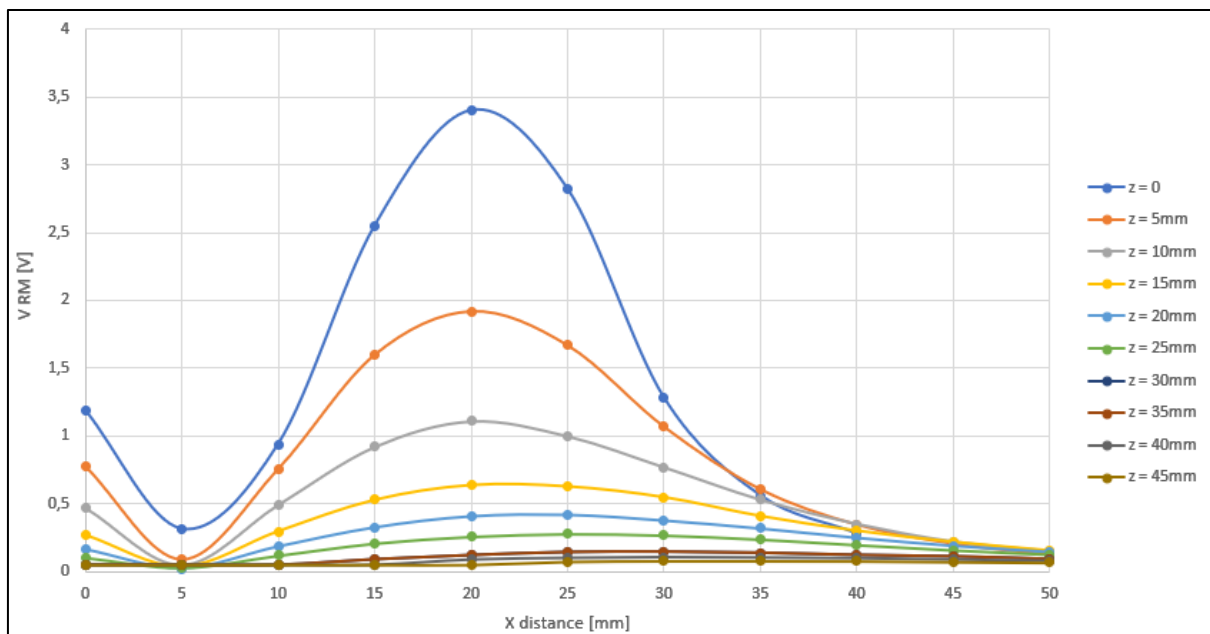


Figure 4.13 - RMS Voltage from the coil-sample, at varying of z, and x positions, in perpendicular orientation.

For the coil, and coil+ferrite configuration, the RMS output voltage at the varying of z, and x-positions is reported in Figure 4.14:

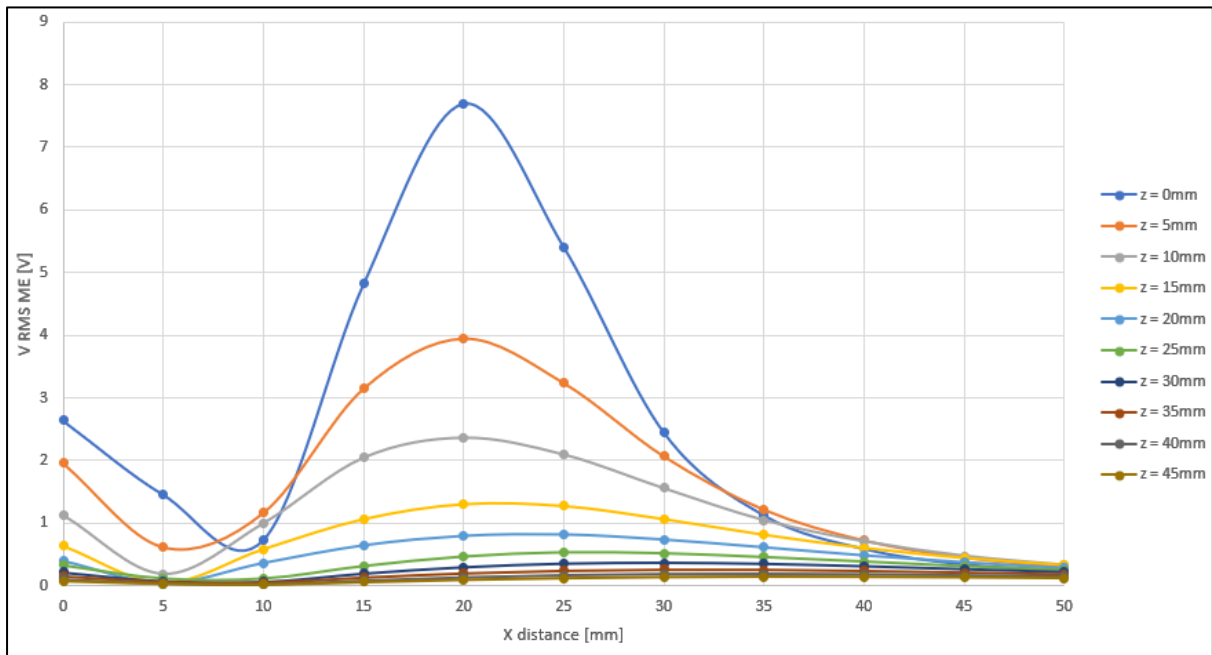


Figure 4.14 - RMS Voltage from the sample, coil with ferrite, at varying of z, and x positions, in perpendicular orientation.

For the coil, and ME transducer configuration, the output RMS voltage at the varying of z, and x-positions is reported in Figure 4.15:

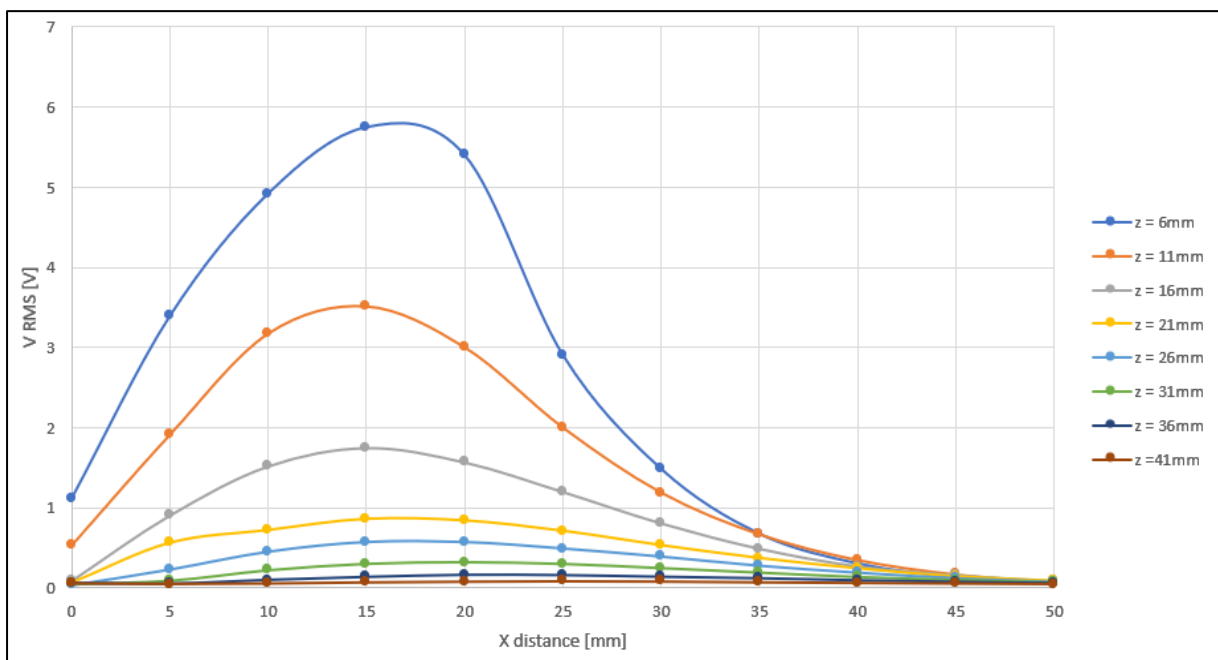


Figure 4.15 - RMS Voltage from the ME transducer, at varying of z, and x positions, in perpendicular orientation.

In this case the ME transducer and coil+ferrite are still the most efficient configurations. However, the curves show a peak of the maximum voltage at the correspondence of the transmitter coil's side, instead of the center. This is due to the magnitude and disposition of the magnetic flux lines. The map of the magnetic flux density is shown in Figure 4.3. In this position, the coil+ferrite achieves a high peak of RMS power (4 V for a height of 5 mm). For the same position, the ME transducer arrives to 5.8 V. For the ME transducer it was not possible to perform measurements at a position of z = 0mm, due to the strong magnetic attraction with the permanent magnets.

4.4.3 Experiments in the α -orientation

For the third, and the last type of in-vitro test, the three samples were tested at different displacements along the x, and z-axis. In this case, the z-position is counted from the lower part of the sample. The bases of the samples were turned with the mechanical robot of an α -angle, and the RMS voltage was measured. In Figure 4.16, it is reported a photo of the setup.

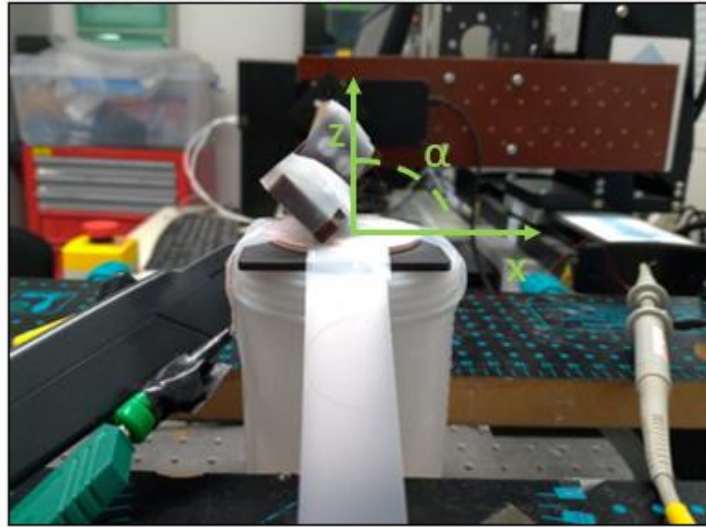


Figure 4.16 - Experiment in α -orientation.

In this configuration, it is interesting to see the evolution of the samples' performances at the varying of the α -alignment between the transmitter coil and the devices. For the coil, and coil configuration, the output RMS voltage at the varying of z, and x-directions is reported in Figure 4.17:

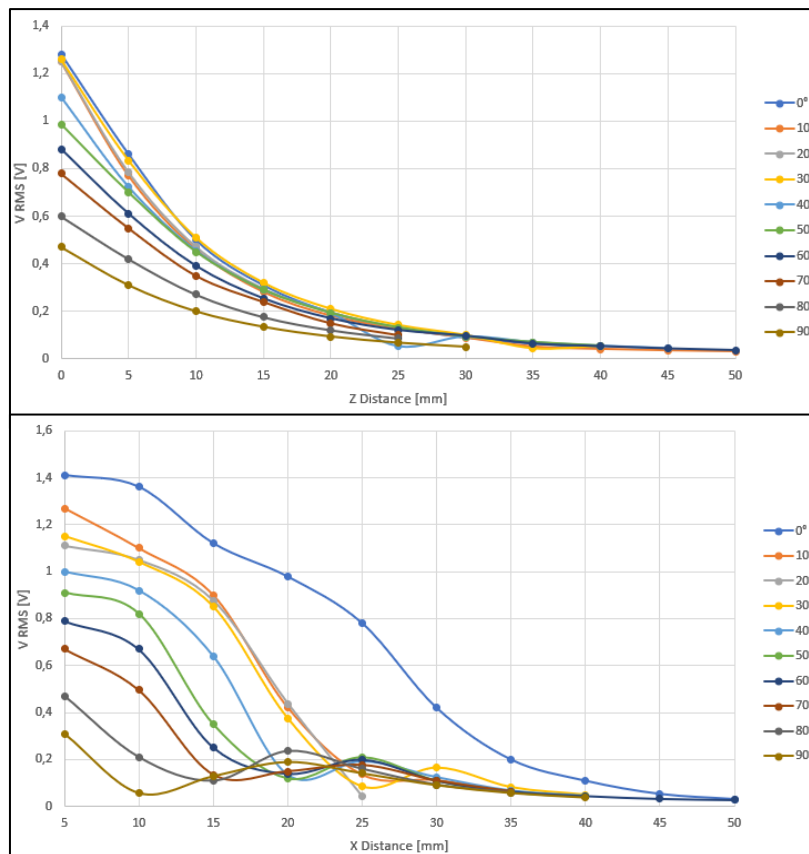


Figure 4.17 - RMS Voltage from the coil-sample, at varying of z, and x positions, in α -direction.

For the transmitter coil and coil+ferrite configuration, the output RMS voltage at the varying of z, and x-directions is reported in Figure 4.18:

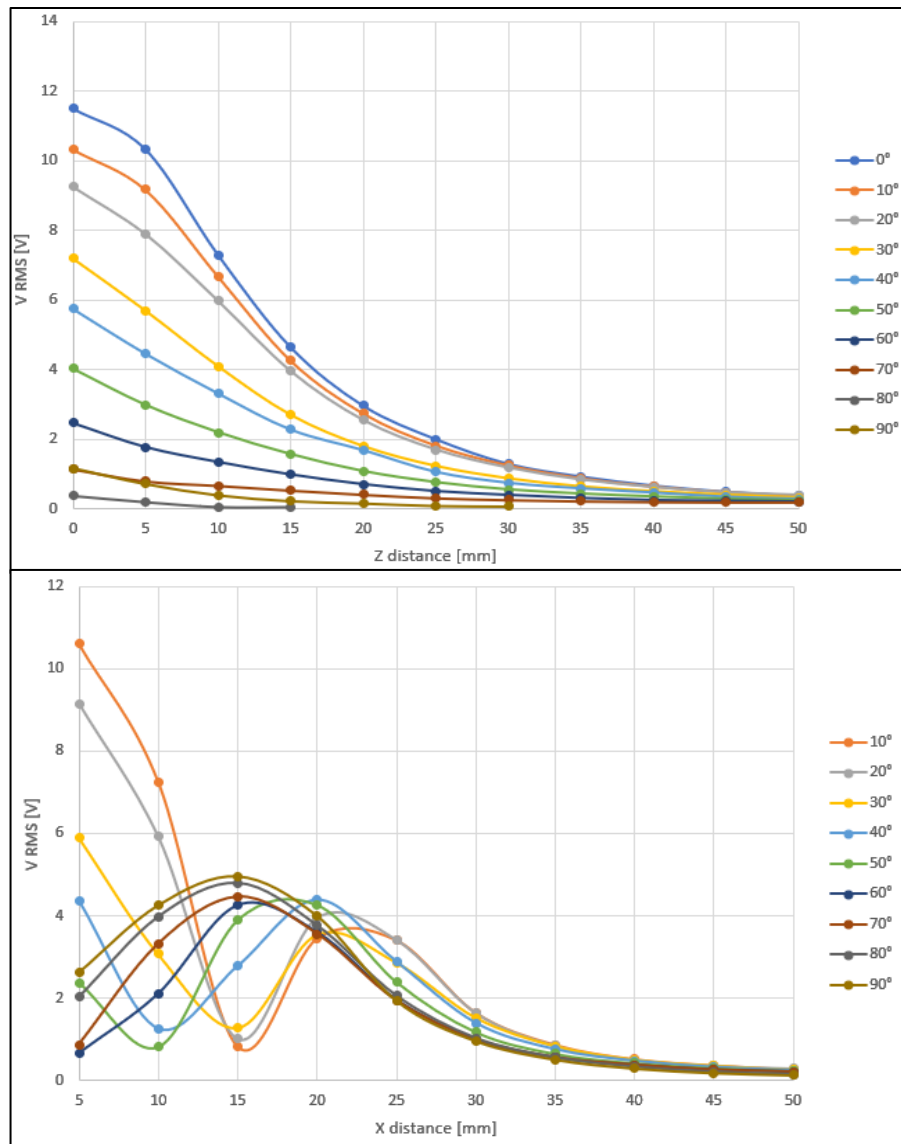


Figure 4.18 - RMS Voltage from the sample, coil with ferrite, at varying of z, and x positions, in α -orientation.

For the coil, and ME transducer configuration, the output RMS voltage at the varying of z , and x -positions is reported in the following graphs:

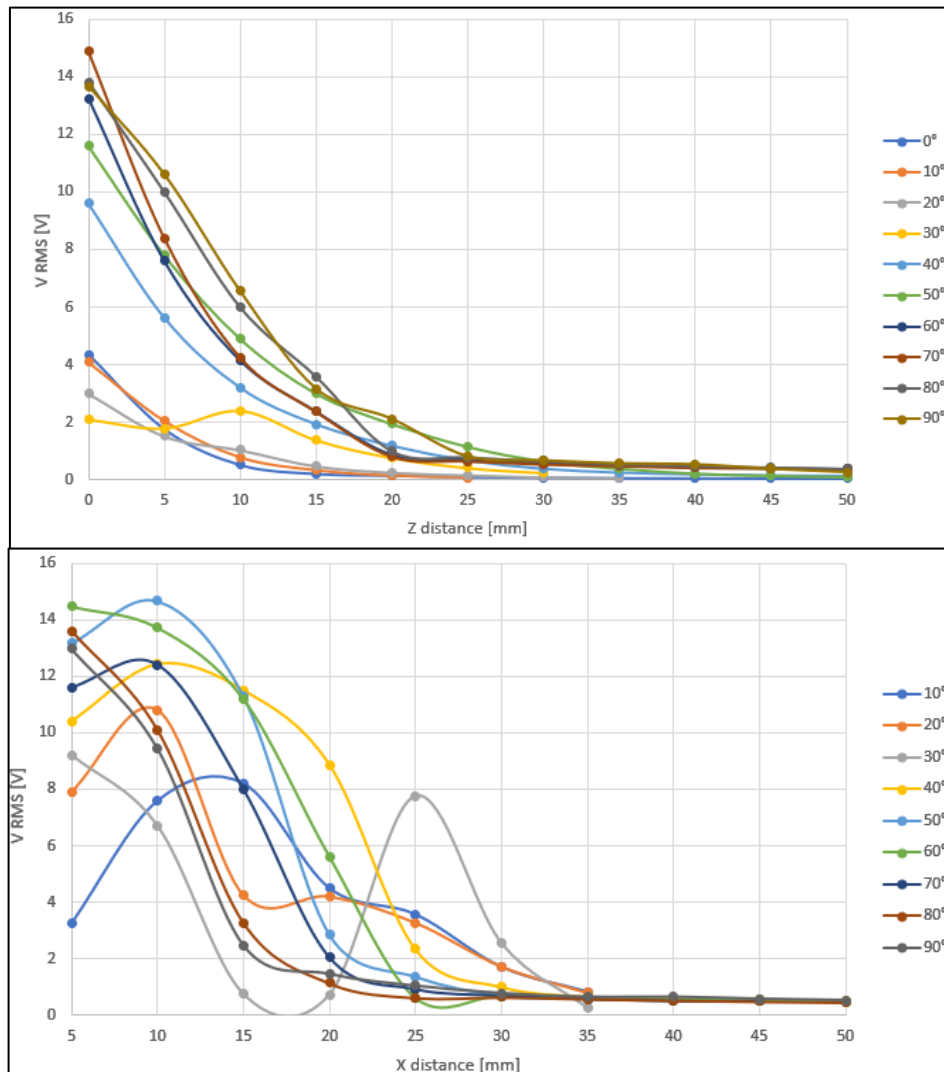


Figure 4.19 – RMS voltage from the ME transducer, at varying of z , and x directions, in α -orientation.

In this last test, the performances of the ME transducer, and the coil+ferrite samples confirm the previous trend. It is possible to notice that along the z -axis, so moving vertically the sample, the output voltage tends to decrease drastically after 15/20 mm.

On the contrary, along the x -axis, so moving the sample along a horizontal direction, the output voltage does not follow a linear behavior, but it varies with the magnitude and disposition of the magnetic flux lines. Good values of output voltage have been measured until 35/40 mm of distance along the x -axis.

In conclusion, this experiment wanted to study the potentialities of a ME transducer in a WPT configuration. As shown from the results, the strong dependency of the orientation of the coil-coil system can be reduced by substituting a ME device in the receiver block. However, the measured ME output voltage remains dependent on the mutual orientation with the transmitter coil.

In the in-vitro test the receiver block, described in Figure 4.15.A of Chapter 2, was not implemented here. For future works, it could be interesting to include the AC/DC rectifier in the ME sample, to study the output response in terms of DC voltage.

5. Phantom Test

The ME technology has been studied to make more efficient wireless power transfer at low frequency. In this thesis, the ME transducer has been proposed as an alternative to the classical receiver coil. Firstly, the response of the ME transducer has been characterized under different controlled inputs, to examine the influence of the external magnetic fields over the ME composite, and to determine its potentialities.

Once the sample working conditions have been identified, the ME transducer has been measured in an in-vitro context. In this case, the behavior of the ME transducer was studied through a wireless power transmission configuration. In particular, the in-vitro experiments wanted to reproduce a real application of wireless power transmission, between an out-body transmitter block, and an in-body receiver one, testing different orientations of the transmitter, and receiver. The limitation of this test, compared to reality, is the location of the receiver. In the vitro experiments, the ME device was placed over a mechanical robot and measured in an air medium.

To improve this aspect, a phantom test has been performed. The experiment aimed to record the performances of the ME devices in an environment close to human tissue (duck meat). The interests of this experiment consisted of measuring the ME transducer through a medium, close to the real application, and to see the ME response in terms of efficiency and orientation sensitivity. For these measurements, the device was inserted in a polymeric capsule, to preserve the ME resonator characteristics, and avoid any influence of the environment on their mechanical vibration. Furthermore, concerning the test bench, the same transmitter charger of the in-vitro tests was employed and deeply described in the following paragraphs.

5.1 Measurement Set up

The phantom tests aim to reproduce and to study the performances of the ME device in a configuration close to an in-body application. The measurements consist of exciting the samples with a constant AC, and a variable DC magnetic fields, for different samples orientations, through a medium, close to human tissue (duck meat). The duck meat was chosen for the composition of the layers of meat, so the separation between muscles, and fat-tissues. The test bench, used to measure the ME voltage over the samples, is represented in Figure 5.1.

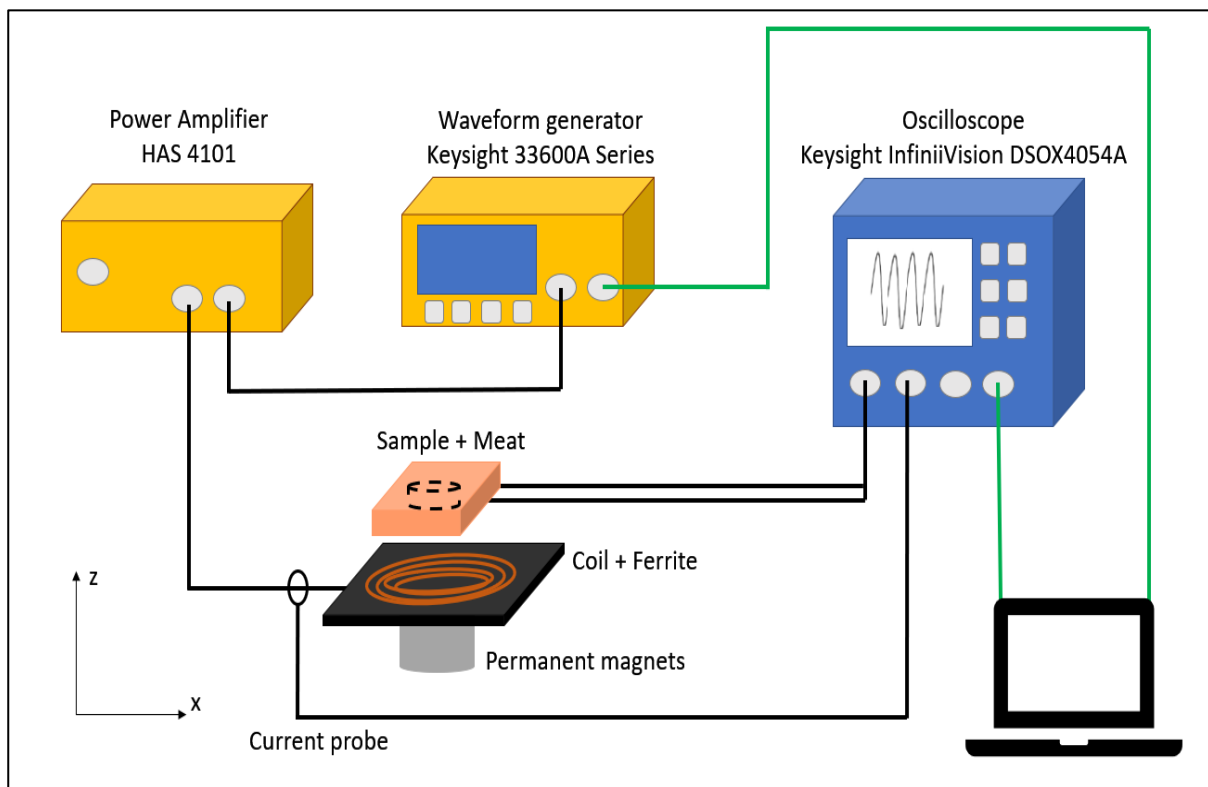


Figure 5.1 - Scheme of the test bench for the tests in phantom.

In this setup, the sample has been excited with a magnetic source, made with a layer of ferrite, with a 20-turns coil in litz wire, and 2 permanent neodymium magnets. It is supplied by the waveform generator (Keysight 33600A Series), and power amplifier (HAS 4101A). The DC field is created through two neodymium magnets. The AC field through the coil and controlled simultaneously with the current probe. The Figure 5.2 reports two photos of the employed transmitter.

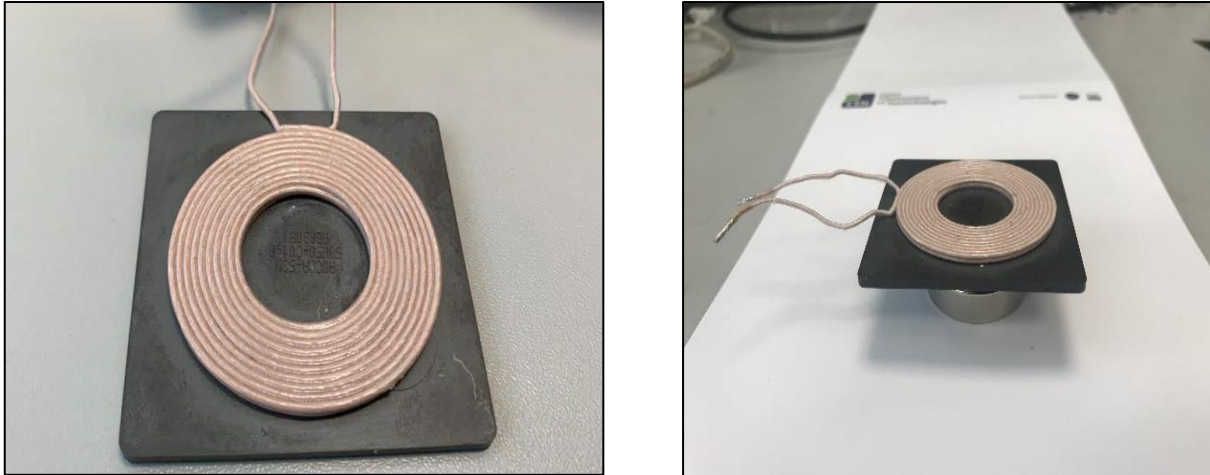


Figure 5.2 – Magnetic source for in-vitro tests.

5.2 Tested Samples

As described in the Chapter 2, Paragraph 4.4, the fabricated ME transducers have a disk-shape with diameters of 10 mm, and 16 mm, and thickness from 2 mm to 5 mm, depending on the number of layers. The chosen sample for the phantom tests, showed in Figure 5.3, is a ME transducer with 16 mm-diameter, and thickness of 3 mm for the bi-layer one (sample B), Table 2.4. The sample was inserted in a capsule of biocompatible polymer, PEEK, to preserve the ME resonator characteristics, and avoid any influence of the environment on their mechanical vibration.

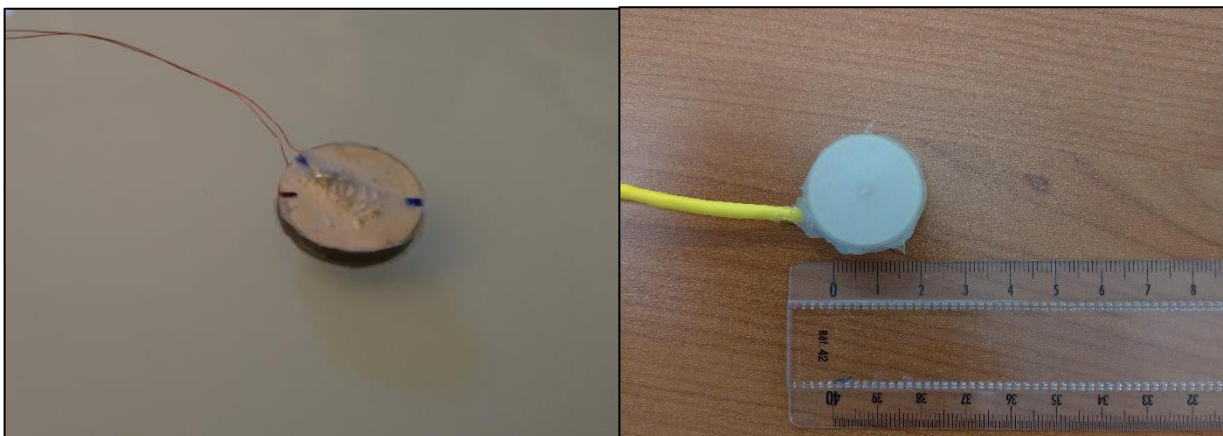


Figure 5.3 - Used ME transducers in the in-vitro tests. On the left, the photo of the bi-layer composite, with diameter of 16 mm, and thickness of 3 mm. On the right, the photo of the encapsulated sample in a polymeric packaging.

5.3 Method

For the phantom tests, the sample was tested outside, and inside the meat, at different depths, with vertical, and horizontal positions of the capsule. The experiments were performed moving the samples along the z-axis, for fixed distances, and along XY-plane, to search for the best orientation. The sample was stimulated with different DC magnetic fields, and a constant AC magnetic field, generated by a current of 2 A in the coil. The ME voltage and power were measured manually, searching for the resonance frequency.

The used test bench is showed in Figure 5.4.

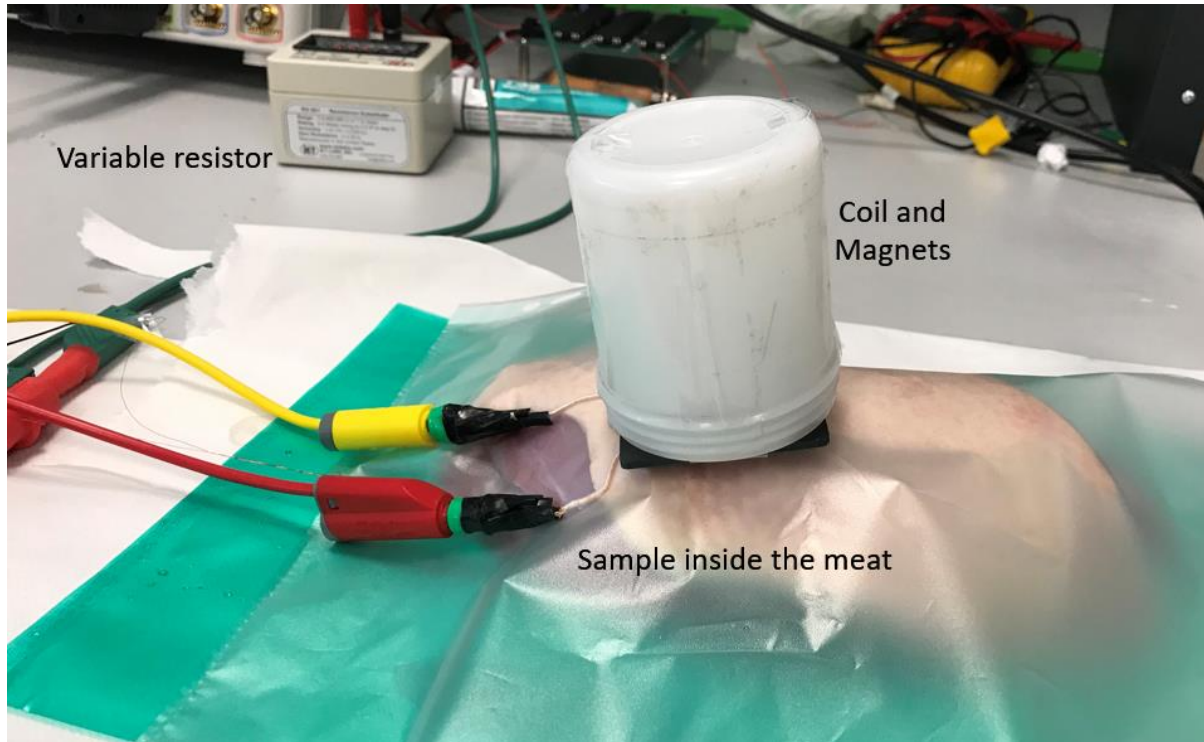


Figure 5.4 - Test bench employed for the in-vitro tests.

5.4 Results, and Discussion

The sample has been tested outside and inside the meat, at different positions and orientations with respect to the transmitter coil. Firstly, the ME transducer was characterized in parallel and perpendicular orientations in the air-environment, as in the previous in-vitro test. As shown in Figure 5.5, the capsule's center and the transmitter coil are perpendicular. In this case, the distance of the capsule from the transmitter coil was set by the white ceramic supports, shown in Figure 5.5, of 5 mm thickness each. In this configuration the sample was connected to two optimal resistive loads, corresponding to its two power peaks (200 Ω and 5000 Ω). It was studied in 5 different z-distances, [0, 5, 10, 15, 20] mm, so under 5 different values of the DC and a constant AC magnetic fields. The map of the DC field is reported in Figure 4.3.



Figure 5.5 – Photo of the test outside the meat.

Once the output characteristics have been evaluated for different positions and orientations, the same procedure was repeated in the meat-environment. The sample has been connected to loads of 200 Ω and 5 k Ω and measured in the parallel and perpendicular orientations to the transmitter coil. Following the protocol of the test in the air-environment, 5 different z-distances have been tested [0, 5, 10, 15, 20] mm. In Figure 5.6, the phantom test set-up has been reported.



Figure 5.6 – Photo of the phantom test.

In Figure 5.8 and Figure 5.7 the measured ME RMS powers are reported. As shown in the graphs, the two load cases reach the same order of ME power, with a maximum value for a 0 mm of distances and decreasing with the increment of the height. The largest load resistance achieves a slightly higher power, 12 mW, following the behavior of the previous characterization tests, with preferential orientation in a “flat configuration”. The same preferential orientation is reported in the first case, with a maximum power of 10 mW. In both cases, the power decreases and reaches near 0-power after 20 mm, the same distance found in the in-vitro test. Interestingly, a similar amount of ME power can be transmitted in the flat and vertical position. The presence of meat does not directly impact the electromagnetic transmission.

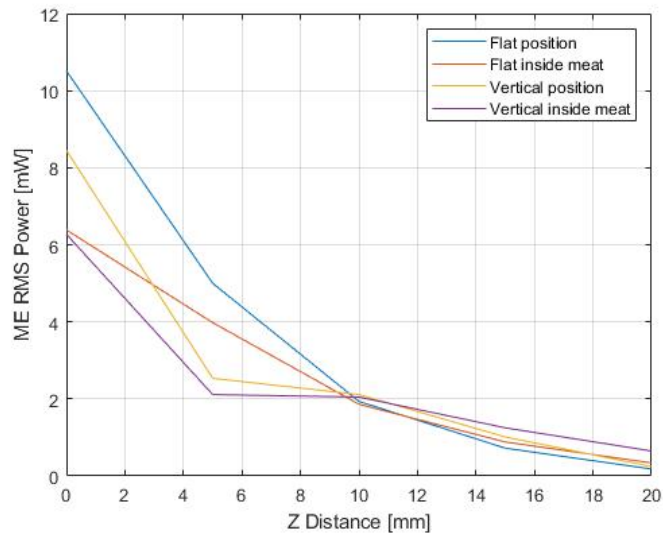


Figure 5.8 – RMS power measured over a load of 200 Ω.

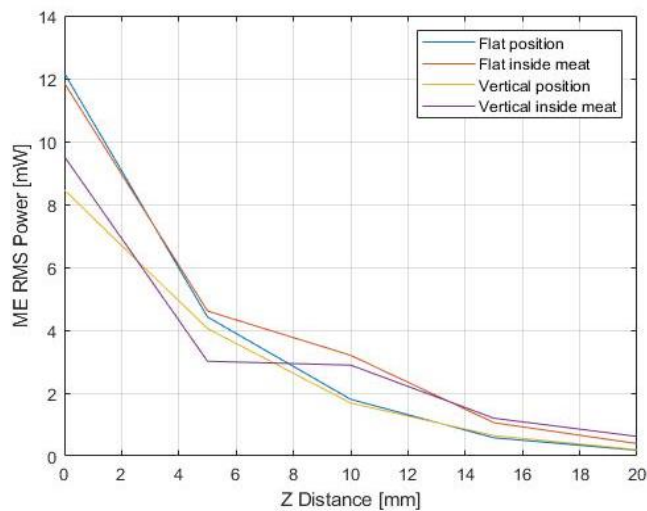


Figure 5.7 - RMS power measured over a load of 5000 Ω.

The difference in power levels between the outside and inside-meat measurements is attributed to fact that the distance measurement was more difficult and less accurate in the second case.

In conclusion, the test positively confirms the previous characterization and in-vitro experiments. However, the measured ME output voltage remains dependent on the mutual orientation of the ME transducer with the transmitter coil. During these tests, a measurement of temperature was missing, it could be interesting to add it, to see the evolution, and the impact on the ME performances during the experiment time.

6. Conclusion

In the experimental study of the ME transducer, three sets of experiments have been conducted. The first part consisted of the characterization of the ME transducers. The samples have been stimulated with a DC magnetic field, to set their magnetostrictive working point, and with an AC field to measure their performances at different frequencies. The responses of the ME samples have been measured in terms of ME voltage, and power, with different magnitude, and orientations of the input magnetic field. The aim was to test the efficiency of the device with different boundary conditions. During the characterization tests, it has been possible to show that the samples have an optimal working frequency, defined as the resonance frequency. In addition, the most efficient samples resulted the ones with the biggest diameter and tri-layer (MPM) with an achieved output power of 40 mW. The values of output ME power reported in the literature, described in Paragraph 4.5 of Chapter 2, are of the order of 800 μ W for Yang et al., [8] and 600 μ W for Malleron et al., [10]. So, the obtained value of 40 mW could be defined as an important step towards the integration of ME transducers for powering wireless implants.

Moreover, a second, and interesting result shows that thicker samples, with smaller magnetostrictive volume ratio, could achieve lower power (30% less), and lower density of power than a thinner sample, with a higher magnetostrictive volume ratio. In other terms, a big sample PMP with 20% of magnetostrictive material, and a total thickness of 5 mm reached a lower power than the smaller sample MP with 50% of magnetostrictive material, and a total thickness of 2 mm. This observation opens good perspectives in terms of miniaturization of the ME transducer while increasing the Wireless Power Transfer efficiency.

Furthermore, the results of the characterization tests have been used to validate the theoretical model, proposed to simulate the behavior of the ME transducer. The theoretical circuit of the complete ME system has been deduced, starting from the equivalent circuit of a piezoelectric transducer. In this case, the coupling phenomenon between the magnetostrictive part, and the piezoelectric layer has been represented through three main blocks, linked by two coupling coefficients. A first measurement of the samples has been conducted in a static regime. The impedance of the ME device has been measured under different DC magnetic fields. From this first test, it has been possible to quantify the influence of the DC field over the resonance frequency of the sample, and on the mechanical stiffness, and damping parameters. A second measurement has been conducted in a dynamic regime, applying an AC magnetic field, and measuring the ME output in open circuit condition. From this measurement, it could be possible to theoretically predict the behavior of the ME device in terms of output power over a resistive load. The obtained curves are promising, but there is a shift of frequency in the model, attributed to the non-linearities of the system. The final purpose of the characterization consisted to quantify the quality factor, coupling coefficients, and losses due to the magneto-elastic-electric non-linearities of a ME system, directly from the experimental measurement. However, the theoretical model shows a difference of 10% with the experimental measurements, which makes it acceptable. It could be further optimized, taking into account other factors such as the component of Eddy's currents, induced in the ME transducer and the related heating effect on the system's behavior.

Since the final application of the studied magnetoelectric transducer is powering an implantable medical device, through the charge of its battery or internal accumulator, a classical full-bridge rectifier was connected to the sample, and in a second time a half bridge AC/DC rectifier. All the characterization tests have been repeated with this configuration, and the theoretical model was modified to integrate the rectifiers. In terms of ME transducer behavior, it has been possible to see an achieved output power a bit lower than the without-rectifier case, due to the diodes losses (34 mW compared to 40 mW). Furthermore, the performances of the ME transducers with the two types of AC-DC converters result quite similar in the two cases. In terms of output voltage, the half-bridge output is higher than the full-bridge one. This is due to the voltage doubling effect of the half-bridge. In addition, the diodes losses are smaller, because of their lower number in the circuit. From the point of view of the theoretical model, it still presents an error of 10% with respect to the experimental values.

Once the sample working conditions have been identified through the characterization experiments, and the theoretical model validated, the ME transducer has been measured in an in-vitro context. This set of tests was focused on the comparison of Wireless Power Transfer effectiveness of a ME-coil system, and a coil-coil system, under different orientations of the two blocks. The aim was to recreate a real application of wireless power transmission, between an out-body transmitter block, and an in-body receiver one. The samples were connected

to a mechanical robot with 5-degrees of freedom, which could precisely move the devices along different orientations, and distances from the transmitter. In this case, the devices (MP) have been tested until 50 mm of distances along a vertical, and a horizontal direction from the center of the transmitter source. The employed transmitter block consisted of a coil system, with two permanent magnets, to guarantee a DC and an AC magnetic stimulation of the device. For the receiver system, a coil, a coil with a ferrite core, and a ME transducer of the same dimensions have been tested. The advantage of the ME device consists of the possibility to collect a usable amount of electrical energy independently of its orientation. However, they can reach a good level of output voltage, even if they are not orientated along this optimal direction. For example, 1.5V of output has been measured at 20 mm of distance in the condition of the worst alignment of the ME transducer. Such result is not achievable for a coil-coil system (perpendicularly orientated, the received magnetic flux is zero). The necessity of having power transmission whatever the orientation between an out-body block and in-body device is fundamental for the active medical implants, whose position is very difficult to track in real-time, especially for the devices connected to organs or muscles.

Finally, to move towards a more realistic set up, a phantom test was performed. The experiment aimed to record the performances of the ME devices in an environment close to human tissue: duck meat. The interests of this experiment consisted of measuring the ME transducer through a medium, close to the real application, and to see the ME response in terms of efficiency and orientation sensitivity. The duck meat was chosen for the composition of the fat tissues inside the meat. For these measurements, the device was inserted in a polymeric capsule, to preserve the ME resonator characteristics, and avoid any influence of the environment on their mechanical vibration. The performances can confirm the results obtained in the vitro-test, showing a maximum output ME RMS power of 12 mW, and a density power of $2 \cdot 10^4$ W/m³, in the best configuration of the transmitter, and receiver blocks.

The in-vitro and phantom tests confirm the dependency of preferential orientation of the ME transducer with the transmitter coil, less accentuated than the coil-coil system, but still present. However, the encouraging results obtained regarding the output ME voltage and power, in the best and worst alignments, can open the perspective to employ ME as an efficient transducer in wireless powering implantable devices.

7. Bibliography

1. Sarraute E., Vasic D., Costa F., *Transformateurs piezoelectriques*, Ref. D3015 V1
2. Koteiche A., Brenes A., Malleron K., Sou G., *Power limiting phenomena in a magnetoelectric transducer for wireless power transfer*
3. Pyrhonen J., Jokinen T., Hrabovcova V., *Design of Rotating Electrical Machines*, John Wiley, and Sons, p.232, (2009), ISBN 978-0-470-69516-6
4. Badel A., and Lefeuvre E., *Nonlinear Conditioning Circuits for Piezoelectric Energy Harvesters*, Nonlinearity in Energy Harvesting Systems, Springer (2016), doi:10.1007/978-3-319-20355-3_10
5. Rupp T., Truong B.D., Williams S., and Roundy S., *Magnetoelectric Transducer Designs for Use as Wireless Power Receivers in Wearable, and Implantable Applications*, Materials 2019, 12, 512; doi:10.3390/ma12030512
6. Brenes A., Morel A., Juillard J., Lefeuvre E., Badel A., *Maximum power point of piezoelectric energy harvesters: a review of optimality condition for electrical tuning*, Smart Materials, and Structures, IOP Publishing, 2020, 29, pp.033001, doi:10.1088/1361-665X/ab6484
7. *ICNIRP GUIDELINES for limiting exposure to electromagnetic fields (100 kHz to 300 GHz)*, Health Phys 118(5):483-524;2020
8. Yang G., *Contribution to modelling of magnetoelectric composites for energy harvesting*, theses.fr/2016PA066731
9. Dong S., Li J.F., Viehland D., *Magnetoelectric coupling efficiency, and voltage gain effect in piezoelectric-piezomagnetic laminate composites*, Journal of Materials Science, 41(1), 97–106. doi:10.1007/s10853-005-5930-8
10. Malleron K., Gensbittel A., Talleb H., Ren E., *Experimental study of magnetoelectric transducers for power supply of small biomedical devices*, doi: 10.1016/j.mejo.2018.01.013

8. List of figures

FIGURE 2.1 – SCHEME OF THE TEST BENCH FOR THE CHARACTERIZATION TESTS.	100
FIGURE 2.2 - PHOTOS OF THE SAMPLE’S HOLDER. IN THE LEFT PICTURE, THERE IS THE HOLDER WITH PERMANENT MAGNETS, AND THE SAMPLE.....	101
FIGURE 2.3 - TREND OF DC MAGNETIC FIELD, VARYING THE DISTANCE BETWEEN PERMANENT MAGNETS.....	101
FIGURE 2.4 – EQUIVALENT CIRCUIT MODEL FOR MAGNETOELECTRIC TRANSDUCER [8, 9]. GREEN FOR MAGNETIC BLOCK, RED FOR MECHANICAL PART, AND BLUE FOR THE ELECTRIC ONE.....	103
FIGURE 2.5 - ADAPTED EQUIVALENT CIRCUIT MODEL UNDER FREE BOUNDARY CONDITIONS [8].	103
FIGURE 2.6 - EXPERIMENTAL, AND THEORETICAL BEHAVIOR OF A ME TRANSDUCER IN STATIC REGIME, WITH $H_{AC} = 0$. SAMPLE C. .	104
FIGURE 2.7 - EXPERIMENTAL, AND THEORETICAL BEHAVIOR OF A ME TRANSDUCER IN STATIC REGIME, UNDER A BIAS FIELD H_{DC} OF 0.1 T. SAMPLE C.	105
FIGURE 2.8 – ADMITTANCE AND PHASES OF MPM SAMPLE FOR DIFFERENT BIAS FIELDS. SAMPLE C.....	106
FIGURE 2.9 - TREND OF THE COMPLEX αME FOR THE SAMPLE C FOR DIFFERENT FREQUENCIES WITH A BIAS FIELD OF 0.1 T.	108
FIGURE 2.10 - THE ME VOLTAGE OF A TRI-LAYER TRANSDUCER (MPM) IS REPORTED AT THE VARYING FREQUENCY FOR A BIAS FIELD OF 0.1 T, AND OVER A LOAD OF 10 k Ω . THE MEASURED V_{OUT} IS REPRESENTED WITH THE BLUE CURVE, AND THE ESTIMATED V_{OUT} WITH THE RED ONE.	109
FIGURE 2.11 – MEASUREMENTS OF THE ME VOLTAGE FOR DIFFERENT DC MAGNETIC FIELDS.....	109
FIGURE 2.12 – EQUIVALENT CIRCUIT MODEL OF A TRI-LAYER TRANSDUCER (MPM) IN DYNAMIC REGIME, FOR 0.1 T DC MAGNETIC FIELD.	111
FIGURE 2.13 – ME TRANSDUCER PERFORMANCES OF A TRILAYER COMPOSITE (\varnothing 16 MM, AND T 4 MM), SAMPLE C. THE GREEN CURVE REPRESENTS THE ME VOLTAGE RMS OVER RL 10 k Ω , WITH A MAXIMUM VALUE OF 22 V AT RESONANCE. THE RED CURVE REPRESENTS ME POWER RMS OVER RL 10 k Ω , WITH A MAXIMUM VALUE OF 51 mW AT RESONANCE.	112
FIGURE 2.14 - EQUIVALENT CIRCUIT MODEL OF A TRI-LAYER TRANSDUCER (MPM) IN DYNAMIC REGIME, FOR 0.1 T DC MAGNETIC FIELD, FOLLOWED BY A HALF BRIDGE RECTIFIER. SAMPLE C.	113
FIGURE 2.15 - EQUIVALENT CIRCUIT MODEL OF A TRI-LAYER TRANSDUCER (MPM) IN DYNAMIC REGIME, FOR 0.1 T DC MAGNETIC FIELD, FOLLOWED BY A FULL BRIDGE RECTIFIER. SAMPLE C.	113
FIGURE 2.16 - ME TRANSDUCER PERFORMANCES OF A TRILAYER COMPOSITE (\varnothing 16 MM, AND T 4 MM). THE GREEN CURVE REPRESENTS THE INPUT VOLTAGE (V_1). THE BLUE CURVE IS THE OUTPUT VOLTAGE OVER RL, AND THE RED CURVE IS THE POWER OVER RL.....	114
FIGURE 2.17 – EMPLOYED TEST BENCH FOR THE CHARACTERIZATION TESTS.....	116
FIGURE 2.18- TOP VIEW OF THE SAMPLE’S HOLDER WITH THE ME COMPOSITE.....	118
FIGURE 2.19 – ME RMS VOLTAGE OF THE ME TRANSDUCER (DIAMETER OF 16 MM, AND TRI-LAYER M-P-M) MEASURED OVER DIFFERENT LOADS, IN A FREQUENCY SPECTRUM BETWEEN 100 KHZ, AND 200 KHZ. SAMPLE STIMULATION WITH 0.1 T OF DC MAGNETIC FIELD, AND 0.8 mT OF AC MAGNETIC FIELD.	119
FIGURE 2.20 - ME RMS POWER OF THE ME TRANSDUCER (DIAMETER OF 16 MM, AND TRI-LAYER M-P-M) MEASURED OVER DIFFERENT LOADS, IN A FREQUENCY SPECTRUM BETWEEN 100 KHZ, AND 200 KHZ. SAMPLE STIMULATION WITH 0.1 T OF DC MAGNETIC FIELD, AND 0.8 mT OF AC MAGNETIC FIELD.	120
FIGURE 2.21 - ME RMS POWER OF THE ME TRANSDUCER (DIAMETER OF 16 MM, AND TRI-LAYER M-P-M) MEASURED OVER DIFFERENT LOADS, IN A FREQUENCY SPECTRUM BETWEEN 100 KHZ, AND 200 KHZ. SAMPLE STIMULATION WITH 0.1 T OF DC MAGNETIC FIELD, AND 0.8 mT OF AC MAGNETIC FIELD. THE BLACK CURVE REPRESENTS THE MAXIMUM RMS POWER FROM THE THEORETICAL MODEL.	121
FIGURE 2.22 - ME RMS POWER OF THE ME TRANSDUCER (DIAMETER OF 16 MM, AND TRI-LAYER M-P-M) MEASURED OVER DIFFERENT LOADS, IN A FREQUENCY SPECTRUM BETWEEN 100 KHZ, AND 200 KHZ. SAMPLE STIMULATION WITH 0.058 T OF DC MAGNETIC FIELD, AND 0.8 mT OF AC MAGNETIC FIELD.	122
FIGURE 2.23 - ME RMS POWER OF THE ME TRANSDUCER (DIAMETER OF 16 MM, AND TRI-LAYER M-P-M) MEASURED OVER DIFFERENT LOADS STIMULATION WITH DIFFERENT DC MAGNETIC FIELD, AND 0.8 mT OF AC MAGNETIC FIELD.	122
FIGURE 2.24 – ME RMS POWER AT VARYING OF THE MAGNETOSTRICTIVE VOLUME RATIO, FOR THE EXCITATION FIELDS OF 0.058 T DC MAGNETIC FIELD, AND 0.8 mT AC MAGNETIC FIELD.	123
FIGURE 2.25 - ME DENSITY OF POWER AT VARYING OF THE MAGNETOSTRICTIVE VOLUME RATIO, FOR THE EXCITATION FIELDS OF 0.058 T DC MAGNETIC FIELD, AND 0.8 mT AC MAGNETIC FIELD.	123

FIGURE 2.26 – EQUIVALENT CIRCUIT MODEL OF ME TRANSDUCER WITH HALF-BRIDGE RECTIFIER (IN THE UPPER SCHEME), WITH FULL-BRIDGE RECTIFIER (IN THE LOWER SCHEME)	125
FIGURE 2.27 – ME DC OUTPUT VOLTAGE, AND POWER ARE REPRESENTED FOR THE ME TRANSDUCER (DIAMETER OF 16 MM, AND TRI-LAYER M-P-M) CONNECTED TO A FULL BRIDGE RECTIFIER. THE OUTPUT MEASURED OVER DIFFERENT LOADS, IN A FREQUENCY SPECTRUM BETWEEN 100 KHZ, AND 200 KHZ. SAMPLE STIMULATION WITH 0.058 T OF DC, AND 0.8 MT OF AC MAGNETIC FIELD.	125
FIGURE 2.28 – ME DC OUTPUT VOLTAGE, AND POWER ARE REPRESENTED FOR THE ME TRANSDUCER (DIAMETER OF 16 MM, AND TRI-LAYER M-P-M) CONNECTED TO AN HALF BRIDGE RECTIFIER. THE OUTPUT MEASURED OVER DIFFERENT LOADS, IN A FREQUENCY SPECTRUM BETWEEN 100 KHZ, AND 200 KHZ. SAMPLE STIMULATION WITH 0.058 T OF DC, AND 0.8 MT OF AC MAGNETIC FIELD.	126
FIGURE 2.29 – ME OUTPUT POWER IS REPRESENTED FOR THE ME TRANSDUCER (DIAMETER OF 16 MM, AND TRI-LAYER M-P-M) CONNECTED TO FULL-BRIDGE RECTIFIER, AND MEASURED OVER DIFFERENT LOADS, IN A FREQUENCY SPECTRUM BETWEEN 100 KHZ, AND 200 KHZ. SAMPLE STIMULATION WITH 0.1 T OF DC MAGNETIC FIELD, AND 0.8 MT OF AC MAGNETIC FIELD. THE BLACK CURVE REPRESENTS THE MAXIMUM POWER FROM THE THEORETICAL MODEL.....	127
FIGURE 2.30 – ME RMS POWER IS REPRESENTED FOR THE ME TRANSDUCER (DIAMETER OF 16 MM, AND TRI-LAYER M-P-M) MEASURED OVER 10 K Ω -LOAD, AND STIMULATED WITH DIFFERENT DC, AND AC MAGNETIC FIELDS.	128
FIGURE 2.31 – ME RMS POWER IS REPRESENTED FOR THE ME TRANSDUCER (DIAMETER OF 16 MM, AND TRI-LAYER M-P-M) MEASURED OVER 200 Ω , AND 10 K Ω LOADS, AND STIMULATED WITH DIFFERENT DC, AND AC MAGNETIC FIELDS.	128
FIGURE 2.32 – ME OUTPUT POWER OF THE ME TRANSDUCER (DIAMETER OF 16 MM, AND TRI-LAYER M-P-M) MEASURED OVER 10 K Ω , AND 20 K Ω LOADS, WITH, AND WITHOUT RECTIFIER, STIMULATED WITH DIFFERENT DC, AND AC MAGNETIC FIELDS.	129
FIGURE 2.33 – PHOTO OF THE SET UP IN THE BEST, AND WORST ORIENTATION, USING THE SIGN OVER THE PIEZOELECTRIC FACE AS A REFERENCE.	130
FIGURE 2.34 – ME RMS POWER OF THE TRANSDUCER A (DIAMETER OF 16 MM, AND BI-LAYER M-P) MEASURED OVER DIFFERENT LOADS, STIMULATED WITH DIFFERENT DC MAGNETIC FIELD AND A 1.1 MT AC MAGNETIC FIELD. THE LEFT GRAPH CORRESPONDS TO THE WORST ORIENTATION AND THE RIGHT-ONE THE BEST ORIENTATION.	130
FIGURE 4.1 – SCHEME OF THE TEST BENCH FOR THE IN-VITRO TESTS.	133
FIGURE 4.2 – MAGNETIC SOURCE FOR IN-VITRO TESTS.....	133
FIGURE 4.3 – COMPONENT Z OF THE MAGNETIC FLUX DENSITY IN THE LEFT GRAPH, AND COMPONENT X OF THE MAGNETIC FLUX DENSITY IN THE RIGHT GRAPH, ALONG X, AND Z-DIRECTIONS	134
FIGURE 4.4 – USED ME TRANSDUCERS IN THE IN-VITRO TESTS. PHOTO OF THE BI-LAYER COMPOSITE, WITH DIAMETER OF 16 MM, AND THICKNESS OF 3 MM.	134
FIGURE 4.5 - COIL-SAMPLE FOR THE IN-VITRO TESTS, MADE WITH COPPER WIRE, EXTERNAL DIAMETER OF 16 MM, INTERNAL DIAMETER OF 9.25MM, THICKNESS OF 4.25 MM, AND 120 TURNS.....	135
FIGURE 4.6 – PHOTOGRAPH OF THE SAMPLE, FERRITE-CORE COIL USED FOR THE IN-VITRO TESTS, MADE WITH COPPER WIRE, EXTERNAL DIAMETER OF 15 MM, INTERNAL DIAMETER OF 10MM, THICKNESS OF 4.35 MM, 120 TURNS, AND FERRITE CORE.	135
FIGURE 4.7 – TEST BENCH EMPLOYED FOR THE IN-VITRO TESTS.....	136
FIGURE 4.8 – EXPERIMENT IN PARALLEL ORIENTATION	137
FIGURE 4.9 – RMS VOLTAGE FROM THE COIL-SAMPLE, AT VARYING OF Z, AND X POSITIONS, IN PARALLEL ORIENTATION.	137
FIGURE 4.10 – RMS VOLTAGE FROM THE SAMPLE, COIL WITH FERRITE, AT VARYING OF Z, AND X POSITIONS, IN PARALLEL ORIENTATION.	138
FIGURE 4.11 - RMS VOLTAGE FROM THE ME TRANSDUCER, AT VARYING OF Z, AND X POSITIONS, IN PARALLEL ORIENTATION.....	138
FIGURE 4.12 – EXPERIMENT IN PERPENDICULAR ORIENTATION.	139
FIGURE 4.13 - RMS VOLTAGE FROM THE COIL-SAMPLE, AT VARYING OF Z, AND X POSITIONS, IN PERPENDICULAR ORIENTATION....	139
FIGURE 4.14 - RMS VOLTAGE FROM THE SAMPLE, COIL WITH FERRITE, AT VARYING OF Z, AND X POSITIONS, IN PERPENDICULAR ORIENTATION.	140
FIGURE 4.15 - RMS VOLTAGE FROM THE ME TRANSDUCER, AT VARYING OF Z, AND X POSITIONS, IN PERPENDICULAR ORIENTATION.	140
FIGURE 4.16 - EXPERIMENT IN A-ORIENTATION.	141
FIGURE 4.17 - RMS VOLTAGE FROM THE COIL-SAMPLE, AT VARYING OF Z, AND X POSITIONS, IN A-DIRECTION.....	141
FIGURE 4.18 - RMS VOLTAGE FROM THE SAMPLE, COIL WITH FERRITE, AT VARYING OF Z, AND X POSITIONS, IN A-ORIENTATION. ..	142
FIGURE 4.19 – RMS VOLTAGE FROM THE ME TRANSDUCER, AT VARYING OF Z, AND X DIRECTIONS, IN A-ORIENTATION.	143
FIGURE 5.1 - SCHEME OF THE TEST BENCH FOR THE TESTS IN PHANTOM.	144
FIGURE 5.2 – MAGNETIC SOURCE FOR IN-VITRO TESTS.....	145

FIGURE 5.3 - USED ME TRANSDUCERS IN THE IN-VITRO TESTS. ON THE LEFT, THE PHOTO OF THE BI-LAYER COMPOSITE, WITH DIAMETER OF 16 MM, AND THICKNESS OF 3 MM. ON THE RIGHT, THE PHOTO OF THE ENCAPSULATED SAMPLE IN A POLYMERIC PACKAGING.....	145
FIGURE 5.4 - TEST BENCH EMPLOYED FOR THE IN-VITRO TESTS.	146
FIGURE 5.5 – PHOTO OF THE TEST OUTSIDE THE MEAT.....	147
FIGURE 5.6 – PHOTO OF THE PHANTOM TEST.....	147
FIGURE 5.7 – RMS POWER MEASURED OVER A LOAD OF 200 Ω	148

9. List of tables

TABLE 2.1 - MODEL PARAMETER VALUES FOR STATIC REGIME MEASUREMENTS, WITHOUT, AND WITH DC FIELD FOR TRI-LAYERS COMPOSITE.SAMPLE C.	105
TABLE 2.2 – CIRCUIT PARAMETERS OF SINGLE PIEZOELECTRIC LAYER.	106
TABLE 2.3 - CIRCUIT PARAMETERS (L_M , C_M , R_M , C_0), ELASTO-ELECTRIC COUPLING COEFFICIENT K_{EE} , QUALITY FACTOR Q , AND RESONANCE FREQUENCY FOR 6 DIFFERENT ME TRANSDUCERS.	107
TABLE 2.4 – LIST THE ME SAMPLES, AND PHOTO OF THE SAMPLE A, C, AND D.	115
TABLE 2.5 – SUMMARY OF THE ME OUTPUT RESPONSES FOR THE TESTED SAMPLES AT THE 0.058 T OF DC MAGNETIC FIELD. THE BIGGEST SAMPLES (A, B, C, AND D) HAVE BEEN STIMULATED WITH A CONSTANT AC MAGNETIC FIELD OF 0.8 mT, AND THE SMALLEST ONES (E, AND F) WITH AN AC FIELD OF 0.7 mT.	124
TABLE 3.1 – RESTRICTION VALUES RELATED TO ANY REGION OF THE BODY, AND TO RMS-EMF VALUES. WITH f IS INTENDED THE WORKING FREQUENCY IN [Hz], f_M THE FREQUENCY EXPRESSED IN [MHz], [7].	131

Conclusion

Table of Contents

Chapter 4 Conclusion	157
1. Conclusion.....	159
2. Bibliography	161
Appendix I	163
Appendix II	165
Appendix III	168
Abstracts	205

1. Conclusion

Every year, millions of patients improve their quality of life through the use of implanted medical devices. Nowadays, advances in microfabrication, and bio/chemical engineering technology are enabling a large variety of miniaturized implantable systems for diagnosing, healthy monitoring, treatment, and injury compensation. This trend of progress in medical implants will continue for the coming super-aged society, which will result in more consumers of these devices, especially for one or more diseases. Since the first pacemaker implant in 1958, this progress is driving physicians, and patients to express an increasing desire for miniaturized implantable devices, as they are offering less invasive implantation procedures, greater comfort for the patient, improved performances, and often provide innovative measurements, and treatments [5]. From the point of view of the device's consumption, the most employed energy source is the single-use batteries. Nonetheless, to ensure the longevity of the implants, it is necessary to replace the discharged battery, which requires a costly, and invasive surgical procedure. To overcome these issues, different techniques have been developed. A technology that could make efficient the use of low-frequency electromagnetic power transfer at a distance, without the need of specific orientation, is the MagnetoElectric transducer (ME). The principle of this device is based on the coupling phenomenon between electric, and magnetic fields, through mechanical deformation of the matter. Fundamentally, a magnetoelectric transducer is a device that converts energy from the magnetic domain to the electrical domain and vice versa. This occurs because the electromagnetic wave is converted to a mechanical acoustic wave before being transduced to electricity. As described in Chapter 2 Paragraph 2.3.2, magnetostrictive material does not need to be aligned with the external source, to convert the electromagnetic wave into an acoustic wave. Due to the physical properties of a ME system, it could be an efficient receiver of orders of magnitude smaller than the classical inductive, and RF WPT systems.

For this purpose, a ME transducer has been developed in this thesis, and compared to a coil-coil system, maintaining the same boundary conditions, such as working frequency, and dimensions of the receiver. The development of the ME transducer started with a physical analysis of the magnetostrictive properties of specific magnetic materials, and piezoelectricity. The two phenomena were then analyzed in a coupled system, showing an extrinsic MagnetoElectric effect.

Different samples have been fabricated with the experimental aim to quantify the correlation between composite dimensions and deliverable output power. In literature, there are reported examples of rectangular and cylindrical ME transducer [2, 3], with multiple layers [4, 9], and composites [10, 9]. In the case of this thesis, a composite made of Terfenol-D, for the magnetostrictive component, and PIC-181, for the piezoelectric material, has been studied. A disk-shaped system has been chosen to avoid secondary magnetic effects at the angles of the device (Chapter 2, Paragraph 4.4), and two diameter values have been adopted, 10 mm and 16 mm. As shown through the characterization tests, the highest value of output power has been achieved from the samples with the biggest diameter and tri-layer configuration; in this case, 40 mW of ME power is achieved, compared to the 12 mW of the sample with tri-layer configuration and small diameter. Moreover, an interesting result shows that thicker samples, with smaller magnetostrictive volume ratio, could achieve lower power, and lower density of power than a thinner sample, with a higher magnetostrictive volume ratio. Table 2.5 of Chapter 3 summarizes the output ME responses of the tested sample. This result shows the potentialities in the miniaturization of the ME transducer, without losing Wireless Power Transfer effectiveness.

Furthermore, from the need to understand and optimize the output characteristics of the ME system a theoretical model has been developed. Thanks to the piezoelectric transducer model [6, 7], and a multiphysics FEM analysis [4], an equivalent electronic circuit has been developed. This circuit has been designed to reproduce the non-linear magnetoelectric behavior of the ME composite, through three main blocks interacting with two coupling coefficients. The circuit model has been estimated integrating and adapting the theoretical formula with the experimental measurements, conducted in the characterization tests of the ME transducer. The theoretical power characteristics results (Chapter 3, Paragraph 2.6.2) are close to the experimental ones, with a difference of about 10%. The estimated accuracy could be further improved considering not only the linear magneto-elastic-electric properties, but also other factors such as the effect of Eddy's currents inside the magnetostrictive material, and the effect of the temperature.

The second part of the thesis was focused on the comparison of Wireless Power Transfer technology of a ME-coil system, and a coil-coil system, under different alignments of the receiver. The aim was to recreate a real

application of wireless power transmission, between an out-body transmitter block, and an in-body receiver one. To guarantee multiple device's excitations with DC and AC magnetic fields, a transmitter coil, with two permanent magnets has been used. For the receiver system, a coil, and a ME transducer of the same dimensions have been tested. The advantage of the ME device consists of the theoretical possibility to collect a usable amount of electrical energy independently on its orientation. For this purpose, a set of in-vitro tests have been performed to measure the response of the ME sample and coil-sample in the air-environment. Furthermore, a set of phantom tests has been made to determine the behavior of the ME device in an environment closer to reality. The experiments show that the strong dependency on the orientation of the coil-coil system can be reduced by substituting a ME device in the receiver block. Therefore, the ME sample started to record negligible output voltages from 20 mm (Chapter 3, Paragraph 4), even if it was orientated in the worst orientation, in a parallel configuration in this case. However, the measured ME output voltage remains dependent on the mutual orientation with the transmitter coil because the magnetostrictive and piezoelectric materials have a preferential axis of magnetization/mechanical deformation/polarization, in which they could be more efficient. Integrating an electronic interface to the ME transducer as shown in Figure 4.15 of Chapter 2 and inserting an amplification component, the output characteristics of the transducer could be stabilized and the dependency on the orientation could be further decreased, especially for a possible application in deep implantable devices.

In conclusion, this thesis reports promising results in the use of MagnetoElectric transducer in Wireless Power Transfer for the recharge of medical implantable devices. As said before, the achieved results in the characterization tests in terms of density of power, open the possibility to optimize and reduce the size of the ME transducers without losing system efficiency. The trend of miniaturized implantable devices makes it highly relevant to try to develop a clean-room process of ME composite fabrication to control the magnetostrictive compounds at the nanoscale. The fabrication regards not only multi-layered compounds but also multiphase material such as 0-3 structures (Figure 4.3, Chapter 2) or multiferroic materials, based on Ni-Zn-Co composites as substitutes of the giant-magnetostrictive composites [1618, 11]. Furthermore, as explained in Chapter 2 Paragraph 2.3.2, there are several new magnetostrictive materials available on the market with large magnetostriction at room temperatures, such as Galfenol, and MetGlas. Some works on this subject are already presented in the literature [9]. To these examples, the optimization of transducer shapes and dimensions could be integrated to enhance the coupling coefficients and to increase the achieved output power.

Finally, several aspects could improve the performances of the ME transducer at microscopic and macroscopic levels, such as the used materials, composite's fabrication, miniaturization, shape of the transducer, and Multiphysics models. In the next decade, all these developments could help to achieve an efficient and compact active implantable device powered with an integrated ME transducer.

2. Bibliography

1. Deterre M., *Toward an energy harvester for leadless pacemakers*, October 2013, theses.fr/2013PA112114
2. Zhai J., Xing Z., Dong S., Li, J., Viehland D., *Magnetoelectric Laminate Composites: An Overview*, Journal of the American Ceramic Society, 2008, 91(2), 351–358. doi:10.1111/j.1551-2916.2008.02259.x
3. Dong S., Li J.F., Viehland D., *Magnetoelectric coupling efficiency, and voltage gain effect in piezoelectric-piezomagnetic laminate composites*, Journal of Materials Science, 41(1), 97–106. doi:10.1007/s10853-005-5930-8
4. Nguyen T.T., *Modélisation par éléments finis de matériaux composites magnéto-électriques*, theses.fr/2011PA112271
5. Malleron K., *Modelisation multiphysique, caractérisation et conception de transducteurs magnétoélectriques pour l'alimentation de capteurs biomédicaux autonomes*, theses.fr/2018SORUS203
6. Badel A., and Lefeuvre E., *Nonlinear Conditioning Circuits for Piezoelectric Energy Harvesters*, Nonlinearity in Energy Harvesting Systems, Springer (2016), doi:10.1007/978-3-319-20355-3_10
7. Brenes A., Morel A., Juillard J., Lefeuvre E., Badel A., *Maximum power point of piezoelectric energy harvesters: a review of optimality condition for electrical tuning*, Smart Materials, and Structures, IOP Publishing, 2020, 29, pp.033001, doi:10.1088/1361-665X/ab6484
8. Aubert A., *Synthèse, caractérisation et modélisation de matériaux multiferroïques (magnétoélectriques) composites massifs*, October 2018, theses.fr/2018SAACLN036
9. Yang G., *Contribution to modelling of magnetoelectric composites for energy harvesting*, theses.fr/2016PA066731
10. Malleron K., *Modelisation multiphysique, caractérisation et conception de transducteurs magnétoélectriques pour l'alimentation de capteurs biomédicaux autonomes*, theses.fr/2018SORUS203
11. V. Morin, *Elaboration de composites multiferroïques et caractérisation de l'effet magnéto-électrique*, theses.fr/2015SAACLN030

Appendix I

WiBEC (Wireless In-Body Environment) – A European Commission ‘Horizon 2020’ Innovative Training Network

WiBEC (Wireless In-Body Environment) is an Innovative Training Network for 16 young researchers, who were recruited, and trained in coordinated manner by academia, industry, and medical centers. WiBEC’s main objective is to provide high quality, and innovative doctoral training to develop the wireless technologies for novel implantable devices that will contribute to the improvement in quality, and efficacy of healthcare. Two devices will be used as a focus for the individual researcher’s projects: cardiovascular implants, and gastroenterological capsules. These devices will enable medical professionals to have timely clinical information at the point of care. The medical motivation is to increase survival rates, and improvement of health outcomes with easy, and fast diagnosis, and treatment. In this Innovative Training Network, inter-sectorial, and multi-discipline work is essential, as the topic requires cooperation between medical, and engineering institutions, and industry. Thus, the WiBEC consortium is composed of 3 Universities, 2 hospitals, and 3 companies located in different countries (Spain, France, Germany, and Norway) in Europe.

Partners

Hospitals



Academy



Industry



Appendix II

Datasheet of Terfenol-D

Terfenol-D Physical Properties	
Standard Composition	Tb _{0.3} Dy _{0.7} Fe _{1.92}
Mechanical Properties	
Density	9200 - 9300 kg/m ³
Young's Modulus at constant l	18 - 55 GPa
Young's Modulus at constant V	50 - 90 GPa
Bulk Modulus	90 GPa
Speed of Sound	1395 - 2444 m/s
Tensile Strength	28 - 40 MPa
Compressive Strength	300 - 880 MPa
Vicker's Hardness	650HV
Minimum Laminate Thickness	1mm
Thermal Properties	
CTE	11 ppm / °C @ 25 °C
Specific Heat	0.33 kJ/(kg - K)
Thermal Conductivity	13.5 W/(m - K) @ 25 °C
Melting Point	1240 °C
Electrical Properties	
Resistivity	60 x 10 ⁻⁸ Ohm-meters
Curie Temperature	380 °C
Magnetostrictive Properties	
Strain (estimated linear)	800 - 1200 ppm
Energy Density	4.9 - 25 kJ/m ³
Piezomagnetic Constant, d ₃₃	6-10 nm/A
Magnetomechanical Properties	
Coupling Factor	0.7 - 0.8
Magnetic Properties	
Relative Permeability	2 - 10
Saturation Flux Density	1 Tesla

Reference

<http://tdvib.com/terfenol-d/>

Material coefficients PIC181					
Coefficient	Unit	Value	Coefficient	Unit	Value
Density	kg/m³	7850	N1	Hzm	1646
Qm		2200	N3*	Hzm	2004
Tc	°C	330	N5*	Hzm	1222
tan δ		3.0E-3	Np	Hzm	2265
			Nt*	Hzm	2302
ε 11Tr		1224			
ε 33Tr		1135	d31	m/V	-1.080E-10
ε 11Sr		740	d33	m/V	2.530E-10
ε 33Sr		624	d15	m/V	3.890E-10
β 11T	Vm/As	9.232E+07	g31	Vm/N	-1.080E-02
β 33T	Vm/As	9.955E+07	g33	Vm/N	2.520E-02
β 11S	Vm/As	1.527E+08	g15	Vm/N	3.590E-02
β 33S	Vm/As	1.811E+08			
			e31	N/Vm	-4.500E+00
k31		0.32	e33	N/Vm	1.470E+01
k33		0.66	e15	N/Vm	1.100E+01
k15		0.63			
kp		0.55	h31	N/As	-8.149E+08
kt		0.46	h33	N/As	2.662E+09
			h15	N/As	1.680E+09
Poisson (σ)		0.35			
s11E	m²/N	1.175E-11	c11E	N/m²	1.523E+11
s33E	m²/N	1.411E-11	c33E	N/m²	1.341E+11
s55E	m²/N	3.533E-11	c55E	N/m²	2.830E+10
s12E	m²/N	-4.070E-12	c12E	N/m²	8.909E+10
s13E	m²/N	-4.996E-12	c13E	N/m²	8.547E+10
s44E	m²/N	3.533E-11	c44E	N/m²	2.830E+10
s66E	m²/N	3.164E-11	c66E	N/m²	3.161E+10
s11D	m²/N	1.058E-11	c11D	N/m²	1.550E+11
s33D	m²/N	7.930E-12	c33D	N/m²	1.664E+11
s55D	m²/N	2.134E-11	c55D	N/m²	4.686E+10
s12D	m²/N	-5.235E-12	c12D	N/m²	9.182E+10
s13D	m²/N	-2.268E-12	c13D	N/m²	7.061E+10
s44D	m²/N	2.134E-11	c44D	N/m²	4.686E+10
s66D	m²/N	3.164E-11	c66D	N/m²	3.161E+10

v2.0 / 16.09.2008

The table contains consistent numerical data for simulation purposes.

Values are no specifications.

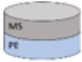
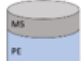

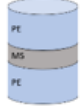

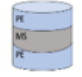
* N3, N5 and Nt are defined as fp*length and fp*thickness, according to DIN EN 50324

Reference

https://static.piceramic.com/fileadmin/user_upload/pi_ceramic/files/brochure_BRO/PI_Dynamic_Behavior_Pi_ezoceramics.pdf

Appendix III

Table of MagnetoElectric samples:

Sample	# layers	\varnothing [mm]	tp [mm]	tm [mm]	m (g)
A) 	2 layers	16	1	1	3.7
B) 	2 layers	16	2	1	5.16
C) 	3 layers (M-P-M)	16	2	1 and 1	6.97
D) 	3 layers (P-M-P)	16	2 and 2	1	8.41
E) 	2 layers	10	1	1	2.53
F) 	3 layers	10	1 and 1	1	4.03

Sample A)

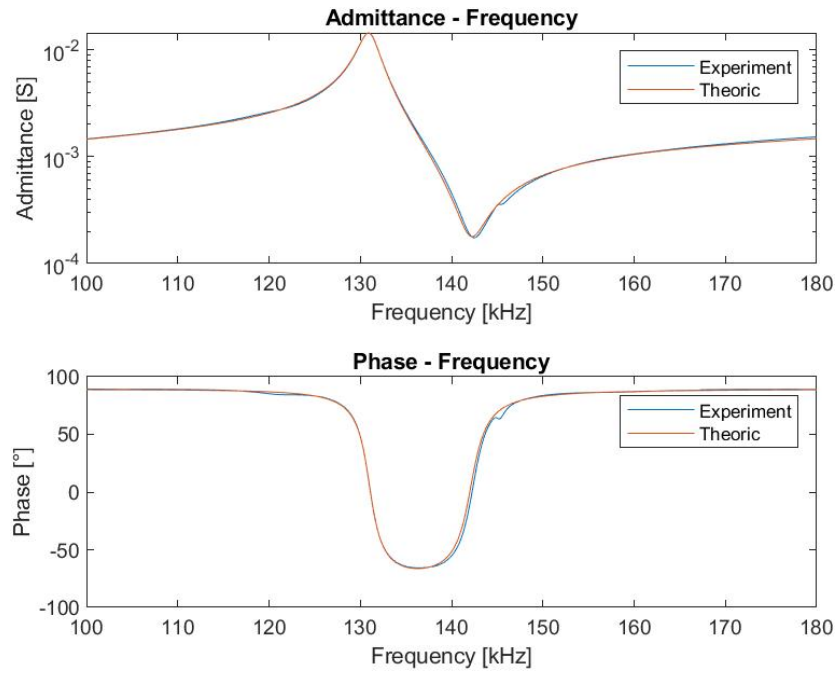


Figure 0.2 - Experimental, and theoretical behavior of a ME transducer in static regime in open circuit. Sample A.

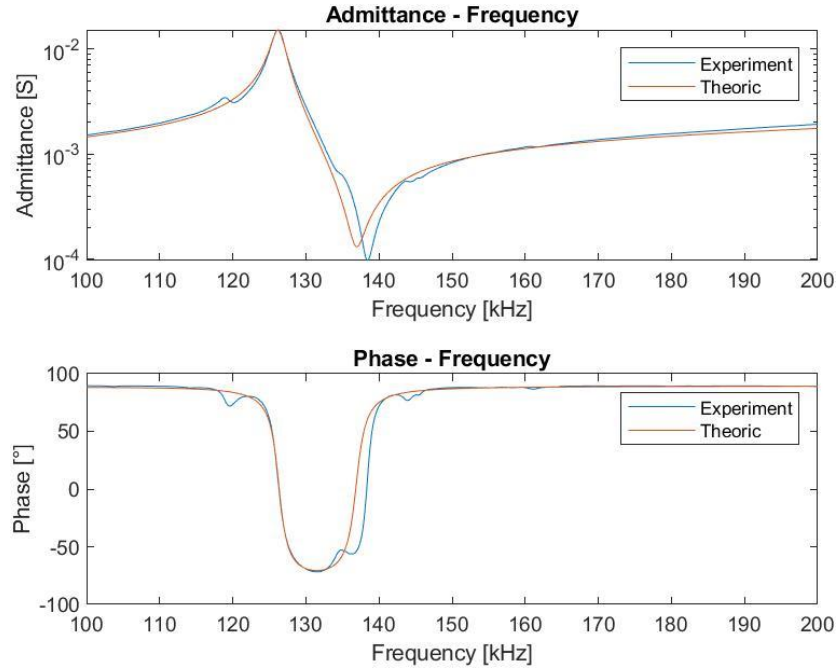


Figure 0.2 - Experimental, and theoretical behavior of a ME transducer in static regime, under a bias field of 0.1 T. Sample A.

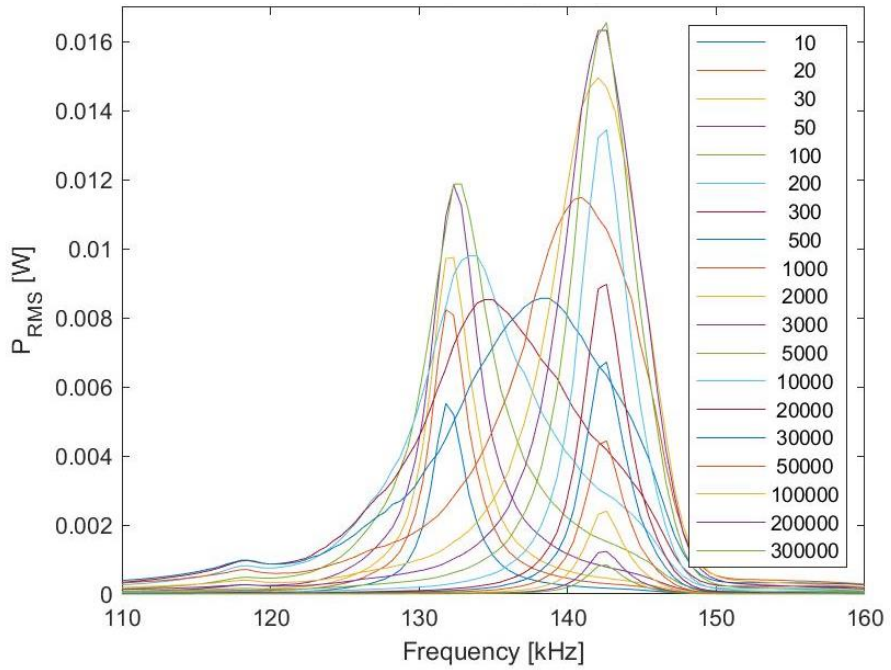
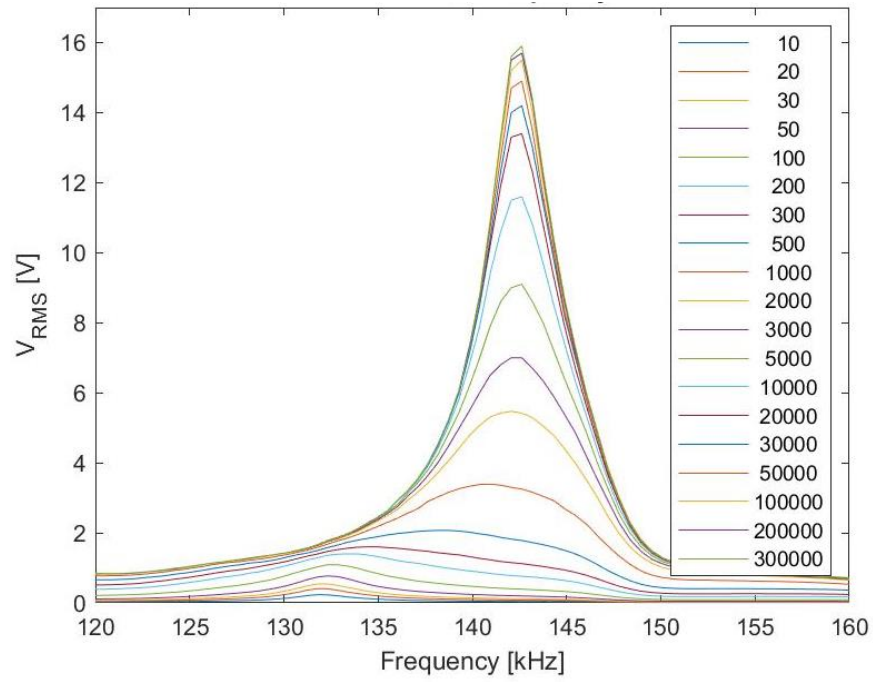


Figure 0.3 – ME RMS Voltage, and ME RMS Power at 0.1 T DC magnetic field, and 0.8 mT AC magnetic field, over the spectrum of frequency for different loads. Sample A.

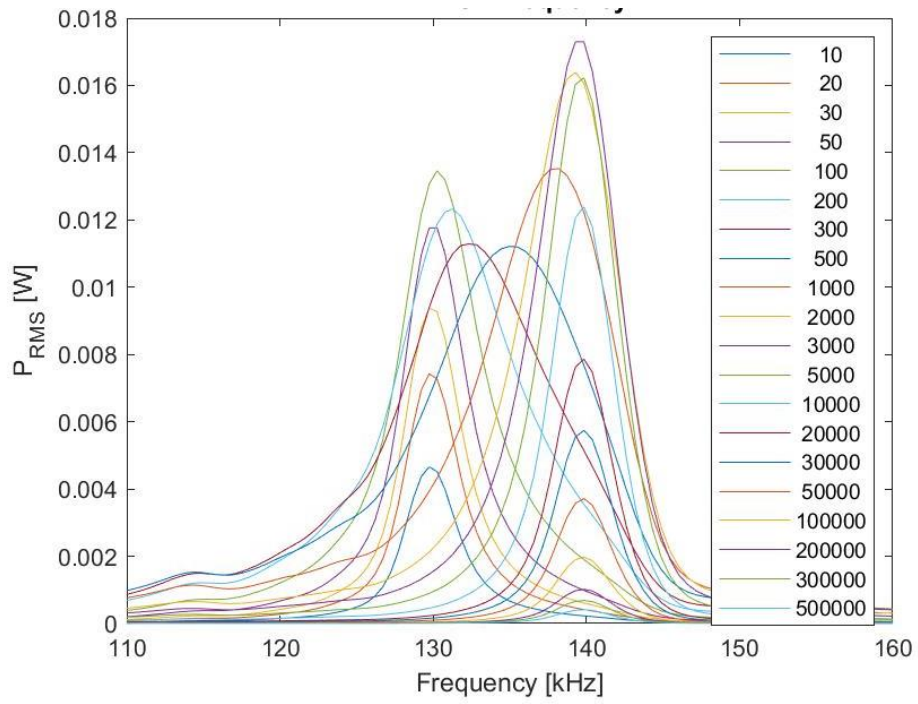
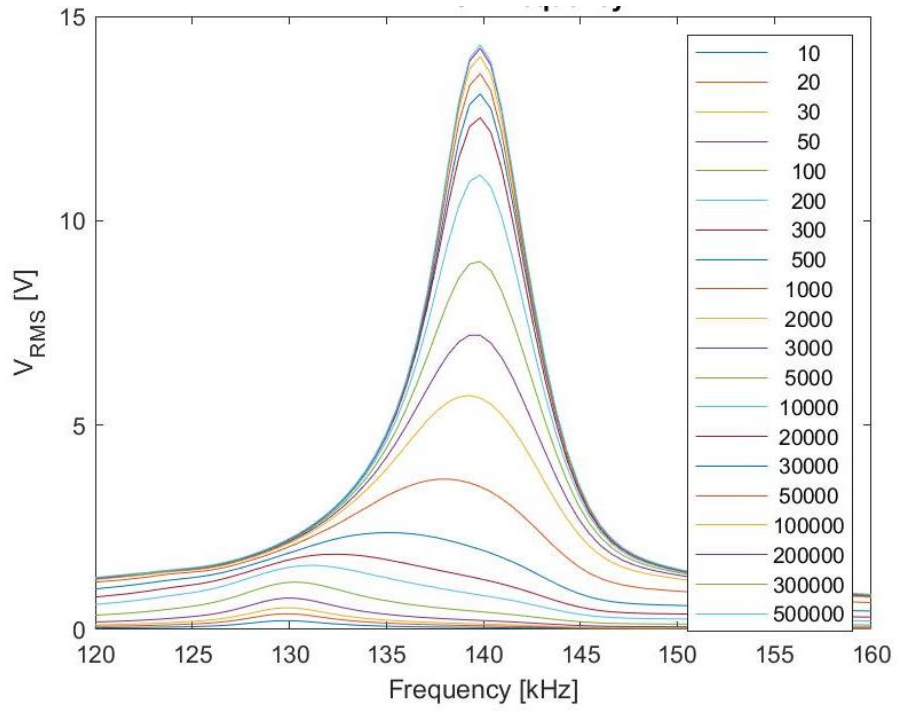


Figure 0.4 - ME RMS Voltage, and ME RMS Power at 0.058 T DC magnetic field, and 0.8 mT AC magnetic field, over the spectrum of frequency for different loads. Sample A.

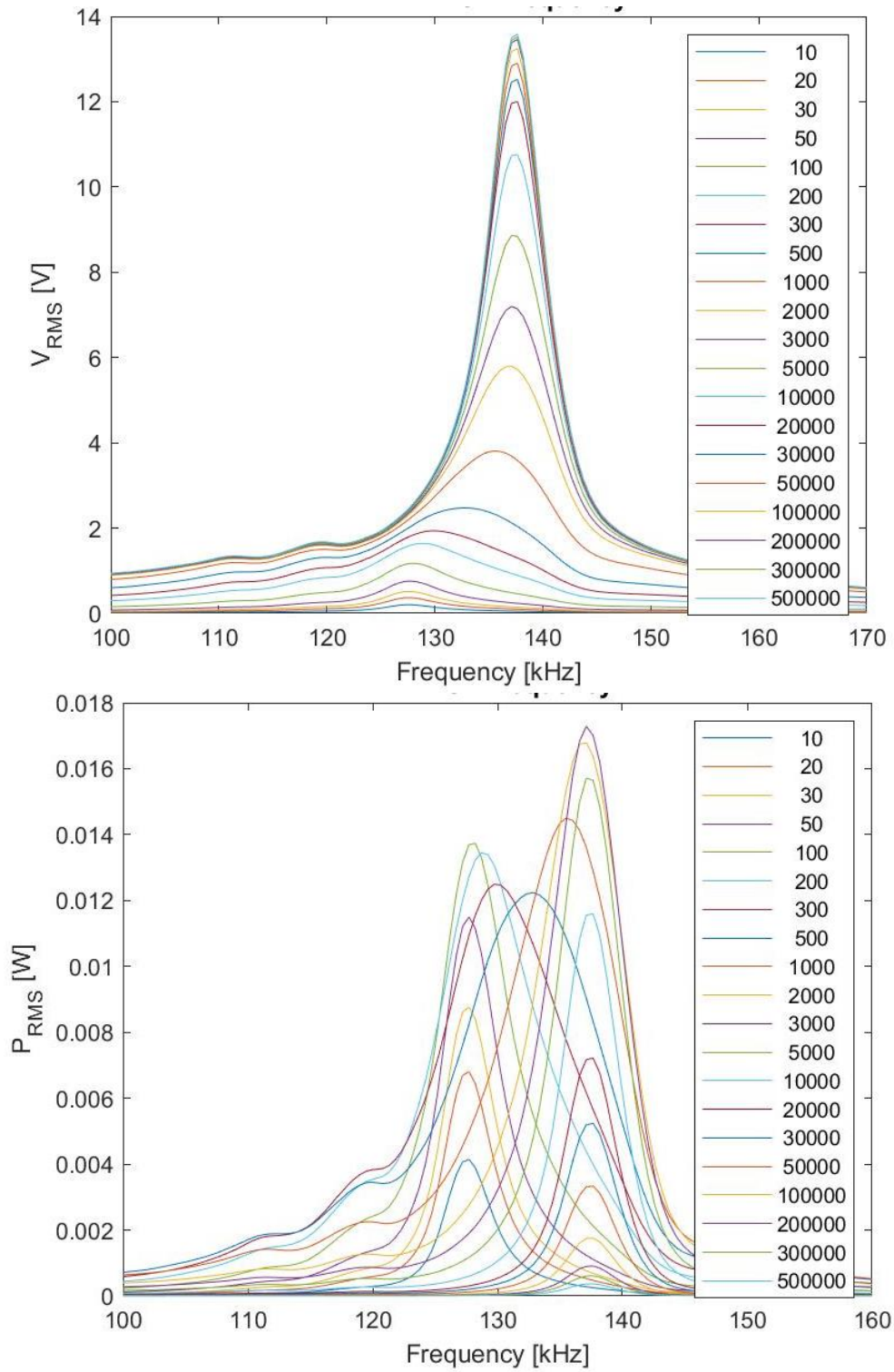


Figure 0.5 - ME RMS Voltage, and ME RMS Power at 0.036 T DC magnetic field, and 0.8 mT AC magnetic field, over the spectrum of frequency for different loads. Sample A.

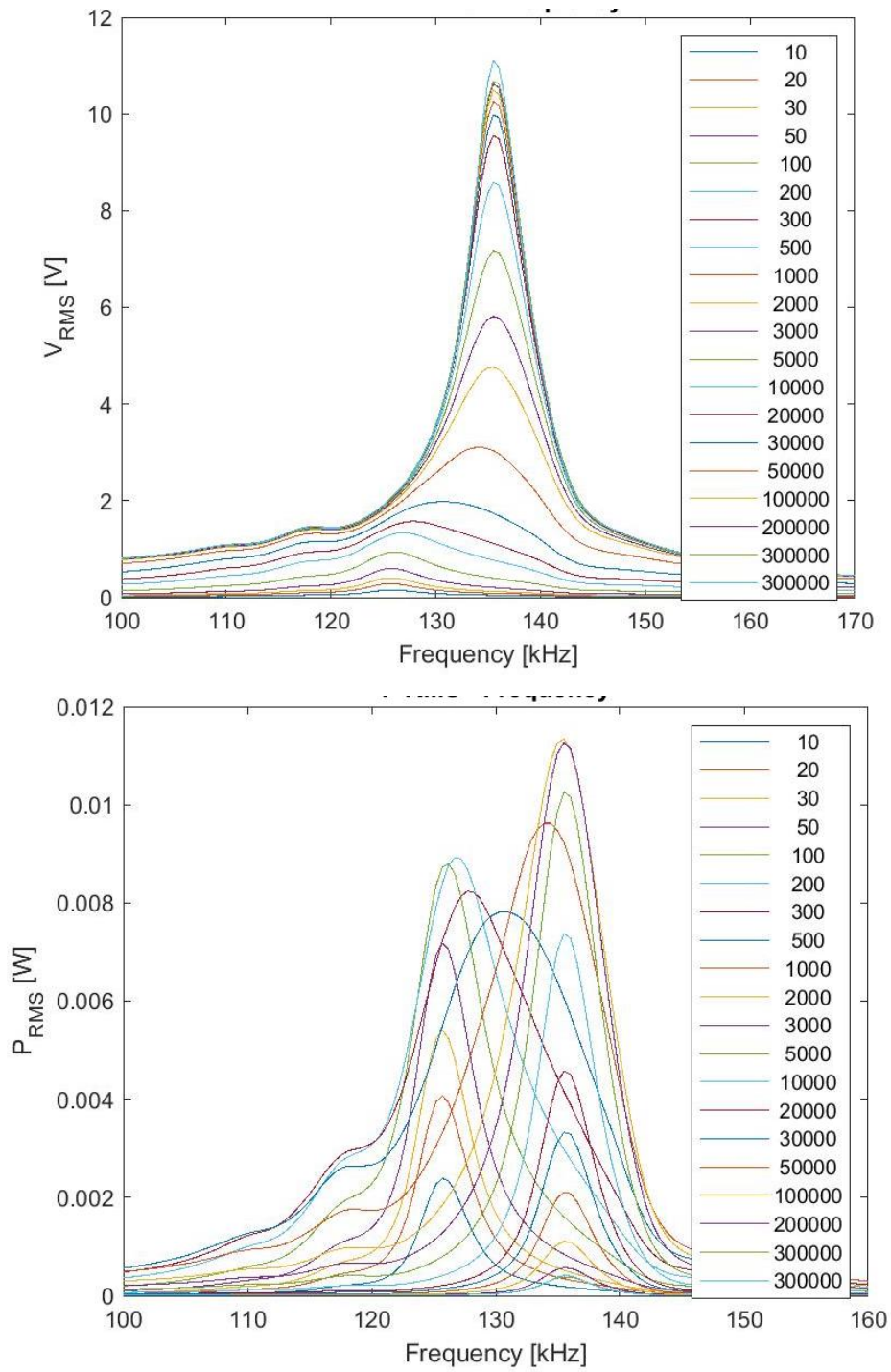


Figure 0.6 - ME RMS Voltage, and ME RMS Power at 0.023 T DC magnetic field, and 0.8 mT AC magnetic field, over the spectrum of frequency for different loads. Sample A.

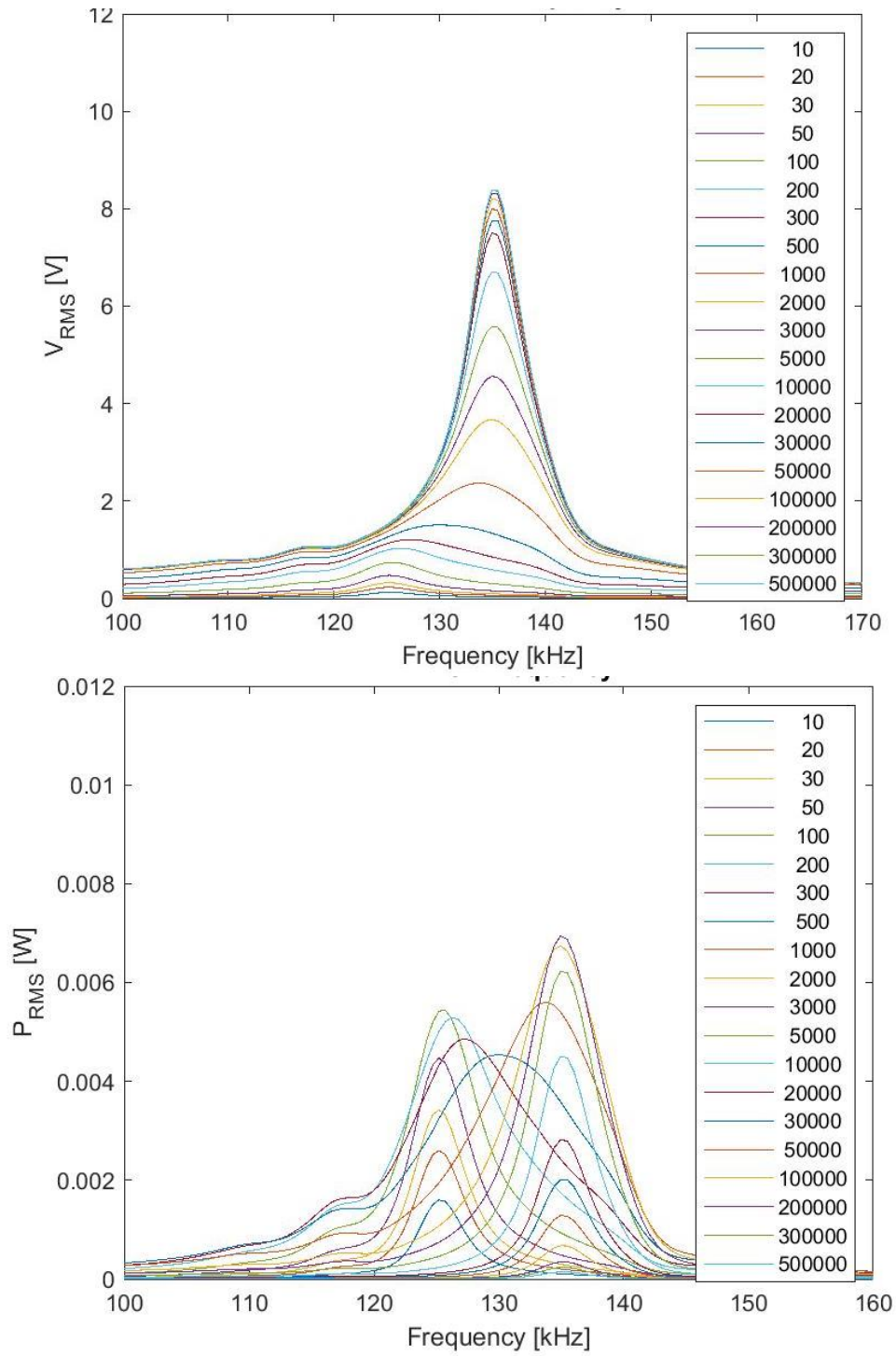


Figure 0.7 - Figure 0.8 - ME RMS Voltage, and ME RMS Power at 0.016 T DC magnetic field, and 0.8 mT AC magnetic field, over the spectrum of frequency for different loads. Sample A.

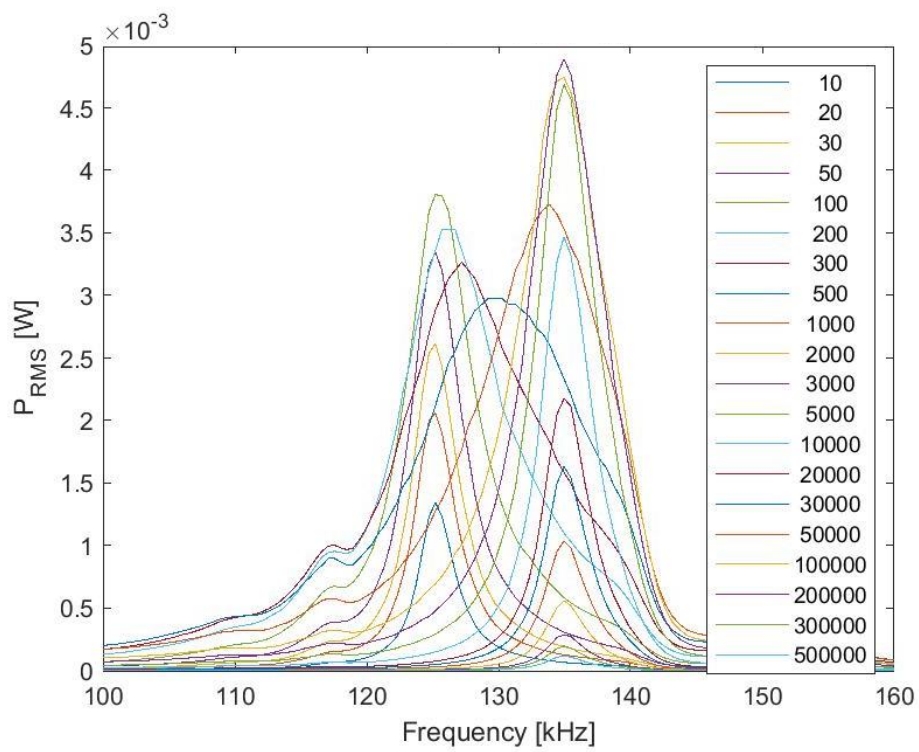
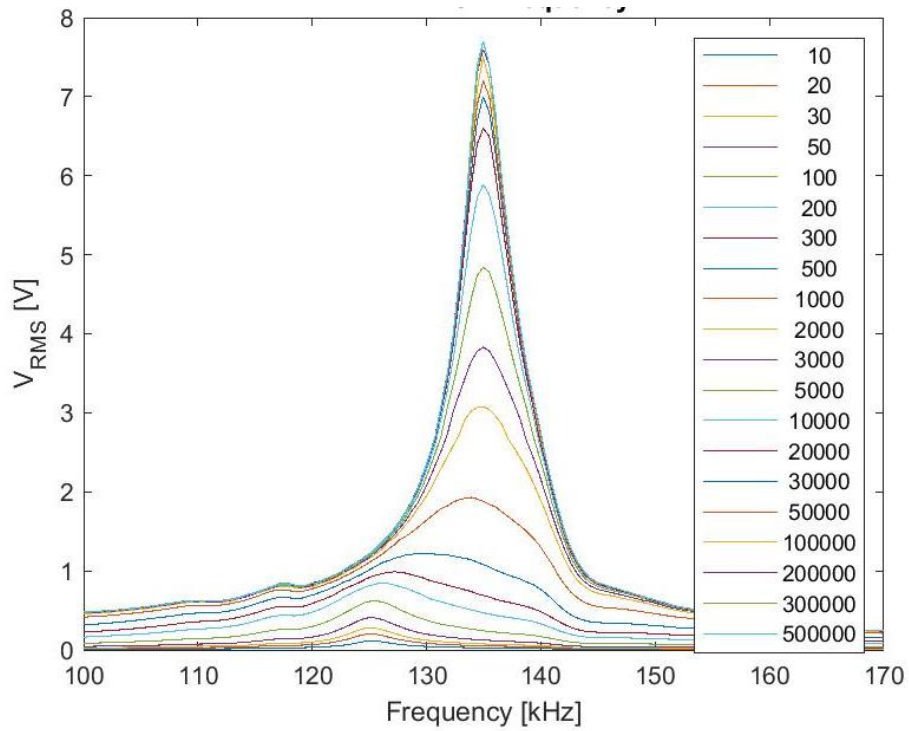


Figure 0.9 - ME RMS Voltage, and ME RMS Power at 0.012 T DC magnetic field, and 0.8 mT AC magnetic field, over the spectrum of frequency for different loads. Sample A.

Sample B)

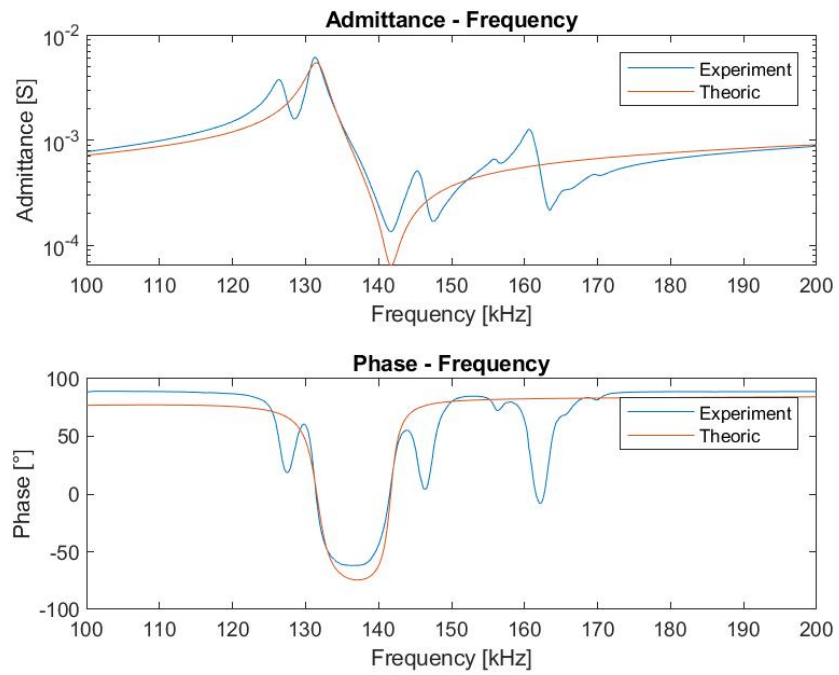


Figure 0.11 - Experimental, and theoretical behavior of a ME transducer in static regime in open circuit. Sample B.

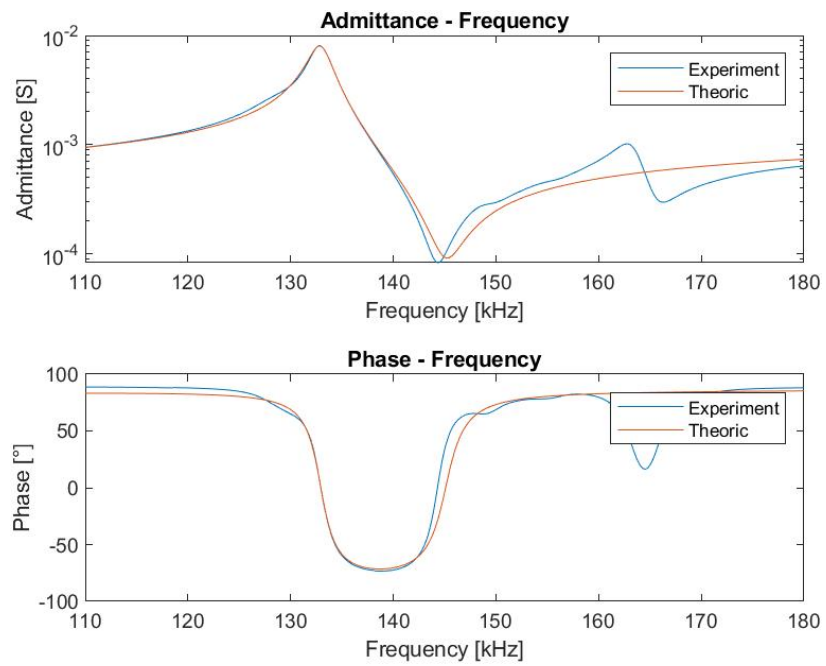


Figure 0.11 - Experimental, and theoretical behavior of a ME transducer in static regime, under a bias field of 0.1 T. Sample B.

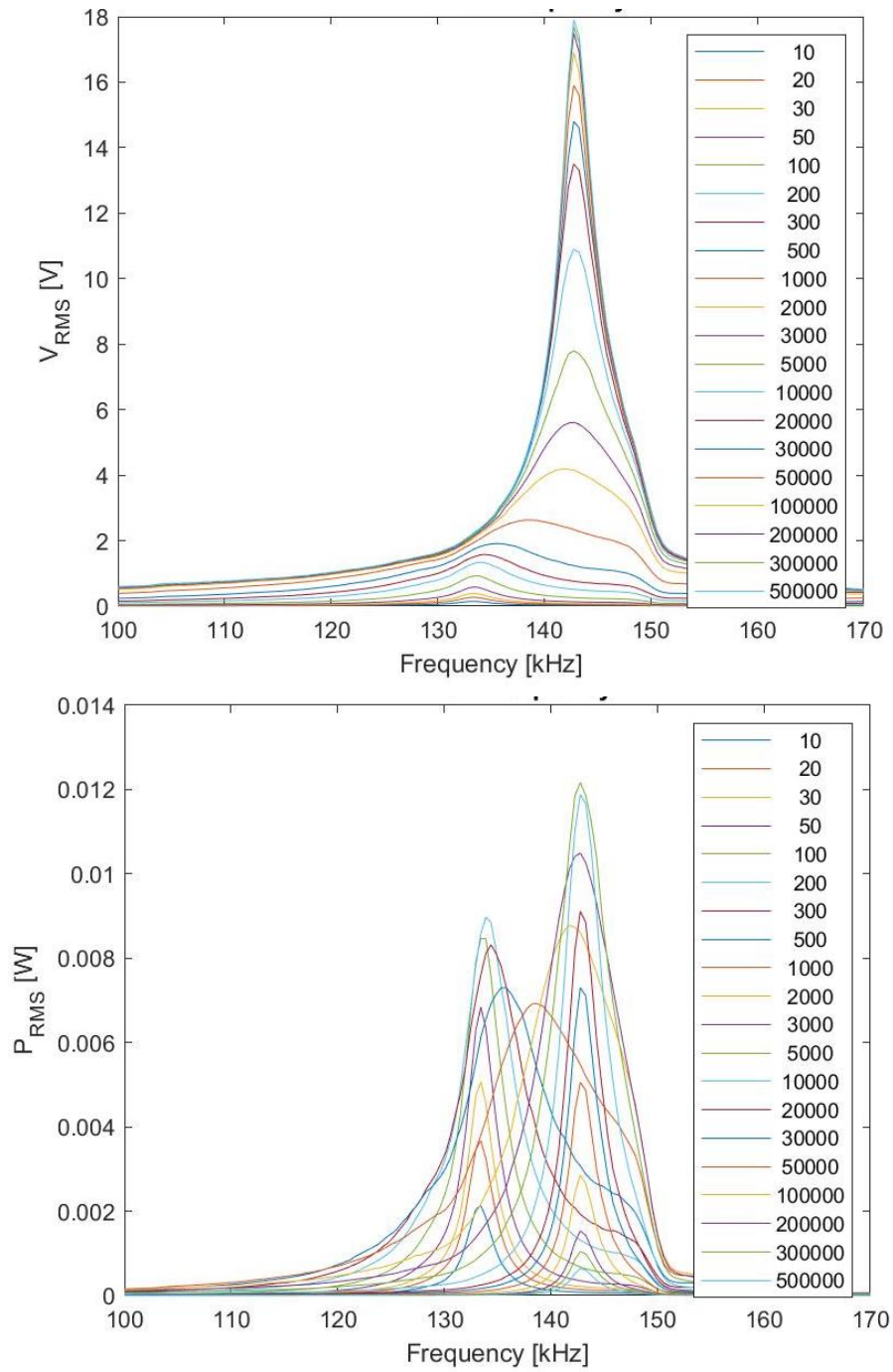


Figure 0.12 - ME RMS Voltage, and ME RMS Power at 0.1 T DC magnetic field, and 0.8 mT AC magnetic field, over the spectrum of frequency for different loads. Sample B.

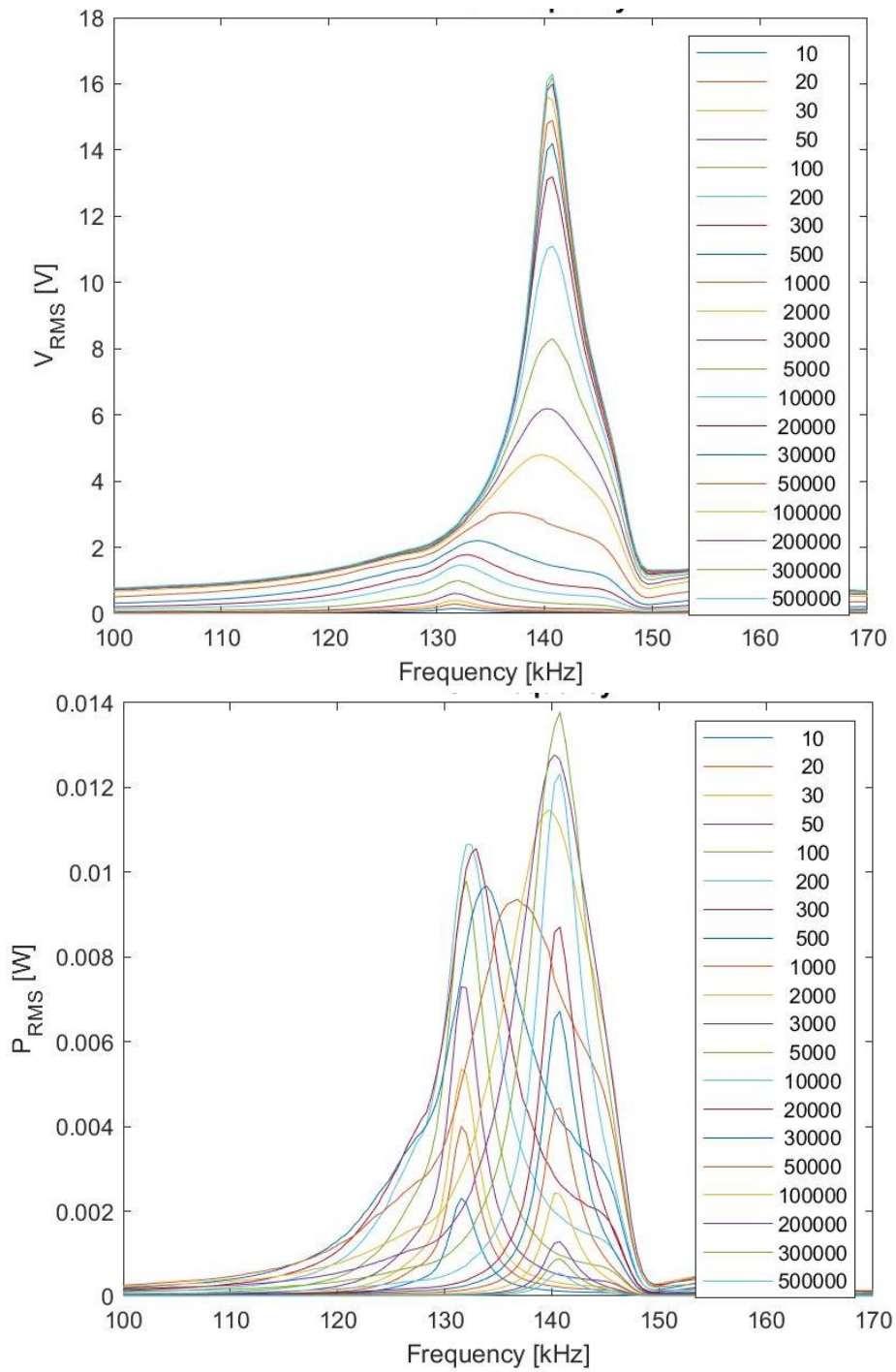


Figure 0.13 - ME RMS Voltage, and ME RMS Power at 0.058 T DC magnetic field, and 0.8 mT AC magnetic field, over the spectrum of frequency for different loads. Sample B.

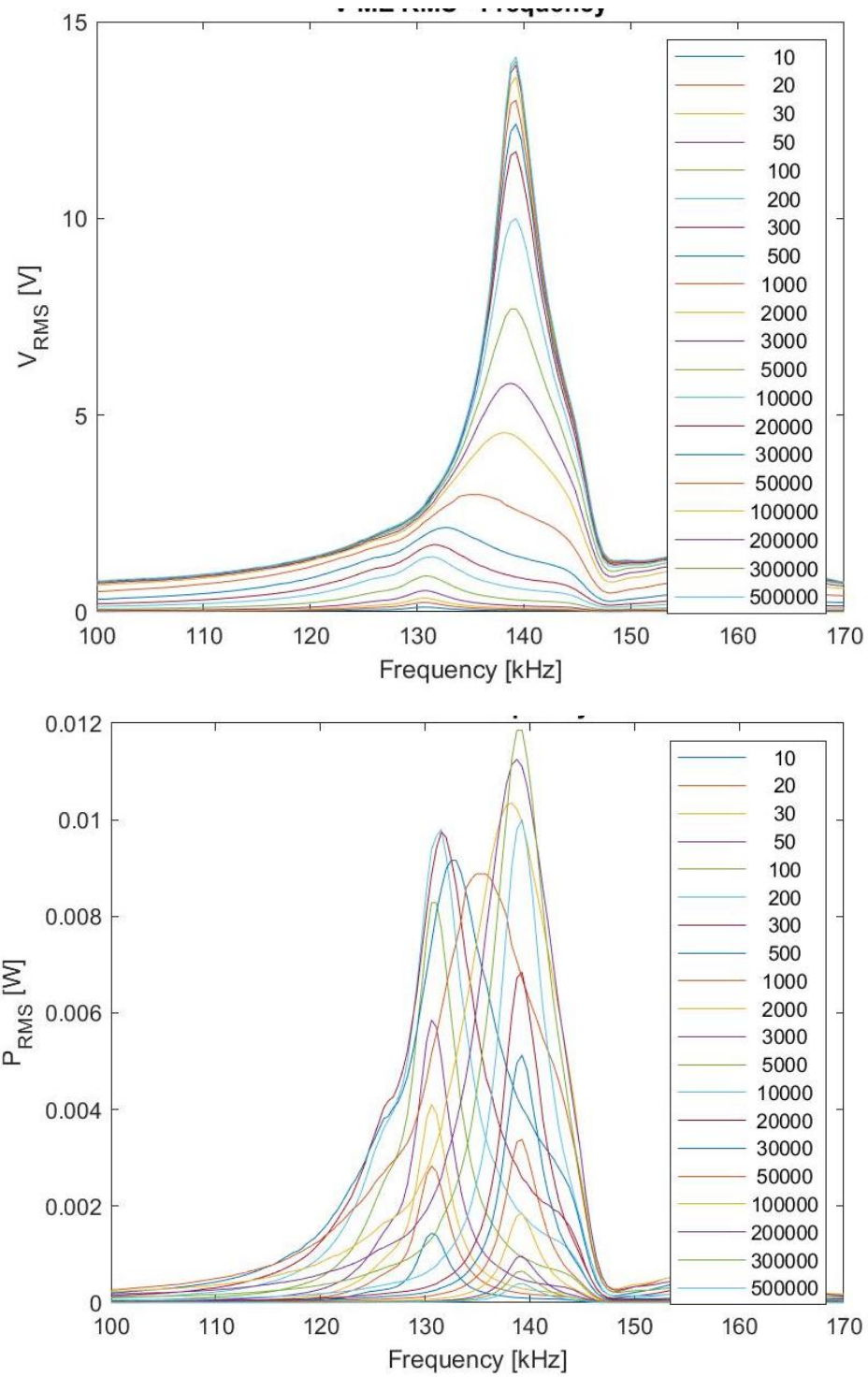


Figure 0.14 - ME RMS Voltage, and ME RMS Power at 0.036 T DC magnetic field, and 0.8 mT AC magnetic field, over the spectrum of frequency for different loads. Sample B.

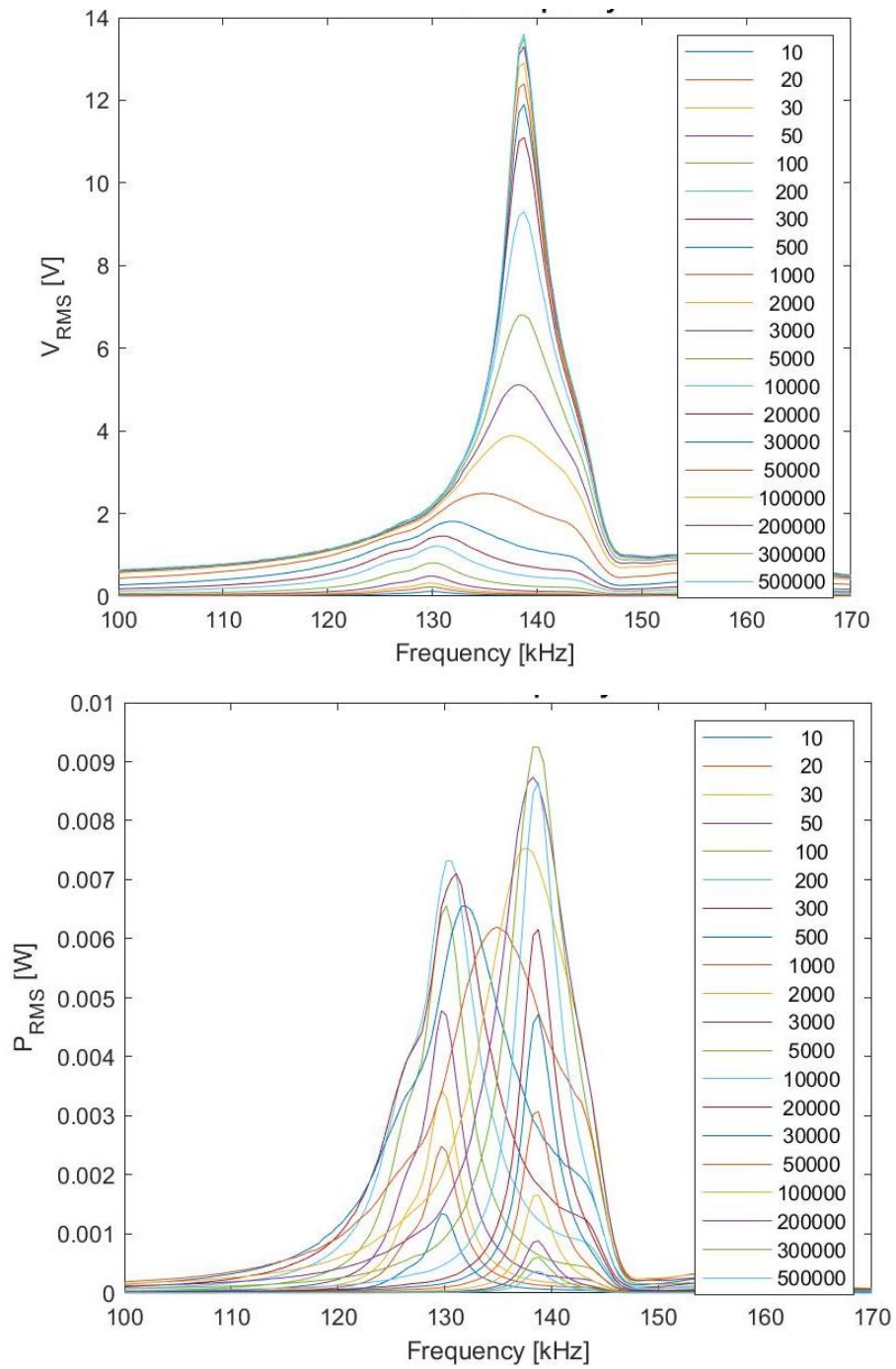


Figure 0.15 - ME RMS Voltage, and ME RMS Power at 0.023 T DC magnetic field, and 0.8 mT AC magnetic field, over the spectrum of frequency for different loads. Sample B.

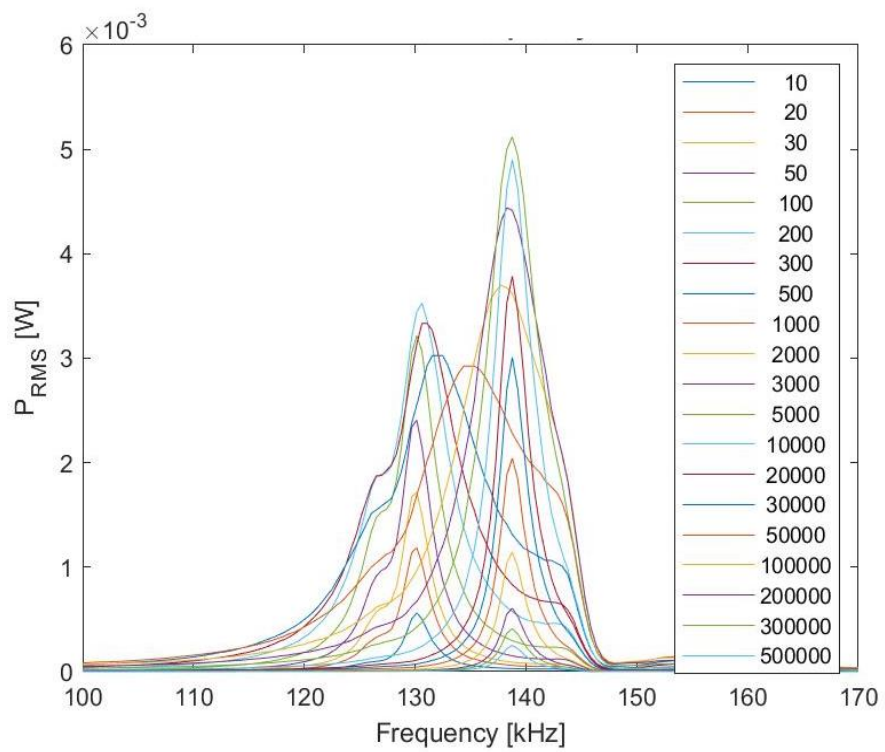
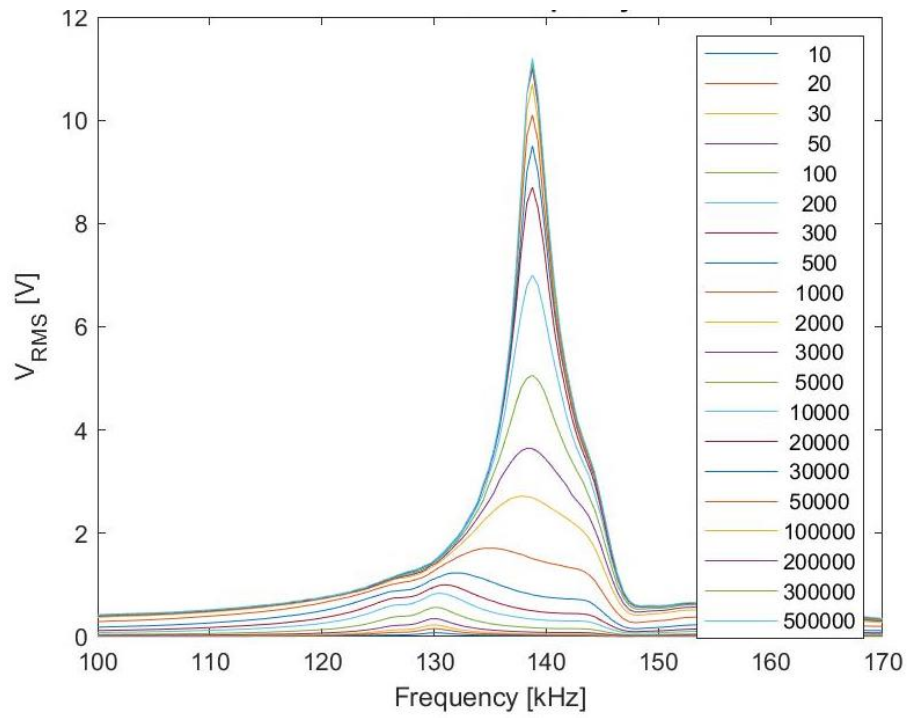


Figure 0.16 - ME RMS Voltage, and ME RMS Power at 0.016 T DC magnetic field, and 0.8 mT AC magnetic field, over the spectrum of frequency for different loads. Sample B.

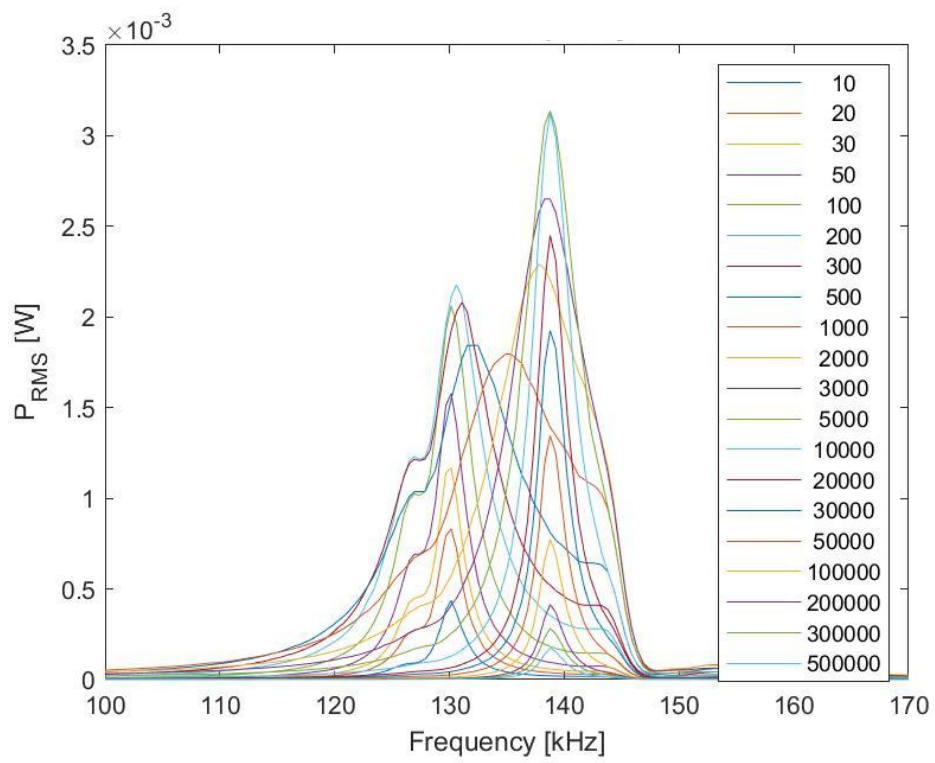
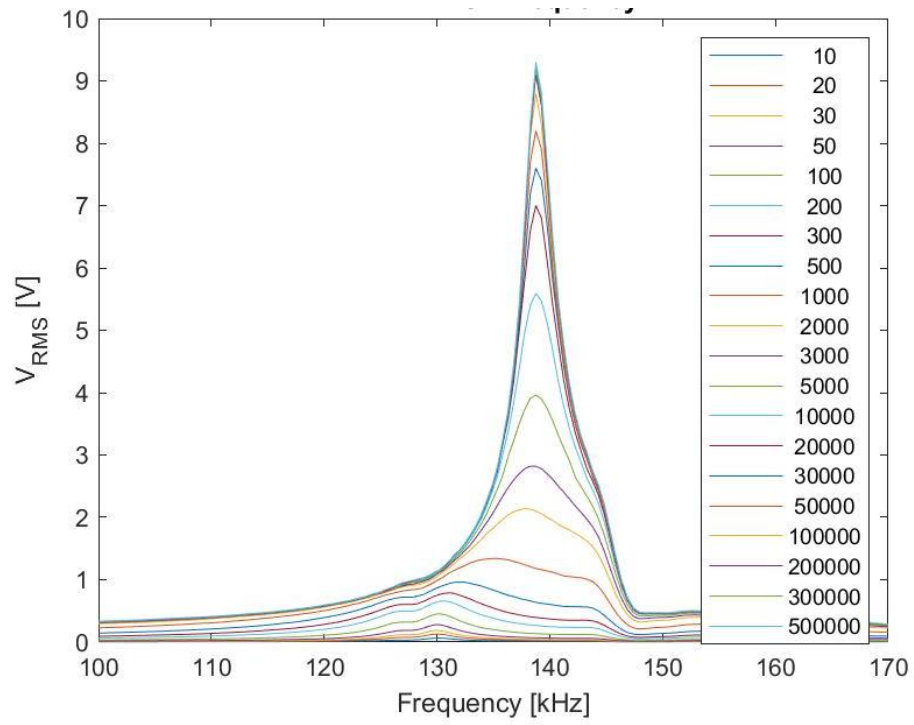


Figure 0.17 - ME RMS Voltage, and ME RMS Power at 0.012 T DC magnetic field, and 0.8 mT AC magnetic field, over the spectrum of frequency for different loads. Sample B.

Sample D)

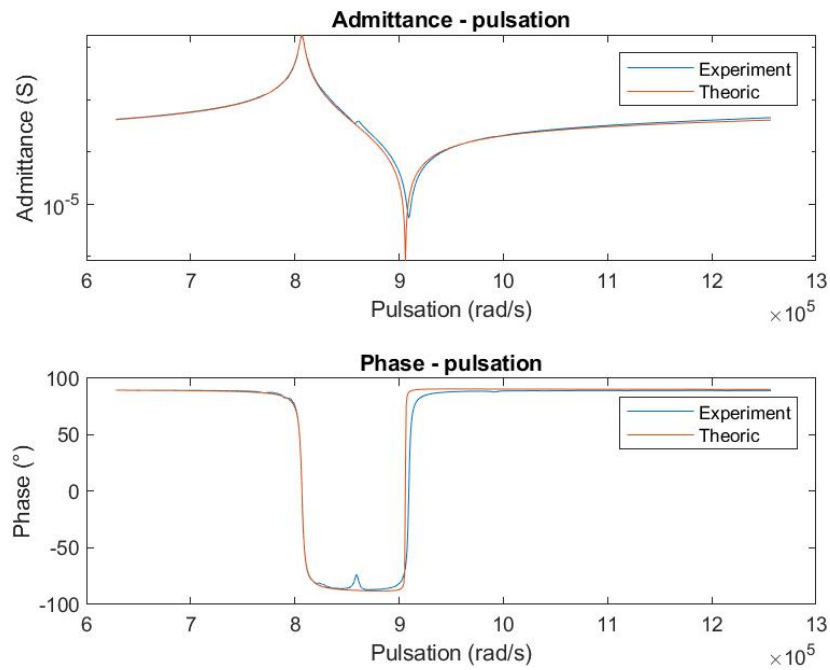


Figure 0.19 - Experimental, and theoretical behavior of a ME transducer in static regime in open circuit. Sample D.

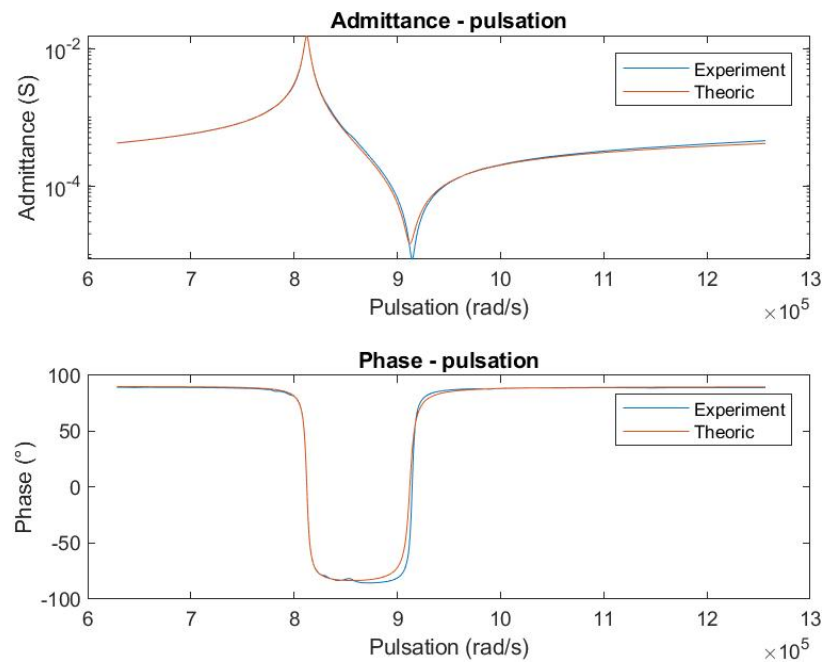


Figure 0.19 - Experimental, and theoretical behavior of a ME transducer in static regime, under a bias field of 0.1 T. Sample D.

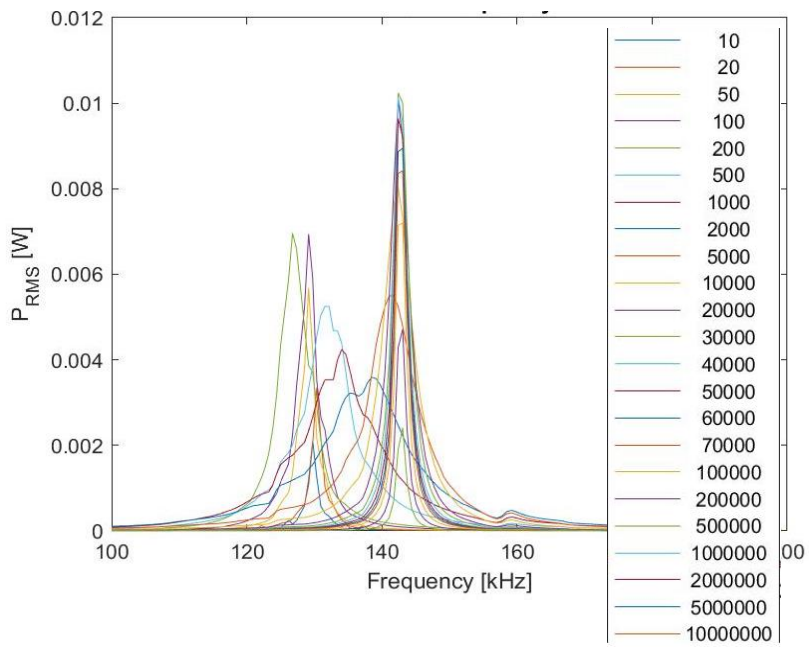
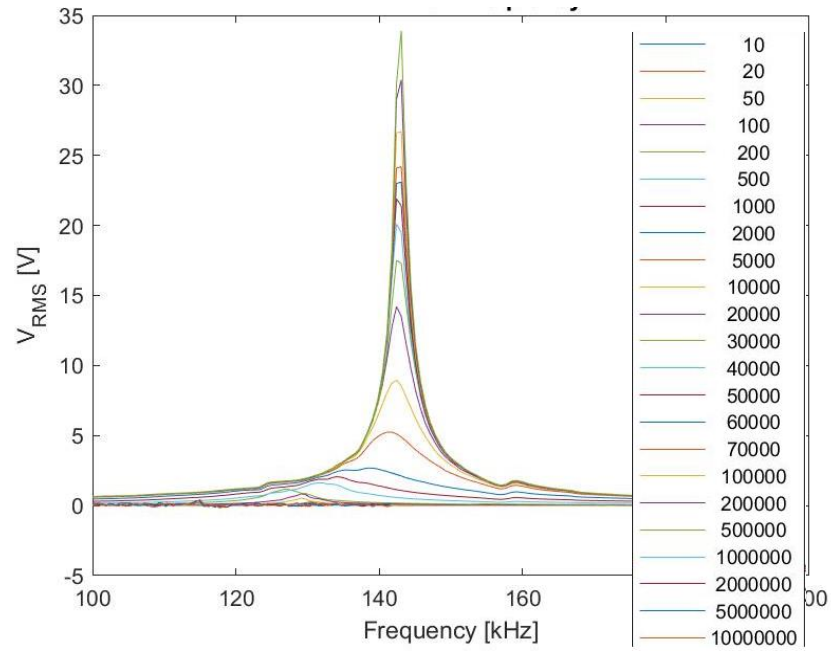


Figure 0.20 - ME RMS Voltage, and ME RMS Power at 0.1 T DC magnetic field, and 0.8 mT AC magnetic field, over the spectrum of frequency for different loads. Sample D.

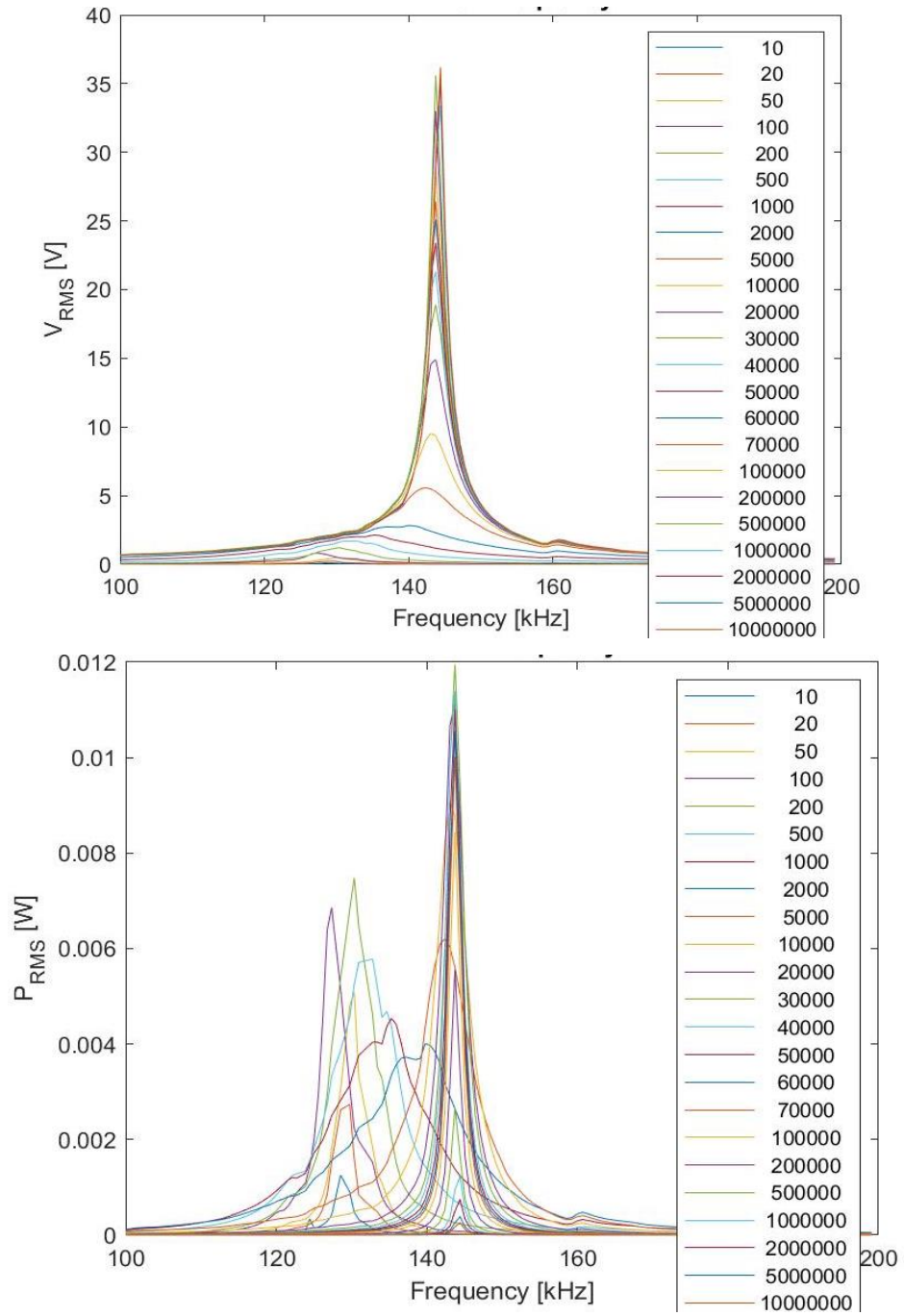


Figure 0.21 - ME RMS Voltage, and ME RMS Power at 0.058 T DC magnetic field, and 0.8 mT AC magnetic field, over the spectrum of frequency for different loads. Sample D.

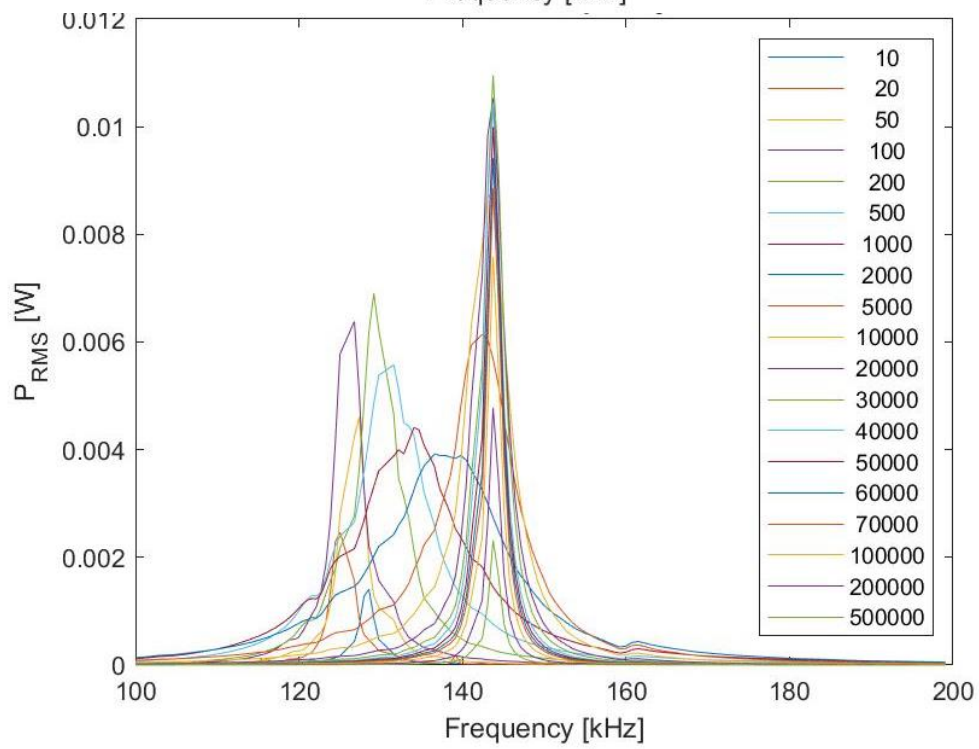
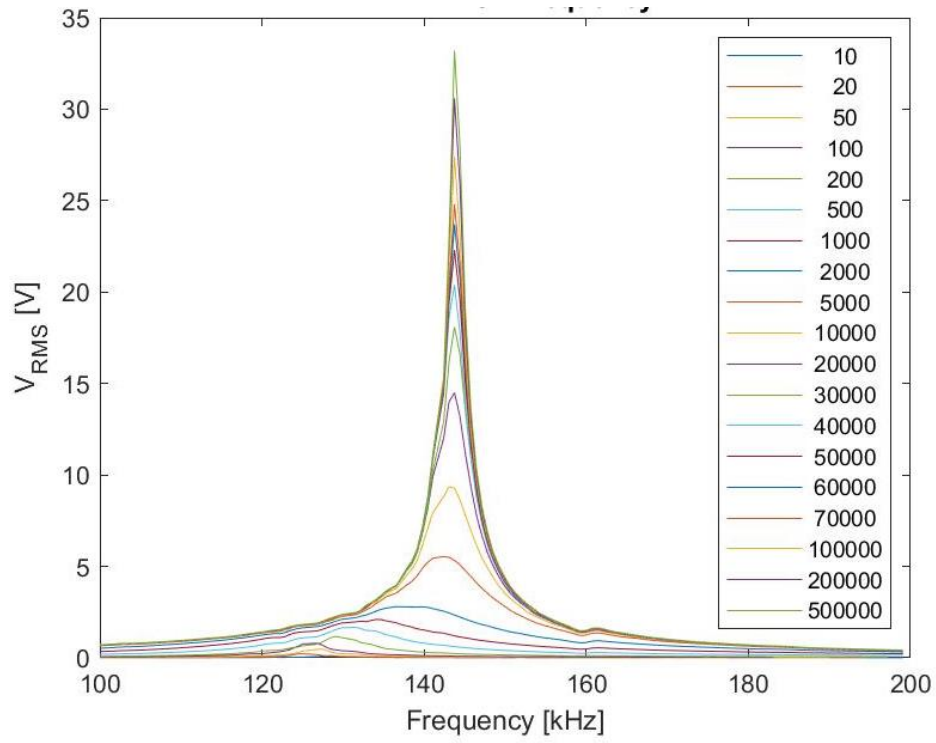


Figure 0.22 - ME RMS Voltage, and ME RMS Power at 0.036 T DC magnetic field, and 0.8 mT AC magnetic field, over the spectrum of frequency for different loads. Sample D.

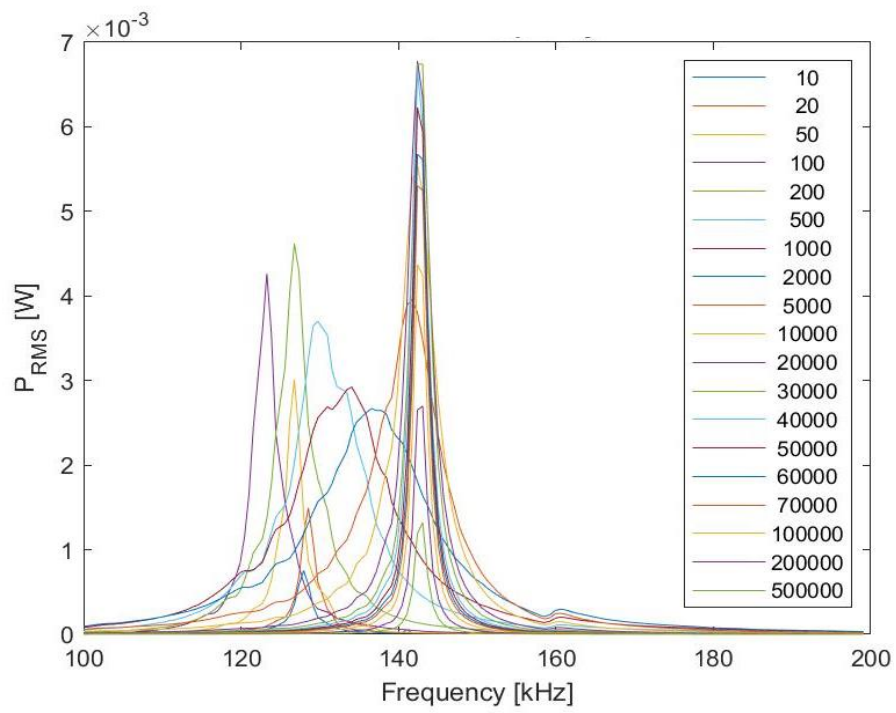
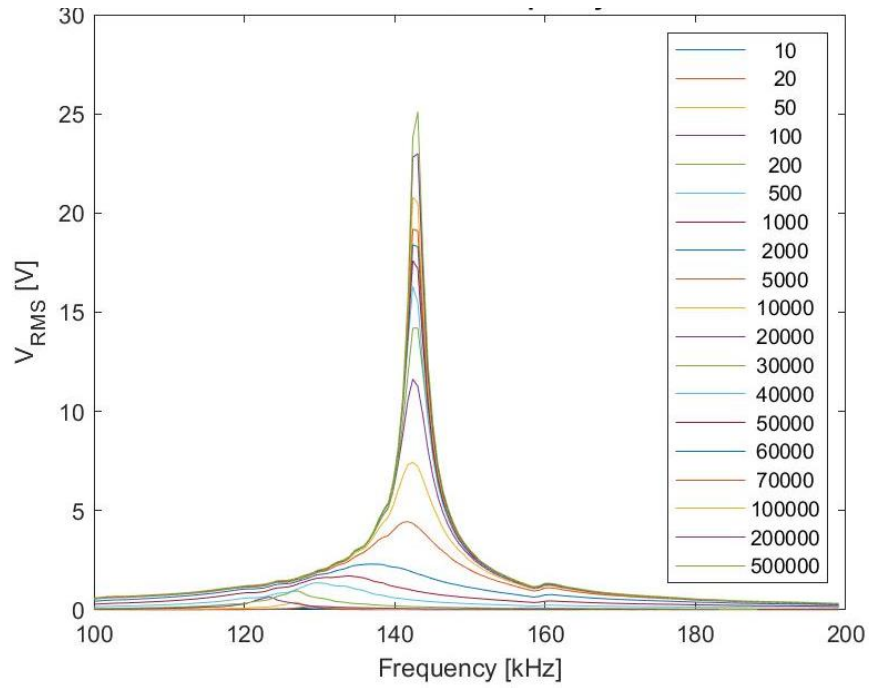


Figure 0.23 - ME RMS Voltage, and ME RMS Power at 0.023 T DC magnetic field, and 0.8 mT AC magnetic field, over the spectrum of frequency for different loads. Sample D.

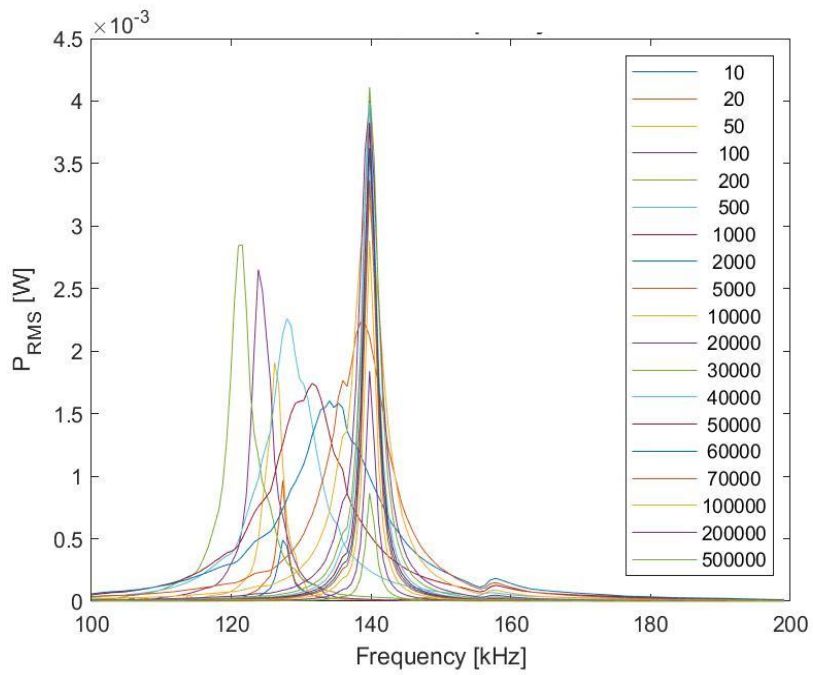
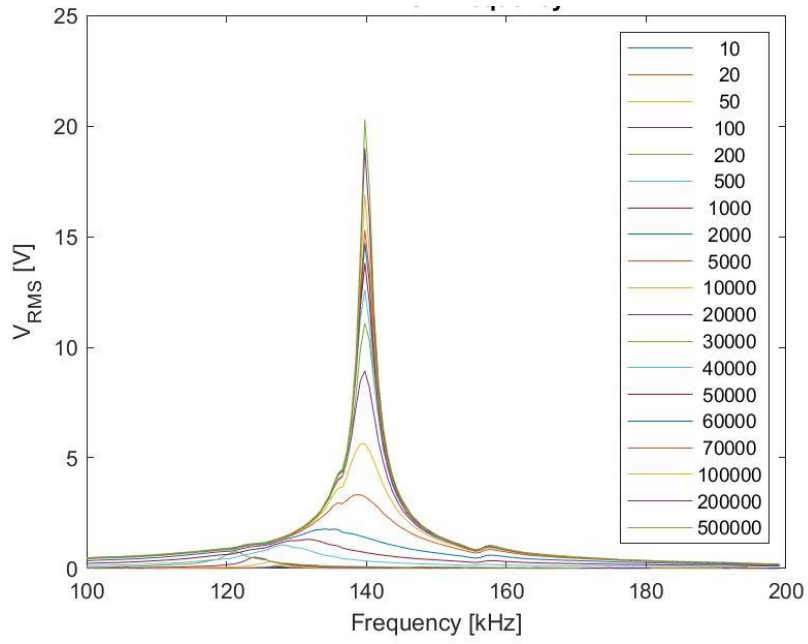


Figure 0.24 - ME RMS Voltage, and ME RMS Power at 0.016 T DC magnetic field, and 0.8 mT AC magnetic field, over the spectrum of frequency for different loads. Sample D.

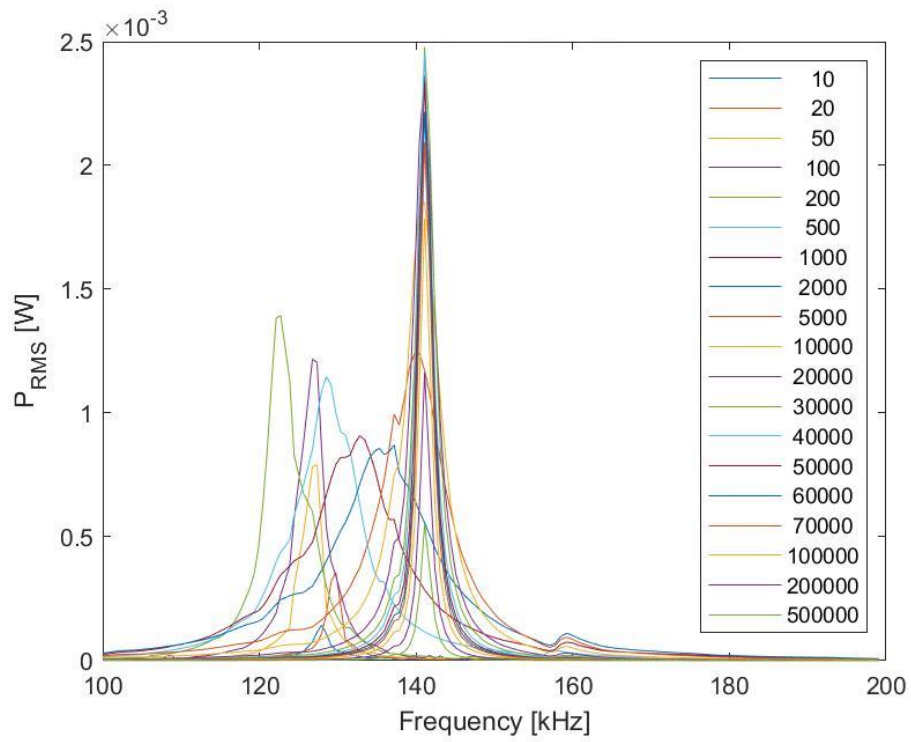
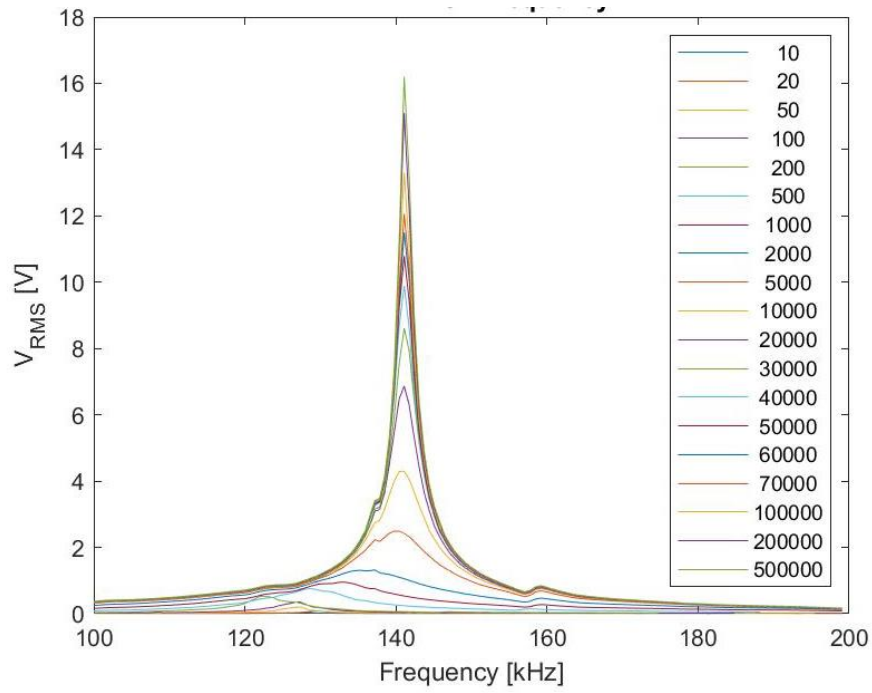


Figure 0.25 - ME RMS Voltage, and ME RMS Power at 0.012 T DC magnetic field, and 0.8 mT AC magnetic field, over the spectrum of frequency for different loads. Sample D.

Sample E)

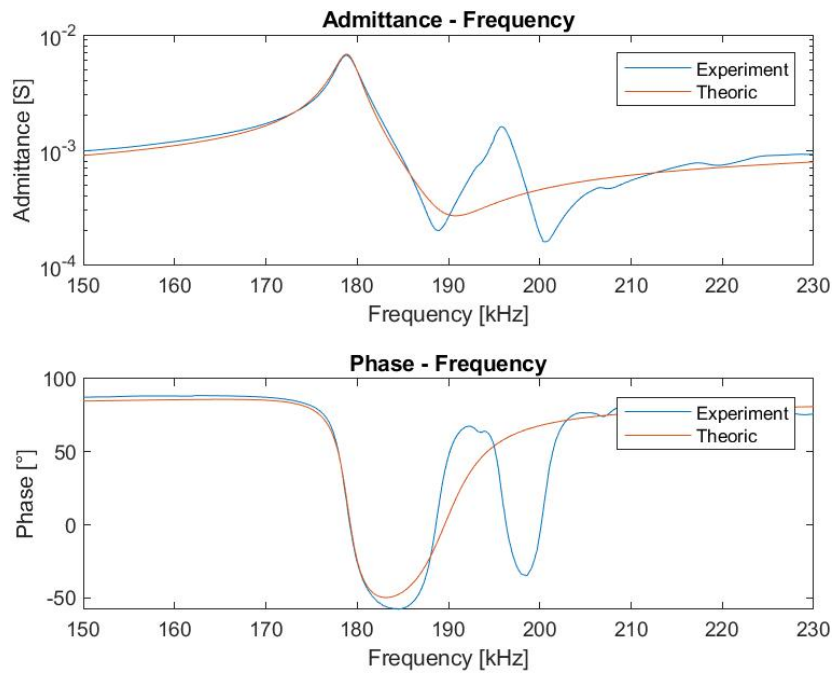


Figure 0.27 - Experimental, and theoretical behavior of a ME transducer in static regime in open circuit. Sample E.

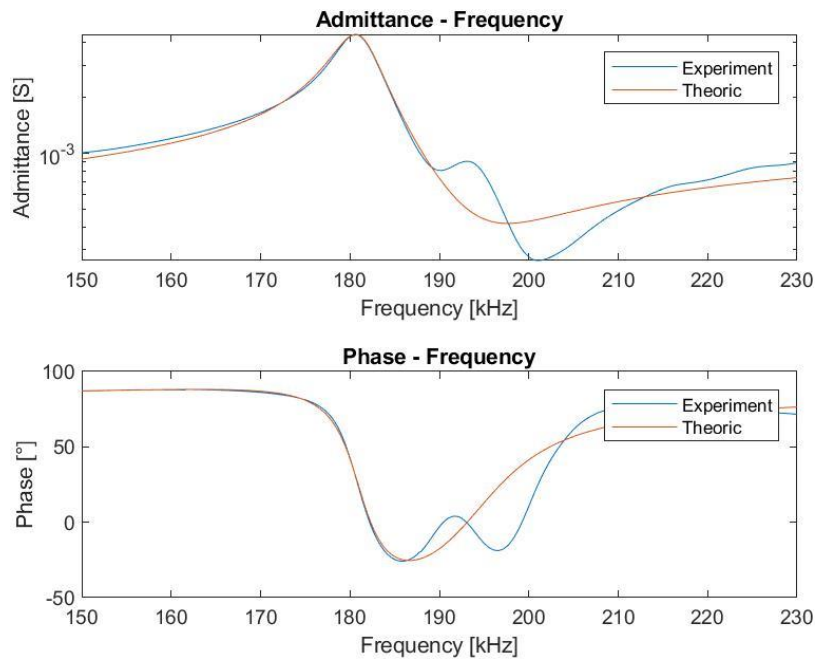


Figure 0.27 - Experimental, and theoretical behavior of a ME transducer in static regime, under a bias field of 0.1T. Sample E.

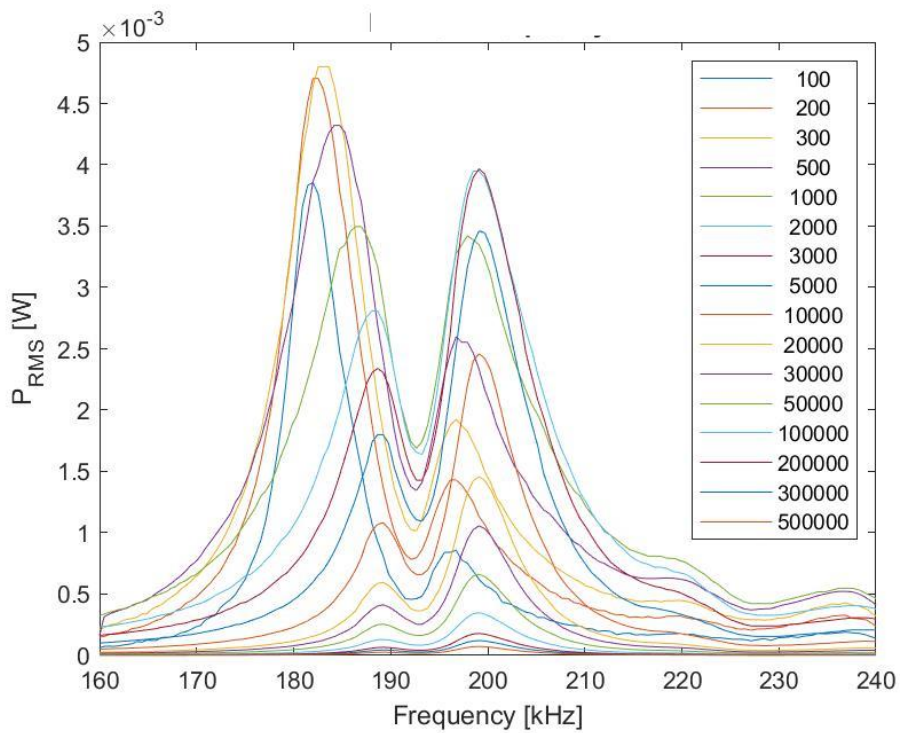
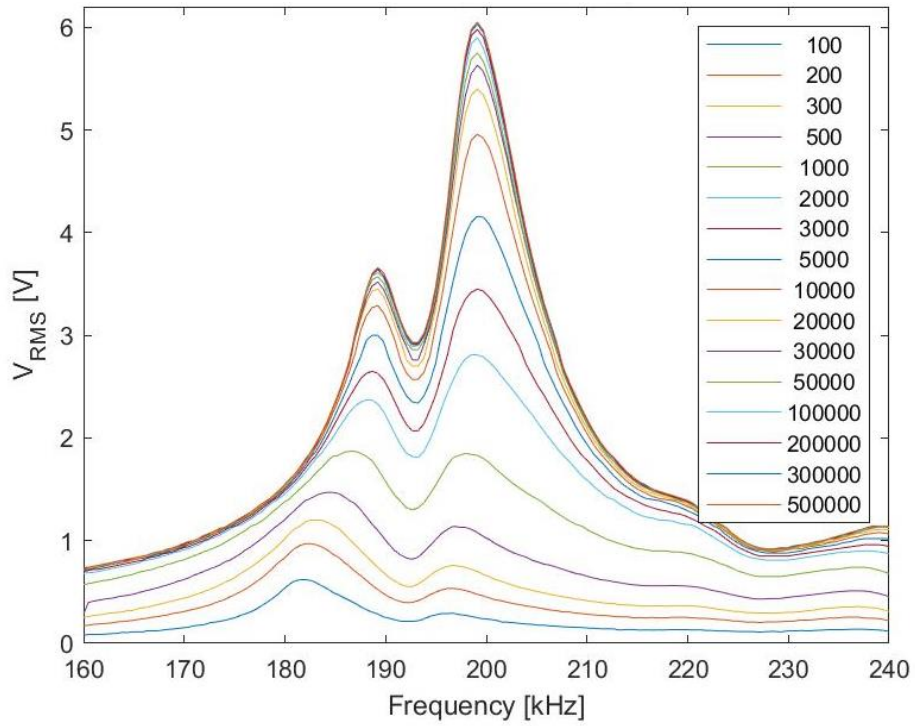


Figure 0.28 - ME RMS Voltage, and ME RMS Power at 0.1 T DC magnetic field, and 0.7 mT AC magnetic field, over the spectrum of frequency for different loads. Sample E.

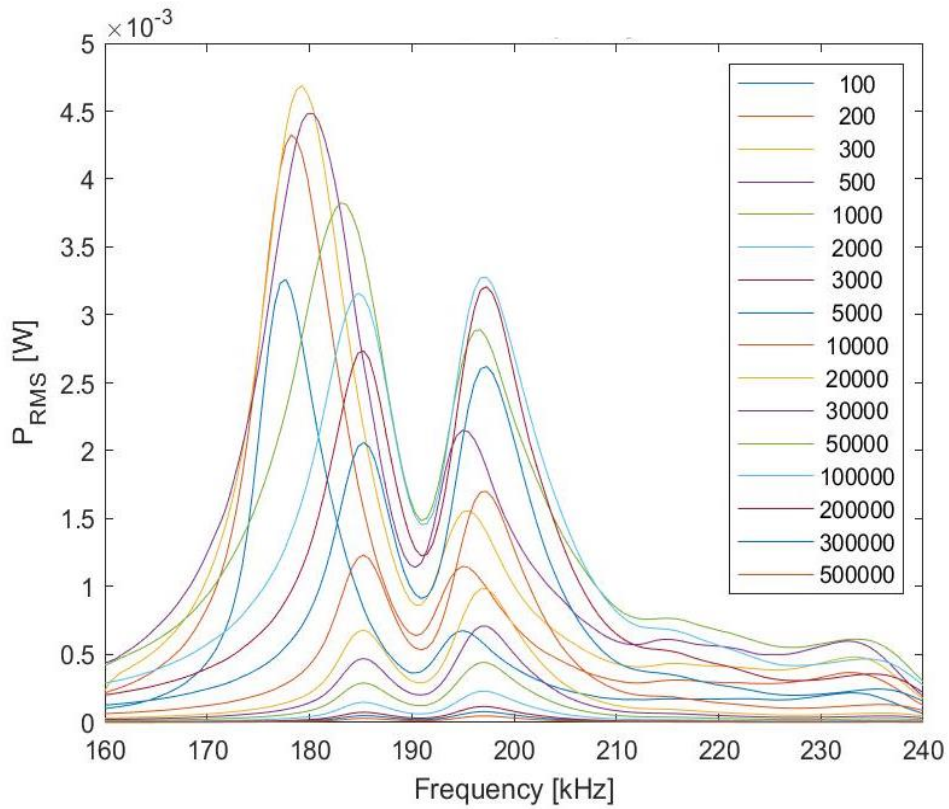
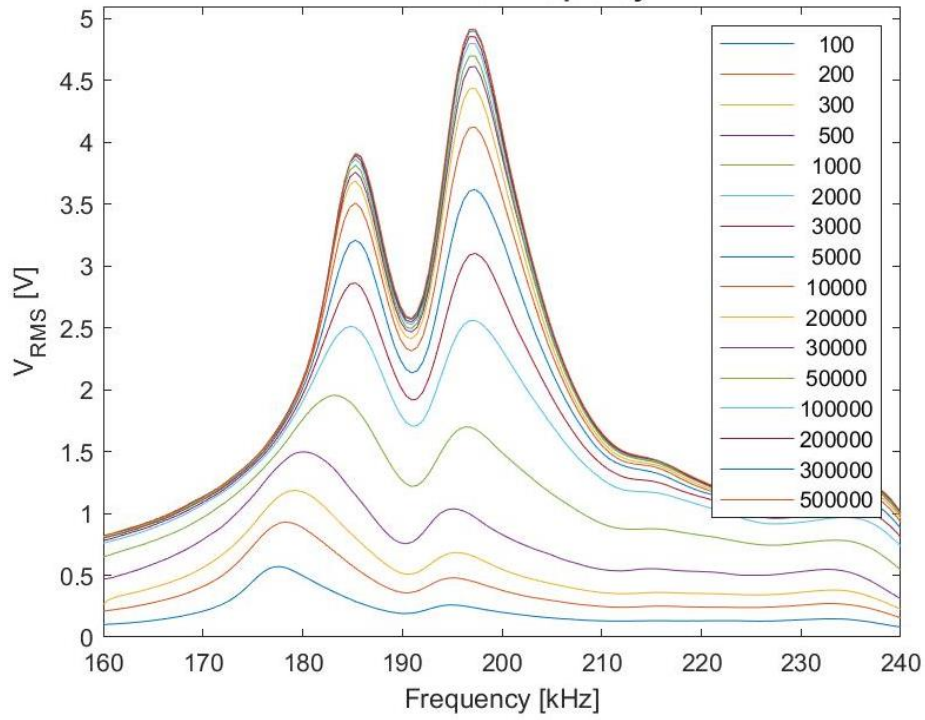


Figure 0.29 - ME RMS Voltage, and ME RMS Power at 0.058 T DC magnetic field, and 0.7 mT AC magnetic field, over the spectrum of frequency for different loads. Sample E.

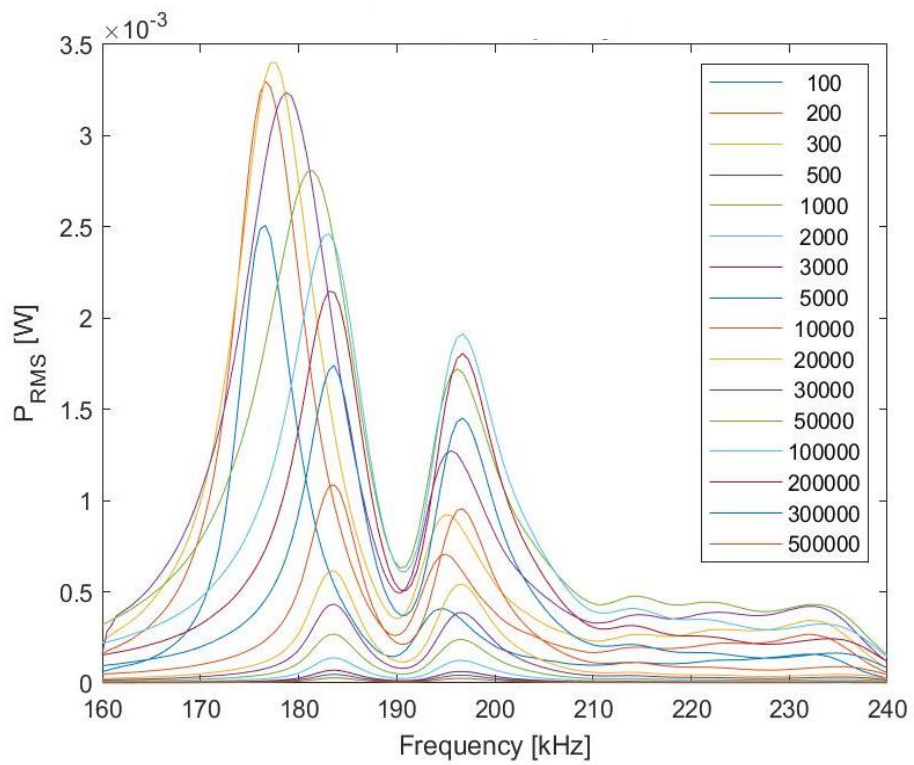
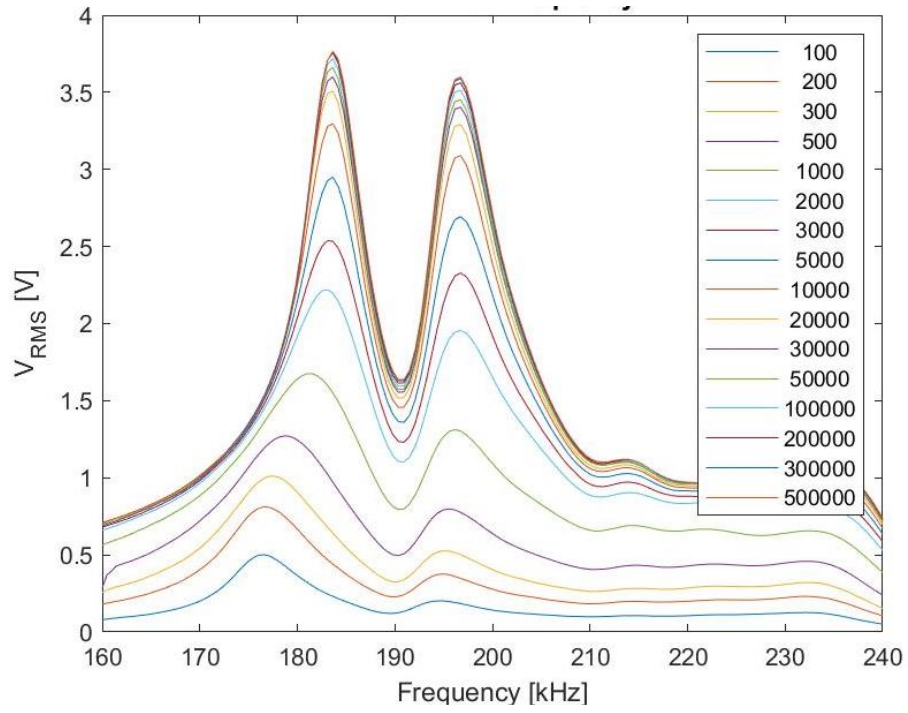


Figure 0.30 - ME RMS Voltage, and ME RMS Power at 0.036 T DC magnetic field, and 0.7 mT AC magnetic field, over the spectrum of frequency for different loads. Sample E.

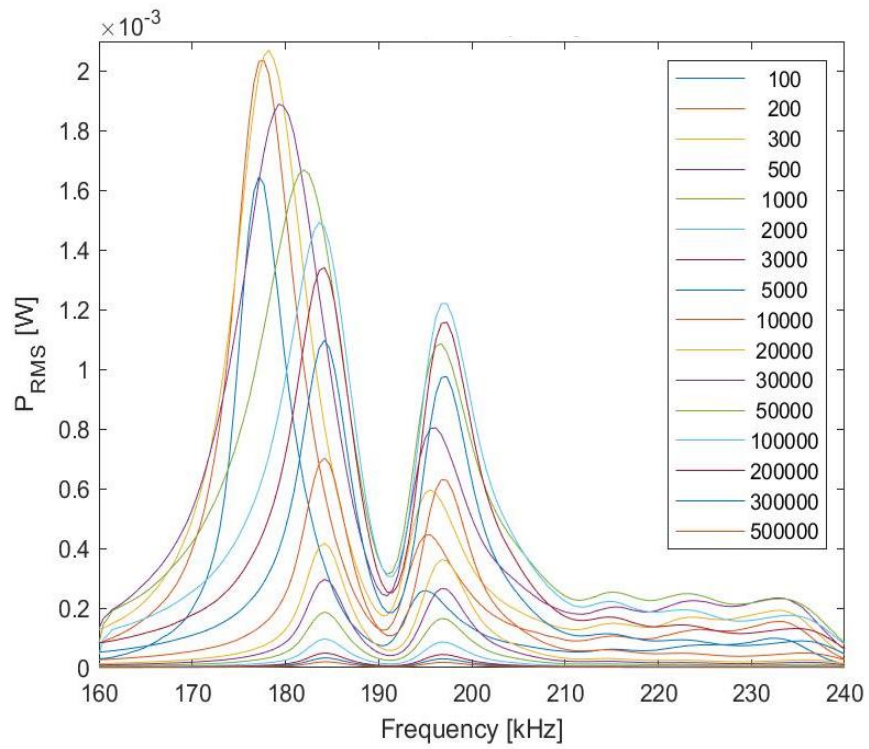
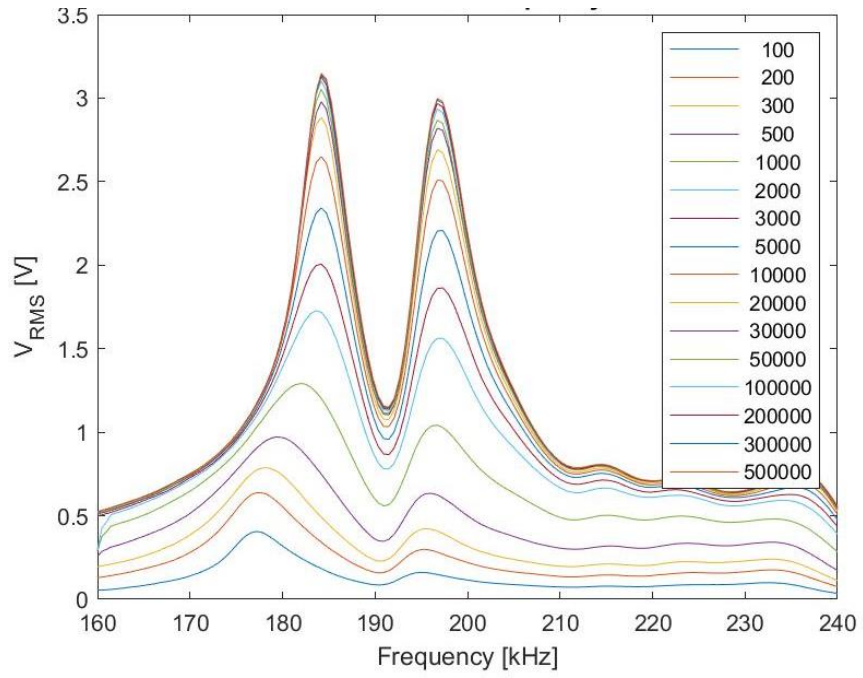


Figure 0.31 - ME RMS Voltage, and ME RMS Power at 0.023 T DC magnetic field, and 0.7 mT AC magnetic field, over the spectrum of frequency for different loads. Sample E.

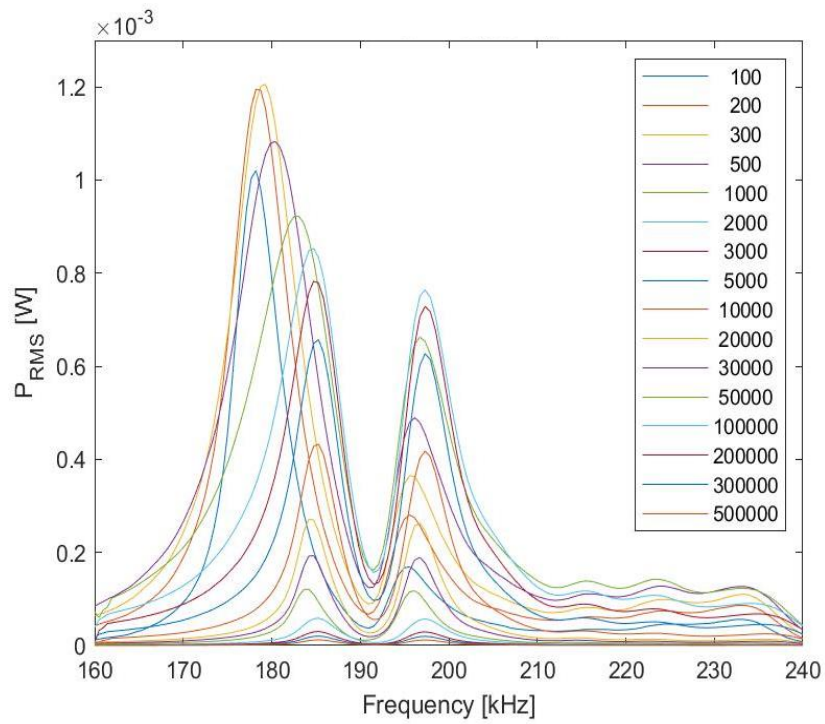
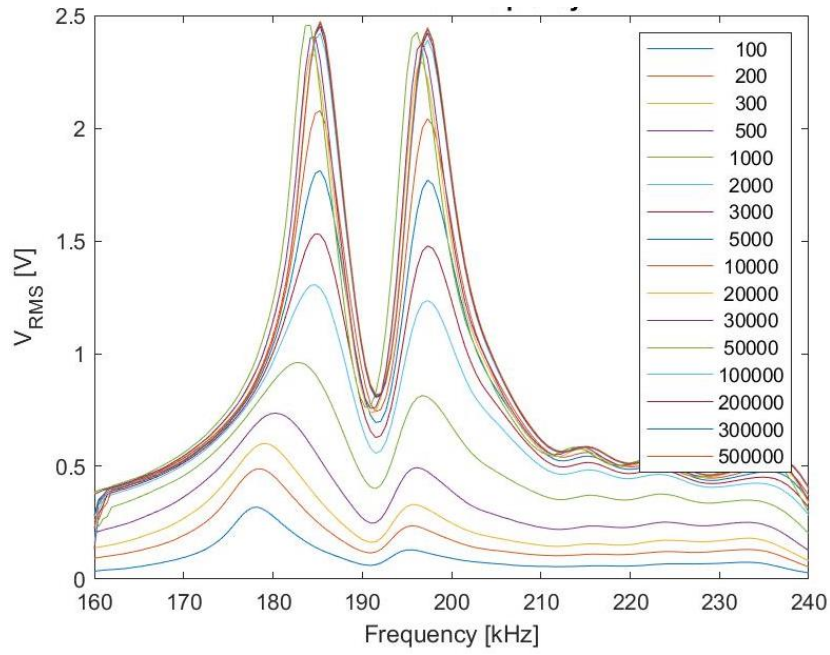


Figure 0.32 - ME RMS Voltage, and ME RMS Power at 0.016 T DC magnetic field, and 0.7 mT AC magnetic field, over the spectrum of frequency for different loads. Sample E.

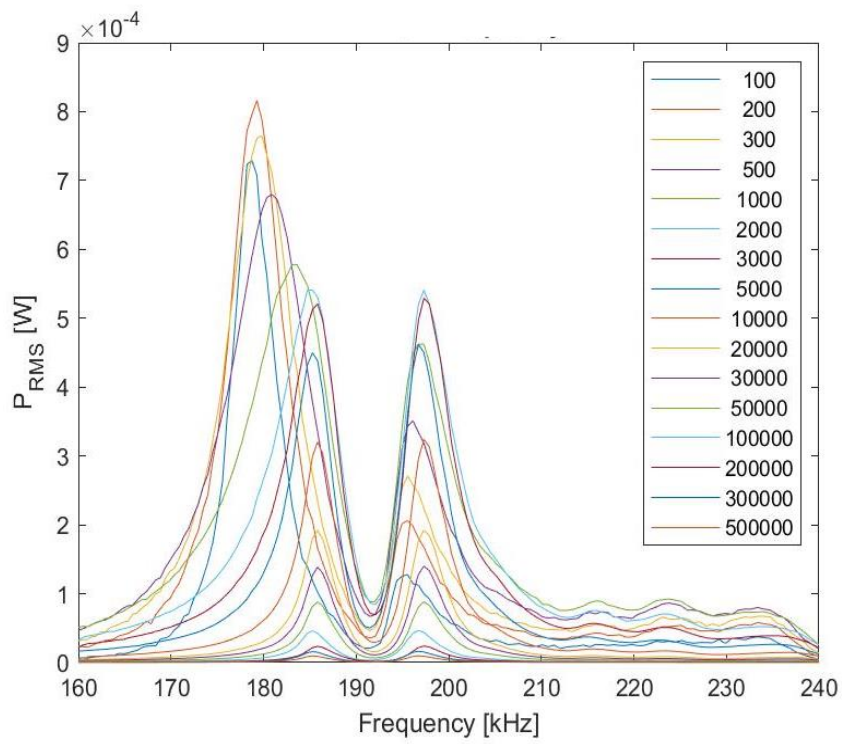
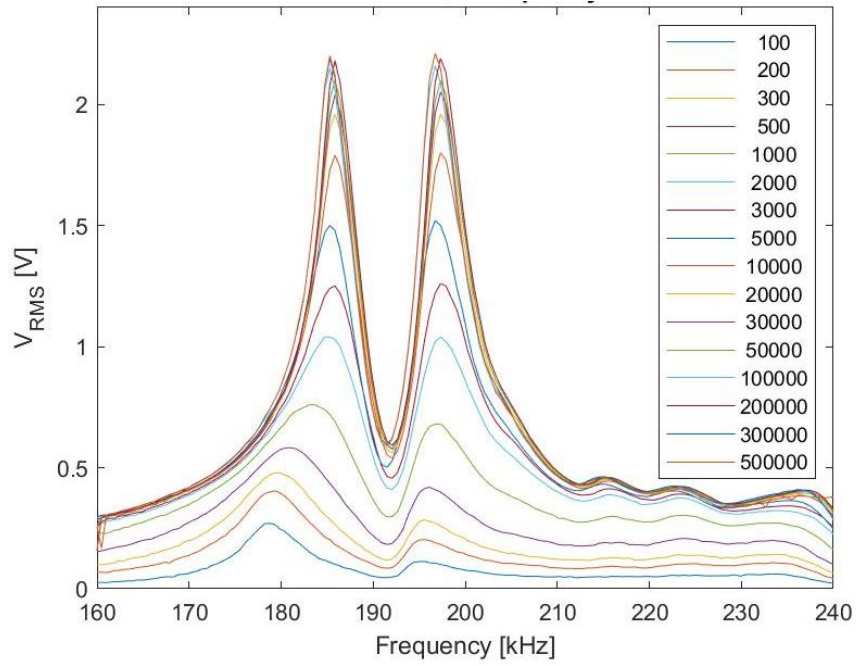


Figure 0.33 - ME RMS Voltage, and ME RMS Power at 0.012 T DC magnetic field, and 0.7 mT AC magnetic field, over the spectrum of frequency for different loads. Sample E.

Sample F)

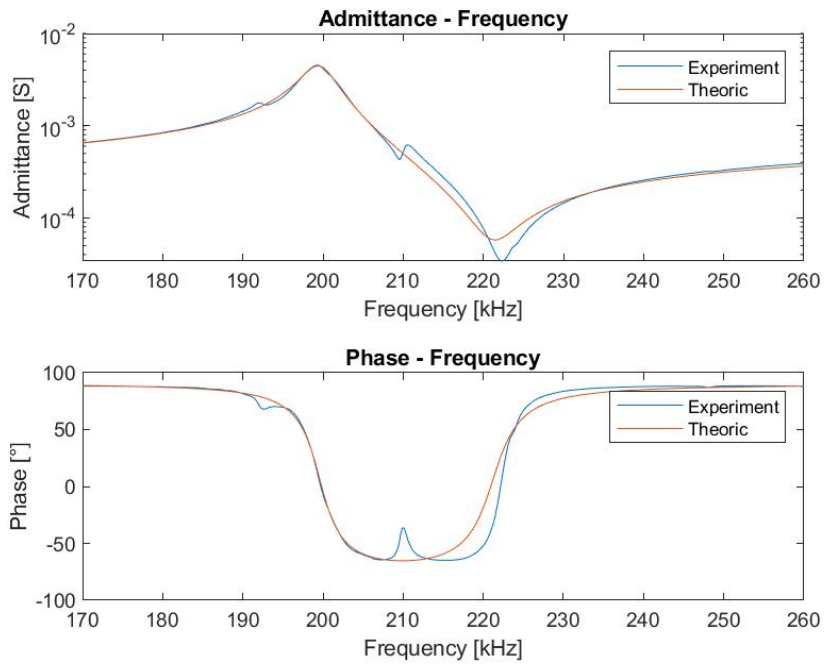


Figure 0.35 - Experimental, and theoretical behavior of a ME transducer in static regime in open circuit. Sample F.

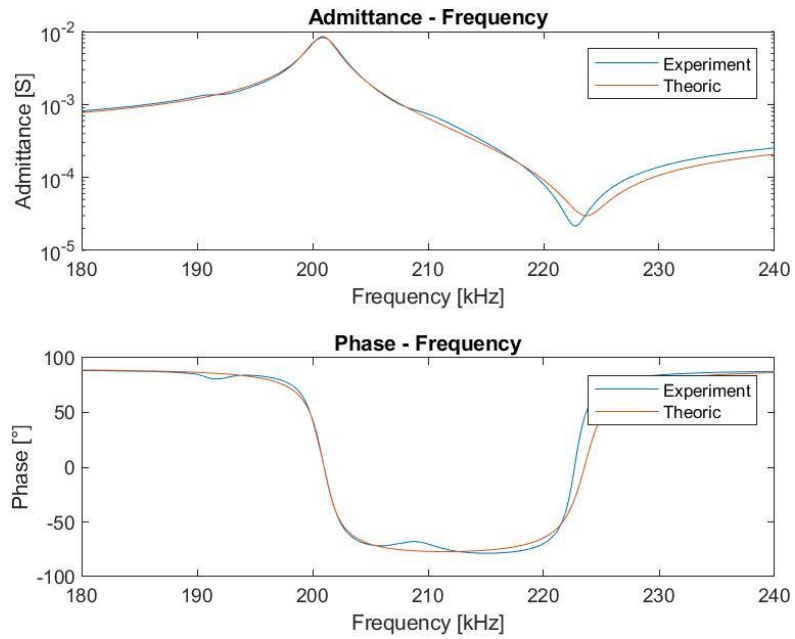


Figure 0.35 - Experimental, and theoretical behavior of a ME transducer in static regime, under a bias field of 0.1 T. Sample F.

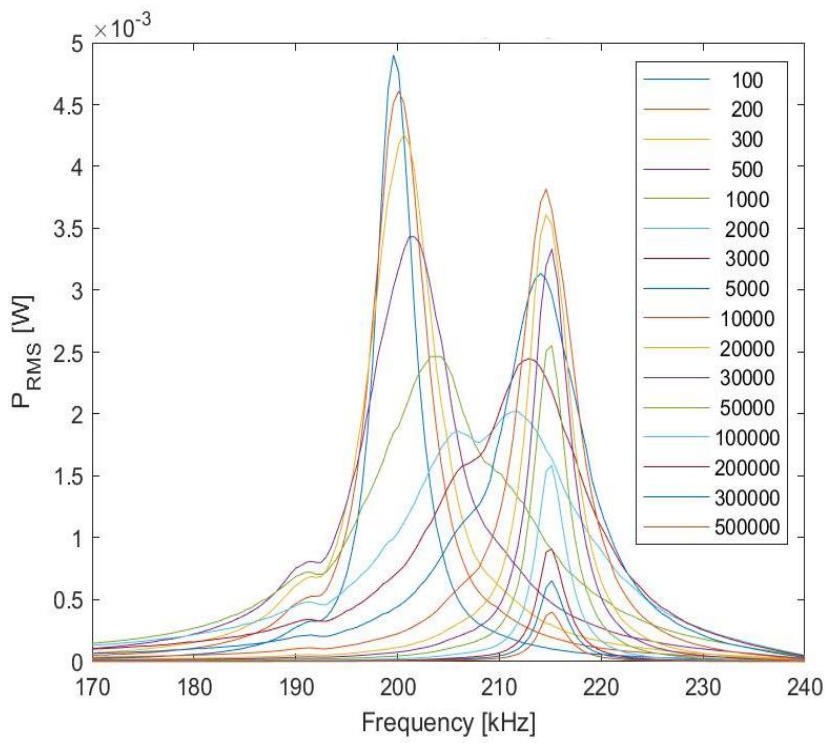
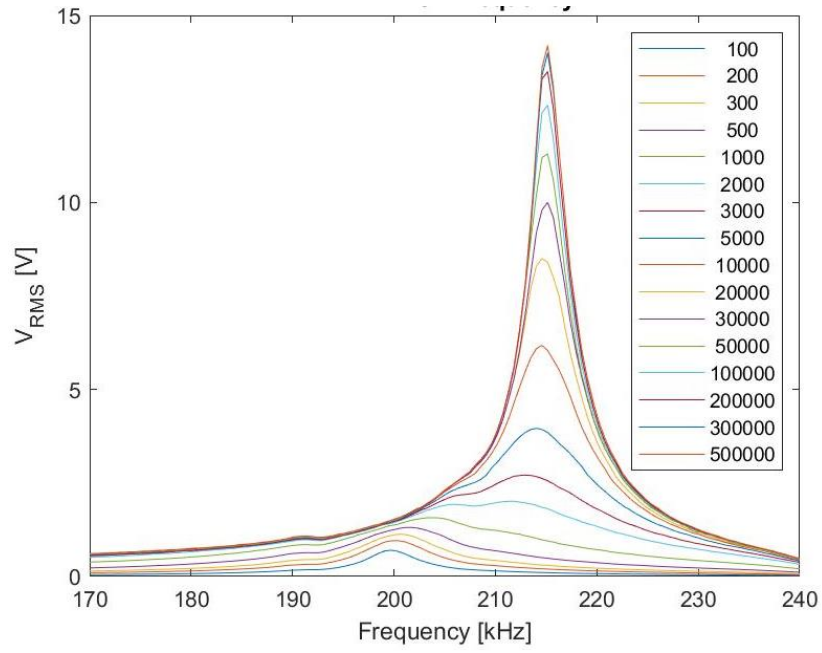


Figure 0.36 - ME RMS Voltage, and ME RMS Power at 0.1 T DC magnetic field, and 0.7 mT AC magnetic field, over the spectrum of frequency for different loads. Sample F.

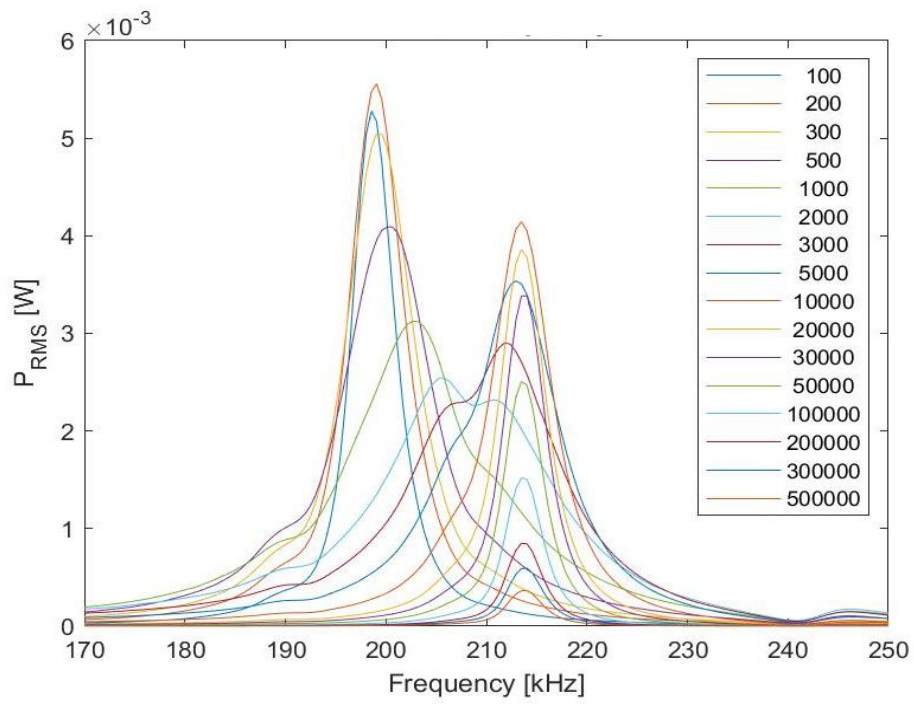
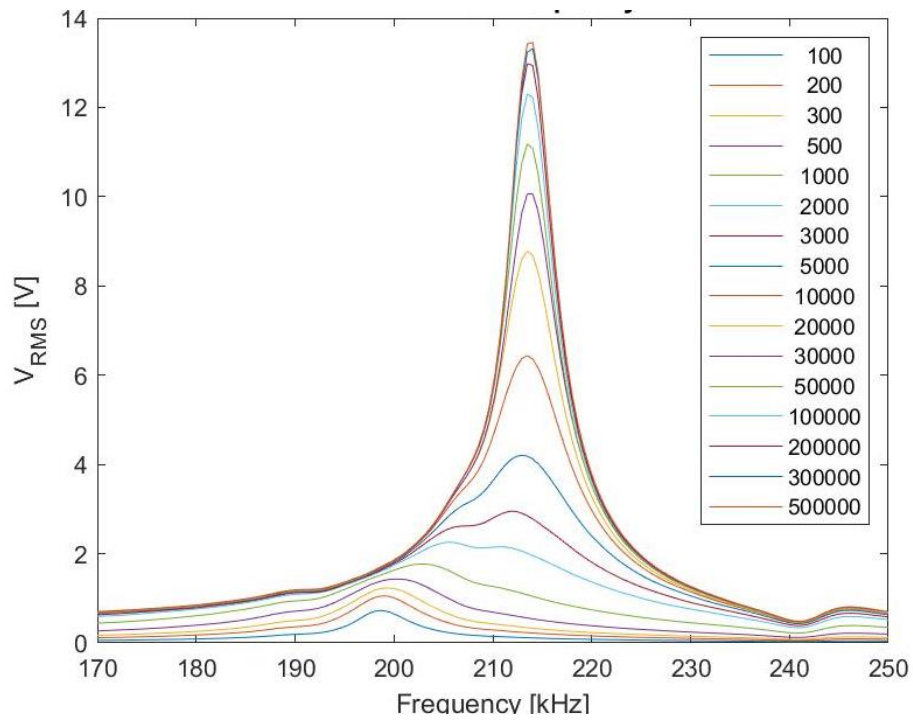


Figure 0.37 - ME RMS Voltage, and ME RMS Power at 0.058 T DC magnetic field, and 0.7 mT AC magnetic field, over the spectrum of frequency for different loads. Sample F.

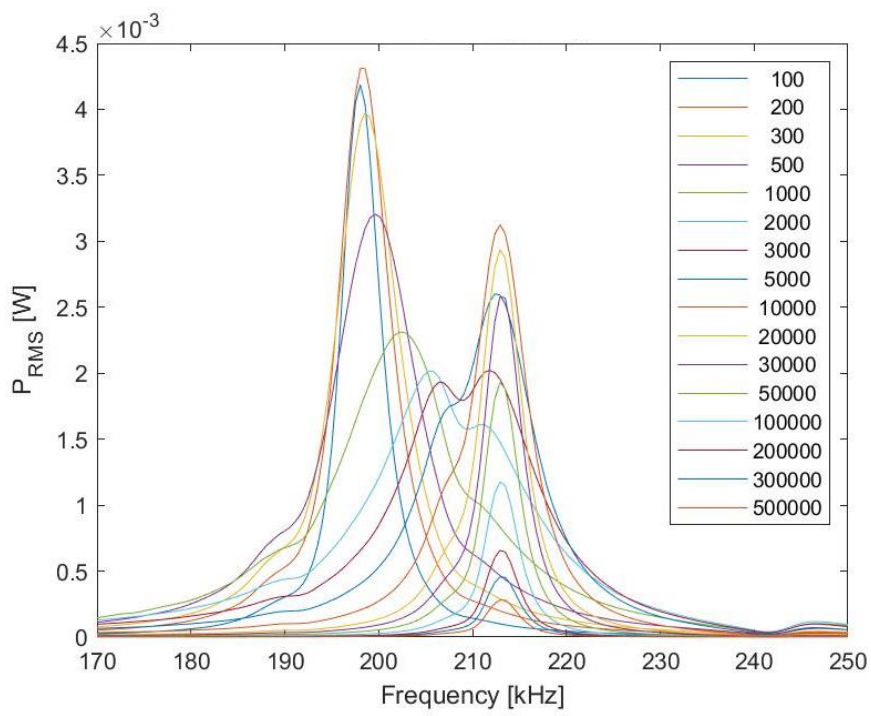
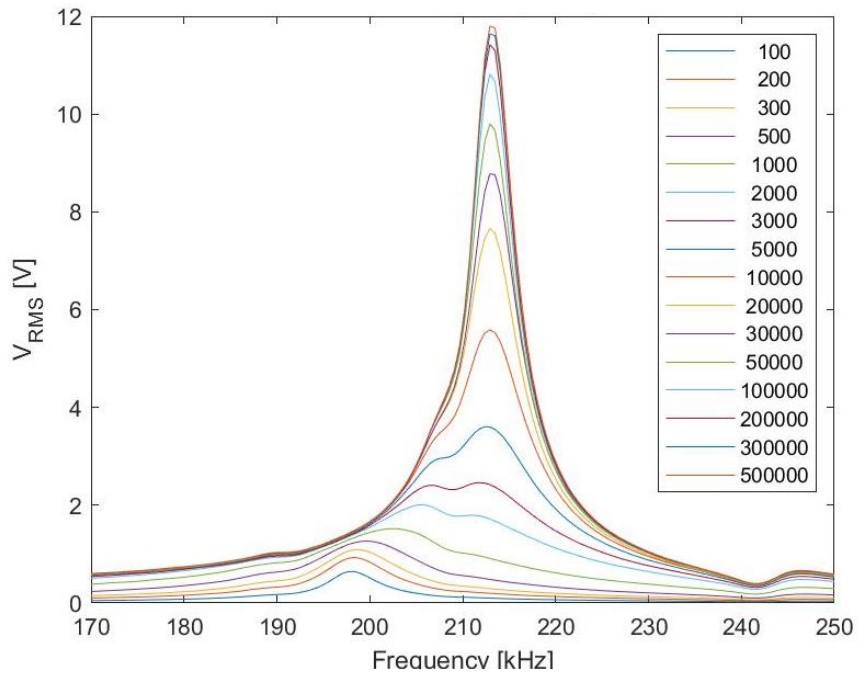


Figure 0.38 - ME RMS Voltage, and ME RMS Power at 0.036 T DC magnetic field, and 0.7 mT AC magnetic field, over the spectrum of frequency for different loads. Sample F.

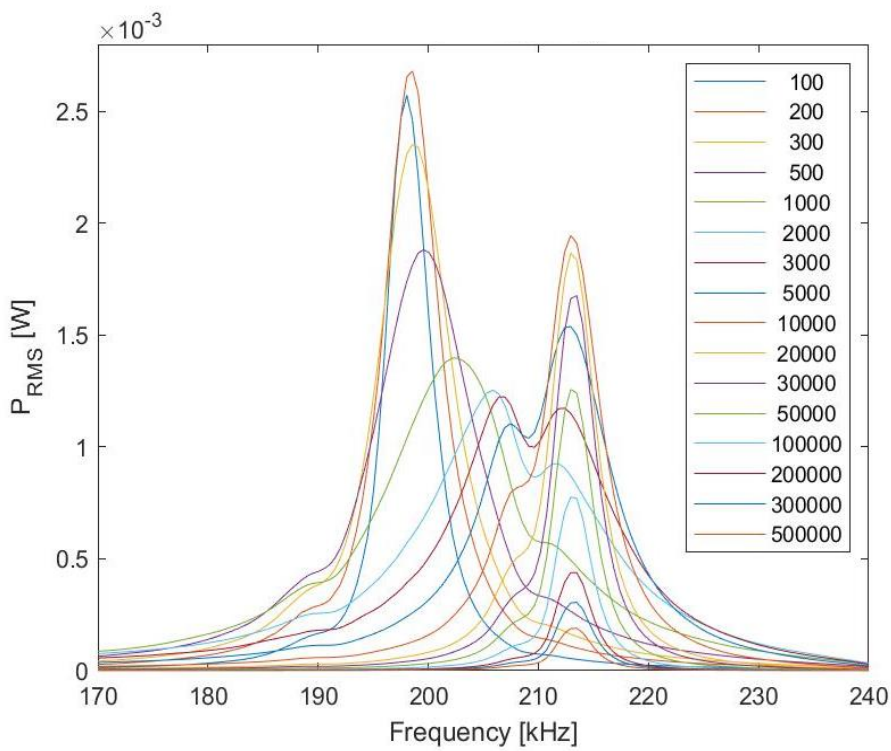
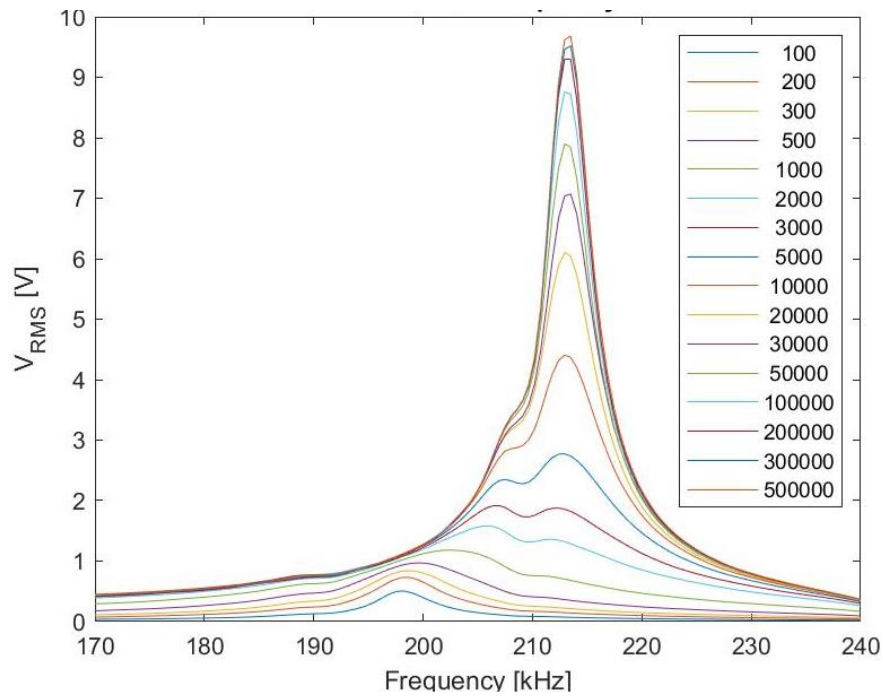


Figure 0.39 - ME RMS Voltage, and ME RMS Power at 0.023 T DC magnetic field, and 0.7 mT AC magnetic field, over the spectrum of frequency for different loads. Sample F.

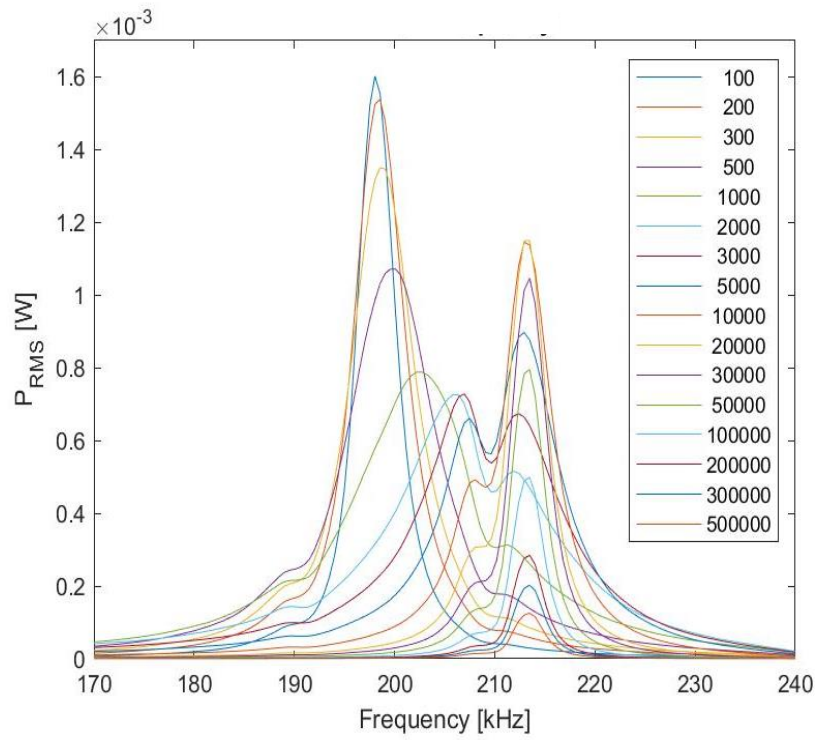
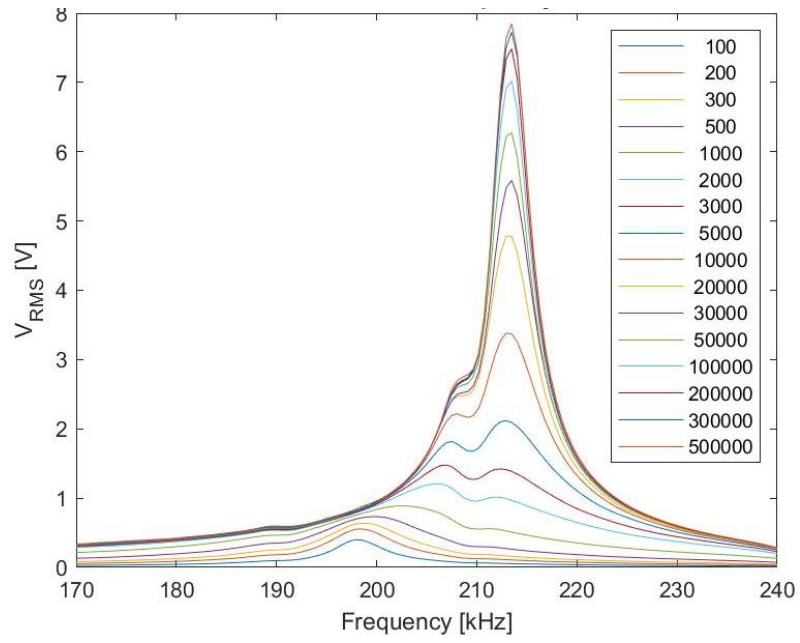


Figure 0.40 - ME RMS Voltage, and ME RMS Power at 0.016 T DC magnetic field, and 0.7 mT AC magnetic field, over the spectrum of frequency for different loads. Sample F.

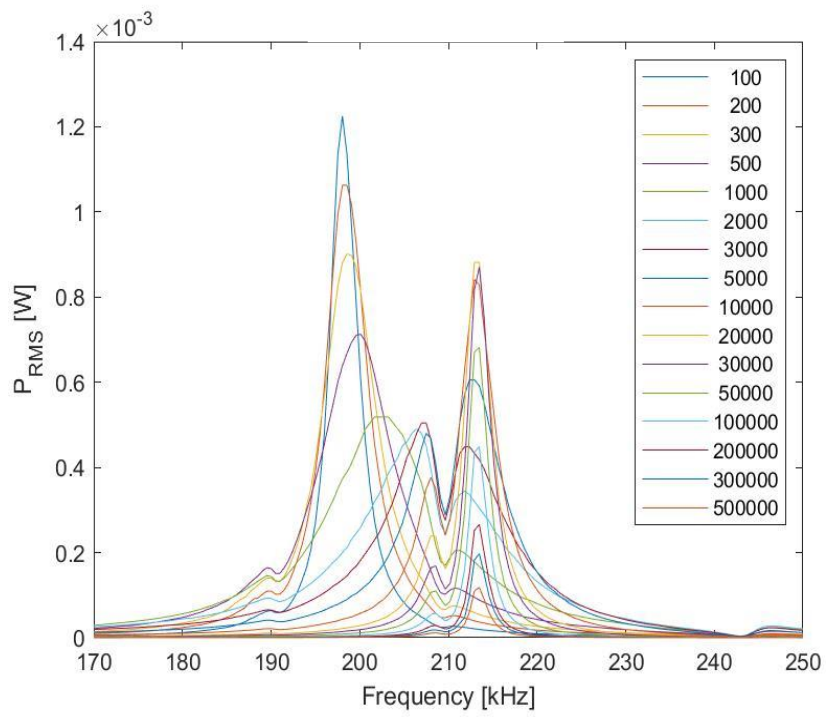
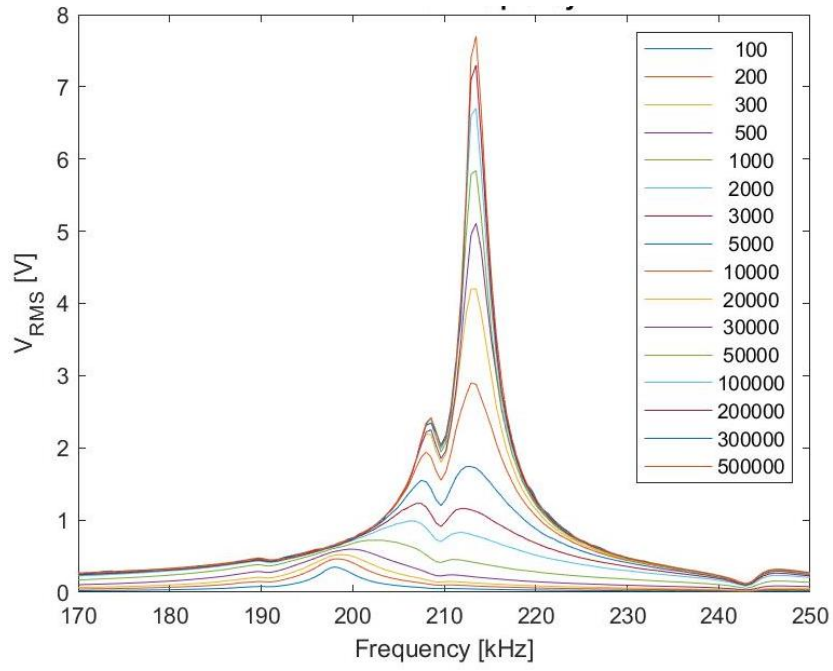


Figure 0.41 - ME RMS Voltage, and ME RMS Power at 0.012 T DC magnetic field, and 0.7 mT AC magnetic field, over the spectrum of frequency for different loads. Sample F.

Abstracts

Title : *Study of a MagnetoElectric Transducer to Wireless Power Medical Implants*

Keywords : *Wireless Power Transfer, MagnetoElectric transducer, Implantable Medical Devices, Magnetostriction, Piezoelectricity*

Abstract : Nowadays, the market of implantable medical devices is very large, and heterogeneous: of the order of 4,000 different device types tracked by the FDA in 2018 that can diagnose, monitor, and treat patients. Over the past decades, significant research has made to develop implanted systems more durable, and less invasive. Despite dramatic progress in all directions, energy autonomy remains the Achilles heel of active implants. The most employed energy source remains today the single-use battery. For long-lasting implants such as pacemakers, the replacement of depleted batteries is necessary, and requires a costly, and invasive surgical procedure. To overcome these issues, different techniques have been investigated. The first approach consists of using the biomechanical energy available inside of the body, and the second is to transmit energy from outside of the human body. In the first case, it is possible, for example, to power the new generations of pacemakers using MEMS energy harvesting devices supplied by the heartbeat. In the second case, the wireless power transmission by induction between two coils (one in the implant, the other outside the body) is an increasingly widespread technology in the biomedical sector, and in everyday life. The main difference between these two approaches is their power range: typically, a few microwatts for biomechanical energy harvesters, and milliwatts to watts for wireless power transmission. As part of this thesis, a new wireless power transmission technology has been developed. The considered system consists of two main blocks: the transmitter (out-body), and the receiver (located in the implant). The transmitter is a coil with no major constraints in terms of size, and on-body position. The receiver is a magnetolectric (ME) transducer. Investigating the use of a ME receiver, instead of the classical coil receiver, was in particular motivated by the willingness to reduce the alignment constraints of the classical coil-coil system, which is difficult to manage for implantable medical devices.

The considered ME transducer is a composite made of piezoelectric, and magnetostrictive layers. A magnetostrictive material has the property of mechanically deforming its structure, when exposed to a magnetic field. A piezoelectric material can be polarized, and create an electric field under mechanical stress (direct effect). Therefore, the magnetic field, generated by the transmitter coil, induces an elastic deformation of the magnetostrictive material. This mechanical deformation is transmitted to the piezoelectric material, in which an electric field appears, generating an electric voltage across its electrodes. Thanks to the magnetic-mechanical-electrical energy conversion, achieved by the ME transducer, the medical implant can be wirelessly supplied or recharged. In this thesis, receivers with different sizes have been tested: 10 mm or 16 mm in diameter, and thickness comprised between 2 mm, and 5 mm. Amongst numerous interesting experimental results, it was observed that thinner ME transducers with higher magnetostrictive volume ratio could generate higher electrical power than thicker samples with smaller magnetostrictive volume ratio. This result opens good prospects for the possibility of miniaturizing the ME transducer without losing efficiency in wireless power transfer. Concerning the in-vitro, and phantom tests, the ME transducer exhibited very promising performances, converting enough power to recharge an implant up to 20 mm away from the transmitter coil, in the most unfavorable orientation. Such results are impossible to get using a coil-coil energy transmission system is the most unfavorable position (receiver perpendicular to the transmitter). In conclusion, the obtained results present very promising prospects for wireless energy transmission, in terms of miniaturised devices, and adaptability to the localization of the implanted medical devices

Titre : *Etude d'un transducteur MagnétoElectrique pour la télé-alimentation sans fils des implants médicaux*

Mots clés : *Télé-alimentation sans fils, dispositifs médicaux implantables, effet magnétoélectrique, magnétostriction, piézoélectricité*

Résumé Actuellement, le marché des implants offre milliers de dispositifs différents pour diagnostiquer, traiter et suivre le patient. Dans la dernière décennie, d'importants travaux de recherche ont permis de rendre les dispositifs implantés plus durables et moins invasifs. La source d'énergie la plus utilisée reste néanmoins la pile électrochimique à usage unique. Pour un implant à long terme, il est nécessaire de remplacer la pile déchargée, ce qui nécessite une intervention chirurgicale coûteuse et invasive. Pour résoudre ces problèmes, deux approches ont été récemment proposées, la première consiste à utiliser l'énergie biomécanique du corps, et la deuxième consiste à transmettre de l'énergie depuis l'extérieur du corps humain. Dans le premier cas, par exemple, il est possible d'alimenter la nouvelle génération de pacemaker avec un MEMS piézoélectrique en utilisant l'énergie mécanique fournie par les battements cardiaques. Dans le deuxième cas, la télé-alimentation par induction entre deux bobines (l'une dans l'implant, l'autre à l'extérieur du corps) est une technologie de plus en plus répandue dans le secteur biomédical. Une différence importante entre ces deux techniques concerne les niveaux de puissance atteints : quelques μW pour la récupération d'énergie, et de quelques mW au W pour la télé-alimentation. Durant cette thèse, une nouvelle technologie de télé-alimentation a été développée. Le système considéré est constitué de deux blocs principaux, l'émetteur (situé à l'extérieur du corps) et le récepteur (situé dans l'implant). L'émetteur est constitué d'une bobine, sur laquelle il y a peu de contraintes en termes de taille et de position sur le corps. Le récepteur est un transducteur magnétoélectrique (ME). L'utilisation de ce système ME est notamment motivée par la possibilité de s'affranchir -au moins en partie- des contraintes d'alignement du système classique de bobine-bobine, alignement difficile à assurer dans le cas des dispositifs implantables. Le transducteur ME considéré est un composite constitué de matériaux piézoélectriques et magnétostrictifs.

L'élément magnétostrictif a la propriété de se déformer mécaniquement, lorsqu'il est exposé à un champ magnétique. L'élément piézoélectrique se polarise et crée un champ électrique sous l'effet d'une contrainte mécanique. Ainsi, lorsque la bobine émettrice génère un champ magnétique, à la résonance, elle crée une déformation élastique du matériau magnétostrictif. Cette déformation mécanique est transmise à la couche piézoélectrique, dans laquelle apparaît un champ électrique, générant ainsi une tension électrique. Grâce à cette conversion magnéto-mécano-électrique, l'implant médical peut être alimenté ou rechargé. Pendant cette thèse, des transducteurs de différentes dimensions ont été réalisés et testés : 10mm et 16mm de diamètre, et de 2 à 5 mm d'épaisseur. Parmi de nombreux résultats de caractérisation, un résultat très intéressant montre qu'à diamètre égal les transducteurs les plus minces avec une fraction volumique de matériau magnétostrictif plus importante permettent d'atteindre des puissances plus importantes qu'avec des échantillons plus épais et dont la fraction volumique de matériau magnétostrictif plus faible. Ce résultat ouvre d'intéressantes perspectives pour la miniaturisation de transducteurs ME tout en conservant une efficacité satisfaisante dans le transfert d'énergie. Concernant les tests in vitro, les résultats obtenus sont très prometteurs, montrant des puissances suffisantes pour recharger un implant jusqu'à 20 mm de distance de la bobine émettrice, dans l'orientation la plus défavorable. Un tel résultat est impossible à obtenir dans le cas d'un système bobine-bobine dans la position la plus défavorable (bobines perpendiculaires). En conclusion, les résultats obtenus présentent des perspectives très intéressantes pour la télé-alimentation, en termes de dispositifs miniaturisés et d'adaptabilité à la localisation des dispositifs médicaux implantés.